FERMILAB-THESIS-1979-16

# Measurements of Elastic Rho, Omega and Phi Meson Photoproduction Cross Sections on Protons from 30 to 180 GeV

by

Roland M. Egloff

A thesis submitted in partial fulfillment
of the requirements for the degree of

Doctor of Philosophy
(Physics)

in the
University of Toronto
1979

R. M. Egloff © 1979

# ABSTRACT

## Measurements of Elastic Rho, Omega and Phi Meson Photoproduction Cross Sections on Protons from 30 to 180 GeV

by

Roland M. Egloff

University of Toronto

The elastic photoproduction cross sections for rho ($\rho$) and phi ($\phi$) mesons from protons have been measured from 30 to 180 GeV and for omega ($\omega$) mesons from 46 to 180 GeV. The data were taken at the Tagged Photon Facility of Fermilab with a particle detection apparatus consisting of multilayer lead-iron-scintillator hadrometers, lead glass shower counter arrays, and multiwire proportional chambers (MWPC's).

The observed decay modes of the $\rho$ and $\phi$ mesons were $\rho \rightarrow \pi^+\pi^-$ and $\phi \rightarrow K^+K^-$. The apparatus, designed for the photon total cross section measurement, does not have a magnet or a Cerenkov counter. As a result, it is not possible to directly measure invariant mass spectra for the $\rho$ and the $\phi$ or to discriminate between pions and kaons. However, due to the full coverage of the forward hemisphere in the $\gamma p$ center-of-mass frame, it is possible to select events having exactly two tracks in the MWPC's and being consistent with

exclusive $\rho$ and $\phi$ production. A distribution of track opening angles, multiplied by the tagged photon energy, exhibits distinct peaks corresponding to $\rho \rightarrow \pi^+\pi^-$ and $\phi \rightarrow K^+K^-$ and provides an excellent substitute for the invariant mass spectrum.

The $\omega$ meson was detected in its all-neutral decay mode, $\omega \rightarrow \pi^0\gamma$, with all three photons measured in the lead glass shower counter arrays. The hadrometers were used to veto events with additional particles and thus ensure exclusive $\omega$ production. Two of the three photons were required to have an invariant di-photon mass consistent with neutral pion decay, $\pi^0 \rightarrow \gamma\gamma$. The resulting $\pi^0\gamma$ invariant mass distribution shows a clean peak at the $\omega$ mass with little background.

The energy dependences of the $\rho$, $\omega$ and $\phi$ photoproduction cross sections agree well with predictions made by using vector meson dominance (VMD) and an additive quark model. The $\rho$ and $\omega$ cross sections are approximately constant with energy while the $\phi$ cross section rises from 0.5 $\mu$b to 0.7 $\mu$b with increasing energy. The photon-vector meson coupling constants, obtained from a normalization of hadron elastic scattering cross sections to the photoproduction cross sections (using VMD and an additive quark model) are consistent with previous measurements at lower photon energies.

The differential cross section, $d\sigma/dt$ ($t$ = four momentum transfer squared), has been measured for $\omega$ photoproduction.

The t-dependence is of the form exp(bt) with b approximately 8.4 $GeV^{-2}$. The observed decay angular distribution for $\omega \rightarrow \pi^0\gamma$ is consistent with s-channel helicity conservation.

Published results from other experiments extend up to 18 GeV in photon energy for $\rho$ and $\phi$ photoproduction and up to 10 GeV for the $\omega$. The energy range covered by this experiment (up to 180 GeV) is thus unique and significantly higher than previously attained.

# PUBLICATIONS

Free to Bound Recombination and Screening Effects in CdS.
R. M. Egloff, K. Colbow; Can. J. Phys. 52, 721 (1974).

Measurement of J/ψ (3100) Photoproduction in Deuterium at 55 GeV.
With T. Nash et al.; Phys. Rev. Lett. 36, 1233 (1976).

Measurement of the Photon Total Cross Section on Protons from 30 to 180 GeV.
With D. O. Caldwell et al.; Paper submitted to the International Conference on Photon and Lepton Interactions, Hamburg, August, 1977.

Measurement of the Photon Total Cross Section on Protons from 18 to 185 GeV.
With D. O. Caldwell et al.; Phys. Rev. Lett. 40, 1222 (1978).

Measurement of Shadowing in Photon-Nucleus Total Cross Sections from 20 to 185 GeV.
With D. O. Caldwell et al.; Phys. Rev. Lett. 42, 553 (1979).

Measurement of Elastic Rho and Phi Meson Photoproduction Cross Sections on Protons from 30 to 180 GeV.
R. M. Egloff et al.; submitted to Phys. Rev. Lett. (May 1979).

Measurement of Elastic Omega Photoproduction Cross Section on Protons from 46 to 180 GeV.
R. M. Egloff et al.; in preparation.

ACKNOWLEDGEMENTS

I gratefully acknowledge the efforts of the many people who have contributed to the success of this experiment. I would especially like to thank all of the members of the experiment:

Drs. David O. Caldwell, John P. Cumalat, Phil J. Davis, Alan M. Eisner, Al Lu, George J. Luste, John F. Martin, Rollin J. Morrison, Tom Nash, Jim D. Prentice, and Steve J. Yellin.

It is a pleasure to thank my advisor Dr. George Luste and also Dr. Jim Prentice for their support and encouragement.

Special thanks go to Dr. Alan Eisner for his much appreciated help, particularly during the data analysis phase of the experiment. I also wish to thank Drs. Phil Davis and Steve Yellin for their help with the data analysis.

I particularly wish to thank my fellow graduate student (now Dr.) John Cumalat for sharing the hard work. I have very much enjoyed his company during the many long hours at the laboratory.

Many more people have contributed their efforts at different stages of this experiment. With apologies to those not explicitly mentioned, I wish to extend my appreciation to Drs. F. Murphy, A. Belousov, B.

Govorkov, M. G. Donnelly, and M. Franklin. I also thank the personell of the Fermilab Proton and Physics Departments, the Hydrogen Target Group and the Computing Department.

This research was supported in part by the U.S. Department of Energy and by the National Research Council of Canada through the Institute of Particle Physics of Canada.

TABLE OF CONTENTS

Chapter

I INTRODUCTION . . . . . 1

A: Background. . . . . 1
B: This Experiment . . . . . 9

II REVIEW . . . . . 15

A: Vector Mesons and VMD . . . . . 15
B: Photoproduction of ρ, ω and ϕ Mesons. . . . . 25
1. Rho Photoproduction. . . . . 25
2. Omega Photoproduction. . . . . 35
3. Phi Photoproduction. . . . . 40

III APPARATUS. . . . . 51

A: Introduction. . . . . 51
B: The Electron Beam . . . . . 52
C: The Tagging System. . . . . 54
D: The Target. . . . . 60
E: The Detectors . . . . . 64
1. General Description. . . . . 64
2. Central Shower Counters C and D. . . . . 65
3. Hadrometers S1, S2 and S3. . . . . 68
4. Hadrometer K (Z+TANC). . . . . 70
5. Pb Glass Arrays G2 and G3. . . . . 71
6. Pair and Recoil Counters . . . . . 74
7. MWPC . . . . . 75
F: Trigger Electronics and Data Storage. . . . . 77

IV ρ, ϕ ANALYSIS AND RESULTS. . . . . 99

A: Introduction. . . . . 99
B: Data Accumulation . . . . . 103
C: Data Analysis . . . . . 104
1. General. . . . . 104
2. Track Reconstruction . . . . . 106
3. Data and Monte Carlo . . . . . 109
4. Inelastic Events . . . . . 112
5. Corrections. . . . . 116
D: Results and Discussion. . . . . 118

V ω ANALYSIS AND RESULTS . . . . . 153

A: Introduction. . . . . 153
B: Data Accumulation . . . . . 154

cont.

C: Data Analysis . . . . . 155
1. General. . . . . 155
2. Shower Reconstruction. . . . . 157
3. Data and Monte Carlo . . . . . 170
4. Inelastic Events . . . . . 173
5. Corrections. . . . . 177
D: Results and Discussion. . . . . 179

VI SUMMARY. . . . . 210

APPENDIX A . . . . . 213
APPENDIX B . . . . . 216
APPENDIX C . . . . . 221
APPENDIX D . . . . . 226

LIST OF REFERENCES . . . . . 228

## LIST OF FIGURES

Figure

### CHAPTER I


I.A.1 Energy dependence of the $\gamma p$ total cross section and the average of the $\pi^+ p$ and $\pi^- p$ total cross sections divided by 200 . . . . . 12

I.B.1 Energy dependence of the photon total cross section . . . . . 13

I.B.2 Energy and atomic weight dependence of the photon absorption on complex nuclei. . . . . 14


### CHAPTER II


II.A.1 The vector meson dominance (VMD) model for photon-hadron interactions. . . . . 45

II.A.2 Diffractive elastic rho photoproduction diagram . 45

II.B.1 Diagram for non-resonant diffractive pion pair photoproduction . . . . . 46

II.B.2 Diagram for coherent diffractive rho photo-production from deuterons . . . . . 46

II.B.3 Reference frames for rho photoproduction. . . . . 47

II.B.4 Natural ($0^+$) and unnatural ($0^-$) spin parity exchange in the t-channel . . . . . 48

II.B.5 VMD diagrams for $\rho \to \pi^0\gamma$ and $\omega \to \pi^0\gamma$. . . . . 49

II.B.6 Suppression of $\pi\phi\rho$ coupling by Zweig's rule . . . 50


### CHAPTER III


III.A.1 Aerial view of Fermilab . . . . . 80

III.A.2 The beam lines to the experimental areas. . . . . 81

III.A.3 The Proton Area . . . . . 82

III.B.1 Electron beam line schematic. . . . . 83

III.B.2 Typical electron yield per incident 400 GeV proton as a function of electron energy . . . . . 84

III.C.1 Schematic of the tagging system . . . . . 85

III.C.2 Schematic of the tagging counters . . . . . 86

III.C.3 Typical fractional electron energy distribution across the tagging counters . . . . . 87

III.C.4 Schematic of tagging system logic . . . . . 88

III.D.1 Schematic of hydrogen target. . . . . 89

III.E.1 Experimental apparatus. . . . . 90

III.E.2 Fraction of tagged photon energy in C-counter on hadronic candidate events . . . . . 91

III.E.3 C-counter energy for 200 GeV incident electrons . 92

III.E.4 A: Energy sum in S3
B: Energy sum in K (Z+TANC)
for 90 GeV incident pions . . . . . 93


cont.

III.E.5 Schematic layout of the laser calibration system. 94
III.E.6 Schematic of MWPC amplifier card. . . . . 95
III.F.1 H-trigger logic . . . . . 96

CHAPTER IV

IV.A.1 Experimental apparatus. . . . . .128
IV.A.2 Track seperation at the MWPC'S versus decay angle for $M \rightarrow m+m$. . . . . .129
IV.A.3 Monte Carlo generated scatter plot of R versus $M_{\pi\pi}$ for $\rho \rightarrow \pi\pi$ . . . . . .130
IV.A.4 Monte Carlo generated R distribution for
A: $\rho \rightarrow \pi\pi$
B: $\phi \rightarrow KK$. . . . . .131
IV.C.1 A: Summed ADC pulse height spectrum for planes 2 and 3 of S1
B: Missing energy spectrum for H3 . . . . . .132
IV.C.2 Energy in the C-counter and G3 Pb glass array (G3IC) as a fraction of
A: the tagged photon energy
B: the total energy in H3 . . . . . .133
IV.C.3 Distribution of y-coordinate for MWPC tracks. . .134
IV.C.4 A: Schematic of track reconstruction. . . . . .135
B: Number of MWPC groups for $\rho$-$\phi$ candidates . . .136
IV.C.5 R distribution for the $E_o$ = 90 GeV data. . . . . .137
IV.C.6 R distribution for the $E_o$ = 135 GeV data . . . . . .138
IV.C.7 R distribution for the $E_o$ = 135 GeV empty target data. . . . . .139
IV.C.8 R distribution for non-interacting $e^+e^-$ pairs . .139
IV.C.9 Monte Carlo generated dipion mass spectrum resulting from the fit to the $E_o$ = 135 GeV data. .140
IV.C.10 Fraction of events with 0, 1 and >1 recoil counter signals . . . . . .141
IV.C.11 Monte Carlo generated scatter plot of recoil proton momentum versus recoil angle for elastic $\rho$ events. . . . . .142
IV.D.1 Energy dependence of the $\rho$ photoproduction cross section . . . . . .143
IV.D.2 $\phi$ signal above background (all the data). . . . . .144
IV.D.3 Energy dependence of the $\phi$ photoproduction cross section . . . . . .145
IV.D.4 Energy dependence of $d\sigma(\gamma p \rightarrow \phi p)/dt$ at t=0 . . . . .146
IV.D.5 VMD-quark model cross section normalized to the $\phi$ data of this experiment . . . . . .147

cont.

CHAPTER V


V.A.1 Schematic of Pb glass arrays G3 and G2. . . . . 184
V.C.1 A: $1-(1/\beta n)^2$ versus kinetic energy
B-F: Shower properties. . . . . 185
V.C.2 Radial dependence of dT/dr. . . . . 187
V.C.3 Fraction of the total shower energy contained in a Pb glass block. . . . . 188
V.C.4 Fraction of the total shower energy contained in a slab of Pb glass. . . . . 189
V.C.5 Shower data obtained with $E_e$= 90 GeV electrons incident on I-counter number 26 . . . . . 190
V.C.6 Two-photon invariant mass spectrum for $\omega \rightarrow \pi^0\gamma$ candidates (all the data) . . . . . 192
V.C.7 Three-photon invariant mass spectrum consistent with $\omega \rightarrow \pi^0\gamma$ (most of the data). . . . . 193
V.C.8 Energy distributions for $\omega \rightarrow \pi^0\gamma$ candidates in the $\omega$ mass region . . . . . 194
V.C.9 Mass distribution for $\pi^0\gamma$ events ($E_o$= 135 GeV data) . . . . . 196
V.C.10 Mass distribution for events which fail $\omega \rightarrow \pi^0\gamma$ analysis cuts because of an extra photon (all the data) . . . . . 198
V.D.1 Energy dependence of the $\omega$ photoproduction cross section . . . . . 199
V.D.2 Differential cross section for $\omega$ photoproduction. 200
V.D.3 Differential cross section for $\omega$ photoproduction for all the data. . . . . 201
V.D.4 The slope of the $\gamma p \rightarrow \omega p$ differential cross section as a function of energy . . . . . 202
V.D.5 Decay polar angle distribution for $\omega \rightarrow \pi^0\gamma$ (all the data) . . . . . 203

## LIST OF TABLES

Table

### CHAPTER III


III.E.1 Properties of lead glass. . . . . 97
III.F.1 Trigger definitions . . . . . 98


### CHAPTER IV


IV.B.1 Tagged photon and TgH trigger totals ($\rho$-$\phi$ data) . 148
IV.C.1 Analysis cuts . . . . . 149
IV.C.2 Fraction of events with 0, 1 and >1 recoil counter signals for $\rho$ and $\phi$ events. . . . . 150
IV.C.3 Correction factors ($\rho$-$\phi$ data) . . . . . 151
IV.D.1 Results for $\gamma p \rightarrow \rho p$ and $\gamma p \rightarrow \phi p$ . . . . . 152


### CHAPTER V


V.B.1 Tagged photon and TgH trigger totals ($\omega$ data) . . 204
V.C.1 Analysis cuts . . . . . 205
V.C.2 Shower table. . . . . 206
V.C.3 Fraction of events with 0, 1 and >1 recoil counter signals for $\omega$ events. . . . . 207
V.C.4 Correction factors ($\omega$ data) . . . . . 208
V.D.1 Results for $\gamma p \rightarrow \omega p$. . . . . 209

# CHAPTER I INTRODUCTION

## A: Background

The study of the nature and behaviour of light has fascinated scholars for centuries.

> Are not all hypotheses erroneous which have hitherto been invented for explaining the phenomena of light, by new modifications of the rays?
>
> Newton (1642-1727), Opticks

The concept of the photon, or light quantum, exhibiting properties associated with both waves and particles was introduced during the first years of quantum mechanics. Electromagnetic interactions of photons with matter became well understood and accurately predictable.

> Are there not other original properties of the rays of light, besides those already described?
>
> Newton, Opticks

With the advent of high energy particle accelerators in the past few decades it became possible to study the interaction of high energy photons with protons and neutrons in nuclei. A great variety of experiments revealed a strong

similarity between photon-hadron ($\gamma p$, $\gamma n$) and hadron-hadron (pp, $\pi p$, Kp, etc.) collisions. That is, a photon with a billion times as much energy as a photon of visible light exhibits properties once thought to be possessed exclusively by hadrons, the relatively massive particles which undergo strong interactions. For example, the $\gamma p$ and $\pi p$ total cross sections both show the clear excitation of the same nucleon ($N^*$) resonances and above about 2 GeV level out and become approximately energy independent as shown in Fig. (I.A.1). The magnitude of the photon total cross section is, however, smaller than the hadronic cross section by about 200, or by approximately the fine structure constant in order of magnitude.

The photon total cross section on neutrons, extracted from measurements with deuteron targets, is nearly the same as for protons. High energy photon-nucleon interactions thus become charge independent and are therefore not of an electromagnetic nature.

The number of hadrons produced in $\gamma p$ interactions is consistent with a logarithmic increase as a function of photon energy, similar to the hadron multiplicities in purely hadronic interactions (such as pp). A measure of the probability that an interaction produces particles of a certain type (p, $\pi$, K, etc.) is called an inclusive cross section. Again, photon initiated inclusive reactions display similar features to those initiated by hadrons,

particularly in terms of the longitudinal and transverse momentum dependence of the inclusive cross sections.

The most striking characteristics of photon hadron interactions is the copious production of neutral vector mesons, i.e. hadrons with the same spin (1) and parity (-) quantum numbers as the photon (most prominently the $\rho$). The vector meson ($\rho$, $\omega$, $\phi$, $\psi$, etc.) photoproduction process exhibits the properties of diffraction scattering. There is a sharp forward peak in the angular dependence of the cross section, a scattering amplitude which is mainly imaginary (absorptive), and an (approx.) energy independent cross section.

The small cross section for $\gamma p$ interactions ($\simeq$115 $\mu$b at high energies; 1 $\mu b = 10^{-30} cm^2$) implies a mean free path for photons in nuclear matter which is much larger than nuclear dimensions. A high energy photon would therefore be expected to illuminate complex nuclei uniformly and the photon total cross section should be proportional to A, the atomic weight number of the target nucleus. Experiments have shown however that the cross section increases less rapidly with A (see Fig. [I.B.2]). This result is familiar for hadron interactions and is due to the strong absorption (small mean free path) of hadrons in nuclear matter, which is to say that the incident particle's interaction is almost always on the surface layer of the nucleus.

All these features suggest that the photon is in a

(virtual) hadronic state a small fraction of the time.

> The changing of bodies into light, and light into bodies, is very conformable to the course of nature, which seems delighted with transmutations.
>
> Newton, Opticks

The most direct information about the hadronic states of the photon is obtained from electron-positron annihilation experiments. Machines, known as particle storage rings, have been built in which high energy electrons and positrons are made to circulate in opposite directions with equal speed. When an electron and a positron meet head on and annihilate each other, the resulting energy (typically a few billion electron volts) is to a very good approximation entirely electromagnetic. The most likely outcome of an annihilation is the creation of a single, but virtual, photon. The photon is said to be virtual because it does not satisfy the energy-momentum relation, $E = pc$, valid for real photons. The momenta of the colliding electron and positron are equal in magnitude but opposite in direction and the total momentum before and after the annihilation is zero. The created photon thus has the summed energy of the electron and positron but zero momentum. For any particle (including the photon), $E^2 = (pc)^2 + (mc^2)^2$. It follows that a virtual photon resulting from a particle-antiparticle

annihilation has a non-zero mass, corresponding to $E = mc^2$.

According to Werner Heisenberg's uncertainty principle, the virtual photon only exists for an exceedingly short time before it materializes into real particles. A large fraction of the particles thus created are pairs of electrons and positrons and pairs of muons and antimuons. This process is a result of the electromagnetic nature of the photon and is very successfully described by the theory of quantum electrodynamics.

Evidence for the hadronic nature of photons is obtained by studying the production of hadrons resulting from the decay of the virtual photon. Experiments have shown that hadrons are indeed observed when the energy of the photon equals the rest mass of a vector meson ($\rho$, $\omega$, $\phi$, $\psi$). The vector meson lifetimes, although much longer than the lifetime of a virtual photon, are quite short. The observed hadrons are the long-lived particles into which the mesons decay, for example $\rho \rightarrow \pi^+\pi^-$ and $\phi \rightarrow K^+K^-$. Photons thus transform into vector mesons some fraction of the time which give rise to resonances and their decay products in electron-positron colliding beam experiments.

Real (m=0) high energy photons can be produced when high energy electrons are scattered in the Coulomb field of nuclei (bremsstrahlung). The energy of the emitted photon is equal to the difference in the electron energies before and after the collision.

Another method for producing high energy photons is to scatter visible light (from a laser) 180 degrees from a beam of high energy electrons (backward Compton scattering). The scattered photons are monoenergetic (for a fixed scattering angle) and retain the initial polarization of the laser light to a high degree (a useful property for certain experiments).

The decay of the neutral pion into two photons can also be used as a source of photons. A high flux of pions is readily produced by high energy collisions of protons with nuclei. The decay photons cover a wide range of energies which can only be known within some (kinematical) limits - a clear disadvantage of this method.

Real photons, unlike virtual photons from electron-positron annihilations, cannot produce massive particles in free space. A nucleus must be present to exchange momentum in order to satisfy energy and momentum conservation. The nature of real photons is studied by observing their interactions with protons and neutrons in targets made of different materials. For example, photon-proton interactions are best investigated with a target consisting of a flask filled with liquid hydrogen.

A physical photon can make transitions between a bare photon and virtual hadron states for a time interval consistent with Heisenberg's uncertainty principle. Such transitions are called vacuum polarization fluctuations.

The hadron states have the quantum numbers and the momentum of the photon but differ in energy by

$$\Delta E = E_H - E_\gamma = \sqrt{E_\gamma^2 + m_H^2 c^4} - E_\gamma \qquad \text{(I.A.1)}$$
$$\simeq m_H^2 c^4 / 2E_\gamma \quad (E_\gamma \gg m_H c^2)$$

where $m_H$ is the mass of the virtual hadron. According to the uncertainty principle, the lifetime of the virtual hadron state is

$$\Delta t = \hbar/\Delta E \simeq 2\hbar E_\gamma / m_H^2 c^4 \qquad \text{(I.A.2)}$$

Thus, for a fixed hadron mass, the photon is more and more likely to behave like a hadronic state with increasing energy. The velocity of the virtual hadron is at most the velocity of light, c, and the distance traversed during its lifetime is thus

$$\Delta z < c\,\Delta t \simeq 2\hbar E / m_H^2 c^4$$
$$\simeq 2\lambda\!\!\!^{-} E_\gamma / m_H c^2 \qquad \text{(I.A.3)}$$

where $\lambda\!\!\!^{-}$ is the reduced Compton wavelength of the hadron. The lowest mass vector meson is the $\rho$(773 MeV) for which $\lambda\!\!\!^{-} \simeq 0.3$ fm (1 fm = $10^{-13}$cm). The radius of a proton is approximately R = 0.8 fm. Therefore, the distance traversed by the virtual hadron becomes much larger than nuclear

dimensions at energies exceeding a few billion electron volts. Consequently, the interaction of a high energy photon with a target nucleus can be pictured as an interaction of a hadron which has become detached from the photon. The hadron's initial interaction will be primarily with the nucleons on the incoming side of the target nucleus due to the large cross section (small mean free path) for hadron-hadron collisions. The results of photon total-absorption studies on nuclei of increasing size (A dependence) and as a function of energy are consistent with this view as is shown in Fig. (I.B.2).

Diffractive photoproduction of vector mesons may be regarded as arising from the photon becoming a virtual vector meson, with the vector meson then scattering elastically on the target to produce the real vector meson final state. This process would be expected to have the characteristics of meson-nucleon ($\pi p$) elastic scattering, which is indeed found to be the case.

The simplest framework for describing the features of high energy photon interactions, and one which works remarkably well overall, is the Vector Meson Dominance (VMD) model. In this model the photon is assumed to be a well-defined linear superposition of vector mesons, most importantly the low mass $\rho$, $\omega$ and $\phi$, which mediate the interaction of the photon with other hadrons. A brief outline of VMD is given in Chapter II.

## B: This Experiment

This thesis reports a study of diffractive photoproduction of the rho, omega and phi ( $\rho$, $\omega$, $\phi$ ) vector mesons from protons at high energies. The data were taken at Fermilab's tagged photon facility by a collaboration of physicists from the University of Toronto, the University of California at Santa Barbara, and Fermilab, operating as Fermilab Experiment 25A. The main purpose of the experiment was to measure the photon total cross section on protons and complex nuclei (carbon, copper, lead) from 18 to 185 GeV. The energy dependence of the total cross section on protons, as measured by this experiment, is shown in Fig. (I.B.1) [Caldwell, 1978]. Results obtained from the A-dependence measurements are shown in Fig. (I.B.2) [Caldwell, 1979].

The collaboration of this experiment was involved in the design, construction and testing of the tagged photon facility which boasts the world's highest energy electron beam (operated at up to 200 GeV during this experiment). In 1975, the year after the discovery of the narrow vector meson $\psi$(3100), a low statistics measurement of $\psi$ photoproduction on deuterium was part of a test run using the just completed tagged photon facility in conjunction with a lead-glass spectrometer [Nash, 1976].

Data for the photon total cross section experiment were taken during 1976 [Cumalat, 1977]. The results on vector

meson photoproduction described in this thesis are based on the same data. Published results from other experiments extend up to 18 GeV in photon energy for $\rho$ and $\phi$ photoproduction and up to 10 GeV for the $\omega$. The energy range covered by this experiment (up to 180 GeV) is thus unique and significantly higher than previously attained.

The particle detection apparatus of this experiment was designed with the total cross section measurement in mind. As a result, some aspects of the apparatus are less than ideal for the study of exclusive processes. For example, there are no magnets for particle momentum measurements and no Cerenkov counters to aid in particle identification. This necessitates some novel techniques for the analysis of $\rho \rightarrow \pi^+\pi^-$ and $\phi \rightarrow K^+K^-$ events (Chapter IV).

About 90% of the omegas decay into charged and neutral pions ($\omega \rightarrow \pi^+\pi^-\pi^0$). This decay mode cannot be identified without an analysing magnet. The next most dominant decay of the omega, and the one employed in this experiment (Chapter V), is into three photons, $\omega \rightarrow \pi^0\gamma \rightarrow \gamma\gamma\gamma$, with a probability of about 9%. The photons are detected by two lead-glass arrays which were designed principly to aid in the identification of electron-positron pairs, a major background for the total cross section measurement. The construction of the arrays and their positions in the apparatus are not very favourable for the detection of omegas. The energy and position resolution for photons is

not ideal. This is evident from the broad $\pi^0$ and $\omega$ invariant mass spectra. However, the physics results of the analysis are not seriously affected by these difficulties due to the nearly background free nature of this all-neutral event category.

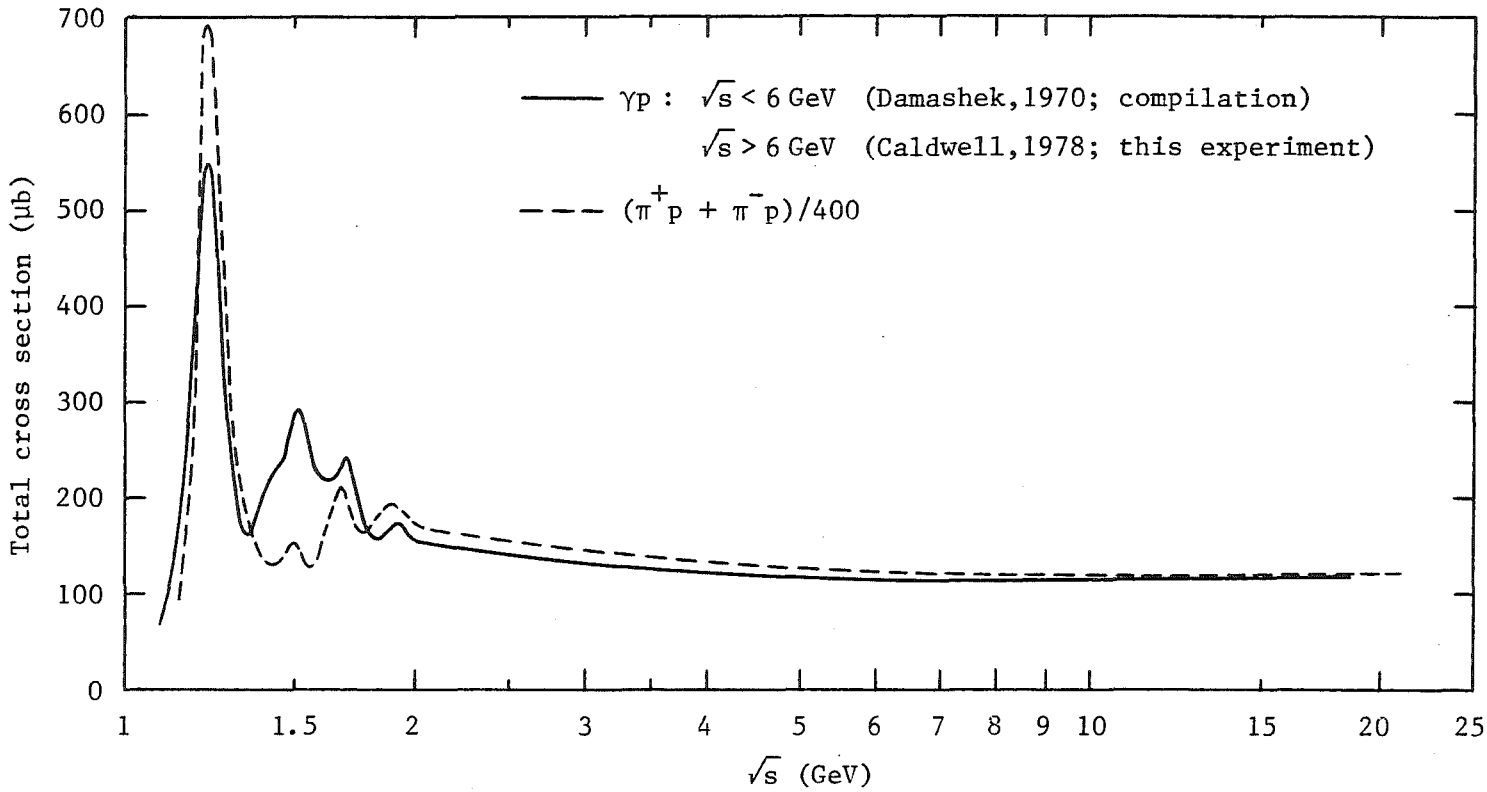


Figure (I.A.1) Energy dependence of the $\gamma p$ total cross section and the average of the $\pi^+ p$ and $\pi^- p$ total cross sections divided by 200.

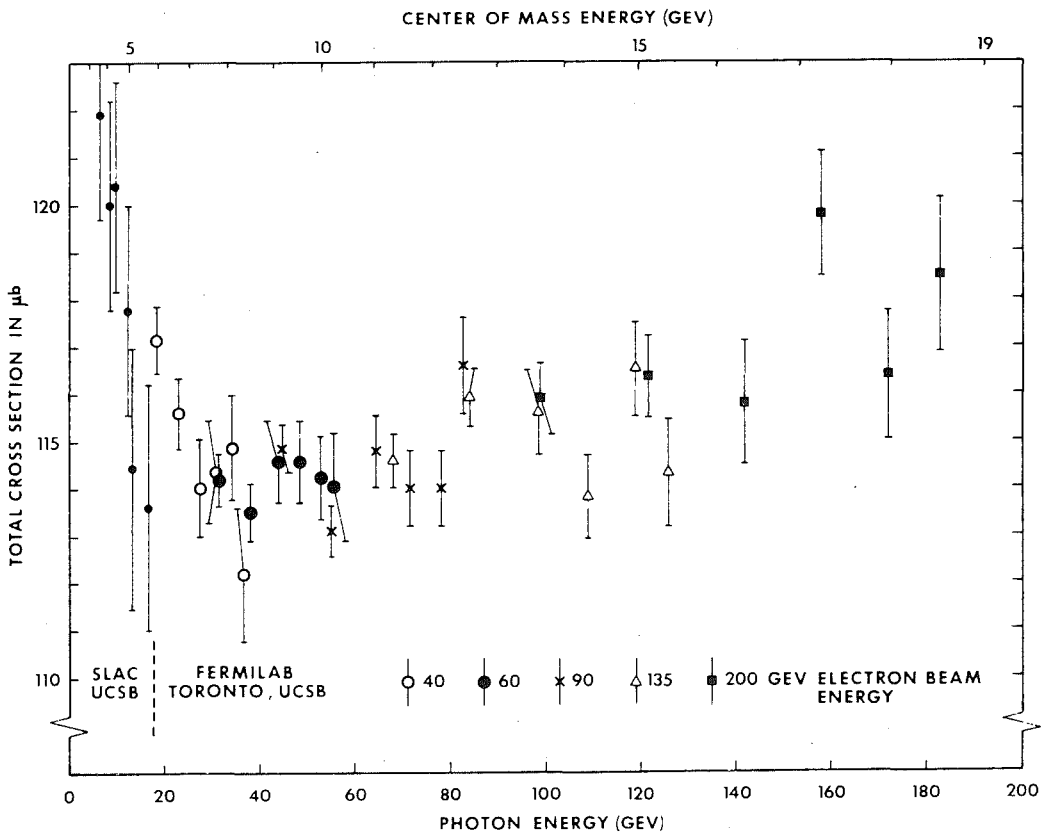


Figure (I.B.1) Energy dependence of the photon total cross section.

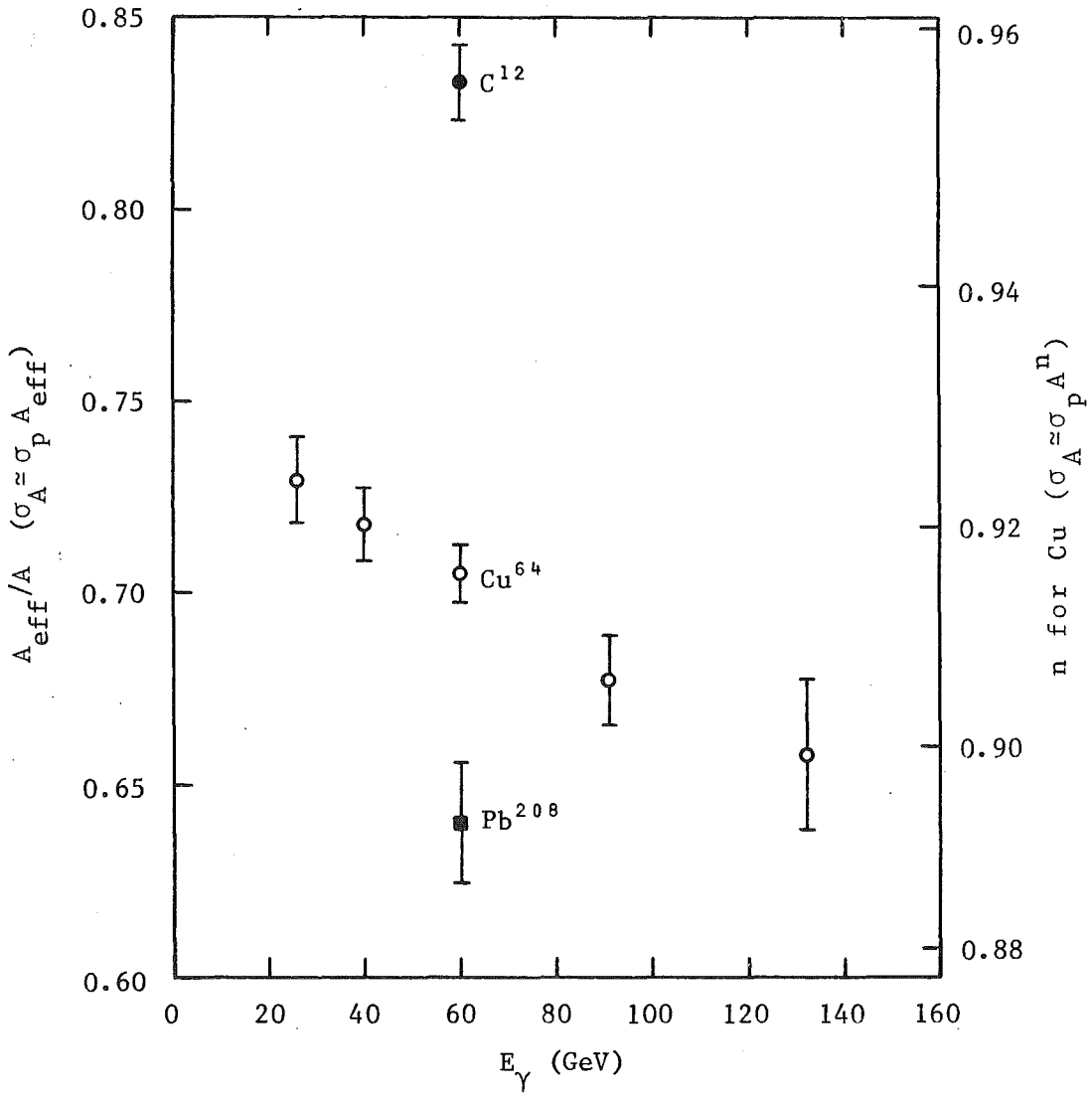


Figure (I.B.2) Energy and atomic weight dependence of the photon absorption on complex nuclei (carbon, copper, lead). $A_{eff}$ and n are defined by

$$\sigma_A = \frac{(A-Z)\sigma_n + Z\sigma_p}{A} A_{eff} \simeq \sigma_p A_{eff}$$

$$\sigma_A = \frac{(A-Z)\sigma_n + Z\sigma_p}{A} A^n \simeq \sigma_p A^n \qquad (A_{eff} = A^n)$$

where A, Z = atomic weight, atomic number (of the target)

$\sigma_p$, $\sigma_n$, $\sigma_A$ = photon total cross section on protons, neutrons, and complex nuclei.

# CHAPTER II REVIEW

## A: Vector Mesons and VMD

Some fifteen years of photon-hadron physics in the multi-GeV (billion electron volt) range can be summarized by stating that high energy photons can behave like hadrons. Except for the difference in magnitude of the cross sections, inclusive and exclusive photon induced reactions as well as the total photoabsorption cross section on nucleons and complex nuclei may be understood on the basis of hadronlike behaviour as formulated by VMD (vector meson dominance).

The hadronic part of the electromagnetic current is linked to the fields of the vector mesons as expressed by the current-field identity [Sakurai, 1960]

$$\begin{aligned} j(x) &= \sum_V \{em_V^2/2\gamma_V\} V(x) \qquad \text{(II.A.1)} \\ &= \frac{e}{2} \{ \frac{m_\rho^2}{\gamma_\rho} \rho(x) + \frac{m_\omega^2}{\gamma_\omega} \omega(x) + \frac{m_\phi^2}{\gamma_\phi} \phi(x) + \ldots \} \end{aligned}$$

The $\gamma_V$ are dimensionless coupling constants of the electromagnetic current to the vector meson fields V(x) and are assumed to be independent of the energy and mass of the photon. The electromagnetic current has the quantum numbers of the vector mesons, namely $J = 1$, $P = -1$, $C = -1$, $Y = 0$. The $m_V$ are the vector meson masses which enter into the

formula mainly for dimensional reasons, and e is the electron charge ($e^2/4\pi = \alpha = 1/137$).

The current-field identity relates the matrix elements for photon and vector meson induced reactions

$$T(\gamma A \to B) = \langle B | j | A \rangle$$
$$= \sum_V \frac{e m_V^2}{2\gamma_V} \frac{1}{m_V^2 - q^2} T(VA \to B) \qquad \text{(II.A.2)}$$

where V is a vector meson ( $\rho$, $\omega$, $\phi$, etc.), A and B are arbitrary hadrons, $q^2 = m_\gamma^2$ is the four-momentum squared of the photon, and $1/(m_V^2 - q^2)$ is the meson propagator. Finite width corrections in the propagator are necessary if $q^2 = m_V^2$ in electron-positron annihilation experiments. Relation (II.A.2) is represented by the diagram of Fig. (II.A.1). The photon is viewed as virtually dissociating into vector mesons which then interact hadronically with other hadrons.

Initially, the series in Eqn. (II.A.1) included only the low mass vector mesons $\rho$, $\omega$ and $\phi$. Comparison of VMD predictions with experimental data has shown that the $\rho$, $\omega$ and $\phi$ alone fail to saturate the current of Eqn. (II.A.1). For example, the predicted high energy photon ($q^2 = 0$) total cross section (or equivalently the imaginary part of the forward Compton amplitude) accounts for only about 80% of the measured cross section. The $q^2$ dependence of the total cross section as measured from inelastic electron-proton scattering ($q^2 < 0$) falls off with $q^2$ much more slowly than

predicted by Eqn. (II.A.2) for $\rho$, $\omega$, $\phi$ dominance. The difference is attributed to the coupling of the photon to higher mass vector mesons such as the $\rho''(1600)$ and the $\psi$ (3100), possibly including a spectrum (not necessarily discrete) of hypothesized vector states [Schildknecht, 1976]. The higher mass states have increased importance for virtual photon interactions because of the propagator factor in Eqn. (II.A.2).

A further generalization of the simple version of VMD includes diffraction-dissociation type transitions, particularly between neighbouring vector states (eg. $\rho'' \rightarrow \rho'$) [Schildknecht, 1976]. Transitions of this kind might be more probable for high mass states which are expected to be very broad resonances with significant overlap between neighbours. No experimental evidence exists at present for such transitions.

The scattering amplitude is defined by

$$\frac{d\sigma}{d\Omega} = |f(s,\Omega)|^2$$

and for elastic scattering

$$f(s,\Omega)\cdot 8\pi\sqrt{s} = T_{AA}(s,\Omega) = \langle A|T|A\rangle$$

Using Eqn. (II.A.2), VMD expresses the Compton scattering amplitude as a sum of vector meson photoproduction

amplitudes

$$f(\gamma p \to \gamma p) = \sum_V \frac{e}{2\gamma_V} f(\gamma p \to Vp) \qquad \text{(II.A.3)}$$

Also, vector meson photoproduction is related to vector meson elastic scattering

$$f(\gamma p \to Vp) = \frac{e}{2\gamma_V} f(Vp \to Vp) \qquad \text{(II.A.4)}$$

It is assumed that transitions like $V'p \to Vp$ $(V' \neq V)$ do not take place (diagonal assumption). Rho photoproduction is represented by the diagram of Fig.(II.A.2). Compton scattering can thus be written as

$$f(\gamma p \to \gamma p) = \sum_V \frac{e^2}{4\gamma_V^2} f(Vp \to Vp) \qquad \text{(II.A.5)}$$

The optical theorem relates the imaginary part of the elastic forward scattering amplitude, $f_o$, to the total cross section, $\sigma_T$,

$$\text{Im } f_o(A \to A) = \frac{p}{4\pi} \sigma_T(A) \qquad \text{(II.A.6)}$$

where p is the incident momentum in the c.m. system. Applying the optical theorem to Eqn.(II.A.5) gives

$$\sigma_T(\gamma p) = \sum_V \frac{\alpha\pi}{\gamma_V^2} \sigma_T(Vp) \qquad \text{(II.A.7)}$$

( $\alpha = e^2/4\pi$ ). Thus, the photon total absorption cross section is equal to the sum of vector meson total cross sections, scaled by the appropriate photon-vector meson coupling constants.

The differential cross section is related to amplitudes by

$$\frac{d\sigma}{d\Omega^*} = \frac{p^2}{\pi}\frac{d\sigma}{dt} = |f(t)|^2 \qquad \text{(II.A.8)}$$

where t is the square of the four-momentum transfer. For forward cross sections ($f_o = f(t=0)$)

$$\left.\frac{d\sigma}{d\Omega^*}\right|_{\theta=0} = \frac{p^2}{\pi}\left.\frac{d\sigma}{dt}\right|_{t=0} = |f_o|^2 = (\mathrm{Im}\ f_o)^2 + (\mathrm{Re}\ f_o)^2$$
$$= (1+\eta^2)(\mathrm{Im}\ f_o)^2 \qquad \text{(II.A.9)}$$

where $\eta$ is the ratio of the real to imaginary forward scattering amplitude ($\eta \to 0$ at high energies). Expressing the optical theorem in terms of a differential cross section then gives

$$\left.\frac{d\sigma}{dt}\right|_{t=0}(A \to A) = \frac{1+\eta^2}{16\pi}\sigma_T(A) \qquad \text{(II.A.10)}$$

Eqns. (II.A.4) and (II.A.8) give the differential cross section for vector meson photoproduction

$$\frac{d\sigma}{dt}(\gamma p \to Vp) = \frac{p_V^2}{k_\gamma^2}\frac{\alpha\pi}{\gamma_V^2}\frac{d\sigma}{dt}(Vp \to Vp) \qquad \text{(II.A.11)}$$

and with Eqn. (II. A. 10),

$$\left.\frac{d\sigma}{dt}\right|_{t=0} (\gamma p \to Vp) = \frac{p_V^2}{k_\gamma^2} \frac{\alpha\pi}{\gamma_V^2} \frac{1+\eta^2}{16\pi} \sigma_T^2(Vp) \qquad \text{(II. A. 12)}$$

The variables $k_\gamma$ and $p_V$ are the incident momenta for the $\gamma p \to Vp$ and $Vp \to Vp$ processes in the c.m. system, respectively ($s(\gamma p)=s(Vp)$). The threshold factor $(p_V/k_\gamma)^2$ is derived in Appendix B. VMD thus relates the cross section for vector meson photoproduction to vector meson-nucleon elastic scattering and total absorption cross sections.

It should be noted that the t=0 limit in Eqn. (II. A. 12) is not accessible experimentally. A minimum momentum transfer,

$$-t_{min} \simeq m_V^4/(2\, E_\gamma^{lab})^2 \quad (s \gg m_V^2) \qquad \text{(II. A. 14)}$$

is required to make up the mass difference in the photon-vector meson transition, $\gamma \to V$. The zero momentum transfer cross section is obtained from an extrapolation of measurements in the physical region.

The photon-vector meson coupling constants can be measured from the decay of the mesons into lepton pairs (electrons or muons). In the one photon exchange approximation the partial decay width $\Gamma(V \to e^+e^-)$ is related to the coupling constant by [Gell-Mann, 1962]

$$\Gamma(V \to e^+e^-) = \frac{\alpha^2}{12} \frac{4\pi}{\gamma_V^2} m_V \qquad \text{(II. A. 14)}$$

A partial decay width is given in terms of the experimentally measured total decay width, $\Gamma(V \to all)$:

$$\Gamma(V \to e^+e^-) = B(e^+e^-)\ \Gamma(V \to all) \qquad \text{(II. A. 15)}$$

where $B(e^+e^-)$ is the measured branching ratio into $e^+e^-$ pairs,

$$B(e^+e^-) = \sigma(V \to e^+e^-)/\sigma(V \to all) \qquad \text{(II. A. 16)}$$

The leptonic decay widths have been determined at electron-positron storage ring facilities (Orsay, Frascati, SLAC) from the reactions $e^+e^- \to V \to e^+e^-$ and $V \to all$ (it is an assumption of VMD that the coupling constants should be independent of $q^2$). The results are listed below [Leith, 1977] together with the coupling constants as given by Eqn. (II. A. 14) (coupling constants are generally quoted as $\gamma_V^2/4\pi$ ):

| V(MeV) | $\Gamma_{e^+e^-}$(keV) | $\gamma_V^2/4\pi$ |
|---|---|---|
| $\rho(773)$ | $6.48 \pm 0.9$ | $0.53 \pm 0.07$ |
| $\omega(783)$ | $0.76 \pm 0.08$ | $4.60 \pm 0.5$ |
| $\phi(1020)$ | $1.34 \pm 0.14$ | $3.4 \pm 0.3$ |

(II. A. 17)

| | | |
|---|---|---|
| $\psi(3100)$ | $4.8 \pm 0.6$ | $2.9 \pm 0.4$ |
| $\psi'(3685)$ | $2.2 \pm 0.3$ | $7.4 \pm 1.0$ |

Photoproduction of vector mesons provides an independent (but less direct) method for the determination of the photon-vector meson coupling constants. If the vector meson-nucleon total cross section, $\sigma_T(Vp)$, is known, Eqn. (II.A.12) can be used to determine the coupling constant. At energies above a few GeV most photoproduced vector mesons live long enough to traverse the target nucleon or nucleus before decaying. The nuclear absorption of the vector mesons can therefore be determined from a measurement of the relative yield of vector mesons in coherent photoproduction on complex nuclear targets of different sizes (A dependence). The calculation of $\sigma_T(Vp)$ from the data involves nuclear optics theory [Yennie, 1971] and an estimate for the ratio of the real to imaginary forward scattering amplitude, $\eta$. Results are consistent with hadronic cross sections, e.g. $\sigma_T(\rho p)$ and $\sigma_T(\omega p)$ measurements are typically 25-30 mb, $\sigma_T(\phi p)$ 10-12 mb (at around 7 GeV) and $\sigma_T(\psi p) \simeq 3.5$ mb (near 17 GeV) [Bauer, 1978].

Photoproduction measurements on protons can be used to determine coupling constants with the help of quark model predictions for vector meson elastic scattering cross sections and the VMD relation given by Eqn. (II.A.11). The

quark model predictions are based on the assumption that the scattering amplitude for hadron-hadron scattering is the sum of amplitudes for scattering of their quark constituents [Lipkin, 1966]. Quark-quark and quark-antiquark scattering is described in terms of three independent amplitudes, P, S and A, where (considering only u, d and s quarks)

$$\begin{aligned} P &= (ud) = (du) = (\bar{u}d) = (\bar{d}u) = (uu) = (dd) \\ P - S &= (su) = (sd) = (\bar{s}u) = (\bar{s}d) \\ P + A &= (u\bar{u}) = (d\bar{d}) \end{aligned} \qquad \text{(II. A. 18)}$$

Given the quark compositions

$$\begin{gathered} \pi^+ = u\bar{d} \qquad \pi^- = \bar{u}d \qquad K^+ = u\bar{s} \qquad K^- = \bar{u}s \\ \rho^0 = (u\bar{u}-d\bar{d})/\sqrt{2} \qquad \omega = (u\bar{u}+d\bar{d})/\sqrt{2} \qquad \phi = s\bar{s} \\ p = uud \end{gathered} \qquad \text{(II. A. 19)}$$

the assumption of additivity for quark scattering amplitudes implies that the $\phi p$ scattering amplitude is given by

$$\begin{aligned} f(\phi p \to \phi p) \equiv (\phi p) &= (s\bar{s})(uud) = 2(su) + (sd) + 2(\bar{s}u) + (\bar{s}d) \\ &= 6\,(P - S) \end{aligned} \qquad \text{(II. A. 20)}$$

and similarly

$$(\rho p) = (\omega p) = \frac{1}{2}(6P + 2A) + \frac{1}{2}(6P + A) = 6P + \frac{3}{2}A$$

$$(\pi^+p) = 6P + A \qquad (\pi^-p) = 6P + 2A$$
$$(K^+p) = 6P - 3S \qquad (K^-p) = 6P - 3S + 2A$$

It follows that

$$(\rho p) = (\omega p) = \frac{1}{2}\{(\pi^+p) + (\pi^-p)\} \qquad \text{(II.A.21)}$$
$$(\phi p) = (K^+p) + (K^-p) - (\pi^-p)$$

Using the optical theorem, Eqn. (II.A.6), and assuming the forward scattering amplitudes to be purely imaginary, the vector meson total cross sections are related to pseudoscalar meson total cross sections, i.e.

$$p_\rho\sigma_T(\rho p) = p_\omega\sigma_T(\omega p) = \frac{p_\pi}{2}\{\sigma_T(\pi^+p)+\sigma_T(\pi^-p)\} \qquad \text{(II.A.22)}$$
$$p_\phi\sigma_T(\phi p) = p_K\{\sigma_T(K^+p)+\sigma_T(K^-p)\} - p_\pi\sigma_T(\pi^-p)$$

Assuming that any possible phase difference between amplitudes can be neglected, the differential cross sections for elastic scattering are related by

$$p_\rho^2\frac{d\sigma}{dt}(\rho p) = p_\omega^2\frac{d\sigma}{dt}(\omega p) = \frac{p_\pi^2}{4}\{\sqrt{\frac{d\sigma}{dt}(\pi^+p)}+\sqrt{\frac{d\sigma}{dt}(\pi^-p)}\}^2 \qquad \text{(II.A.23)}$$
$$p_\phi^2\frac{d\sigma}{dt}(\phi p) = \{p_K\sqrt{\frac{d\sigma}{dt}(K^+p)}+p_K\sqrt{\frac{d\sigma}{dt}(K^-p)}-p_\pi\sqrt{\frac{d\sigma}{dt}(\pi^-p)}\}^2$$

The cross sections on the the right hand side of Eqns. (II.A.22) and (II.A.23) are measured quantities

[Carroll, 1976; Ayres, 1977] and can be used to predict vector meson cross sections.

The quark model and VMD give a theoretical prediction for the relative magnitudes of the vector meson-photon coupling constants. Writing the hadronic part of the electromagnetic current, Eqn. (II. A. 1), in terms of the quark make-up of the meson fields,

$$j = \frac{A}{\sqrt{2}} m_\rho^2 (u\bar{u}-d\bar{d}) + \frac{B}{\sqrt{2}} m_\omega^2 (u\bar{u}+d\bar{d}) + C\, m_\phi^2 (s\bar{s}) + D\, m_\psi^2 (c\bar{c})$$

and assuming that the photon couples to the quarks according to their charges (q(u)=2/3, q(d)=-1/3, q(s)=-1/3, q(c)=2/3) gives A=1, B=1/3, C=-1/3 and D=2/3. On comparing with Eqn. (II. A. 1) it is seen that

$$\frac{1}{\gamma_\rho^2} : \frac{1}{\gamma_\omega^2} : \frac{1}{\gamma_\phi^2} : \frac{1}{\gamma_\psi^2} = 9 : 1 : 2 : 8 \qquad \text{(II. A. 24)}$$

Several calculations of symmetry breaking schemes alter these ratios to [Oakes, 1967; Das, 1967]:

$$\gamma_\rho^{-2} : \gamma_\omega^{-2} : \gamma_\phi^{-2} = 9 : 0.65 : 1.33 \quad \text{and} \quad 9 : 1.2 : 1$$

## B: Photoproduction of ρ, ω and φ Mesons

### 1. Rho Photoproduction

The ρ meson was discovered in 1961 at Brookhaven (14 inch

hydrogen bubble chamber) in the reactions [Erwin, 1961]

$$\pi^- p \to \rho^0 n \to \pi^+\pi^- n$$
$$\pi^- p \to \rho^- p \to \pi^-\pi^0 p$$

The mass and width of the $\rho$ are 773 MeV and (roughly) 150 MeV, respectively. Its quantum numbers $I^G(J^P)C$ are $1^+(1^-)-$. The dominant ($\simeq$100%) decay mode is $\rho \to \pi\pi$.

From Eqns. (II.A.7) and (II.A.12), the part of the photon total cross section which is due to the $\rho$ component of the photon is given by

$$\sigma_T(\gamma p)\Big|_{\gamma\to\rho} = \frac{k_\gamma}{p_\rho}\sqrt{\frac{4\,\alpha\,\pi}{1+\eta^2}\,\frac{4\pi}{\gamma_\rho^2}\,\frac{d\sigma}{dt}\Big|_{t=0}(\gamma p \to \rho p)} \qquad \text{(II.B.1)}$$

and equals about 67 μb with $d\sigma/dt(t=0) = 80\ \mu b/GeV^2$ for $\rho$ photoproduction at high energies ($E_\gamma$>30 GeV). The $\rho$ thus accounts for about 60% of the photon total cross section which is partly the reason for the relatively large number of $\rho$ photoproduction experiments compared to the number of $\omega$ and $\phi$ experiments.

The photoproduced $\pi^+\pi^-$ invariant mass spectrum is dominated by the $\rho$ peak. What little background exists under the peak is observed to get smaller with increasing photon energy [Eisenberg, 1972; Ballam, 1972; Ballam, 1973]. The shape of the $\rho$ mass peak is skewed and shifted towards the low mass side of the distribution when compared

to a p-wave Breit-Wigner resonance shape. It is believed that the skewing and resultant mass shift is due to a non-resonant diffractive pion pair background [Drell, 1961] as depicted by the diagram of Fig. (II.B.1) which interferes with diffractive ρ production [Soding, 1965]. This background has the property of going to zero at the peak of the resonance and the interference term changes sign from positive to negative in passing through the ρ mass. The problem of the ρ shape is discussed at length in a paper by Spital and Yennie [Spital, 1974]. These authors also give a prescription for the determination of the ρ photoproduction cross section from measured mass spectra which minimizes the difficulties caused by the non-resonant background (see Chapter IV).

The ρ photoproduction cross section rises from threshold (≈1.1 GeV) to about 25 μb near 2 GeV and then gradually decreases with energy. The momentum transfer dependence is of the form $d\sigma/dt=A\exp(bt)$, with $b=8$ GeV$^{-2}$ approximately. The energy and t dependence of the ρ cross section agrees well with that of the elastic $\pi^0 p$ (average of $\pi^+ p$ and $\pi^- p$) scattering cross section as predicted by VMD-quark model relations, Eqns. (II.A.11) and (II.A.23). The ρ photoproduction and $\pi^0$ elastic scattering cross sections differ in magnitude by about 1:350.

The ω meson (mass = 783 MeV) has a small amplitude for $\pi^+\pi^-$ decay (violates G parity) which interferes with the ρ

in the vicinity of the $\omega$ mass [Renard, 1972]. High statistics experiments with good mass resolution have observed this effect for $\rho$ photoproduction on protons and heavier targets. The measured distortion of the $\rho$ mass spectrum in the interference region has been used to deduce the relative phase of the $\rho$ and $\omega$ amplitudes (production plus decay) and the $\omega \rightarrow \pi\pi$ branching ratio [Biggs, 1970a]. The $\rho$-$\omega$ interference phenomenon has also been observed in measurements of the electron-positron invariant mass spectrum ($\rho \rightarrow e^+e^-$) [Biggs, 1970b]. The difficulty of the $\rho$-$\omega$ interference experiment is reflected in a wide spread of the published results. A relative phase angle of $\sim 100^0$ appears favoured.

The phase of the $\rho$ production amplitude has been determined from asymmetry measurements of the electron-positron pair yield in the $\rho$ mass region [Alvensleben, 1970]. The asymmetry (under interchange of $e^+$ and $e^-$ four-vectors) results from the interference between the real Bethe-Heitler pair amplitude and the Compton amplitude, $\rho \rightarrow e^+e^-$. The phase of the $\rho$ photoproduction amplitude at 4-6 GeV (on Be and C targets) is found to deviate from pure imaginary corresponding to a ratio of the real to imaginary $\rho$-nucleon amplitude of $\eta \simeq -0.25$ (approximately).

Photoproduction of the $\rho$ from deuterons yields information on the isospin composition of the t-channel

exchange amplitude. The t-dependence of the measured coherent (no break-up of the deuteron) differential cross section, $d\sigma/dt(\gamma d \rightarrow \rho d)$, exhibits a very steep exponential fall-off for low $-t$ ($<0.4$ GeV$^2$) and decreases with half the slope, $\exp(bt/2)$, for larger $-t$ values [Anderson, 1971]. The low $-t$ behaviour is explained by single scattering production as shown by diagram (a) of Fig. (II.B.2). Here the photon interacts with only one of the nucleons, which then transfers half of its momentum to the spectator nucleon in order for the deuteron to stay bound. For larger $-t$ values the $\rho$ is produced on one nucleon and then re-scatters on the other, giving approximately equal recoil momentum to both nucleons. Double scattering production is illustrated by diagram (b) of Fig. (II.B.2). Coherence is lost if the initial scattering process breaks up the deuteron. Except for low $-t$ ($<0.1$ GeV$^2$), the incoherent deuteron cross section has the same t-dependence as the $\rho$ cross section for proton targets but is larger in magnitude by a factor of two [McClellan, 1971a].

The isovector exchange amplitude couples with opposite sign to the proton and the neutron, i.e.

$$f(\gamma p \rightarrow \rho p) = T_0 + T_1 \qquad f(\gamma n \rightarrow \rho n) = T_0 - T_1 \qquad \text{(II.B.2)}$$

where $T_0$ and $T_1$ are the isoscalar (I=0) and isovector (I=1) amplitudes. Incoherent $\rho$ photoproduction from deuterons can

be used to measure the production cross section on protons and on neutrons. The momentum transfer must be large enough so that the recoil nucleon can be kinematically separated from the spectator nucleon. According to Eqn. (II.B.2), the isovector contribution can be estimated from a comparison of the proton and neutron cross sections and is found to be consistent with zero at 4.3 GeV [Eisenberg, 1976].

The differential cross section for $\gamma d \rightarrow \rho pn$, including both coherent and incoherent processes, is predicted as [Glauber, 1966; Eisenberg, 1976]

$$\frac{d\sigma}{dt}(\gamma d \rightarrow \rho d + \rho pn) = \qquad \text{(II.B.3)}$$

$$4|T_0|^2\{\tfrac{1}{2}(1+S(t))e^{bt} - G\,e^{3bt/4}\} + 4|T_1|^2\,\tfrac{1}{2}(1-S(t))$$

where G is the glauber shadowing correction (proportional to $\sigma_T(\rho p)$) and S(t) is the deuteron form factor. At t=0,

$$\left.\frac{d\sigma}{dt}\right|_{t=0}(\gamma d \rightarrow \rho d) = 4|T_0|^2(1-G) \qquad \text{(II.B.4)}$$

The forward differential cross section has no isovector exchange contribution and is entirely coherent. From Eqns. (II.B.2) and (II.B.4), the predicted ratio of the deuteron to proton cross sections at t=0, assuming only I=0 exchange, is [Bauer, 1978]

$$R(t=0) = 4(1-G) = 3.75 \pm 0.05 \qquad \text{(II.B.5)}$$

Discrepancies between the above theoretical value for R(t=0) and experimental measurements may be attributed to an I=1 contribution to the t-channel exchange amplitude.

Available data (up to 9 GeV) [Eisenberg, 1976] indicate that t-channel exchange for ρ photoproduction is isoscalar with no compelling evidence for the presence of I=1 amplitudes. Because of experimental and data analysis uncertainties (e.g. due to the ρ width) an isovector contribution of 5-10% of the I=0 amplitude can not be excluded.

Isovector exchange can be measured directly in charged ρ photoproduction from neutrons, $\gamma n \rightarrow \rho^- p$. Diffractive production is excluded due to charge exchange in the t-channel. The measured cross section can be related to isovector exchange in neutral ρ photoproduction and places an upper limit of 3-5% on the I=1 contribution [Benz, 1974].

The decay angular distribution for vector mesons produced by linearly polarized photons may be expressed in terms of nine independent measurable spin density matrix elements [Schilling, 1971]. The nature of the production mechanism is then studied by comparing the experimentally determined values of the matrix elements (as a function of t) with model dependent predictions. Three reference systems, which differ in the choice of the spin quantization axis (z-axis), are of interest for the analysis of the angular decay distribution. The reference systems, shown in Fig. (II.B.3),

are: (a) the helicity system with the z-axis opposite to the direction of the recoiling proton (i.e. the ρ direction) in the c.m. system; (b) the Adair system with the z-axis in the direction of the incident photon in the c.m. system; and (c) the Gottfried - Jackson system where the z-axis is in the direction of the incident photon in the ρ rest frame. The three coordinate systems differ from each other by a rotation around the normal to the production plane and coincide for forward production ($t=t_{min}$).

One of the interesting questions which a study of the ρ decay angular distribution can answer concerns the helicity (particle spin along direction of flight) of the ρ. The photon, due to its zero rest mass, can have helicities $\lambda=+1$ and $-1$ only, whereas the ρ may have helicities $\lambda=+1$, 0 and $-1$. The polar angle distribution which describes the p-wave dipion state in the helicity system has the form

$$W(\cos\theta) = |Y_1^1|^2 \propto \sin^2\theta \qquad \text{for } \lambda=+/-1$$

$$W(\cos\theta) = |Y_1^0|^2 \propto \cos^2\theta \qquad \text{for } \lambda=0$$

Photoproduction data on proton [Ballam, 1973] and deuteron [Eisenberg, 1976] targets are consistent with 100% s-channel helicity conservation, i.e.

$$W(\cos\theta) = \frac{3}{8\pi}\sin^2\theta \qquad \text{(II.B.6)}$$

with no contribution due to helicity flip transitions into the $\lambda=0$ state.

A detailed study of the density matrix elements shows substantial spin flip or t-channel helicity flip contributions (increasing rapidly with t) in the Adair and Gottfried - Jackson systems [Ballam, 1973]. Dominance of a $J^P = 0^+$ t-channel exchange is therefore ruled out. The amplitude for helicity flip is small (consistent with zero at low -t) in the helicity system, i.e. helicity is conserved at the $\gamma$-$\rho$ vertex.

It is noted that the small helicity flip amplitude is not associated with isovector exchange in the t-channel. This follows from the fact that the measured density matrix elements are the same for proton and neutron targets. An isoscalar assignment to the helicity flip exchange amplitude agrees with the observed absence of a large helicity flip amplitude in $\omega$ photoproduction [Ballam, 1973] which is dominated by I=1 t-channel exchange at low energies.

Vector meson production with unpolarized photons displays s-channel helicity conservation (a $\sin^2\theta$ polar angle distribution for $\rho$ decay) and an isotropic azimuthal angle distribution. If the incident photon is linearly polarized, the azimuthal angle distribution reflects the spin-parity of the t-channel exchange amplitude [Schilling, 1971]. The $\rho$ decay pions emerge preferentially in the plane of photon polarization ($\psi \simeq 0^0$) for natural parity exchange ($P=(-1)^J$, i.e. $0^+$, $1^-$, $2^+$, ...) and perpendicular to it ($\psi \simeq 90^0$) for unnatural parity exchange ($P=-(-1)^J$). The situation is

sketched in Fig. (II.B.4). The rotation of the ρ polarization by $90^0$ (w.r.t. the photon polarization) for unnatural parity exchange is analogous to the perpendicular polarization planes of the photons from neutral pion decay [Perkins, 1972; Williams, 1971]. The dipion azimuthal angle distribution in the helicity system for natural parity exchange is expected to be of the form

$$W_+(\psi) \propto 1+P_\gamma \cos(2\psi)$$

and for unnatural parity exchange

$$W_-(\psi) \propto 1-P_\gamma \cos(2\psi)$$

where $P_\gamma$ is the degree of linear polarization of the incident photon beam. The relative contributions to the overall production cross section from natural and unnatural parity exchange are denoted by $\sigma^N$ and $\sigma^U$, respectively. The angular distribution, including both processes, is then given by

$$W(\psi) \propto 1 + P_\gamma P_\sigma \cos(2\psi) \qquad \text{(II.B.7)}$$

where $P_\sigma$ is the parity asymmetry defined by

$$P_\sigma = (\sigma^N - \sigma^U)/(\sigma^N + \sigma^U) \qquad \text{(II.B.8)}$$

The observed $\psi$ distribution [Ballam, 1973] has a $\cos^2\psi$ dependence (i.e. $P_\sigma \simeq 1$) which is clear evidence for dominant natural $J^P$ exchange.

The actual evaluation of $P_\sigma$ is usually done by measuring the relevant density matrix elements. The fraction of unnatural parity exchange is measured to be <5% even for energies just above production threshold [Criegee, 1970] and is consistent with the contribution expected from one-pion exchange. However, the observed small helicity flip amplitude is found to be associated with natural parity exchange.

In summary, ρ photoproduction is of a diffractive nature. The scattering amplitude is largely imaginary, the t-channel exchange is isoscalar and natural parity, and the photon helicity is conserved at the γ-ρ vertex in the s-channel.

## 2. Omega Photoproduction

The ω meson was discovered in 1961 at the Lawrence Radiation Lab, Berkeley (72 inch hydrogen bubble chamber), in the reaction [Maglic, 1961]

$$\bar{p}p \rightarrow \pi^+\pi^-\omega \rightarrow \pi^+\pi^-\pi^+\pi^-\pi^0$$

The mass and width of the ω are 783 MeV and 10.0 MeV, respectively. Its quantum numbers $I^G(J^P)C$ are $0^-(1^-)-$. The dominant decay modes are into $\pi^+\pi^-\pi^0$(89.9%), $\pi^0\gamma$(8.8%) and $\pi^+\pi^-$(1.3%).

Photoproduction of the omega is in some ways a more

difficult experiment than the study of the rho. As a consequence of the lower $\omega$ production cross section, the statistical errors of measurements are typically larger than the corresponding results for $\rho$ production. The analysis of bubble chamber experiments is complicated due to the presence of the neutral pion in the dominant $\omega$ decay modes. On the other hand, the relatively small width of the $\omega$ ensures an accurate background subtraction, having none of the problems associated with the broad (and skewed) $\rho$ mass shape.

The $\omega$ photoproduction cross section rises from threshold ($\simeq$1.1 GeV) to about 7 $\mu$b at around 2 GeV and then drops rapidly to about 2 $\mu$b at 5 GeV, followed by only a small decrease up to the maximum measured energy near 10 GeV. The energy dependence of the cross section is attributed to a large one-pion exchange (OPE) contribution, falling with energy as $1/E^n$ with n=2.0+/-0.5, and an (approximately) energy independent component ($\simeq$2 $\mu$b) due to diffractive production.

OPE in the t-channel is expected to be much more important for $\omega$ photoproduction than for $\rho$ production. VMD diagrams for $\pi V\gamma$ couplings ($V=\rho$ and $\omega$ ) are shown in Fig.(II.B.5). Specifically, $\rho \to \pi^0\gamma$ is represented by the transition $\rho \to \omega\pi^0, \omega \to \gamma$. Conservation of G-parity does not allow the transition $\rho \to \rho\pi^0$ and, as shown in Fig.(II.B.6), $\rho \to \phi\pi^0$ is not allowed (suppressed) by Zweig's rule [Okubo,

1977]. The coupling constants are related by [see Fig. (II.B.5) and Eqn. (II.A.24)]

$$g(\pi\omega\gamma)=g(\pi\rho\omega)/\gamma_\omega \quad \text{and} \quad g(\pi\rho\gamma)=g(\pi\rho\omega)/\gamma_\rho$$

The ratio of the $\omega$ and $\rho$ partial decay widths into $\pi^0\gamma$ is thus given by

$$\frac{\Gamma(\omega\to\pi^0\gamma)}{\Gamma(\rho\to\pi^0\gamma)} = \frac{g^2_{\pi\omega\gamma}}{g^2_{\pi\rho\gamma}} = \frac{\gamma^2_\omega}{\gamma^2_\rho} = \frac{9}{1} \qquad \text{(II.B.9)}$$

The measured partial decay widths [Particle properties, 1978] give a ratio of about 24/1. Therefore, if vector meson photoproduction were dominated by OPE, the $\omega$ cross section would be much larger than the $\rho$ cross section. The data are in obvious disagreement with OPE dominance, both in magnitude and energy dependence.

The decay ($\omega\to\pi\pi\pi$ ) angular distribution resulting from production by linearly polarized photons measured below 5 GeV [Ballam, 1973] does not exhibit a $\sin^2\theta\cos^2\psi$ dependence expected for s-channel helicity conservation and natural spin-parity exchange in the t-channel. It is apparent that the nature of the diffractive component is obscured by the large OPE amplitude at low energies. However, as the incident photon energy approaches 10 GeV, the decay distribution changes into the characteristic $\sin^2\theta\cos^2\psi$ form observed in $\rho$ photoproduction, thus indicating a rapid decrease with energy of the OPE contribution and confirming s-channel helicity conservation

and natural parity exchange for the energy independent (diffractive) part of the total production amplitude.

It is noted here that the same formalism that is used to describe the $\rho$ angular distribution also applies for the $\omega$. The decay angles $\theta$, $\psi$ are defined as the polar and azimuthal angles of a unit vector $\hat{r}$, which, in the case of a two-particle decay of the vector meson, denotes the direction of flight of one of the particles in the V rest frame. For a three-particle decay, $\hat{r}$ is the normal to the decay plane in the V rest frame [Schilling, 1971].

The importance of OPE at low energies is verified from detailed studies of the density matrix elements. The parity asymmetry, $P_\sigma$, defined by Eqn. (II.B.8), is strongly energy dependent, rising from 0 at 3 GeV to approximately 1 at 10 GeV. The decomposition into $\sigma^N$ and $\sigma^U$ demonstrates that the rapid decrease of the total $\omega$ cross section at low energies is due to the unnatural parity exchange contribution ($\sigma^U$). The density matrix elements associated with unnatural parity exchange have been measured in the Gottfried-Jackson system and are found to be consistent with OPE dominance [Ballam, 1973].

The natural parity exchange cross section ($\sigma^N$) is approximately energy independent with a t-dependence given by $d\sigma/dt=A\cdot\exp(bt)$ where $b=7-8$ GeV$^{-2}$, in good agreement with $\rho$ photoproduction. The density matrix elements associated with natural parity exchange are consistent with those from

ρ production although more poorly determined due to measurements of low statistical accuracy.

Only the I=0 exchange amplitude contributes to coherent ρ and ω photoproduction on deuterons [see Eqn. (II.B.4)]. Assuming equal couplings of the pomeron (and f) exchange to the ρ and ω mesons, the ratio of the coherent photoproduction cross sections should be equal to the ratio of the respective photon-vector meson coupling constants,

$$R = \left.\frac{d\sigma/dt(\gamma d \to \rho d)}{d\sigma/dt(\gamma d \to \omega d)}\right|_{t=0} = (\gamma_\omega/\gamma_\rho)^2 \qquad \text{(II.B.10)}$$

Measured values average typically R=7.1+/-1.1 [Alexander, 1975]. This compares with the electron-positron storage ring result [see Eqn. (II.A.17)], R=7.2+/-1.4, and the VMD-quark model prediction [Eqn. (II.A.24)], R=9.

The isovector contribution to the natural parity exchange amplitude can be determined from a comparison of ω photoproduction measurements on proton and deuteron targets [see Eqns. (II.B.2)] and (II.B.4)],

$$\left.\frac{d\sigma}{dt}\right|_{t=0}(\gamma p \to \omega p) = |T_0 + T_1|^2 \qquad \left.\frac{d\sigma}{dt}\right|_{t=0}(\gamma d \to \omega d) = 4|T_0|^2(1-G)$$

Available data [Abramson, 1976] do not provide sufficiently accurate results for definite conclusions. A natural parity candidate for isovector exchange is the $A_2$ meson [$I(J^P)=1(2^+)$]. It has been suggested that $A_2$ exchange might

be more important for $\omega$ photoproduction than for the $\rho$ [Harari, 1969].

To conclude, OPE is an important mechanism for $\omega$ photoproduction at low energies but decreases rapidly to less than 5% of the total $\omega$ cross section near 10 GeV. The natural parity exchange $\omega$ cross section is approximately energy independent and about seven times smaller than the $\rho$ cross section near 10 GeV. The density matrix elements associated with natural parity exchange are compatible with s-channel helicity conservation. The study of (possibly non-negligible) isovector exchange must wait for a new measurement of high statistical accuracy.

## 3. Phi Photoproduction

The $\phi$ meson was discovered in 1962 at Brookhaven (20 inch hydrogen bubble chamber) in the reactions [Bertanza, 1962]

$$K^- p \to \Lambda\phi \to \Lambda K^+ K^-$$
$$\to \Lambda K_L K_S$$

The mass and width of the $\phi$ are 1020 MeV and 4.1 MeV, respectively. Its quantum numbers $I^G(J^P)C$ are $0^-(1^-)-$. The dominant decay modes are into $K^+K^-$ (46.6%), $K_L K_S$ (35.0%), $\rho\pi$ (16.4%) and $\eta\gamma$ (2.0%).

Phi photoproduction is regarded as an ideal reaction for

the study of pomeron exchange. VMD relates $\gamma p \to \phi p$ to $\phi p$ elastic scattering which is exotic (no resonance possible) in the s-channel if the quark composition of the $\phi$ is pure $s\bar{s}$. Exchanges in the t-channel are therefore restricted to the pomeron.

OPE in $\phi$ photoproduction would proceed as shown in Fig. (II.B.6), i.e. $\gamma \to \rho \to \phi\pi^0$. Conservation of G-parity forbids $\phi \to \phi\pi^0$ and $\omega \to \phi\pi^0$. The $\rho\phi\pi^0$ coupling is however strongly inhibited by Zweig's rule as shown by the (disconnected) quark line diagram of Fig. (II.B.6). The rule states that the two ends of a given quark line cannot belong to the same hadron, i.e. whenever a $q\bar{q}$ pair is created, the new $q$ and $\bar{q}$ must belong to different hadrons and whenever a $q$ annihilates a $\bar{q}$, they must have come from different hadrons. The quark line diagram for a Zweig's rule allowed transition is shown in Fig. (II.B.6) for $\phi \to K^+K^-$.

The measured decay rate for $\phi \to \rho\pi$ does not readily suggest a weak $\rho\phi\pi$ coupling. The reason for the relatively large branching ratio (16.4%) is of course the very small phase space available for the $\phi \to KK$ decay modes.

The ratio of the partial decay widths for $\phi \to \pi\pi\pi$ and $\omega \to \pi\pi\pi$ is measured as [Particle properties, 1976]

$$\Gamma(\phi \to \pi\pi\pi)/\Gamma(\omega \to \pi\pi\pi) = 0.074$$

and has been used to estimate the ratio of the coupling constants [Okubo, 1977]

$$g(\phi\rho\pi)^2/g(\omega\rho\pi)^2 = 0.007$$

i.e. the coupling of the $\phi$ to particles which are made-up of non-strange quarks is strongly suppressed. Measured cross sections for $\phi$ production in hadronic interactions present further evidence. For example, the $\rho$ exchange reaction at 3.7 GeV/c [Butler, 1973],

$$\sigma(\pi^+ p \to \phi\Delta^{++})/\sigma(\pi^+ p \to \omega\Delta^{++}) < 0.0033$$

Other examples are given by [Okubo, 1977].

These considerations suggest that the pomeron is the only t-channel exchange for $\phi$ photoproduction.

The measured $\phi$ photoproduction cross section rises from threshold ($\simeq$1.6 GeV) to approximately 0.45 $\mu$b near 10 GeV. The energy dependence is entirely explained by a threshold factor, $(p_\phi/k_\gamma)^2$, where $p_\phi$ and $k_\gamma$ are the momenta of the $\phi$ and the incident photon in the c.m. system [see Eqn.(II.A.11) and Appendix B]. The momentum transfer dependence of the cross section is well described by an exponential form, $d\sigma/dt=A\cdot\exp(bt)$, at low $-t$ ($<$0.4 GeV$^2$). The fitted slope parameter b is typically 5.5-6.5 GeV$^{-2}$ but appears to be less steep for $-t>$0.4 GeV$^2$ [Behrend, 1978]. The smaller slope parameter for $\phi$ photoproduction compared to $\rho$ (and $\omega$) production implies a smaller $\phi$-nucleon interaction radius. The $\phi$-nucleon total cross section, $\sigma_T(\phi p)$, is thus expected to be less than $\sigma_T(\rho p)$ and $\sigma_T(\omega p)$, which is in agreement with data.

The decay angular distribution from polarized photon data has the expected $\sin^2\theta\cos^2\psi$ dependence consistent with

s-channel helicity conservation and natural parity exchange in the t-channel [Ballam, 1973; Halpern, 1972]. A high statistics measurement of the decay polar angle distribution (unpolarized photons) as a function of the $K^+K^-$ invariant mass exhibits a strong mass dependence [Behrend, 1978]. In the $\phi$ mass region (1.01-1.03 GeV) the distribution has a clean $\sin^2\theta$ form, again confirming s-channel helicity conservation. The angular distribution changes abruptly in character for events outside of the $\phi$ mass region, exhibiting a predominantly $\cos^2\theta$ dependence for $K^+K^-$ events above the $\phi$ mass.

The ratio of the forward $\phi$ photoproduction cross sections on deuteron and proton targets, assuming only I=0 t-channel exchange, is predicted as

$$R(t=0) = 4(1-G) = 3.89$$

[analogous to Eqn. (II.B.5)]. The measured ratio at $E_\gamma \simeq 8$ GeV is R(t=0)=3.6+/-0.6 [McClellan, 1971], consistent with no I=1 exchange.

The phase (i.e. the real part) of the $\phi$ production amplitude can be determined from interference measurements between $\phi \to e^+e^-$ and Bethe-Heitler pairs. Data at E=6-7.4 GeV on carbon [Alvensleben, 1971] indicate a production phase which differs from being purely imaginary by $25^0$+/-$15^0$, or a real to imaginary amplitude ratio, $\eta=-0.48^{+.33}_{-.45}$. The large measurement errors on $\eta$ do not allow definite conclusions but suggest that $\phi$ photoproduction may

not be due to pomeron exchange only.

In summary, the $\phi$ photoproduction measurements indicate that the production mechanism is diffractive, conserving s-channel helicity, with natural parity and I=0 exchange in the t-channel. There is an indication that the phase of the production amplitude may not be purely imaginary - an accurate measurement is needed.

Note:

An extensive list of references on vector meson photoproduction (and other photon interactions) may be found in recent review articles by Bauer, Spital, Yennie and Pipkin in Reviews of Modern Physics [Bauer, 1978] and Leith in Electromagnetic Interactions of Hadrons [Leith, 1977].

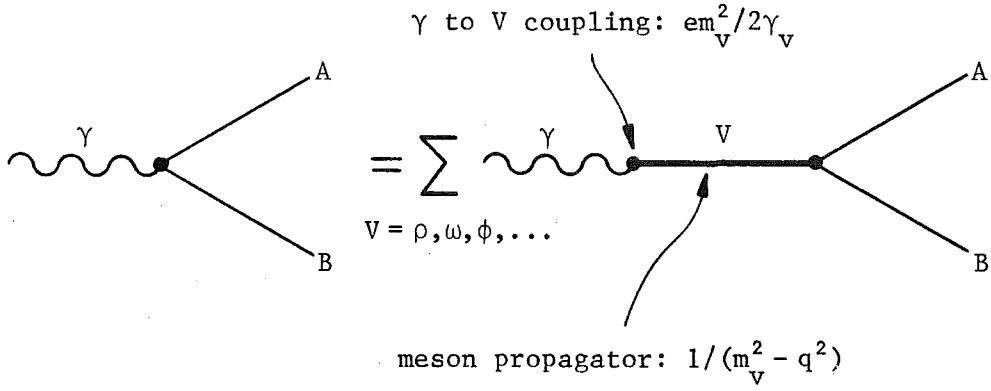


Figure (II.A.1) The vector meson dominance (VMD) model for photon-hadron interactions.

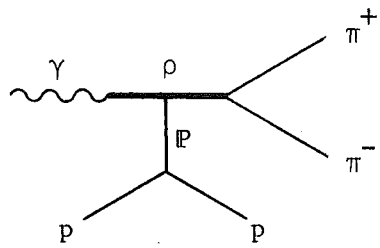


Figure (II.A.2) Diffractive elastic rho photoproduction diagram ($\gamma p \to \rho p$). The exchanged (virtual) particle, $\mathbb{P}$ (the pomeron), has the internal quantum numbers of the vacuum ($I = S = B = 0$).

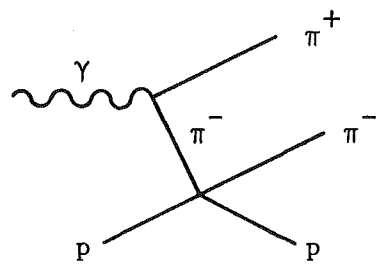


Figure (II.B.1) Diagram for non-resonant diffractive pion pair photoproduction, $\gamma p \rightarrow \pi^+\pi^- p$.

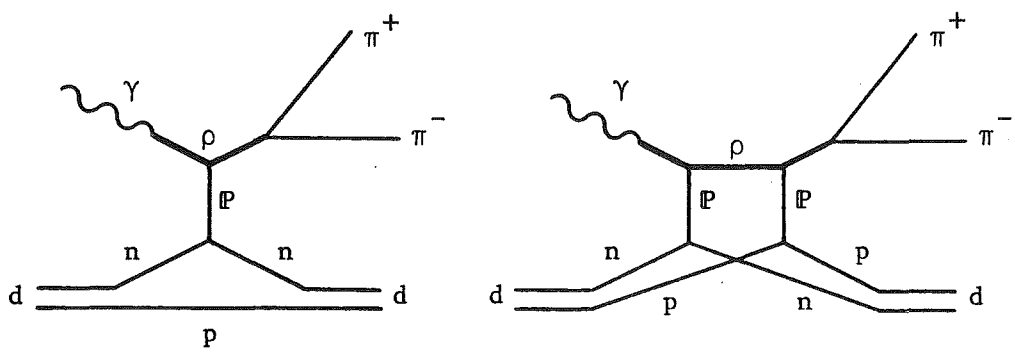


(plus n↔p)

(a) single scattering (b) double scattering

Figure (II.B.2) Diagram for coherent diffractive ρ photoproduction from deuterons. Single scattering is dominant for low -t (<0.4 $GeV^2$) and double scattering dominates higher -t coherent reactions.

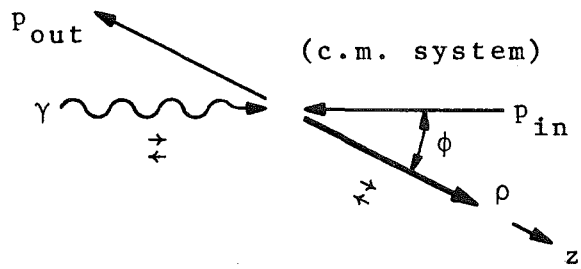


(a) s-channel helicity conservation: z-axis is $\rho$ direction of flight in c.m. system $\equiv$ helicity system.

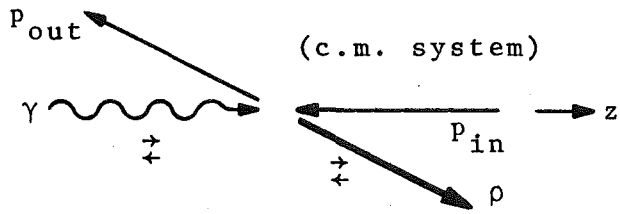


(b) spin direction conservation: z-axis is $\gamma$ direction in c.m. system $\equiv$ Adair system.

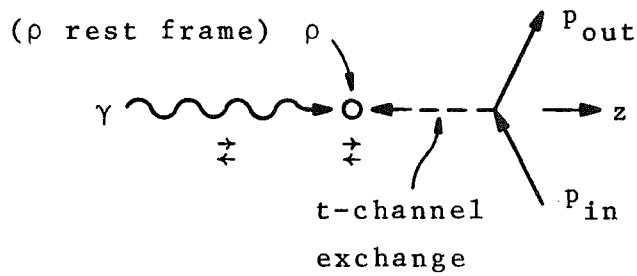


(c) t-channel helicity conservation (i.e. t-channel exchange $J^P = 0^+$) : z-axis is $\gamma$ direction in $\rho$ rest frame $\equiv$ Gottfried-Jackson system.

Figure (II.B.3) Reference frames for $\rho$ photoproduction. The three frames (a, b and c) coincide for forward production ($\phi = 0^0$, $t = t_{min}$).

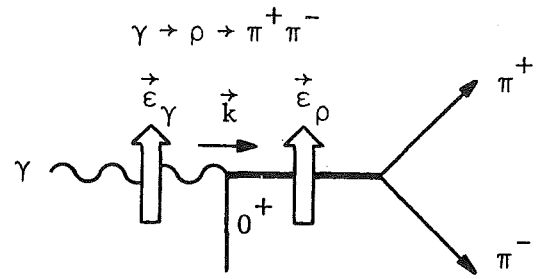


$$\Psi_+ \propto (\vec{\varepsilon}_\gamma \cdot \vec{\varepsilon}_\rho)$$

$$W_+(\psi) = |\Psi_+|^2 \propto \cos^2 \psi$$

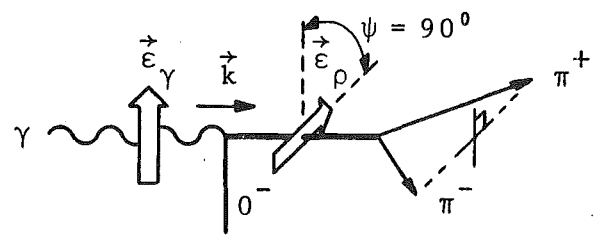


$$\Psi_- \propto (\vec{\varepsilon}_\gamma \times \vec{\varepsilon}_\rho) \cdot \bar{k}$$

$$W_-(\psi) = |\Psi_-|^2 \propto \sin^2 \psi$$

Figure (II.B.4) Natural ($0^+$) and unnatural ($0^-$) spin parity exchange in the t-channel. The transition amplitude, $\Psi_+$, is a scalar (even parity), whereas $\Psi_-$ is a pseudo-scalar and changes sign (odd parity) under spatial reflections.

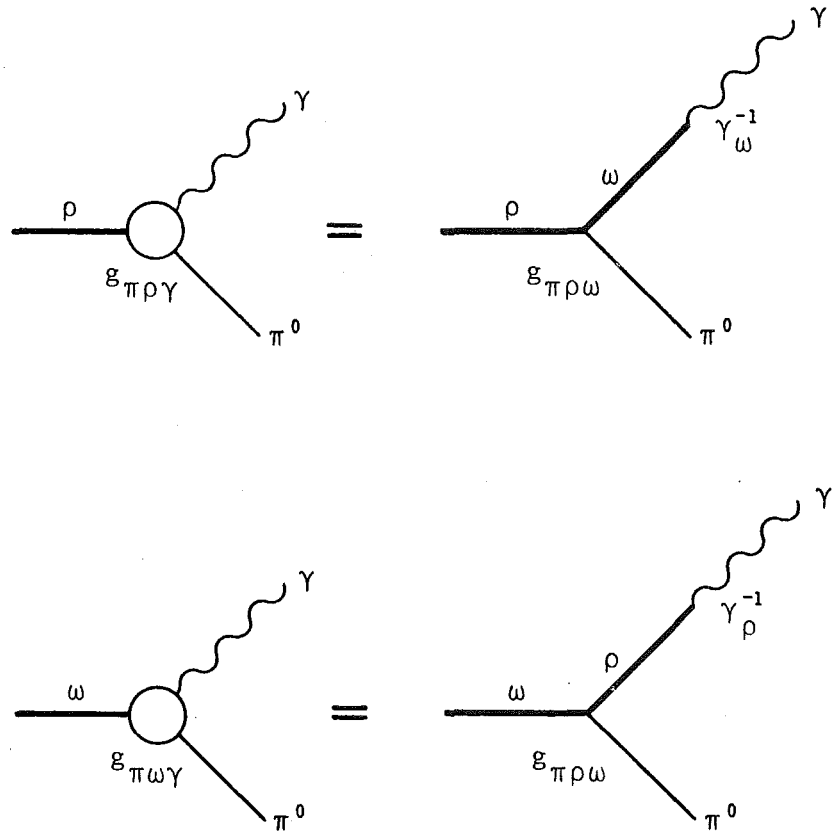


$$\frac{g_{\pi\rho\gamma}}{g_{\pi\omega\gamma}} = \frac{\gamma_\rho}{\gamma_\omega} = \frac{1}{3}$$

Figure (II.B.5) VMD diagrams for $\rho \to \pi^0\gamma$ and $\omega \to \pi^0\gamma$.

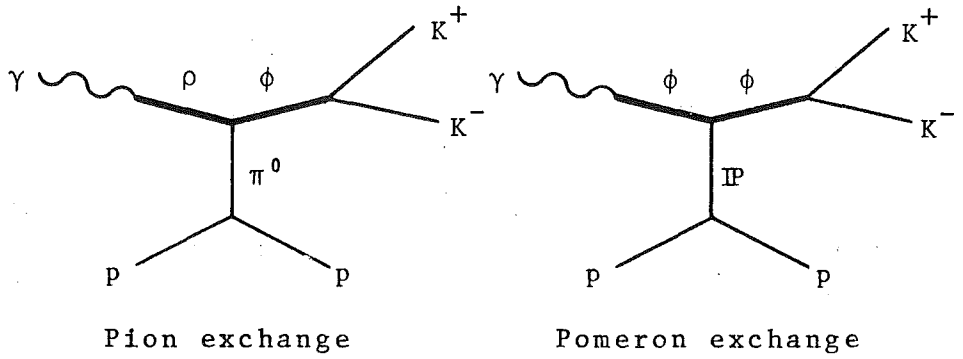


(a) VMD diagrams for $\phi$ photoproduction. OPE is strongly inhibited by Zweig's rule.

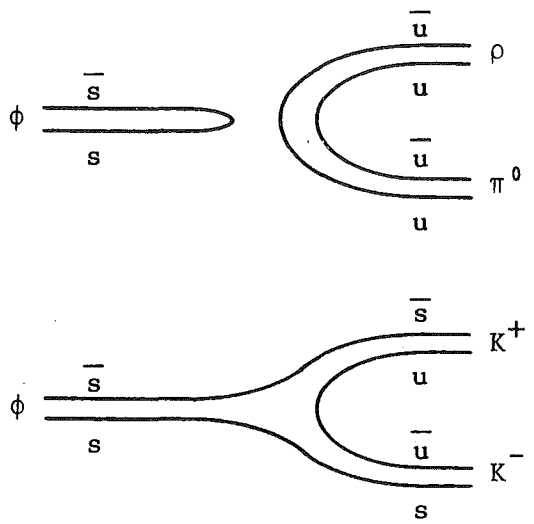


(b) Quark line diagrams for $\phi \to \rho\pi^0$ and $\phi \to K^+K^-$.

Figure (II.B.6) Suppression of $\pi\phi\rho$ coupling by Zweig's rule.

# CHAPTER III APPARATUS

## A: Introduction

The photoproduction data presented in this thesis were taken at Fermilab's tagged photon facility. An aerial view of the Fermilab site is shown in Fig. (III. A. 1). The primary proton beam is extracted from the Main Ring, split horizontally into three components, and transported to the external experimental areas: Meson, Neutrino, and Proton, as shown in Fig. (III. A. 2). In enclosure H, the Proton Area beam is then split vertically into three branches to supply beam to three separate, independently operable areas: Proton East, Proton Center, and Proton West. The tagged photon facility is located in Proton East as shown in Fig. (III. A. 3).

The production of tagged photons is simple in principle. High energy protons (400 GeV) are targeted on a 30 cm long beryllium target. Charged secondaries and non-interacting protons are bent away from the forward direction with vertical dumping magnets. Neutral pions, resulting from the proton interaction in the target, decay to photons which convert to electron-positron pairs in a lead converter, 0.32 cm thick, located 12 m after the target. A 290 m long beam transport system selects and focusses electrons of the desired energy (up to 200 GeV during this experiment) giving

an electron beam of high purity and good momentum resolution.

Photons are produced by electrons interacting in a 0.015 cm thick copper foil (the radiator) placed 27 m before the experimental target. The photons are the result of bremsstrahlung in the radiator. The recoiling electrons are deflected by a set of magnets into a counter hodoscope which measures the energy of the electrons. The photon's energy is then simply the difference between initial and final electron energy. The undeflected tagged photons go on towards the experimental target.

## B: The Electron Beam

A schematic of the electron beam line is shown in Fig.(III.B.1). The proton beam from the accelerator is steered on to a 30 cm long beryllium target located in the Proton East target box. Non-interacting protons and charged particles produced by interacting protons are bent into a beam dump. Neutral particles are allowed to exit the target box through a hole located at $0^0$ (the incident proton direction). These particles are mainly neutrons, kaons, and photons, the latter resulting primarily from neutral pions. The photons make electron positron pairs in a lead converter, 0.32 cm thick ( 0.5 radiation lengths), located

12 m downstream of the Be target. Neutrons and kaons interacting in the converter can make charged pions which contaminate the electron beam. Electrons of the desired energy are then selected and transported through a conventional two-stage beam line, each stage consisting of a quadrupole doublet and a bending magnet string. The first stage (QH409, QV409) focuses the charged particles to an image of the target on to a set of horizontal and vertical collimators (CH423, CV423). The horizontal bending magnet (BH415) provides momentum dispersion so that the opening of the horizontal collimator defines the momentum interval of the electron beam (typically +/-2.5%). Pions produced in the converter have a much larger transverse momentum (relative to the beam direction) than the photoproduced electron positron pairs ( 300 MeV/c versus 10 MeV/c). As a result most of the pions still in the beam are removed by the vertical collimator (CV423). Following the first focus is a single quadrupole (QH424) used as a field lens and bending magnets (BH425, BV426) to reduce the dispersion. A second set of quadrupoles (QV435, QH436) focuses the purified electron beam on to the experimental target. The quadrupoles are followed by another string of bending magnets (BV437, BH438) to sweep out remaining off-energy particles and to bend the beam still further away from its initial direction. The bending of the beam away from $0^0$ is necessary in order to avoid the high intensity cone of muons

emerging from the Be target, the beam dump, and the neutral dump. The electron beam is about 7 m from the $0^0$ line at the experimental target.

The electron yield per incident 400 GeV proton as a function of electron energy is shown in Fig. (III.B.2). The proton intensity during this experiment was typically $3x10^{12}$ protons/pulse, one pulse every 10 seconds, with a pulse duration of about 1 second. The RF acceleration of the proton beam in the Main Ring results in a bunching of protons within each pulse. The bunches (called RF buckets) come at 18.5 ns intervals and are less than 1 ns in duration. The electron beam reflects this structure and any problems in the proton beam (eg. bad extraction from the Main Ring, unstable beam splitting etc.) directly affect the quality of the electron beam.

The pion contamination of the electron beam was measured to be less than a few tenths of a percent. Muon backgrounds near the experimental target were typically $10^4$ /$m^2$ per $10^{12}$ protons at 400 GeV. As expected, the muon rate was observed to be higher nearer the $0^0$ line (the incident proton direction).

## C: The Tagging System

A schematic of the tagging system is shown in

Fig. (III.C.1). The tagged photon beam is produced by the electron beam passing through a thin radiator. Some of the electrons emit a high energy photon along the beam direction. A set of magnets (AN440) deflect the recoiling electrons into a counter hodoscope 19 m downstream from the radiator. The momentum of a recoiling electron is measured by its position in the hodoscope array. Since the hodoscope consists in part of lead glass total absorption counters, the electron energy is measured independently of its momentum. A comparison of the two measurements allows pions and muons to be rejected. The energy of a photon emitted in the radiator is the difference between the electron beam energy and the energy of the recoiling electron. Electrons which do not interact in the radiator are deflected into a dump located between the photon beam and the tagging hodoscope.

Most of the data presented in this thesis were taken with a copper radiator of thickness 0.015 cm (≈0.01 radiation lengths) and an elliptical cross section corresponding to the electron beam profile at the radiator position. For some of the data radiator thicknesses of 0.0076 cm and 0.038 cm (≈0.005 and ∿0.03 radiation lengths) were used. Copper is chosen because of a favorable radiation length to interaction length ratio. It is important to use a thin radiator in order to assure a negligible contribution of double bremsstrahlung events. A thin radiator also reduces

trident production in the radiator ($e^- \rightarrow e^+ e^- e^-$). The lower limit of the radiator thickness is given by the desired photon flux for a given electron beam intensity. The thickness of the radiator in units of interaction lengths should be small to minimize the probability of pions in the electron beam interacting in the radiator. Such interactions can produce neutrons or kaons resulting in a contamination of the photon beam. However, this is a problem only if the tagging system simultaneously registers a recoil electron giving a valid tag. A coincidence of this kind is thus proportional to the number of recoil electrons per interacting pion suggesting the use of a material with a short radiation length and a relatively long interaction length for the radiator.

The separation of the charged particles from the bremsstrahlung photons begins 1 m downstream of the radiator with a set of three magnets. The vertical gaps of the first two magnets are 7.62 cm (3") while the magnet furthest downstream has a 10.2 cm (4") gap. Constructed between the gaps and extending from the radiator to the tagging hodoscope is a vacuum vessel with rectangular cross section which increases with distance from the radiator and measures 12.7 cm x 182.9 cm (5"x72") at the tagging hodoscope. This ensures that the photon and electron beam and all recoil electrons in the tagging range remain in vacuum. The electrons leave the downstream end of the vessel through a

0.25 mm (10 mil) kapton window while the photons head towards the experimental target in a 7.6 cm (3") diameter vacuum pipe.

The end piece of the vessel and the tagging counters are shown schematically in Fig.(III.C.2). The counter array consists of thirteen shower counters located behind a thirteen piece scintillation counter hodoscope. The sizes of the shower counters are listed in Fig.(III.C.2). The larger vertical size of the outer counters, L9 to L13, is needed to allow for the additional vertical bend experienced by lower energy recoil electrons which pass through more of the tagging magnet's fringe fields. The two shower counters closest to the photon beam, L1 and L2, are made of 20 successive layers of lead and lucite while the remaining shower counters, L3 to L13, are made of lead glass. The lead-lucite construction of L1 and L2 avoids problems due to changes in optical properties resulting from radiation damage which is typical for lead glass subjected to electron (photon) beams of high intensity and high energy. L1 and L2 absorb the high energy, high intensity part of the recoil electron spectrum as is shown in Fig.(III.C.3). Because of the high rate, L1 was used as a veto counter for this experiment. Tags from L1 would otherwise have dominated the event triggers.

The light produced in the shower counters is viewed by RCA 6342A (10-stage, low gain) photomultiplier tubes. The

output pulses are digitized by 10 bit Lecroy analog to digital converters (ADC) Model 2249A.

The spacing of the scintillation counter hodoscope is shown in Fig.(III.C.3). The central region of each shower counter is defined by the overlap of adjacent hodoscope elements. A valid tag requires a coincidence between a shower counter and the matching elements of the hodoscope. A tag is not generated if the tagging counters register signals in addition or not consistent with a single electron track. Further discrimination against bad tags is provided by several scintillation counters positioned to detect undesired interactions in the radiator (anti counters), electrons entering the beam dump (dump counters), and muons heading into the experimental area (muon counters).

The locations of the anticounters, A1 to A11, are shown in Fig.(III.C.1). A1 was not used for this experiment. A3, A4 and A6 to A10 are positioned to detect positrons originating from trident ($e^+e^-e^-$) production in the radiator. A2 and A5 detect low energy electrons from tridents or electron-electron scattering. A11 is located about 1.5 m upstream of the experimental target and serves primarily to veto wide angle bremsstrahlung photons. The scintillation counter has a hole for the photon beam measuring 3.8 cm vertically and 4.4 cm horizontally. Masking the counter on the upstream side is 4.4 cm of lead to convert the wide angle photons to electron positron pairs

and also to range out synchrotron radiation originating at the last bend of the electron beam. 0.61 m of steel between A11 and the experimental target protect the counter from backscattered particles produced in the target.

Dump counter D1 is installed inside the beam dump hole and dump counter D2 covers the region between the dump and the first tagging shower counter, L1. Both counters are used to veto tags which had a second electron incident on the radiator at the same time (same bucket) as the recoiling electron.

The muon counters, Mu1 to Mu8, are inserted into a slot between shielding blocks just upstream of the experimental target as indicated in Fig.(III.C.1). The scintillation counters cover an area of approximately 3 $m^2$ with the photon beam pipe going through a hole in the center.

A schematic of the tagging system electronics is shown in Fig.(III.C.4). A delayed signal from the tagging shower counters (isolation signal) and a feed back signal from the tag output gate (tag busy signal) assure that a tagging signal ($T\overline{A}$) is not immediately preceded nor followed by another tag. $T\overline{A}$'s are also vetoed if they occur between beam pulses (beam busy) or if the experimental fast logic or the computer are busy (computer busy).

The energy calibration of the individual shower counters in the tagging system was monitored throughout the data taking period. The energy of photons that did not interact

in the target are measured by the C-counter, a lead-scintillator shower counter which is part of the experimental apparatus (Fig. III.E.1). For these events the energy of the recoil electron is given by the difference between the electron beam energy and the energy deposited into the C-counter. Calibration events were restricted to events with the recoil electron incident in the central region of a particular shower counter.

## D: The Target

The liquid hydrogen target used for this experiment is 100.027 $\pm$ 0.025 cm long (0.11 radiation lengths). A schematic of the target is shown in Fig.(III.D.1). The target flask is made of an aluminum cylinder, wall thickness 0.81 mm, capped at each end with a mylar dome, 0.08 mm thick. Thermal insulation is provided by ten layers of aluminized mylar foil, wrapped around the flask, adding another 0.08 mm overall. The flask is supported in a cylindrical vacuum jacket made of 3.2 mm thick aluminum with mylar end windows. The thickness of the upstream window is 0.11 mm and the downstream window measures 0.18 mm. A vacuum exists on both sides of these windows during data taking.

A calculation of an interaction cross section requires

the number of target nuclei per unit area,

$$a = \rho l N/A \qquad \text{(III.D.1)}$$

$\rho$ and $l$ are the density and length of the target. $N$ is Avogadro's number and $A$ is the gram atomic weight of the target. The density of the liquid hydrogen in the flask was monitored throughout the experiment with four precision platinum resistors and two pressure transducers. The measurements were translated into target densities with the help of manufacturer supplied resistance-temperature curves and standard conversion tables of vapor pressure, molar volume and temperature for liquid hydrogen [Tapper, 1965]. The temperature obtained from the resistance measurements is $20.4 \pm 0.2^0$K while the vapor pressure readings result in $20.5 \pm 0.2^0$K. This corresponds to an average density

$$\rho = 0.07043 \text{ g/cm}^3 \qquad \text{(III.D.2)}$$

The fluctuations of $\rho$ from the average value did not exceed 0.1% during the data taking. The number of target nuclei using the average value for $\rho$ is then

$$a = 4.2089 \cdot 10^{24} \text{cm}^{-2} \qquad \text{(III.D.3)}$$

with $l$=100.027 cm, $N$=6.0221x$10^{23}$ and $A$=1.00797.

The number of photons passing through a target of thickness dl is attenuated due to interactions. The intensity of the photon beam is reduced by

$$dn = -n_o \frac{\rho N}{A} \sigma \, dl \qquad \text{(III.D.4)}$$

where $n_o$ is the initial beam intensity. The constant of proportionality $\sigma$ has the dimension of an area and is defined as the cross section of the attenuation mechanism. The yield of interactions is then given as

$$Y = n_o - n(l) = n_o(1 - \exp\{\frac{-\rho N}{A} \sigma \, l\})$$
$$\simeq n_o a \, \sigma \qquad \text{(III.D.5)}$$

and the cross section

$$\sigma \simeq \frac{Y}{n_o a} \qquad \text{(III.D.6)}$$

The attenuation of the photon beam is primarily due to electron - positron pair production which has a cross section of about 21 mb compared to about 115 μb for high energy hadron photo production. The average photon beam intensity in the target is

$$\bar{n} = n_o \frac{\int \exp\{\frac{-\rho N}{A} \sigma \, l\} dl}{\int dl}$$

$$\bar{n} = n_o \frac{1 - \exp(-a\,\sigma)}{a\,\sigma} \qquad \text{(III.D.7)}$$

where $\sigma$ is the pair production cross section for hydrogen. $\sigma$ is related to the radiation length $X_o$,

$$\sigma = \frac{7}{9}\,\frac{A}{X_o N} \qquad \text{(III.D.8)}$$

$X_o$ can be calculated [Tsai, 1974] and has the value 63.0470 g/cm$^2$ for hydrogen. Rewriting Eqn. (III.D.7) in terms of $X_o$ gives

$$\bar{n} = n_o \frac{1 - \exp\{-(7\rho l)/(9X_o)\}}{(7\rho l)/(9X_o)}$$

$$= n_o\,(0.95778) \qquad \text{(III.D.9)}$$

and Eqn. (III.D.6) now becomes

$$\sigma \simeq \frac{Y}{\bar{n}a} = \frac{Y}{n_o}\,(2.4807\cdot 10^5)\ \mu b \qquad \text{(III.D.10)}$$

Beam attenuation in the mylar windows of the target amounts to less than 0.1% and is thus neglected. Eqn. (III.D.10) is used for all cross section calculations in this thesis.

## E: The Detectors

### 1. General Description

The experimental apparatus was designed to measure the total hadronic photoproduction cross section ($\sigma_T$) between 18 and 184 GeV. The basic challenge is to extract $\sigma_T$ in the presence of an electromagnetic (EM) background, mostly $e^+e^-$ pair production, some 180 times larger than $\sigma_T$. In the case of EM events most or all of the tagged photon energy shows up in electrons or photons at small angles with respect to the beam direction. Hadronic interactions, on the other hand, tend to produce particles at much larger angles, and rarely deposit significant electromagnetic energy near $0^0$. The detecter arrangement is illustrated in Fig.(III.E.1). Non-interacting beam photons and products of electromagnetic events deposit most of their energy in the central shower counter, C. Particles from hadronic interactions are detected by two lead glass shower counter arrays, G2 and G3, six multiwire proportional chambers, MWPC, and several lead-steel- scintillator hadrometers, covering $>90^0$ in the $\gamma p$ center of mass frame. The apparatus is built in three sets (H1,H2 and H3) which can be independently moved along the beam direction to allow easy scaling of the acceptance geometry for different electron beam energies, $E_o$. Total cross section data were collected with $E_o$=40, 60, 90, 135

and 200 GeV corresponding to photon energies, $E_\gamma$, from 18 to 184 GeV with substantial overlap of $E_\gamma$ ranges at adjacent $E_o$ settings.

A vacuum exists in the beam region from the downstream end of the target up to the first MWPC in front of Q3 (12.7 cm diameter pipe at the target, increasing in steps to 61 cm diameter at the MWPC). A mylar tube (6.4 cm diameter), filled with helium gas, extends from the last MWPC, through Q3 and S3, up to the C-counter. The probability of a hadronic interaction in the target is approximately $4.6\times10^{-4}$ per incident photon ($\sigma$=115 μb). In comparison, the hadronic interaction probability in air is about $7\times10^{-6}$ per meter of air, or about 1.5% of the target rate ($\sigma$=115 μb$\cdot A^{0.93}$, $A \simeq 14.4$, $\rho$=0.0012 g/cm$^3$). As the C-counter is several meters from the hydrogen target (eg. 13 m at $E_o$=90 GeV), an intolerable rate of air interactions is thus eliminated by the vacuum/helium system between the target and the C-counter.

## 2. Central Shower Counters C and D

The fraction of the tagged photon energy detected in the C-counter, $E_c/E_\gamma$, provides the primary means for differentiating hadronic and EM events. The great majority of hadronic events have $E_c/E_\gamma$ near 0, while EM events peak near 1. The $E_c/E_\gamma$ spectrum for events passing a loose

hadronic trigger, defined by a tag in coincidence with a hit in any hadron detecter is shown Fig. (III.E.2).

The C-counter could not be made out of lead glass due to its exposure to the high rate of beam photons and $e^+e^-$ pairs with the inevitable result of radiation damage. Instead, it is a 20-layer lead- scintillator sandwich shower counter, each layer consisting of a 0.64 cm thick lead plate followed by an equal thickness of scintillator. The cross sectional area is 11.4x11.4 $cm^2$. Lucite light guides couple the light from all scintillator elements to a RCA 6342A photomultiplier tube. An extra layer of scintillator is inserted after the third, fourth, and fifth lead plate. The light from these additional elements is viewed by a second photomultiplier tube to allow sampling of the initial shower development. Photon and electron initiated showers start within about one radiation length (~3 cm) from the front face of the shower counter. The probability for a hadron induced shower to start in the front part of the counter is, however, small. Most showers initiated by hadron interactions in the C-counter can thus be identified as such on the basis of a low pulse height measured in the three sampling elements.

The C-counter output signal must be linear with energy and stable in time not only because of the importance of the $E_e/E_\gamma$ ratio for hadronic event identification but also because the C-counter energy is essential for the

calibration of the tagging shower counters. With the tagging magnets turned off, the C-counter is calibrated with a fixed energy, low intensity electron beam. A typical C-counter energy spectrum for 200 GeV incident electrons is shown in Fig. (III.E.3). Fluctuations in the gains of the photomultiplier tubes are tracked by a pulsed laser system (details in Section 5 and [Morrison, 1975]). Laser events are monitored between and also during beam spills to take account of rate dependent effects in the photomultiplier tubes. An idependent check on gain variations is provided by photons having an energy approaching that of the electron beam (the bremsstrahlung tip). To record events of this type a special trigger is required because the corresponding recoil electrons have too low an energy to reach the tagging counters. Using both methods, the C-counter energy calibration is maintained stable to better than 1% during data taking.

The D-counter is located directly downstream of the C-counter and serves primarily to absorb shower leakage from the C-counter. It is a 16-layer lead- scintillator sandwich with a cross sectional area measuring 24.1x24.1 $cm^2$ (larger than the beam hole through S3). The lead plates and scintillators are 0.64 cm thick. The light from all layers is coupled to a single photomultiplier tube.

3. Hadrometers S1, S2 and S3

Wide-angle hadronic particles are detected by S1 which is closest to the hydrogen target. The detector consists of three planes of scintillator; each plane is 1.27 cm thick and covers an area of 102x102 $cm^2$. A 3.8 cm thick lead plate is mounted in front of the first plane. The second and third plane are preceded by 10.2 cm of iron. All layers have a 20.3 cm square hole in the beam region. The light from each plane of scintillator is viewed by two photomultiplier tubes on opposite sides. An S1 trigger requires either a summed pulse height equivalent to at least five minimum ionizing particles passing through the planes, or pulse heights in each plane consistent with a 0.3 minimum ionizing particle. The detection efficiency of S1 for muons is >99%.

S2 is mounted behind the lead glass array G2. The distance of S2 from the target is chosen so that its acceptance area matches the hole in S1. The detector consists of eight scintillator counters arranged in three planes. The first plane has two counters which are behind 3.2 cm (5.7 radiation lengths) of lead to absorb shower leakage from G2. The second plane is made of three counters and is separated from the first plane by 1.3 cm of iron and 10.2 cm of lead. 25.4 cm of iron separate the second and third plane which also consists of three counters. The

scintillators are 0.64 cm thick and form planes measuring 76x76 $cm^2$. A 20.3 cm square hole in all layers of S2 allows passage of the beam and most EM products. The light from each counter is viewed by Amperex 56AVP photomultiplier tubes whose gain is monitored by the G2 pulsed laser system. A S2 trigger requires either a summed pulse height equivalent to the passage of at least three minimum ionizing particles, or pulse heights in each of two or three planes consistent with a 0.4 minimum ionizing particle. The efficiency of S2 for detecting muons is >99.9%.

Hadrons passing through the hole in S2 are detected by S3 except for particles in the beam region. S3 is positioned directly behind the lead glass array G3. The acceptance area of the detector measures 102x102 $cm^2$ and is devided into four quadrants. Each quadrant consists of twelve scintillator planes, 0.64 cm thick, with 10.2 cm of iron in front of each plane. An additional iron plate is mounted behind the last scintillator plane to shield against backsplash from the C-counter which is located in the beam region just downstream of S3. The beam enters the C-counter through a 15.2 cm square hole in S3. The twelve counters in each quadrant are optically coupled in sets of four and viewed by Amperex 56AVP photomultiplier tubes. The gain of the tubes is monitored by the G3 pulsed laser system. An energy calibration of S3 is determined with a pion beam of known energy. A very low intensity pion beam can be

obtained by placing a lead brick into the electron beam near the first focus, thereby severely degrading the electron beam and enhancing the pion to electron ratio. Fig. (III.E.4) shows a typical S3 energy spectrum for 90 GeV pions incident on quadrant 4 (bottom, east). The energy resolution is typically no better than 30% (FWHM) of the incident energy. A trigger from S3 is determined by an energy threshold set to about 5 GeV.

4. Hadrometer K (Z+TANC)

The K-counter is furthest away from the target and serves to detect hadrons in the beam region. It consists of two detectors, Z and TANC, which are treated as a unit in the trigger logic. The Z-counter has an acceptance area measuring 51x51 $cm^2$ and is made of four scintillator planes, 0.64 cm thick, with 10.2 cm of iron in front of each plane. The light from the four planes is coupled to an Amperex 56AVP photomultiplier tube.

The TANC (Total Absorption by Nuclear Cascade) is mounted directly behind Z and has an acceptance area of 45x45 cm . It is constructed of 14 iron plates, 5.1 cm thick, immersed in a tank filled with a toluene-base liquid scintillator. Light originating in the scintillator is viewed by a single 20.3 cm diameter Amperex 57AVP photomultiplier tube.

The K-counter is calibrated with a pion beam of known

energy (see S3 description). A typical K energy spectrum for 90 GeV incident pions is shown in Fig.(III.E.4). A K trigger requires a signal from Z or TANC equivalent to the passage of at least one minimum ionizing particle in coincidence with a signal from the pair counter (see Section 6). A K trigger is vetoed, however, if the energy in the C-counter is above some threshold, typically 1/3 of $E_o$ (the electron beam energy).

5. Pb Glass Arrays G2 and G3

Photons and electrons passing through the hole in S1 are detected by two lead glass shower counter arrays, G2 and G3, positioned upstream of S2 and S3 respectively. G2 is a 6x6 array of 6.3x6.3x34.4 $cm^3$ Pb glass blocks surrounded by an additional ring of 18.8x18.8x31.8 $cm^3$ blocks. The central four blocks are removed to allow the passage of the beam and small angle interaction products. The 6.3x6.3 $cm^2$ blocks are glass type SF2 while the large blocks are SF5. Table (III.E.1) lists some of the properties of lead glass. A sheet of lead, 1.3 cm thick, is mounted in front of G2 (to initiate showers earlier) thereby increasing the total length of the detector to approximately 14.4 radiation lengths. The Cerenkov light is viewed end-on by photomultiplier tubes glued directly to the downstream end of the glass blocks. Two types of tubes, RCA 8575 and

Amperex 56AVP, are used for the small blocks; the tubes on the large blocks are 12.7 cm diameter EMI 9815. For the generation of G2 triggers the small blocks, G2S, are treated separately from the large blocks, G2L. A G2S trigger requires about 0.5 GeV in the G2S array while the threshold for G2L is about 2 GeV.

G3 is a 7x7 array of 6.35x6.35x58.5 $cm^3$ blocks, glass type SF2, with the center block removed for the beam to pass through. The Cerenkov light is viewed end-on by 10-stage RCA 6342A photomultiplier tubes. The tubes screw into transparent lucite transition pieces which are glued directly to the end of each Pb glass block. The resolution of the counters is improved (by about 25%) with ultraviolet absorbing yellow glass filters inserted between the lead glass and the photomultiplier tubes [Morrison, 1977]. In effect, the filter reduces light intensity variations caused by longitudinal shower fluctuations and the resulting change in attenuation which is strongest for short wavelengths (see Table [III.E.1]). Optical contact between the Pb glass-filter- phototube surfaces is provided by optical grease. The I-counters, consisting of the eight counters surrounding the beam hole, are subjected to higher rates than the remaining blocks of G3 (eg. wide angle $e^+e^-$ pairs). The energy threshold for a G3 trigger is thus about 2% of $E_o$ (the electron beam energy) for G3 not including the I-counters, and about 5% of $E_o$ for the I-counters. Also, a

trigger from the I-counters is vetoed if the C-counter energy is more than 1/3 of $E_o$.

The G2 and G3 arrays are calibrated with a low intensity electron beam of known energy. Each array has its own laser calibration system to monitor subsequent gain variations of the photomultiplier tubes. To optimize the dynamic range of the counters for different electron beam energy settings, the photomultiplier gains may be changed intentionally by an appropriate change in tube high voltage. The laser systems serve to maintain the energy calibration during this process. Aside from gain monitoring, the lasers are used to examine the linearity of the photomultiplier- ADC system. This is done by inserting a set of neutral density filters between the laser and the counters. A schematic layout of the laser calibration system is shown in Fig.(III.E.5). A detailed description is given in [Morrison, 1975]. The primary light source is a small $N_2$ laser (3371 Å) operated in a pulsed mode, about one pulse per second, with a pulse duration of 3 ns. The laser light is focused onto a small cavity at the center of a lucite sphere. The cavity is filled with a liquid wavelength shifter which re-emitts the light isotropically near 4600 Å. Lucite light guides, glued radially onto one half of the sphere, collect most of the emitted light. The light guides are bent to form a bundle about 2.8 cm in diameter. The other half of the sphere is aluminized to reduce light losses. The light emerging from

the light guides passes through one of several neutral density filters (0% to 100% transmission) which are mounted on a remotely controlled filter wheel. The transmitted light is collected by bundles of optical fiber and guided to the individual counters. The coupling to the counters utilizes 45 degree mirrors which require a minimum of space in front of the Pb glass arrays. The light from the wavelength shifter is measured by the "direct" photodiode (before the filter wheel) and, as a check, is also sampled by the "fiber" photodiode (after the filter wheel). Thus knowing the intensity of each light pulse it is not essential that the laser itself be stable with time. Every 32 laser pulses (or about twice per minute) an average of the counter signal devided by the photodiode signal is calculated for each counter and used to update the energy calibration.

## 6. Pair and Recoil Counters

The pair counter, P, is a plane of scintillator, 18.8 cm square and 1.6 mm thick. It is located just upstream of the multiwire proportional chambers and covers the beam region. A P-counter signal in coincidence with a signal in K generates a hadronic trigger if the energy in the C-counter is less than about 1/3 of $E_o$. The requirement of a P-counter signal eliminates the possibility of a K trigger

resulting from a hadronic beam-photon interaction in the C-counter.

The recoil counters consist of four scintillator planes, 0.64 cm thick, arranged to form a 102 cm long box around the hydrogen target. Between the target and the counters are 0.8 cm of aluminum (the support) and 0.32 cm of lead. The minimum momentum for a particle to exit the target and enter a recoil counter is about 360 MeV/c for protons, 96 MeV/c for pions and 11 MeV/c for electrons. The light is viewed by photomultiplier tubes at each end of the counters. Recoil counter information is not used to generate triggers but is most useful in sorting out ambiguous hadronic events in the off-line analysis and also provides an estimate for the fraction of inelastic events in diffractively produced final states.

## 7. Multiwire Proportional Chambers

Track positions of charged particles entering the H3 acceptance region are provided by six multiwire proportional chambers (MWPC) positioned in front of the Pb glass array, G3. The chambers are of relatively standard construction consisting of a signal wire plane sandwiched between two high voltage wire planes. The wire planes are supported by fiberglass G-10 frames which are bolted onto an aluminum frame for rigidity. The spacing between the wire planes is

8.2 mm. The active area measures 47 cm square and is sealed with mylar windows. The space between the windows is filled with an argon (80%), $CO_2$ (20%) gas mixture. The high voltage wires are made of silver plated Be-Cu alloy, 0.076 mm in diameter. The wire spacing is 1 mm. The signal wires are made of gold plated tungsten, 0.025 mm in diameter. The wire spacing is 2 mm which amounts to 235 active signal wires. Chamber positions and orientations are obtained using standard surveying techniques and are verified by computer fitting routines with data from $e^+e^-$ pairs and $\rho \rightarrow \pi^+\pi^-$ as input. The chambers are separated from each other along the beam direction by an average of 17.7 cm. The chamber closest to G3 has its signal wires some 30 cm in front of the Pb glass. The chambers are rotated around the beam axis by different amounts. The angles between the signal wires and the vertical are approximately $0^0$, $+/-13.5^0$, $+/-70.3^0$, and $90^0$ for the six chambers.

The pulse height from a signal wire is typically 1 mV and thus needs to be amplified to achieve full efficiency in detection. Amplifier cards containing the data output electronics for eight wires plug side by side into sockets on printed circuit boards mounted along two sides of each chamber. The circuit diagram of an amplifier card is shown in Fig. (III.E.6). The signal from each wire is amplified (ac gain $\simeq 2000$) and fed to a discriminator (a one-shot

univibrator) which has a triggering threshold of 1.5 V. The delayed ( 500 ns) and differentiated trailing edge of the discriminator output then sets a bit in a shift register if the signal is in coincidence with a fast load pulse generated by the master trigger of the experiment. The shift registers in a chamber are connected in series and can be read out with clock pulses sent from a scanner module. The scanner unscrambles the serial data and loads its memory (RAM) with wire addresses (13 bits) and spreads (3 bits) of the hit wire groups. The RAM has 64 words of 16 bits. The six chambers are read out in groups of two by three scanners which allows a maximum of 64 wire groups per two chambers. The data in each RAM are transferred to the on-line PDP-15 computer through a CAMAC system.

## F: Trigger Electronics and Data Storage

Typical parameters for the 90 GeV electron beam set-up are $2\times10^{12}$ protons (400 GeV/c) per pulse on target, $1.1\times10^{7}$ electrons at 90 GeV giving about $5.5\times10^{4}$ tagged photons with a 0.01 $X_o$ radiator. At this rate the hadronic yield from the 1 m long (0.11 $X_o$) hydrogen target is about 26 events per pulse corresponding to a 115 μb cross section. Table (III.F.1) lists and defines the six different trigger types which are used to collect and categorize the data. The

triggers are mutually exclusive and ensure that all events initiated by a tagged photon end up in one of the trigger types. The H-trigger logic is shown in Fig.(III.F.1). The TgH trigger contains most of the hadronic events plus a few fake events which are later rejected by the off-line analysis (eg. downstream interactions, muon accidentals, etc.). All TgH events are written on tape. Only a sample of the events from other trigger types are saved however to avoid dead time for TgH events. Scale-down circuits adjust the sampling rate for each trigger type depending on importance. Typical scaledown factors are listed in Table (III.F.1). Trigger type 6 selects non-tag photons from the bremsstrahlung tip for C-counter gain monitoring. The number of good hadronic events found (off-line) in the false tag trigger (TgCH) category is an indication of the fast logic efficiency. TgCH hadronic events represent only 0.07% of the total cross section.

An event which is to be recorded on tape is transferred via CAMAC to a DEC PDP-15 computer. Each event record consists of 157 digitized pulse heights, 24 digitized timing signals, 144 bit latches, and MWPC addresses and spreads. All laser calibration events are written on tape. The current GeV per channel for every counter, 78 scalers, hydrogen target parameters, and the digitized tagging magnet current are written on tape approximately every 5 minutes.

The detection and localization of problems with the

apparatus is aided by the on-line program which allows the display of pulse height and timing spectra for every counter, the computation of MWPC efficiencies, the search for logic errors, etc. A scaler display aides the experimenter to quickly locate inefficient counters, unplugged cables and rate fluctuations.

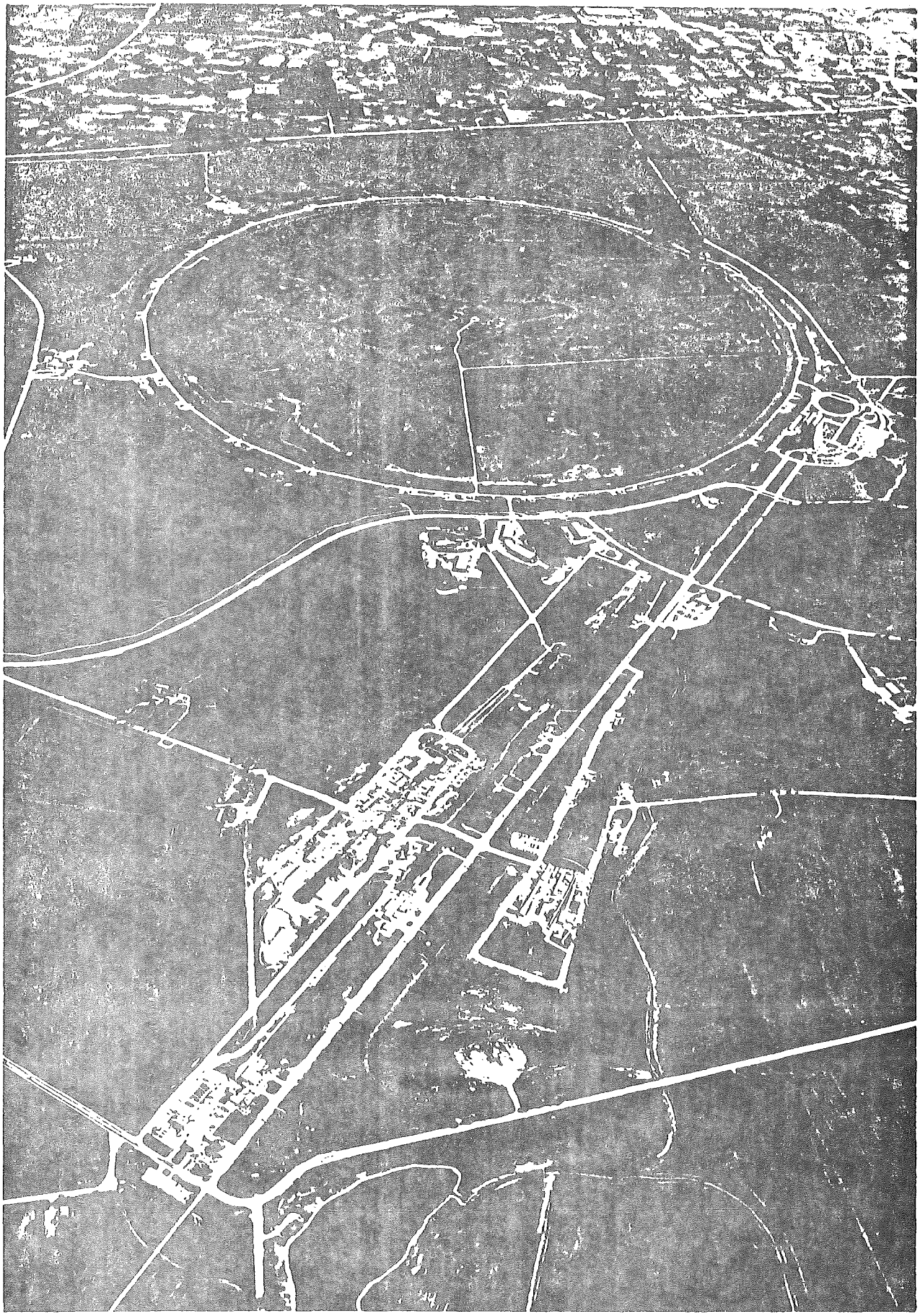

Figure (III.A.1) Aerial view of Fermilab

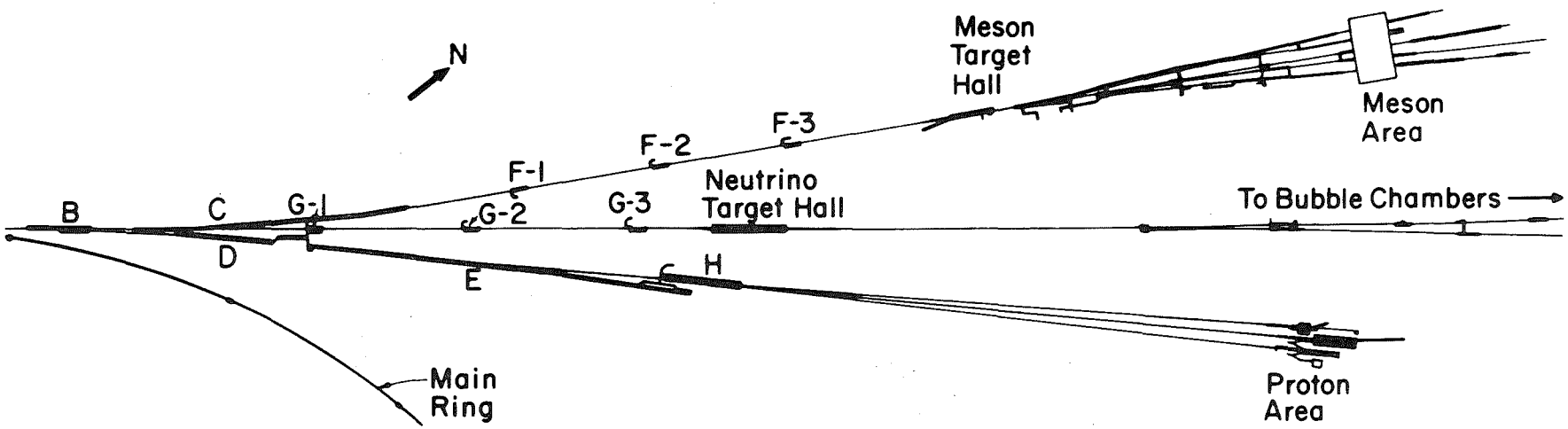


Figure (III.A.2) The beam lines to the experimental areas

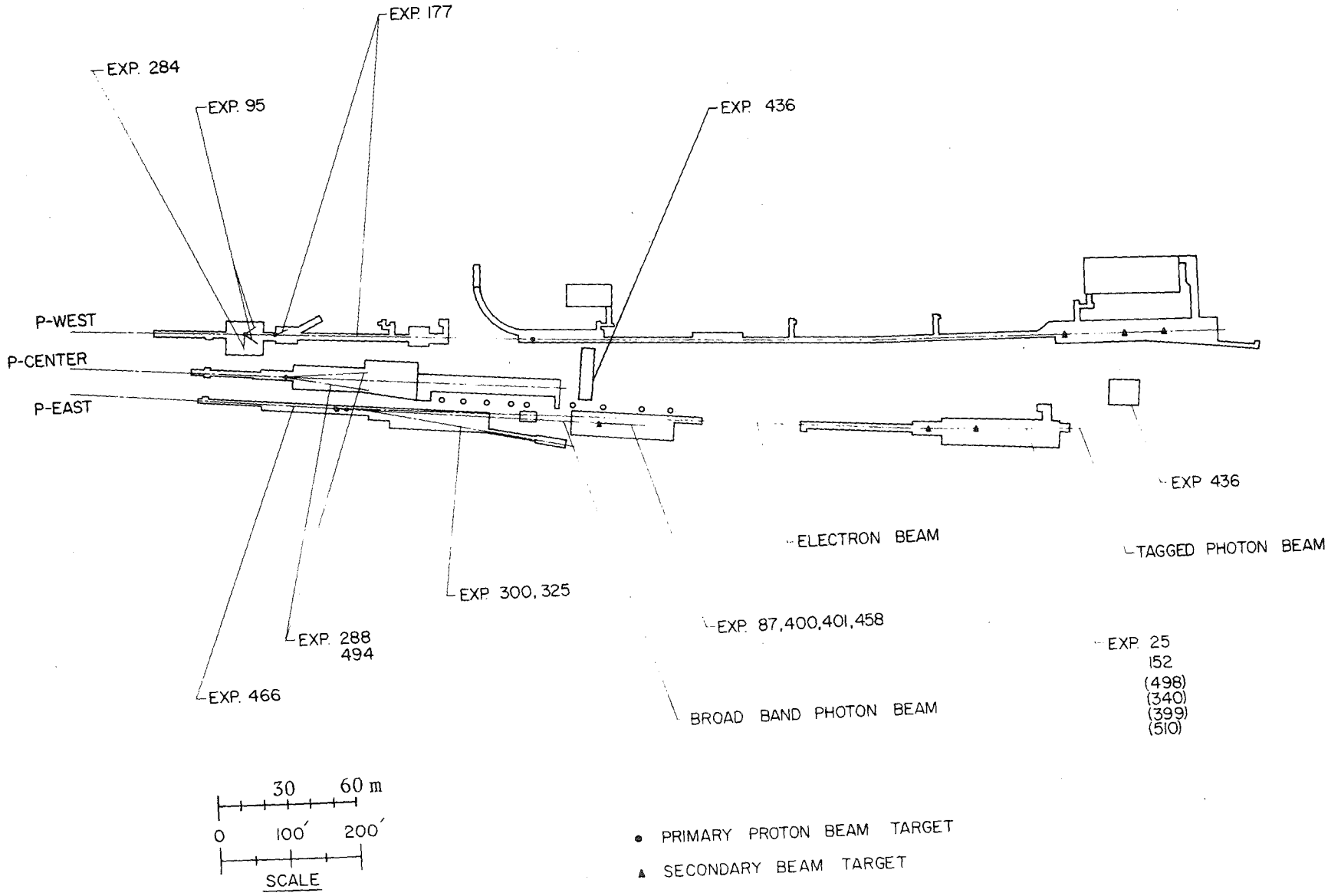


Figure (III.A.3) The Proton Area

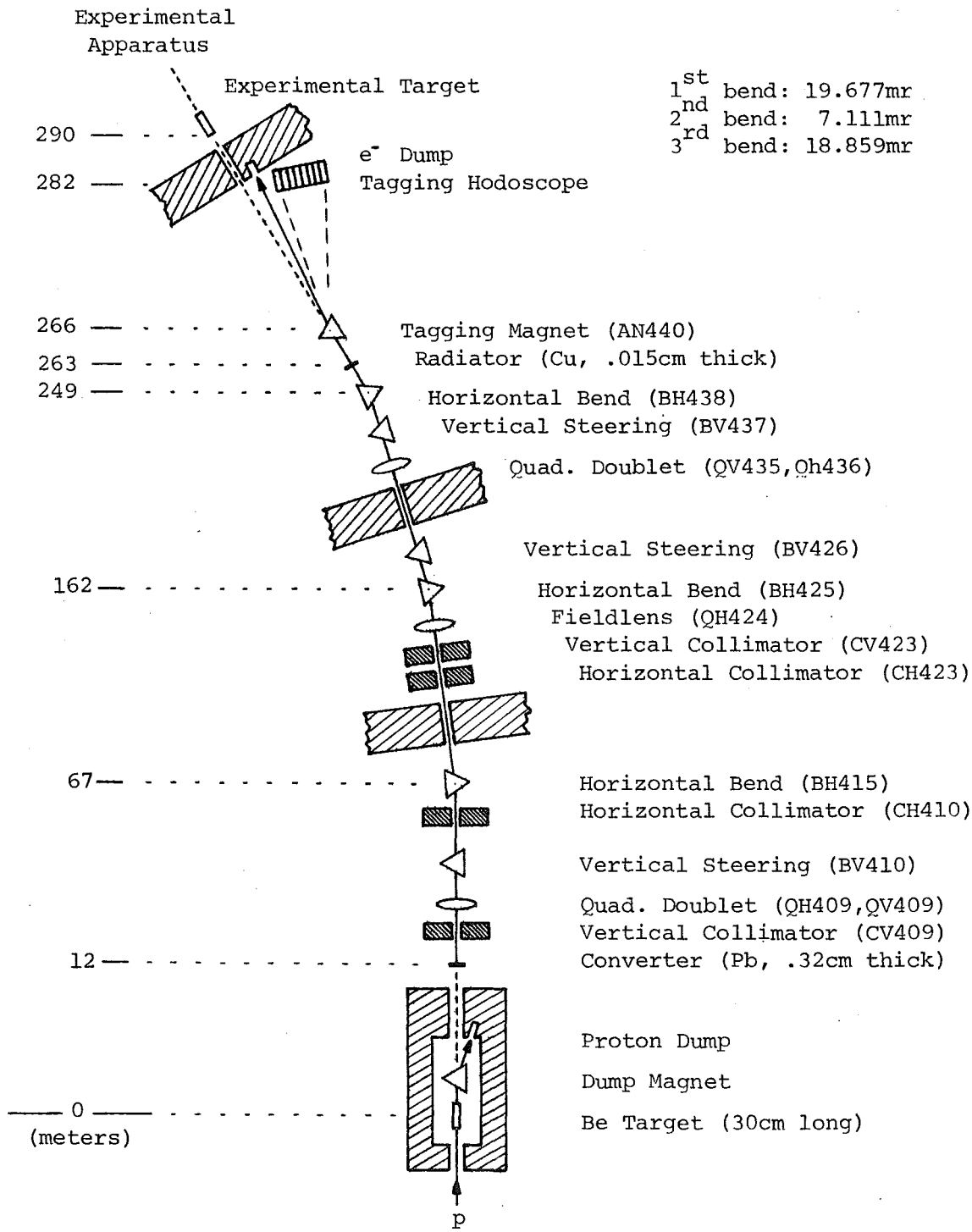


Figure (III.B.1) Electron beam line schematic

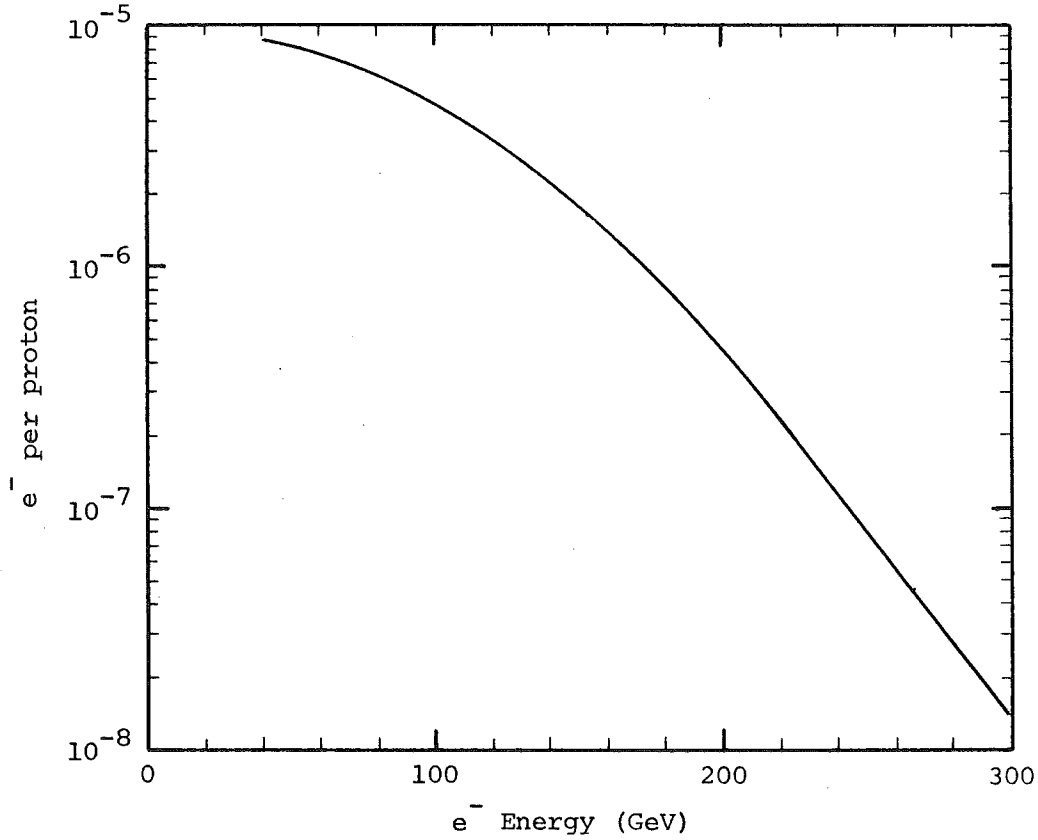


Figure (III.B.2) Typical electron yield per incident 400 GeV proton as a function of electron energy.

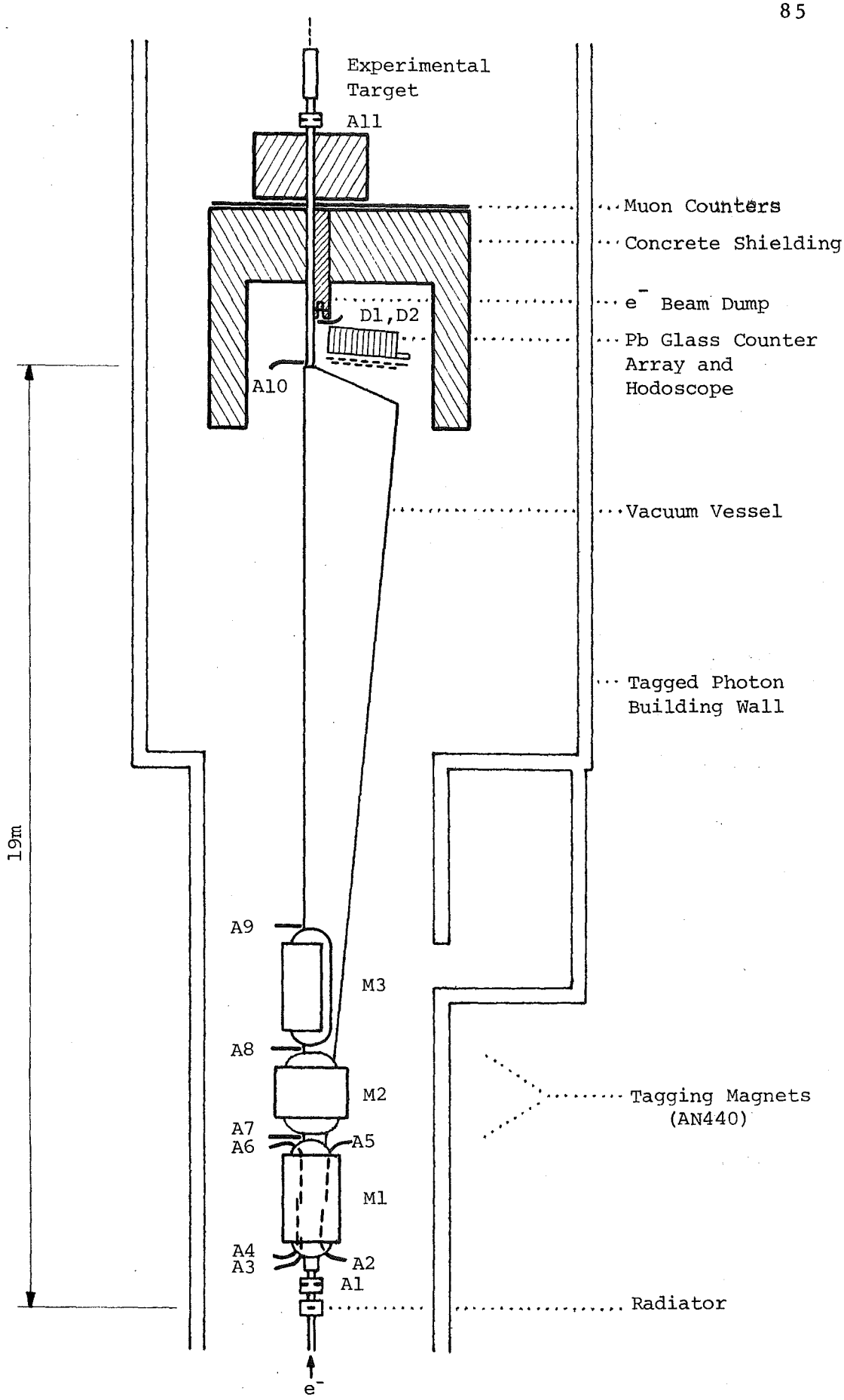


Figure (III.C.1) Schematic of the tagging system

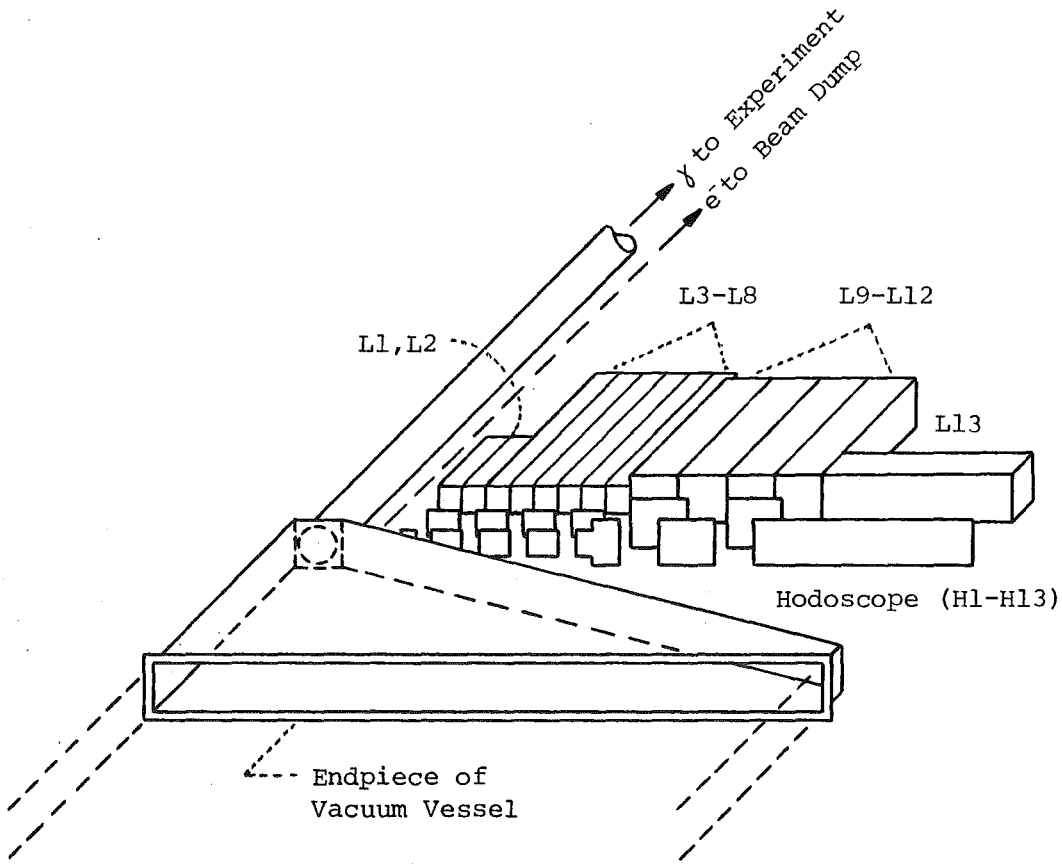


Shower Counter Array:

| | | |
|---|---|---|
| L1-L2 | Pb-Lucite | 6.35 x 6.35 x 25.4 cm |
| L3-L8 | Pb Glass (SF2) | 6.35 x 6.35 x 58.4 cm |
| L9-L13 | Pb Glass (SF5) | 12.7 x 12.7 x 50.8 cm |

Figure (III.C.2) Schematic of the tagging counters

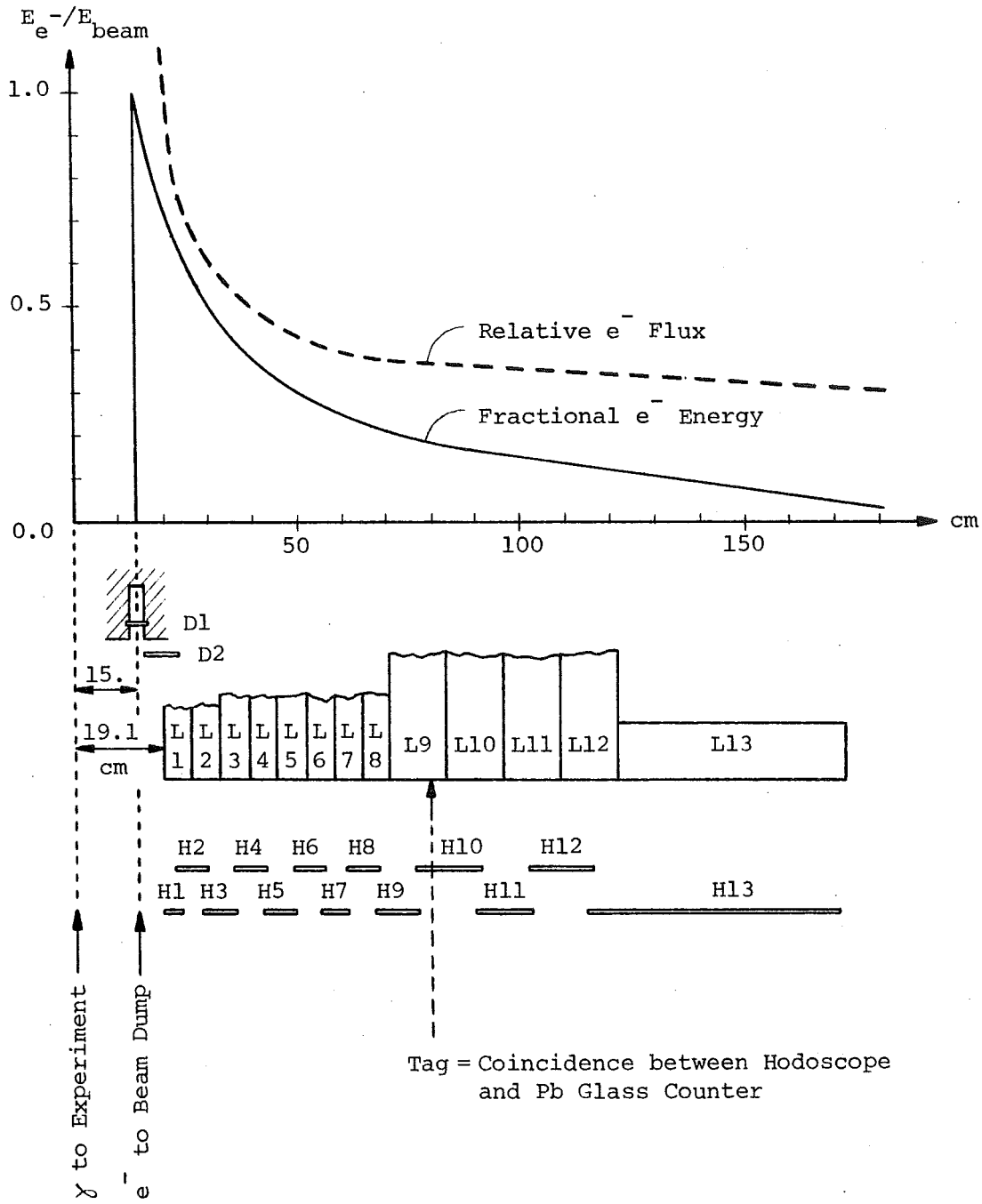


Figure (III.C.3) Typical fractional electron energy distribution across the tagging counters.

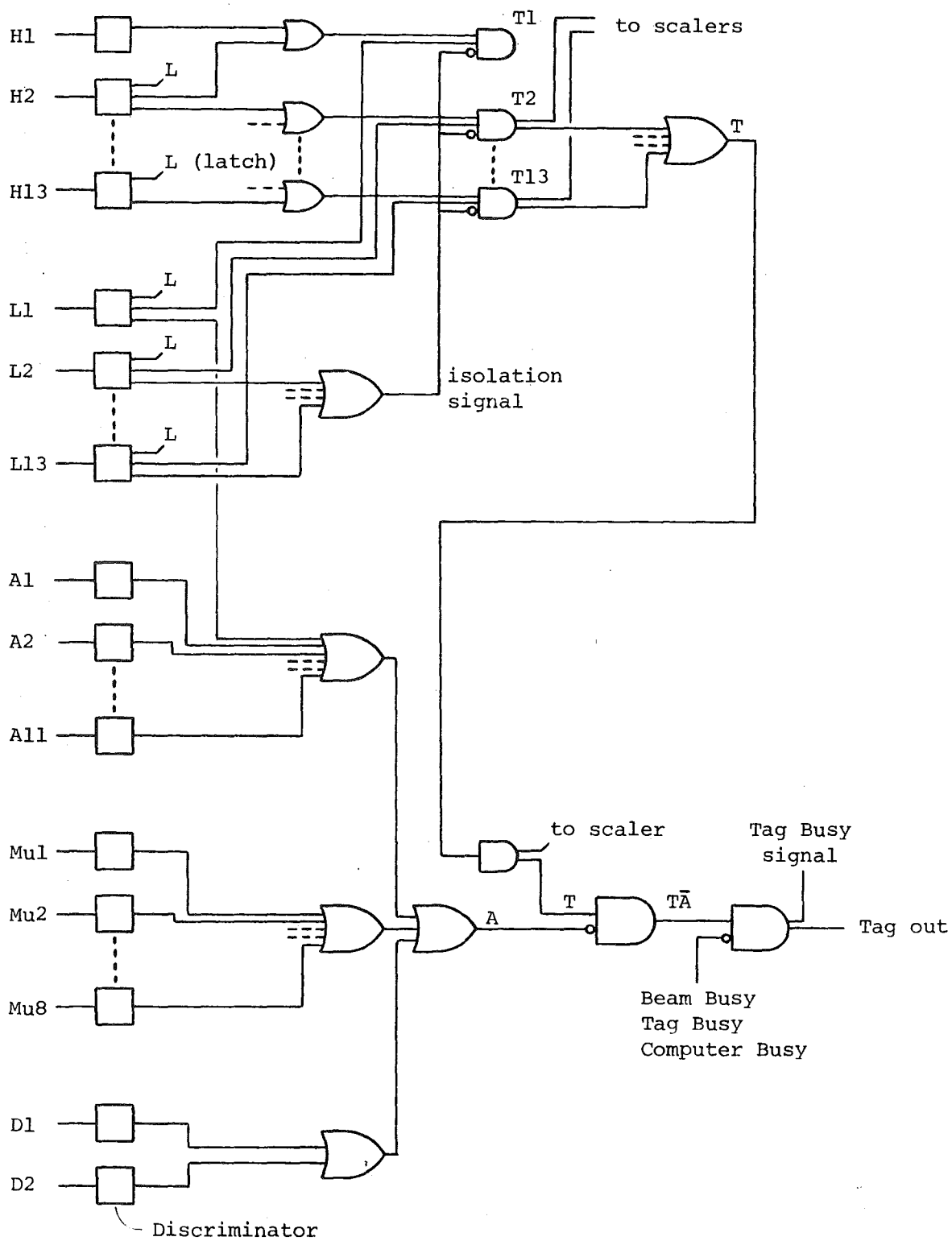


Figure (III.C.4) Schematic of tagging system logic

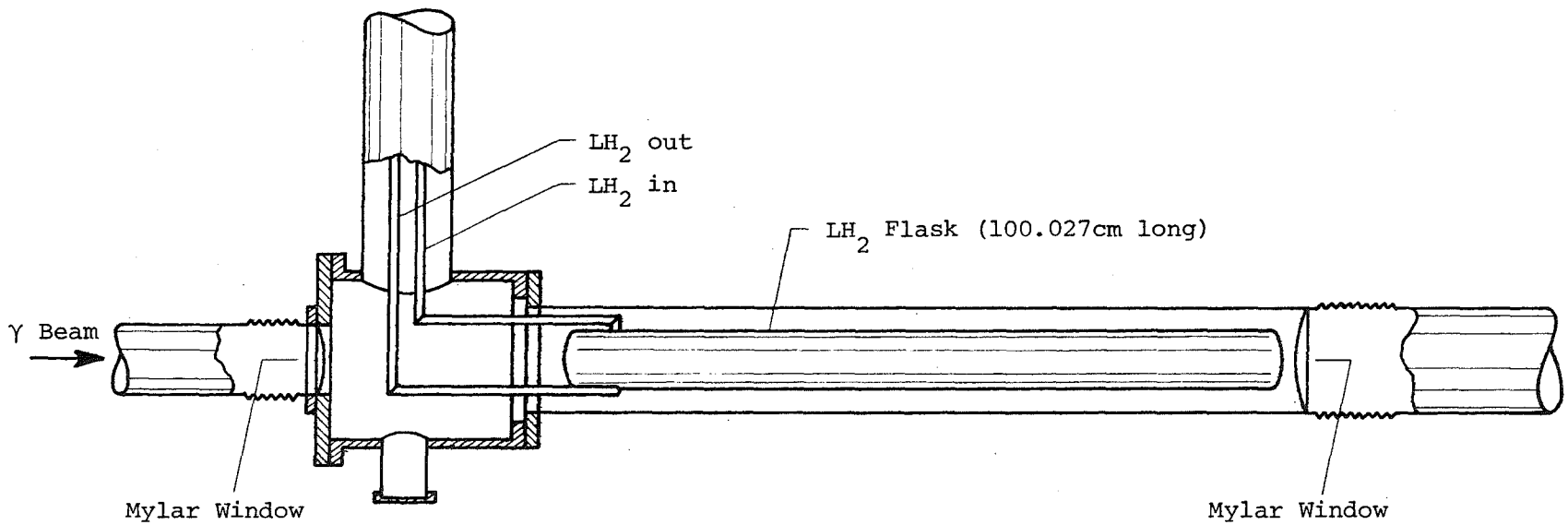


Figure (III.D.1) Schematic of hydrogen target

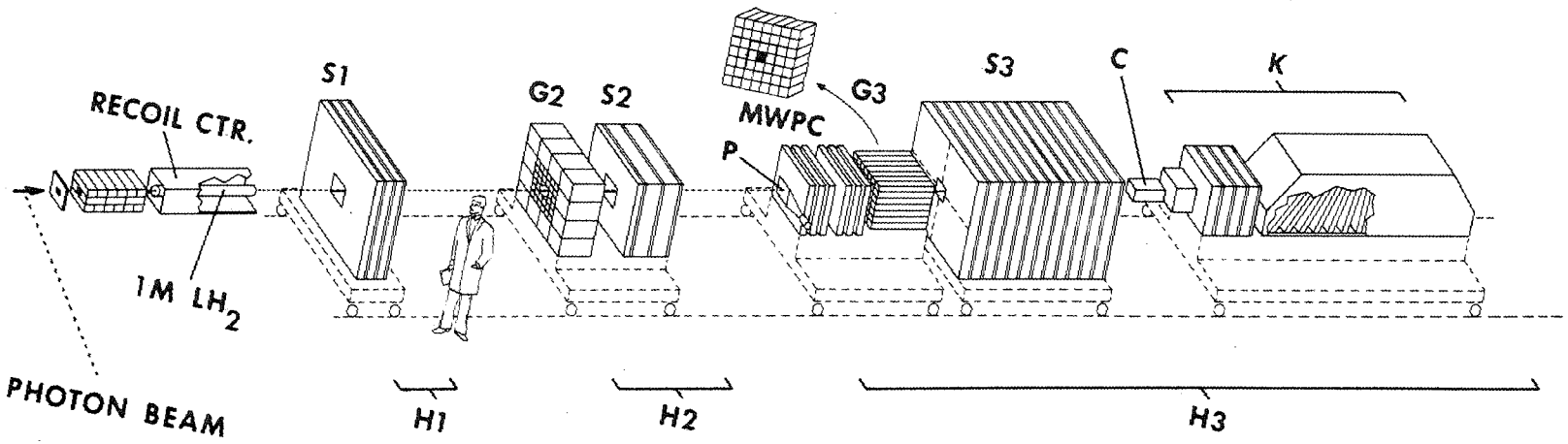


Figure (III.E.1) Experimental apparatus

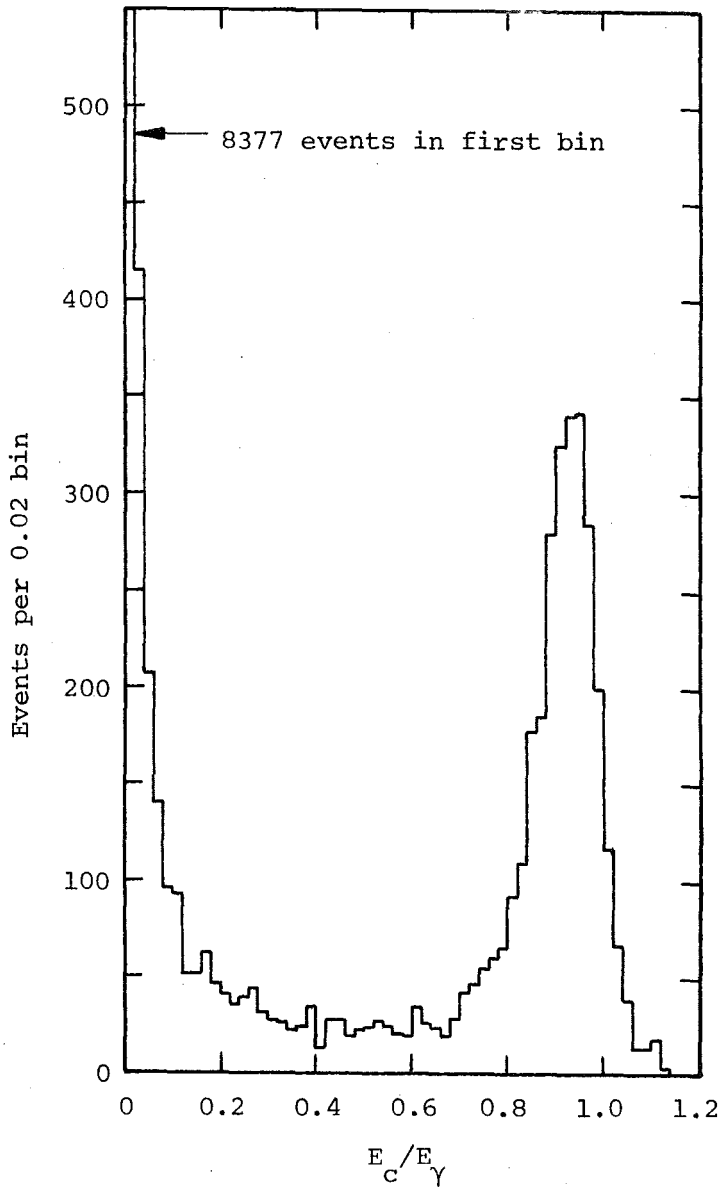


Figure (III.E.2) Fraction of tagged photon energy in C-counter on hadronic candidate events.

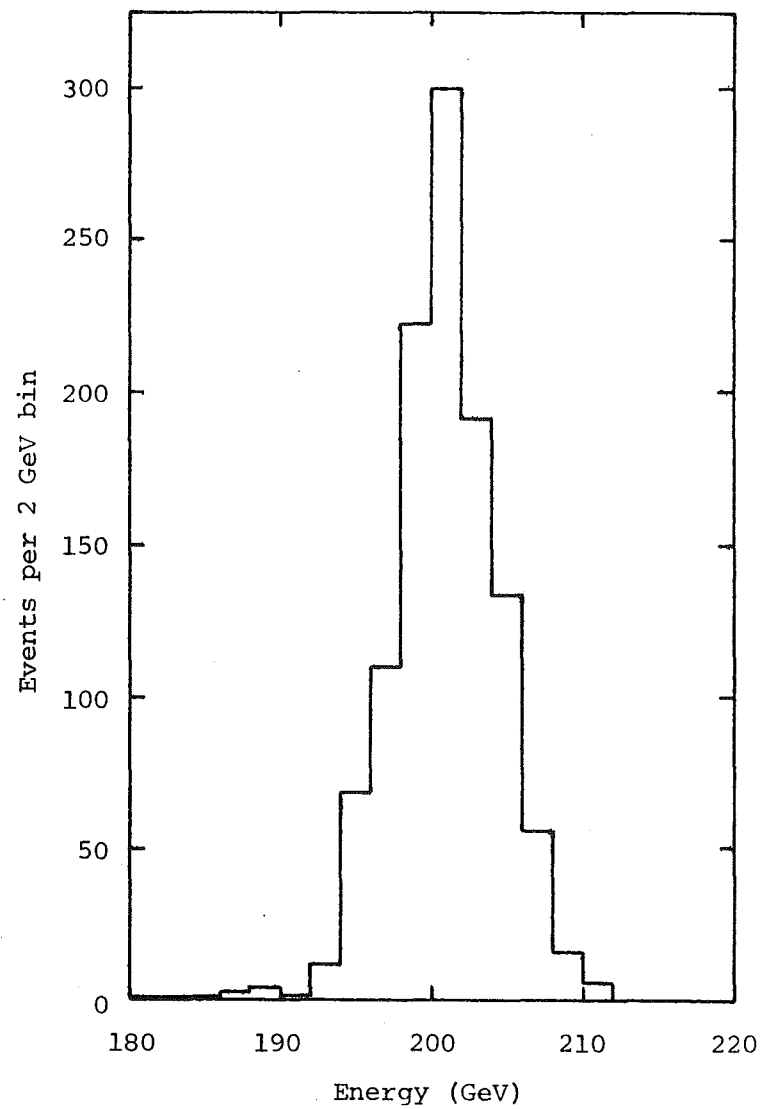


Figure (III.E.3) C-counter energy for 200 GeV incident electrons.

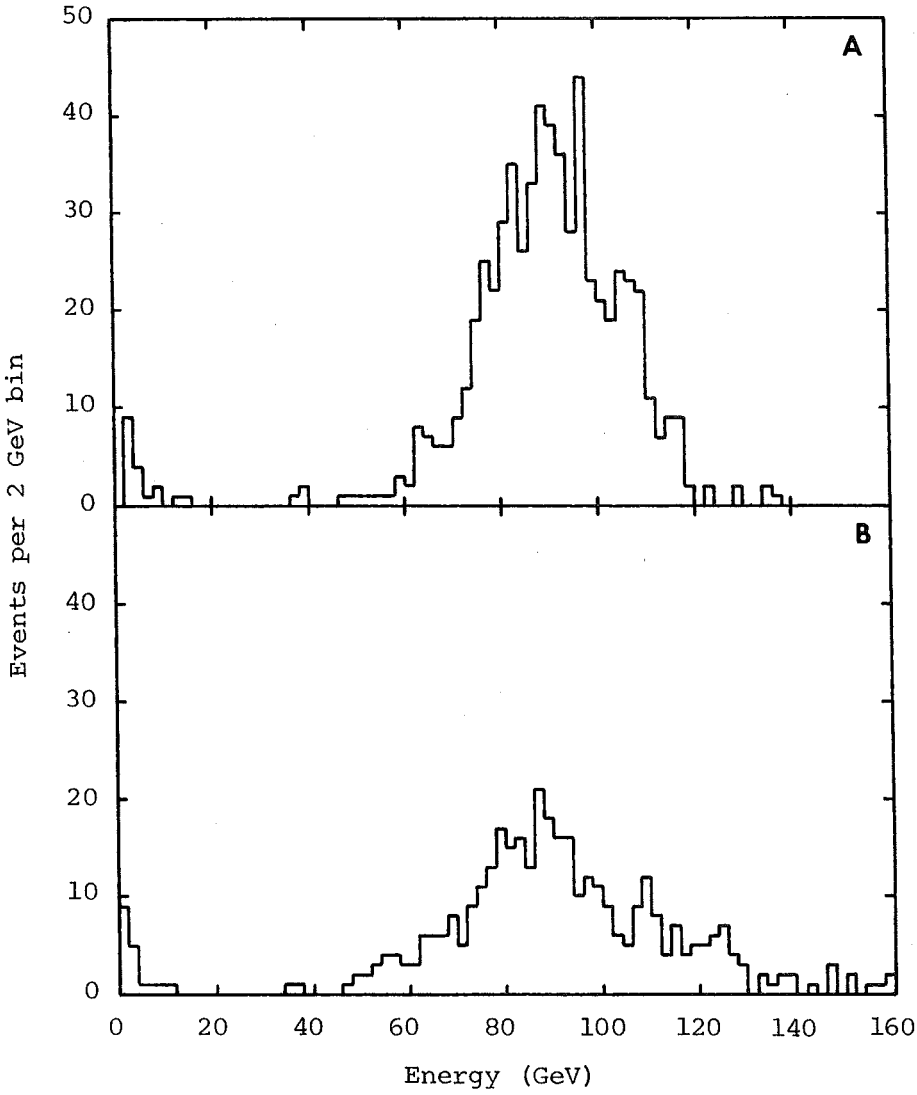


Figure (III.E.4) A: Energy sum in S3 (quadrant 4) for 90 GeV incident pions.

B: Energy sum in K (Z+TANC) for 90 GeV incident pions.

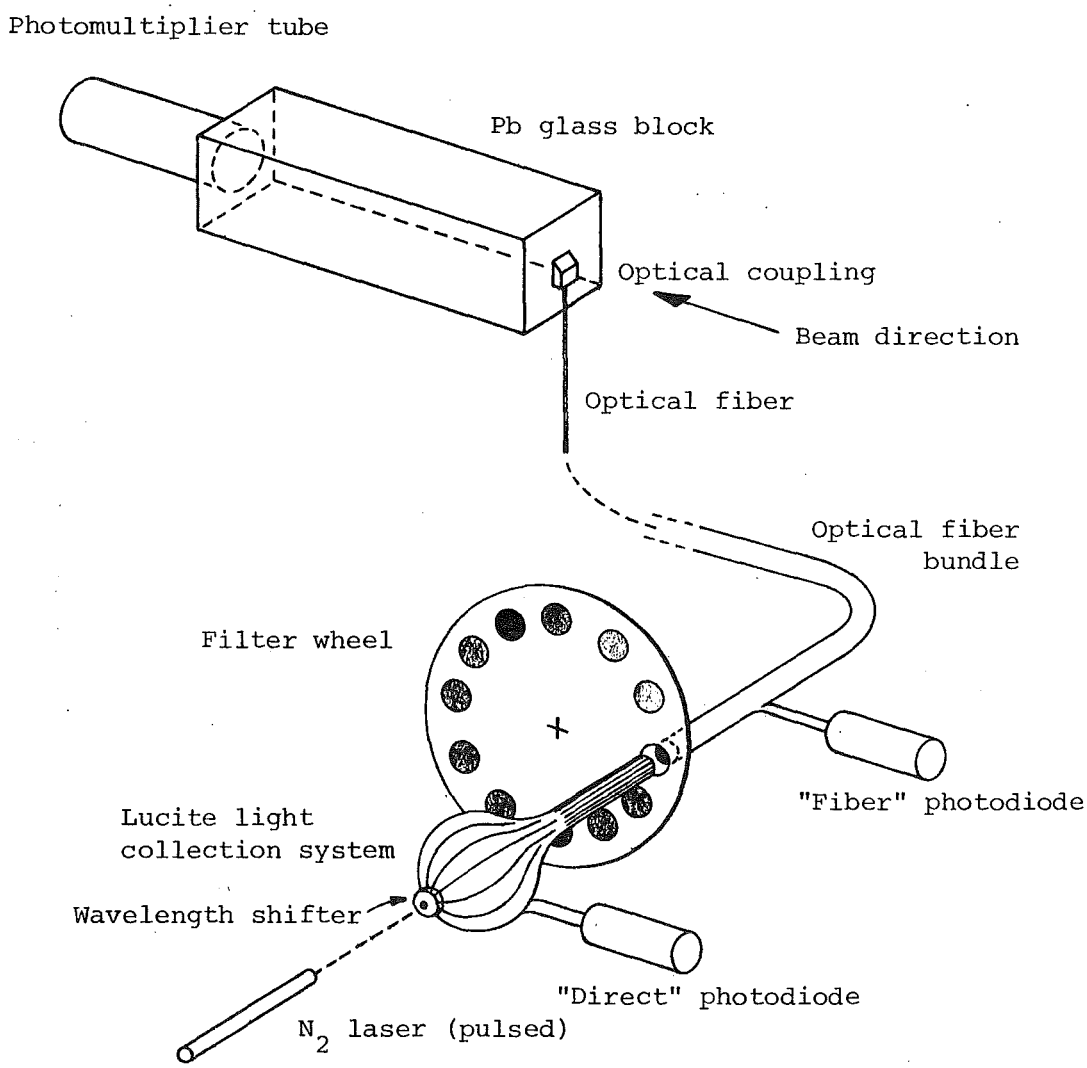


Figure (III.E.5) Schematic layout of the laser calibration system.

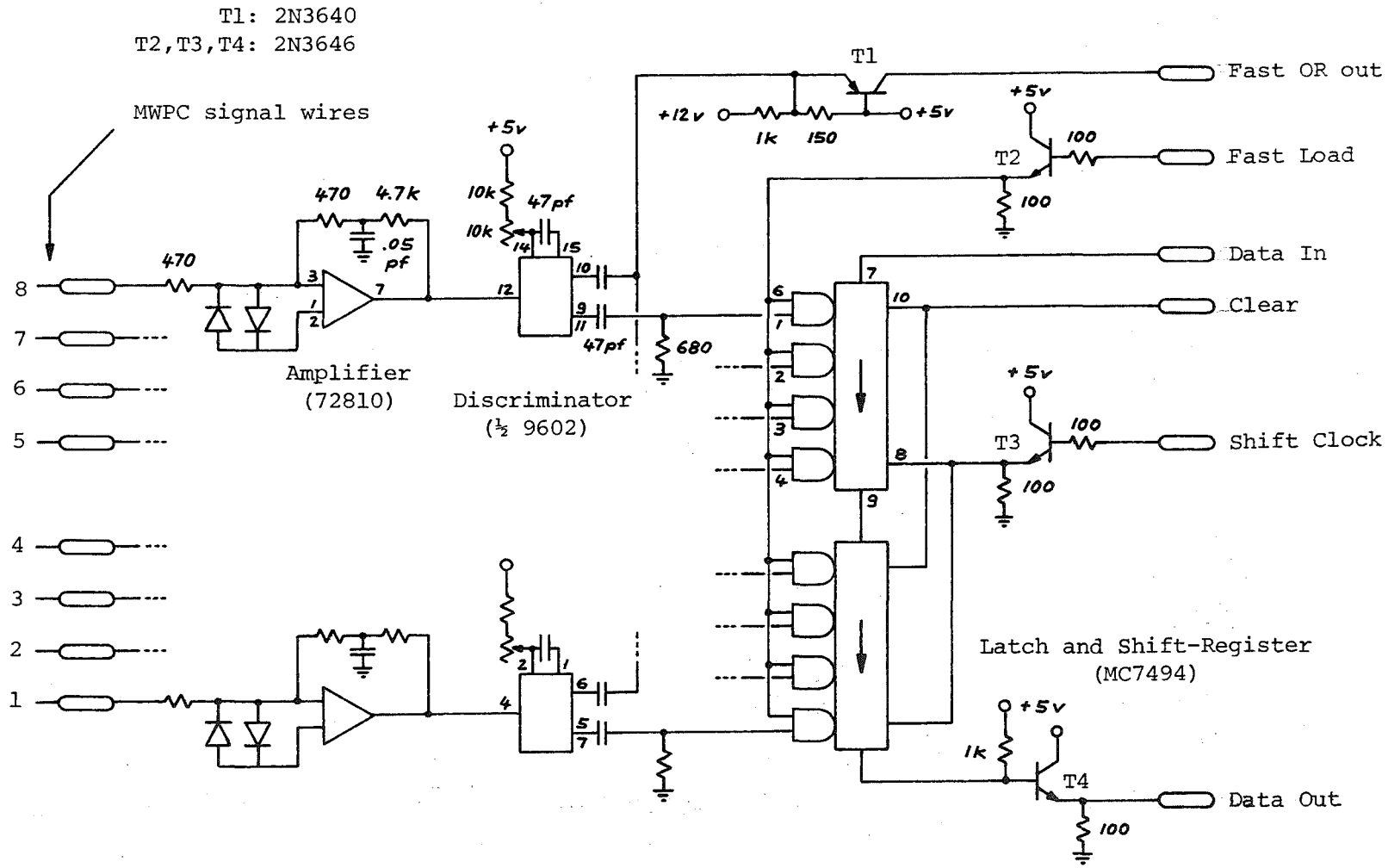


Figure (III.E.6) Schematic of MWPC amplifier card

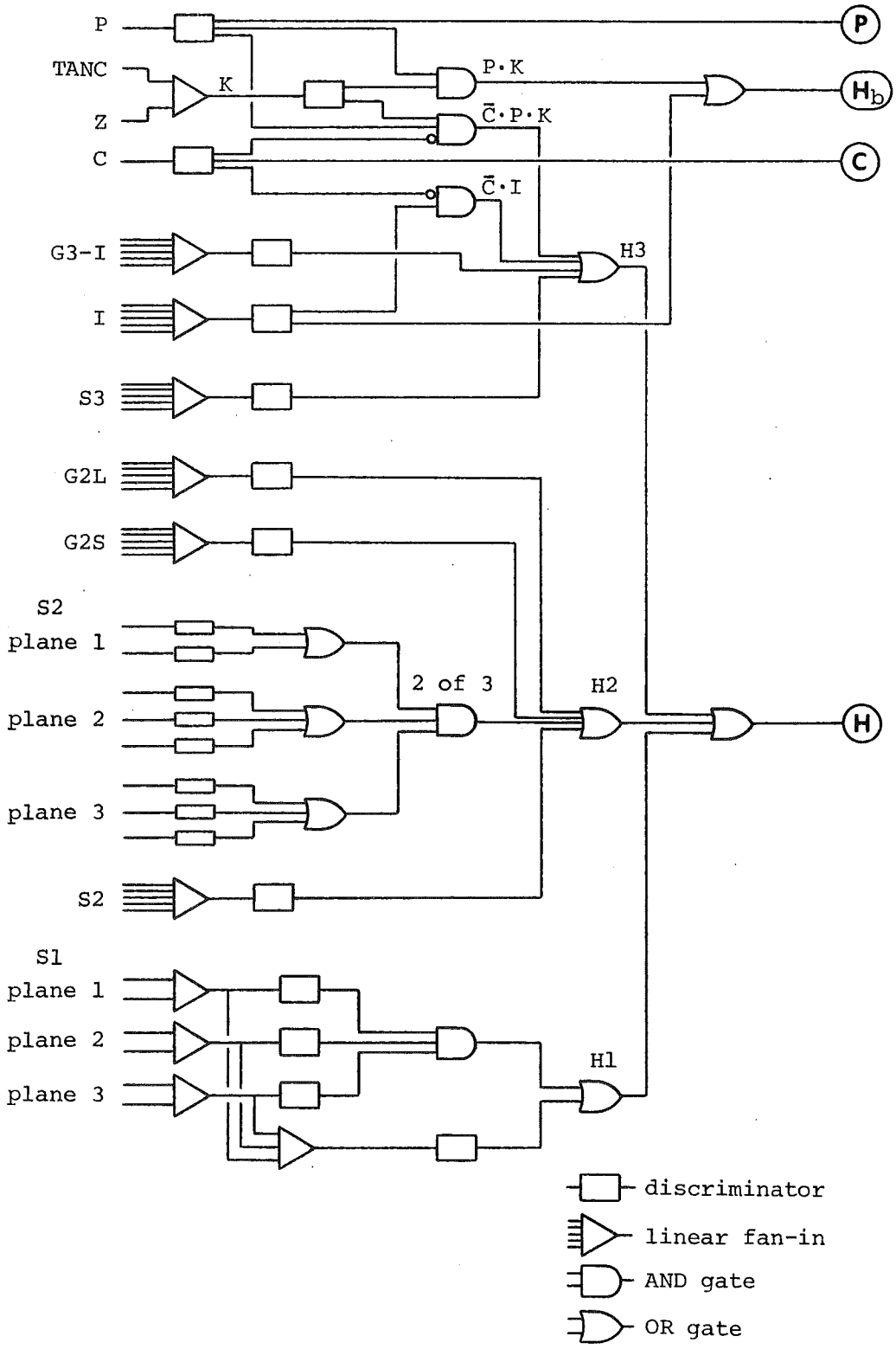


Figure (III.F.1) H-trigger logic

Table (III.E.1)

Properties of Lead Glass

| Glass Type | S F 2 | S F 5 |
|---|---|---|
| Composition (% by weight) | | |
| PbO | 50 | 55 |
| $SiO_2$ | 41 | 38 |
| $K_2O$ | 5 | 5 |
| $Na_2O$ | 3 | 1 |
| Radiation Length (cm) | 2.84 | 2.54 |
| Refractive Index | 1.64769 | 1.67270 |
| Specific Gravity | 3.85 | 4.08 |
| Internal Transmission for 2.5cm Thickness | | |
| $\lambda$=340nm | 0.15 | 0.02 |
| 350 | 0.47 | 0.27 |
| 360 | 0.708 | 0.57 |
| 370 | 0.837 | 0.753 |
| 380 | 0.894 | 0.850 |
| 390 | 0.940 | 0.915 |
| 400 | 0.968 | 0.953 |
| 420 | 0.981 | 0.975 |
| 440 | 0.985 | 0.982 |
| 500 | 0.994 | 0.990 |
| 700 | 0.995 | 0.993 |

Most of our blocks were purchased from Schott Optical Glass, Inc., Duryea, Pennsylvania.

Table (III.F.1)

Trigger Definitions

| Trigger | Definition | Scaledown |
|---|---|---|
| 1 $Tg \cdot H$ | Hadronic events | 1 |
| 2 $Tg \cdot C \cdot \overline{H} \cdot H_b$ | Questionable Hadrons | 3 |
| 3 $Tg \cdot C \cdot \overline{H} \cdot \overline{H_b} \cdot P$ | Pairs | 2000 |
| 4 $Tg \cdot C \cdot \overline{H} \cdot \overline{H_b} \cdot \overline{P}$ | Non-interacting events | 2000 |
| 5 $Tg \cdot \overline{C} \cdot \overline{H}$ | False tags | 50 |
| 6 $\overline{T} \cdot \overline{A} \cdot C \cdot \overline{H} \cdot \overline{P}$ | Bremsstrahlung tip | 20000 |

$Tg = T \cdot \overline{A} \cdot \overline{busy}$ (a tag, no anti-counter signal and no busy signal from the computer or fast-logic)

$H = H1 + H2 + H3$

$H1 = S1$

$H2 = G2L + G2S + S2$

$H3 = (G3-I) + S3 + \overline{C} \cdot H_b$

$H_b = I + (P \cdot K)$

G2L,G2S (G3-I),I : Energy sum above threshold

S1 : Coincidence of 3 planes <u>or</u> energy sum above threshold

S2 : Coincidence of 2 planes (out of 3) <u>or</u> energy sum above threshold

S3 : Energy above threshold

K : Minimum ionizing in TANC+Z

$\overline{C}$ : Energy in C less than 1/3 of $E_o$

P : Minimum ionizing

# CHAPTER IV RHO-PHI ANALYSIS AND RESULTS

## A: Introduction

Elastic $\rho$ and $\phi$ photoproduction cross sections on protons have been measured from 30 to 180 GeV. Schematics of the detection apparatus are shown in Figs. (III.E.1) and (IV.A.1). The apparatus does not include a magnet or Cerenkov counter. It is therefore not possible to directly measure invariant mass spectra. However, a distribution of track separations for events having exactly two tracks and being consistent with exclusive $\rho$ or $\phi$ production, exhibits distinct peaks corresponding to $\rho \rightarrow \pi^+\pi^-$ and $\phi \rightarrow K^+K^-$. Specifically, the small Q value (the momentum of the K's in the $\phi$ rest frame) available for $\phi \rightarrow K^+K^-$ restricts the average $K^+K^-$ opening angle and the corresponding track separation to a value which is about 2.8 times smaller than the average $\pi^+\pi^-$ track separation from $\rho$ decays.

In general, the track separation (distance between particles) at the detector for a particle of mass M decaying into two particles of mass m is given by (for a derivation see APPENDIX A)

$$\Delta = \frac{2ZM\{1 - (2m/M)^2\}^{1/2} \sin\theta}{E\{\sin^2\theta + (2m/M)^2 \cos^2\theta\}} \qquad \text{(IV.A.1)}$$

where

$Z$ = distance from decay vertex to the detector

$E$ = lab energy of decaying particle

$\theta$ = decay angle in M rest frame

The two limiting cases for Eqn. (IV. A. 1) are

$$2m \simeq M : \qquad \Delta \propto \sin\theta$$

and

$$m = 0 : \qquad \Delta \propto 1/\sin\theta$$

The first case approximates $\phi \rightarrow K^+K^-$ whereas the second limit describes $\rho \rightarrow \pi^+\pi^-$ except for $\theta$ near $0^0$ (or $180^0$). The exact behaviour of $\Delta$ (lab frame) vs. $\theta$ (M rest frame) as given by Eqn. (IV. A. 1) is shown in Fig. (IV. A. 2) for $\rho$ and $\phi$ decays. The $K^+K^-$ separation is a maximum when $\theta = 90^0$ (symmetric decay) and is less at all other decay angles. In contrast, the $\pi^+\pi^-$ separation from $\rho$ decays is a minimum when $\theta = 90^0$ and is larger at almost all other decay angles. In addition, the maximum separation for $\phi$ decays is less than the track separation for $\rho$ decays except for $\theta$ near $0^0$ (or $180^0$).

For $\theta = 90^0$: $\quad \Delta_\rho = 1.435\, Z/E\ (\mathrm{GeV}), \quad M_\rho = 0.77$

$$\Delta_\phi = (\Delta_\phi)_{max} = 0.509\, Z/E\ (\mathrm{GeV}) \qquad \text{(IV. A. 2)}$$

Symmetric decays ($\theta = 90^0$) are favoured for both the $\rho$ and

the $\phi$ according to the $\sin^2\theta$ decay angular distribution expected for a $J^P = 1^-$ resonance decaying into a pair of $0^-$ mesons with conservation of s-channel helicity. From Eqn. (IV. A. 2) one can thus expect distinct peaks in plots of track separations corresponding to $\rho$ and $\phi$ decays.

The tagged photon energies range from about 50% to 92% of the electron beam energy. It is therefore necessary to remove the energy dependence of the track separations before plotting. This is accomplished by dividing each measured separation by $(\Delta_\phi)_{max}$. The variable to be plotted is thus defined by

$$R = \Delta/(\Delta_\phi)_{max} \qquad \text{(IV. A. 3)}$$

where $\Delta$ is measured and $(\Delta_\phi)_{max}$ is calculated for each event assuming that the momentum of the $\phi$ is equal to the momentum of the beam photon, $k_\gamma$. For $\phi \rightarrow K^+K^-$ we then expect a narrow peak with $R \leq 1.0$ for all photon energies and $\rho$ decays should peak near $R = 2.8$.

Unfortunately, the R distributions for the $\rho$ meson are not as simple as for the $\phi$. The $\rho$ is a broad resonance (width = 150 MeV approx.) which results in a corresponding broadening of the R distribution. Further, it is well known, that the mass shape of photoproduced $\rho$ mesons is skewed towards lower mass when compared to a p-wave Breit-Wigner resonance shape. The skewing is explained

successfully by the Soding Model as an interference effect between diffractively produced ρ mesons and a non-resonant $\pi^+\pi^-$ background from a Drell diagram [Soding, 1965; Drell, 1961]. The problem of the ρ shape is discussed at length in a paper by Spital and Yennie [Spital, 1974]. A parameterization of the ρ mass distribution is given by

$$\frac{dN}{dM_{\pi\pi}} = C_0 \frac{M_{\pi\pi} M_\rho \Gamma}{(M_{\pi\pi}^2 - M_\rho^2)^2 + M_\rho^2 \Gamma^2} \left\{ 1 + C_1 \left[ \frac{M_\rho^2}{M_{\pi\pi}^2} - 1 \right] + C_2 \left[ \frac{M_\rho^2}{M_{\pi\pi}^2} - 1 \right]^2 \right\} \quad \text{(IV. A. 4)}$$

with the ρ width [Jackson, 1964]

$$\Gamma = \Gamma_o \left\{ \frac{q_{\pi\pi}}{q_\rho} \right\}^3 \cdot \frac{2}{1 + (q_{\pi\pi}/q_\rho)^2} \quad \text{(IV. A. 5)}$$

$q_{\pi\pi}$ and $q_\rho$ are the pion momenta in the ππ rest frame for dipion masses $M_{\pi\pi}$ and $M_\rho$ respectively.

There is a direct correspondence between the ρ mass spectrum and the R distribution. A Monte Carlo (M. C.) generated scatter plot of R versus $M_{\pi\pi}$ for ρ decay illustrates this relationship in Fig. (IV. A. 3). Events in a given R region are associated with a corresponding $M_{\pi\pi}$ range. The Monte Carlo event generation takes into account the resolution and acceptance of the experimental apparatus. The events were generated assuming s-channel helicity conservation and a momentum transfer dstribution given by exp(bt) with b = 8.5 $GeV^{-2}$. The Monte Carlo generated R distribution for the ρ is shown in Fig. (IV. A. 4A) with

$C_1 = 3.0$ and $C_2 = 2.0$. The important effect of skewing and mass shift is apparent on comparing with the dotted curve for which $C_1 = C_2 = 0.0$, i.e. no interference. The actual values for the parameters $C_0$, $C_1$, $C_2$ are determined by fitting Monte Carlo generated R distributions to the real data. Fig.(IV.A.4B) shows the Monte Carlo generated R distribution for the $\phi$. Neglect of the experimental resolution yields a sharp peak with an abrupt cutoff at $R = 1$ as shown by the dotted curve. The broadening caused by the energy resolution of the tagging system and the track position resolution from the MWPC's is indicated by the solid curve.

## B: Data Accumulation

Data were taken with the electron beam energy $E_o = 60$, 90, 135 and 200 GeV. Some data were taken with $E_o = 60$ GeV and the apparatus in a configuration appropriate for $E_o = 90$ GeV to check the effect of changes in geometrical acceptance. As the photon energies cover about 50% to 92% of $E_o$ there is a substantial gamma energy overlap for adjacent $E_o$ settings. At each configuration data were also taken with an empty hydrogen target to obtain spectra of events originating outside the target.

An event is considered an elastic $\rho$ or $\phi$ candidate if it

has exactly two tracks in the MWPC's and a large fraction of the photon energy in the downstream hadrometers S3 and K. The upstream counters S1, S2 and G2 are used as veto counters. Events of this kind are recorded in the TgH trigger category which contains most hadronic events (see Section [III.F] and Table [III.F.1]). The number of tagged photons and TgH triggers for the full hydrogen target are summarized in Table(IV.B.1).

## C: Data Analysis

### 1. General

All events collected in the TgH trigger category are recorded on tape. From these events a subsample consistent with exclusive $\rho$ or $\phi$ production is obtained by requiring the events to pass a number of analysis cuts. The cuts are discussed below and are summarized in Table(IV.C.1). About 1% (for $E_o$= 60 GeV at 90 GeV configuration) to 3.4% (for $E_o$= 135 GeV data) of the TgH events survive all the cuts.

The summed ADC pulse height spectrum for planes 2 and 3 of S1 are shown in Fig.(IV.C.1A) for part of the $E_o$= 135 GeV data. Events pass the S1 cut if this pulse height is less than 1.0. Plane 1 is excluded from consideration to avoid vetoes resulting from very low energy $e^+e^-$ pairs originating

in the target and depositing energy in the front plane of S1. Of the events passing all cuts, less than 3% have S1 (planes 2 + 3) pulse heights between 0.2 and 1.0. Counter noise accounts for about one third of this sample. The remainder is attributed to inelastic $\rho$ or $\phi$ production as most of these events have two or more of the recoil counters firing.

Typical spectra of the variables used in the energy cuts are shown in Figs. (IV.C.1B) and (IV.C.2A and 2B) for part of the $E_o$= 135 GeV data. The missing energy cut requires the energy deposited into the H3 counters to be no less than 35% of the tagged photon energy. The rather poor energy resolution of the TANC counter is in part responsible for this somewhat generous threshold. The probability for a pion or kaon to interact hadronically in the Pb glass array G3 or the C-counter is quite significant (typically 70%). Neutral pions resulting from such interactions initiate electromagnetic showers ($\pi^0 \rightarrow \gamma\gamma$) and thus can deposit a substantial fraction of the total energy in G3 and C. However, if the interaction takes place near the end of the shower counters the remaining length may not be enough to contain all of the e.m. shower and energy will be lost. The hadronic products of such pion or kaon interactions are not expected to always deposit all of their energy in the hadrometers S3 and K. As a result the missing energy distribution peaks at a value between 20% and 30% of the

tagged photon energy.

The summed energy in the C-counter and the Pb glass array G3 (G3IC energy) may be as large as 60% of the tagged photon energy. This allows for energy deposited by pions or kaons interacting in the shower counters. The location of the showers in the Pb glass array are required to agree with the track positions given by the MWPC's. Background events such as $\omega \rightarrow \pi^+\pi^-\pi^0$ are thereby eliminated (about 3-4% of the $\rho$-$\phi$ candidates).

To ensure that at least some of the tagged photon energy registers in S3 or K, independent of the missing mass cut and the energy allowed in the shower counters, the G3IC energy can be no more than 75% of the summed H3 energy, i.e. at least 25% of the visible energy is in S3 and K.

A geometric boundary (acceptance) is imposed on the events by requiring each track to be inside a 33 cm (13") square area at the MWPC's. The distribution of the y-coordinate (vertical) for MWPC tracks ($E_o$= 135 GeV data) is shown in Fig.(IV.C.3). The sharp peak at y = 0 is mainly due to rho's being produced at the steel window of the vacuum pipe just upstream of the MWPC's (see fig.(IV,A.1)) as confirmed by empty target data.

## 2. Track Reconstruction

An event is considered a $\rho$ or $\phi$ candidate only if it has

exactly two reconstructed tracks. Six MWPC's are available for track reconstruction (see Section [III.E.7]). A track is described by a straight line (no bending magnets) in space. A three-dimensional parameterization of a single track passing through the MWPC's requires wire information from four chambers. As is shown schematically in Fig.(IV.C.4A), an event with more than one track requires at least one additional chamber to resolve ambiguities in the track reconstruction, i.e. a minimum of five chambers are needed to determine the positions and angles (with respect to the beam axis) for two tracks. For the purpose of increased reconstruction efficiency it is assumed that the tracks originate at the center of the hydrogen target. As a result, the minimum required number of chambers with complete wire information is reduced to three (out of the total of six) for each two-track event.

Wire information from the MWPC's consists of the addresses and spreads of hit wire groups (wires with a signal). Groups usually have a spread of 1 (only one hit wire) or possibly 2 (two adjacent hit wires) but rarely greater than 2. The number of groups for $\rho$-$\phi$ candidates is shown in Fig.(IV.C.4B) for part of the $E_o$= 200 GeV data. Two charged particles passing through the six MWPC's are expected to yield 12 groups (2 per chamber). It is of course possible for the two particles to hit the same wire in a particular chamber (more so for small track

separations) so that the number of groups would be less than 12. An event is rejected unless the number of groups is at least 10 but no more than 20. Events falling outside this bracket are usually associated with downstream interactions (typically from the steel vacuum window in front of the chambers).

As each event requires only three of the six chambers for the track reconstruction it is possible to keep a running efficiency check of the MWPC's by testing the wire information of the unused chambers for consistency with the reconstructed track positions. Only events which have at least three efficient chambers (i.e. two reconstructed tracks) are considered. The resulting bias requires a small (downward) correction to the efficiencies obtained in this manner. The corrected efficiencies of the individual chambers for detecting both tracks (with no additional hits) ranges from about 62% to 86%. The average reconstruction efficiency for 2-track events is typically 92 ± 1% for the six chambers but decreases for tracks less than 1 cm apart. A study of events which do not have two reconstructed tracks but pass all other cuts for $\rho$-$\phi$ candidates reveals no problems (1%) with lost $\rho$ or $\phi$ events due to extra (accidental) hits.

3. Data and Monte Carlo

The distribution of R (the normalized track separation defined by Eqn. (IV. A. 3)) is shown in Fig. (IV. C. 5) for the $E_o$= 90 GeV data and in Fig. (IV. C. 6) for the $E_o$= 135 GeV data. The data for $E_o$= 60 GeV and 200 GeV look similar. In addition to the dominant ρ peak, all distributions exhibit a clear ϕ peak near R = 1. Most of the events near R = 0 are ρ's produced at the steel window of the vacuum pipe which ends just upstream of the MWPC's. These events produce the peak at y = 0 of the track coordinate distribution shown in Fig. (IV. C. 3). Data taken with an empty target are shown in Fig. (IV. C. 7) and clearly confirm the origin of this background. The empty target data also show a few events in the R>1 region which are produced at the target windows and off the hydrogen gas in the target flask.

A small fraction of the events near R = 0 is due to $e^+e^-$ pairs. If the energies of the electron and the positron differ by a sufficiently large amount, and the higher energy particle interacts hadronically in the C-counter, a significant fraction of the energy may show up in the hadrometer K. An $e^+e^-$ pair can thus end up in the TgH trigger category (instead of $Tg \cdot C \cdot \overline{H} \cdot \overline{Hb} \cdot P$ or possibly $Tg \cdot C \cdot \overline{H} \cdot \overline{Hb}$) and create a source of background. The R distribution for interacting $e^+e^-$ pairs should be no different than the distribution for non-interacting pairs

which is shown in Fig. (IV.C.8). The distribution falls off smoothly toward the $\phi$ region near R = 1 and therefore should not cause any concern regarding interference with the $\phi$ peak.

A small background (less than 1% of the events in the $\rho$ peak) is due to the decay $\phi \rightarrow K_L^0 K_S^0 \rightarrow K_L^0 \pi^+ \pi^-$ (branching ratio = 24%). The shape of the resulting R distribution is shown in Fig. (IV.C.5). There is no contribution from this background to the events in the $\phi \rightarrow K^+ K^-$ peak.

The data are fitted with Monte Carlo generated R distributions for $\rho$ and $\phi$ events. An $e^+e^-$ pair background is included in the computer fitting program. The fitting parameters are the constants $C_0$, $C_1$ and $C_2$ of the $\rho$ mass distribution, Eqn. (IV.A.4), the number of events in the $\phi$ peak and the size of the $e^+e^-$ background. The amount of empty target background is calculated for each set of data and is thus a constant of the fit. The nominal $\rho$ mass and width are held fixed for all fits at $M_\rho$= 773 MeV and $\Gamma_o$= 150 MeV. The $\rho$ and $\phi$ decays are generated according to a $\sin^2\theta$ polar angle distribution with respect to the direction of the decaying meson in the meson rest frame. Detailed experiments at lower energies [Ballam, 1973; Behrend, 1978] show that $\gamma \rightarrow \rho$ and $\gamma \rightarrow \phi$ transitions conserve s-channel helicity to a high degree. The azimuthal angle is randomly distributed as neither the beam photons nor the target protons are polarized. The Monte Carlo momentum

transfer distribution is given by $e^{bt}$ with $b(\phi) = 6.5\ GeV^{-2}$ and $b(\rho) = 8.5\ GeV^{-2}$. Both values for b are consistent with VMD- quark model predictions at high energies, e.g. $b(\rho)$ is approximately equal to the average slope for $\pi^+p$ and $\pi^-p$ elastic scattering (see Appendix D), in good agreement with $\rho$ photoproduction data [Leith, 1977; Behrend, 1978]. The results of the analysis are not significantly affected by the uncertainties in these numbers except for a weak dependence of the $\rho$ acceptance on $b(\rho)$. The photon spectrum and beam size are given the experimentally observed characteristics. The generated events are reconstructed taking into account the geometric acceptance and the energy and track position resolution of the experimental apparatus.

The Monte Carlo generated dipion mass spectrum resulting from the fit to the $E_o = 135$ GeV data is shown in Fig. (IV.C.9) with $C_0 = 1$. The fitted R distribution is the dotted curve shown in Fig. (IV.C.6). The constants $C_1$ and $C_2$ which determine the shape of the $M_{\pi\pi}$ distribution show no substantial energy dependence and have average values of $3.0 \pm 0.7$ and $2.0 \pm 0.5$ respectively. The constant $C_0$ is, of course, proportional to the number of events in the $\rho$ peak.

The Monte Carlo program with the above described input quantities produces very good fits over the entire R range for all data samples. The program is used to determine the uncertainties on all fitted parameters and gives the geometric acceptance for $\rho$ and $\phi$ events.

## 4. Inelastic Events

Measurements of elastic photoproduction cross sections from hydrogen are subject to uncertainty due to the unknown inelastic contribution to the production process,

$$\gamma p \rightarrow VX, \quad X \neq p \qquad \text{(IV.C.1)}$$

where V is a vector meson and X denotes a missing mass different from the proton mass. Inelastic events can be eliminated if the recoil proton is detected in coincidence with the vector meson decay products. An additional criterion for two-body production is the coplanarity of the recoil proton and the vector meson. The fraction of inelastic $\rho$ and $\phi$ events has been measured at Cornell [Berger, 1972] with $E_\gamma = 8.5$ GeV as a function of the momentum transfer t and, for the $\rho$, at various dipion mass intervals. They report an inelastic fraction in $\rho$ photoproduction which is typically less than 5% at $t = t_{min}$ and rises to about 25% near $t = -0.4$ GeV$^2$. There is no obvious dependence on the dipion mass $M_{\pi\pi}$. The inelastic contribution to $\phi$ photoproduction is given as $14 \pm 8\%$ at $t = t_{min}$ and appears to increase slightly with increasing t. These numbers represent the inelastic contribution within the energy acceptance of the experimental apparatus and are in this sense lower limits.

Inelastic $\phi$ photoproduction was also measured at DESY [Behrend, 1978]. The inelastic fraction at $t = t_{min}$ is typically 25%-30% for $E_\gamma \simeq 5$ GeV. The separation of elastic and inelastic events is reported to have a possible systematic error of 20%. The momentum transfer slope parameter for inelastic events is less than for elastic events and decreases with increasing missing mass $M_X$. This implies that the inelastic fraction increases with increasing t, in qualitative agreement with the $\rho$ and $\phi$ data of [Berger, 1972].

In this experiment the fraction of inelastic $\rho$ and $\phi$ events is estimated from the number of events with a signal in one or more of the four scintillator counters surrounding the hydrogen target (see Section [III.E.6]). The observed fraction of events with 0, 1 and >1 recoil counter signals in coincidence with the vector meson decay products is shown as a function of R in Fig. (IV.C.10) for all of the $\rho$-$\phi$ data. For recoil studies the data are divided into subsamples of events with 0, 1 and >1 recoil signals. The number of $\rho$ and $\phi$ events in each subsample is obtained from the respective R distributions using the Monte Carlo fitting routine described in the previous section. The observed fraction of events in each recoil category are listed in Table (IV.C.2). For the $\rho$, the numbers represent averages for events in the peak region of the R distributions.

The Monte Carlo program which is used to fit the

experimentally obtained R distributions also provides an estimate of the fraction of elastic events with a recoil counter signal. The program simulates the ranging out of recoil protons with a momentum too low to penetrate the material between the liquid hydrogen and the scintillator counters. A Monte Carlo generated scatterplot, Fig. (IV.C.11), shows the recoil proton momentum versus recoil angle for elastic $\rho$ events. The proton momentum must be $>360$ MeV at a recoil angle of $80^0$ to fire a recoil counter. As the recoil counters are surrounding the target in a box-like fashion there is a dependence of the minimum momentum to fire a recoil counter on the polar and azimuthal angle of recoil. The counters overlap in the corner regions of the box and thus a recoil proton can occasionally fire two counters. Table (IV.C.2) lists the fraction of elastic $\rho$ and $\phi$ events which fire 0, 1 and $>1$ recoil counters as predicted by the Monte Carlo program. The numbers are corrected for scattering and nuclear absorption of the recoil proton in the material between the target and the scintillator counters. The fraction of events firing a recoil counter is a function of R for events in the $\rho$ region as indicated by the data in Fig. (IV.C.10). This implies that a recoil counter is more likely to fire for elastic $\rho$ events with a large dipion mass (R is proportional to $M_{\pi\pi}$ ). This dependence is easily reproduced by the Monte Carlo program if the momentum transfer slope parameter, b, is made

to be a function of $M_{\pi\pi}$, i.e. b decreases with increasing $M_{\pi\pi}$. The same kind of mass dependence has been seen by several ρ photoproduction experiments, eg. [Ballam, 1973].

A simple model for diffractive dissociation of the target proton is used to give the multiplicities of p, n, $\pi^{\pm}$, $\pi^{0}$ resulting from the proton excitation. The model is outlined in Appendix C. The multiplicities are used to estimate the percentages of inelastic events firing 0, 1 and >1 recoil counters. Almost all (98%) of the inelastic events are expected to fire at least one of the recoil counters. The results are listed in table (IV.C.2).

The Monte Carlo results for the elastic fractions and the model predictions for the inelastic fractions of ρ and ϕ events in the recoil = 0, 1 and >1 categories are fitted to the experimentally measured event numbers with the fraction of inelastic ρ and ϕ events the only adjustable parameters. The resulting inelastic fractions are 12.6% for the ρ and 18.2% for the ϕ. The agreement of the fitted fractions with the ρ data is very good (see Table (IV.C.2)). The ϕ data appear to favour a somewhat higher (recoil = 0)/(recoil = 1) event ratio than predicted. A larger momentum transfer slope parameter, b (taken as 6.5 $GeV^{-2}$), could reduce this difference. However, the overall fraction would not change significantly. The errors assigned to the fractions account for uncertainties in the slope parameters, pulse height discriminator thresholds for the recoil counters and

approximations made to yield the elastic and inelastic recoil predictions.

It is difficult to compare the inelastic fractions determined by different experiments due to the effects of incomplete geometrical acceptance of the different apparatuses. In this experiment, an energetic particle from a target excitation may veto the event if the particle is detected in one of the downstream hadrometers. Inelastic diffractive ρ photoproduction was studied theoretically by [Wolf, 1971]. The integrated (inelastic) cross section is predicted to rise slowly with energy, reaching ∿4 μb at $E_\gamma$ = 100 GeV (inelastic fraction ∿30%).

## 5. Corrections

To calculate cross sections, the number of ρ and ϕ events observed in the data need to be corrected for events lost due to:

- geometric acceptance of the apparatus,
- MWPC inefficiencies,
- hadronic interactions of the vector meson decay products in the target and vacuum windows,
- pion and kaon decay in flight, and
- analysis cuts.

The empty target background is subtracted during the fitting procedure. Correction factors compensate for the

contribution of inelastic events. The number of $\phi$ events is corrected for the branching ratio into $K^+K^-$. Typical values of the correction factors are given in Table (IV.C.3).

Most of the data were taken with a copper radiator of thickness 0.015 cm (0.01 radiation lengths) (see Section [III.C]). To compensate for the relatively low electron beam intensity at $E_o$= 200 GeV (approx. ten times lower than at $E_o$= 90 GeV), about 60% of the 200 GeV data were taken with a radiator of thickness 0.038 cm (≈0.03 radiation lengths). A thicker radiator results in a higher photon flux but also increased probability for double bremsstrahlung. The probability for double bremsstrahlung is given as

$$P \simeq t \ln\{(E_1 + E_2)/E_c\} \qquad \text{(IV.C.2)}$$

where t = 0.03 (radiator thickness), $(E_1 + E_2)$ = total radiated energy (= tagged photon energy $E_\gamma$), and $E_c$= low energy threshold for double bremsstrahlung. The energy of a photon interacting in the target is less than the tagged photon energy determined from the tagging system for a double bremsstrahlung event. A lower photon energy implies a larger opening angle between the secondary particles (in the lab frame) and as a result the event may be lost due to the finite acceptance of the apparatus. The energy carried by the second (non-interacting) photon is deposited in the

C-counter. A $\rho$-$\phi$ event is rejected, however, if the energy in the shower counters (including the C-counter) does not match with the positions of the tracks determined with the MWPC's. The double bremsstrahlung correction for the $E_o$= 200 GeV data is calculated as 2% for the $\rho$ cross section and is negligible for the $\phi$.

## D: Results and Discussion

The determination of the $\rho$ cross section from different experiments, measured in different kinematic regions, is a difficult problem due to the complicated dipion mass spectrum. Spital and Yennie [Spital, 1974] have suggested that the $\rho$ cross section be defined as

$$\sigma = \frac{1}{2}\pi\Gamma_o \left.\frac{d\sigma}{dM_{\pi\pi}}\right|_{M_{\pi\pi}=M_\rho} \qquad \text{(IV. D. 1)}$$

The yield of $\pi^+\pi^-$ pairs at the $\rho$ mass, $M_\rho$, is given by the peak of the Breit-Wigner resonance shape describing an undistorted $\rho$ meson. The Drell and interference terms vanish at $M_\rho$ (see Eqn. (IV. A. 4) with $M_{\pi\pi} = M_\rho$ ) and the cross section given by Eqn. (IV. D. 1) is thus independent of details of the skewing mechanism. From Eqn. (IV. A. 4)

$$\left.\frac{dN}{dM_{\pi\pi}}\right|_{M_{\pi\pi}=M_\rho} = C_0/\Gamma_o \qquad \text{(IV. D. 2)}$$

and Eqn. (IV. D. 1) becomes

$$\sigma = \frac{1}{2} C_0 \pi \beta \qquad \text{(IV. D. 3)}$$

The constant $C_0$ is obtained from fits to the data. Target and photon beam flux parameters, Eqn. (III. D. 10), and the correction factors listed in Table (IV. C. 3) are represented by $\beta$.

The data were divided into two photon energy bins for each electron beam setting except for the $E_o$= 60 GeV data taken with the apparatus in the 90 GeV configuration. The $\rho$ cross section, calculated using Eqn. (IV. D. 3), is listed in Table (IV. D. 1) and shown in Fig. (IV. D. 1) together with some lower energy data. The quoted errors include the uncertainties due to statistics, geometric acceptance, and the correction for inelastic events. The total systematic uncertainty is estimated at ±6% with no energy dependence.

The predictions made by Vector Meson Dominance (VMD) and a quark model relation between $\pi p$ elastic scattering and diffractive $\rho$ photoproduction is given by [Lipkin, 1966; and Chapter II of this thesis]

$$\frac{d\sigma}{dt}(\gamma p \to \rho p) = \frac{p_\pi^2}{k_\gamma^2} \frac{\alpha\pi}{\gamma_\rho^2} \left(\frac{1}{2}\sqrt{\frac{d\sigma}{dt}(\pi^+ p)} + \frac{1}{2}\sqrt{\frac{d\sigma}{dt}(\pi^- p)}\right)^2 \qquad \text{(IV. D. 4)}$$

where $\gamma_\rho$ represents the strength of the photon-vector meson coupling and $\alpha = e^2/4\pi$ . The variables $p_\pi$ and $k_\gamma$ are the

momenta of the $\pi$ and the photon, respectively, in the $\pi p$ and $\gamma p$ center of mass system (see Appendix B). As the $\pi^+ p$ and $\pi^- p$ elastic cross sections are very similar, the above expression can be approximated by

$$\frac{d\sigma}{dt}(\gamma p \to \rho p) = \frac{p_\pi^2}{k_\gamma^2} \frac{\alpha\pi}{\gamma_\rho^2} \frac{1}{2} \cdot \left(\frac{d\sigma}{dt}(\pi^+ p) + \frac{d\sigma}{dt}(\pi^- p)\right) \qquad \text{(IV. D. 5)}$$

The energy dependence of the integrated $\rho$ photoproduction cross section obtained from Eqn. (IV. D. 5) using available $\pi p$ elastic scattering data [Ayres, 1977; Foley, 1963; Ambats, 1974] is shown by the dotted curve in Fig. (IV. D. 1). The $\gamma$-$\rho$ coupling constant is taken as $\gamma_\rho^2/4\pi = 0.64 \pm .10$ from $e^+e^-$ data [Gounaris, 1968]. The agreement of the VMD-quark model prediction with the data is excellent.

The sum total ($\sim$2100 events) of the $\phi$ signal above background is shown in Fig. (IV. D. 2). The solid curve in the figure is a Monte Carlo generated R distribution for the $\phi$ assuming s-channel helicity conservation, i. e. a $\sin^2\theta$ polar angle decay distribution with respect to the direction of the $\phi$ in the overall $\gamma p$ center of mass system. The dotted curve is generated with an isotropic decay of the $\phi$ in its rest frame, i. e. no s-channel helicity conservation. The number of events under the curves is identical. The data are clearly consistent with s-channel helicity conservation (in agreement with measurements at lower energies).

The $\phi$ cross section is calculated using Eqn. (III. D. 10) and the correction factors listed in Table (IV. C. 3). The results are given in Table (IV. D. 1) and shown in Fig. (IV. D. 3) together with some lower energy data. The quoted errors include statistical and background subtraction uncertainties, obtained directly from the Monte Carlo fits to the experimental R distributions (see Section C. 3), and the uncertainty due to the inelastic event correction. The total systematic uncertainty is estimated to be less than 5% with no energy dependence. The branching ratio for $(\phi \to K^+K^-)/(\phi \to all)$ is taken as 46. 6% [Particle properties, 1976].

The dashed curve in Fig. (IV. D. 3) is an empirical fit to the data and has the form (s in $GeV^2$)

$$\sigma(\mu b) = \frac{p_\phi^2}{k_\gamma^2} \{A + \frac{B}{\sqrt{s}} + C \cdot \ln(s)\} \qquad \text{(IV. D. 6)}$$

where

$$A = -0.103 \pm .329$$

$$B = 0.939 \pm .641$$

$$C = 0.135 \pm .057$$

The fit has a chi-squared of 26. 2 for 22 degrees of freedom. The variables $p_\phi$ and $k_\gamma$ are the momenta of the $\phi$ and the photon, respectively, in the $\phi p$ and $\gamma p$ center of mass system. The threshold factor $(p_\phi/k_\gamma)^2$ is derived in

Appendix B.

Vector meson dominance relates $\phi$ photoproduction to the elastic scattering of $\phi$ mesons on nucleons,

$$\frac{d\sigma}{dt}(\gamma p \rightarrow \phi p) = \frac{p_\phi^2}{k_\gamma^2} \frac{\alpha\pi}{\gamma_\phi^2} \frac{d\sigma}{dt}(\phi p \rightarrow \phi p) \qquad \text{(IV. D. 7)}$$

where $\gamma_\phi$ is the $\gamma$-$\phi$ coupling constant. The forward elastic $\phi p$ scattering cross section is related to the total $\phi p$ interaction cross section, $\sigma_T(\phi p)$, by the optical theorem,

$$\left.\frac{d\sigma}{dt}\right|_{t=0} (\phi p \rightarrow \phi p) = \frac{1+\eta^2}{16\ \pi} \sigma_T^2(\phi p) \qquad \text{(IV. D. 8)}$$

where $\eta$ is the ratio of the real to imaginary forward scattering amplitude. Assuming the forward cross section to be purely imaginary ($\eta$ =0), Eqns. (IV. D. 7) and (IV. D. 8) give

$$\left.\frac{d\sigma}{dt}\right|_{t=0} (\gamma p \rightarrow \phi p) = \frac{p_\phi^2}{k_\gamma^2} \frac{\alpha}{16\gamma_\phi^2} \sigma_T^2(\phi p) \qquad \text{(IV. D. 9)}$$

A measurement of the forward $\phi$ photoproduction cross section thus yields information on the $\phi p$ total cross section. The apparatus of this experiment does not permit an accurate determination of the momentum transfer squared, t, for $\phi$ (and $\rho$) events. However, if

$$\frac{d\sigma}{dt}(\gamma p \rightarrow \phi p) = A \cdot e^{bt} \qquad \text{(IV. D. 10a)}$$

then

$$\left.\frac{d\sigma}{dt}\right|_{t=0}(\gamma p \to \phi p) = A = b\,\sigma(\gamma p \to \phi p)\exp(-bt_{min}) \qquad \text{(IV. D. 10b)}$$

i.e., the forward cross section can be calculated from the integrated cross section if the slope parameter is known. Using low energy $\phi$ photoproduction data and VMD-quark model predictions (see Appendix D) for the s = 100-300 $GeV^2$ energy region, the momentum transfer slope parameter is given by [Behrend, 1978]

$$b(s) = (4.66 \pm 0.22) + (0.38 \pm 0.04)\ln s \qquad \text{(IV. D. 11)}$$

with s in $GeV^2$ and b in $GeV^{-2}$. The energy dependence depicts shrinkage, i.e. an increasing slope parameter with increasing energy. Fig. (IV. D. 4) shows the energy dependence of the forward $\phi$ photoproduction cross section obtained by multiplying the measured integrated cross section with the slope parameter of Eqn. (IV. D. 11). Also shown are lower energy data from other experiments which measured the t-dependence of the cross section. A fit to the data in Fig. (IV. D. 4) is given by

$$\left.\frac{d\sigma}{dt}\right|_{t=0}\left(\frac{\mu b}{GeV^2}\right) = \frac{p_\phi^2}{k_\gamma^2}\left\{A + \frac{B}{\sqrt{s}} + C\cdot\ln(s)\right\}^2 \qquad \text{(IV. D. 12)}$$

where

$$A = -0.487 \pm .487$$

$$B = 3.82 \pm .95$$

$$C = 0.443 \pm .085$$

with a chi-squared of 33.9 for 22 degrees of freedom. The fit is shown by the solid curve in Fig. (IV.D.4). Without a $B/\sqrt{s}$ term, the fitted parameters are

$$A = 1.47 \pm .07$$

$$B = \text{set to } 0.0$$

$$C = 0.108 \pm .018$$

with a chi-squared of 49.7 for 23 degrees of freedom. The fit is shown by the dashed curve in Fig. (IV.D.4).

On comparing Eqn. (IV.D.12) with Eqn. (IV.D.9), the energy dependence of the $\phi p$ total cross section is given by

$$\sigma_T(\phi p) = \frac{\alpha}{16\gamma_\phi^2}\{A + \frac{B}{\sqrt{s}} + C\cdot\ln(s)\} \qquad \text{(IV.D.14)}$$

with the above values for the parameters A, B and C.

From the quark model, elastic cross sections satisfy the relation [Lipkin, 1966; and Chapter II of this thesis]

$$p_\phi^2 \frac{d\sigma}{dt}(\phi p) = \left(p_K\cdot\sqrt{\frac{d\sigma}{dt}(K^+p)} + p_K\cdot\sqrt{\frac{d\sigma}{dt}(K^-p)} - p_\pi\cdot\sqrt{\frac{d\sigma}{dt}(\pi^-p)}\right)^2 \qquad \text{(IV.D.15)}$$

The momentum factors are incident momenta in the c.m. system. Assuming $d\sigma/dt(\gamma p \to \phi p) = A\cdot\exp(bt)$, Eqns. (IV.D.7) and (IV.D.15) yield

$$\sigma(\gamma p \to \phi p) = \qquad \text{(IV. D. 16)}$$

$$\exp(bt_{min}) \frac{\alpha\pi}{b\gamma_\phi^2} \frac{1}{k_\gamma^2} \left( p_K \cdot \sqrt{\frac{d\sigma}{dt}(K^+p)} + p_K \cdot \sqrt{\frac{d\sigma}{dt}(K^-p)} - p_\pi \cdot \sqrt{\frac{d\sigma}{dt}(\pi^-p)} \right)^2$$

The Kp and $\pi$p elastic scattering cross sections at $t = 0$ were measured at Fermilab [Ayres, 1977] in the same energy region as the $\phi$ data of this experiment. The constant of proportionality, $\alpha\pi/\gamma_\phi^2 b$, can thus be determined from a fit (i.e. a normalization) of the right hand side of Eqn. (IV. D. 16) to the integrated $\phi$ cross section as measured by this experiment. The resulting $\gamma$-$\phi$ coupling constant, multiplied by the $\gamma p \to \phi p$ momentum transfer slope parameter b, is

$$\frac{\gamma_\phi^2}{4\pi} b = 31.48 \pm 1.54 \ (\text{GeV}^{-2}) \qquad \text{(IV. D. 17)}$$

The fitted quark model cross section points (the right hand side of Eqn. [IV. D. 16]) are shown in Fig. (IV. D. 5). The curve in the figure is the fit to the $\phi$ data given by Eqn. (IV. D. 6) and also shown in Fig. (IV. D. 3). There is good agreement in the energy dependence of the quark model points and the $\phi$ photoproduction data. Also shown in Fig. (IV. D. 5) is the VMD-quark model cross section obtained from lower energy Kp and $\pi$p scattering data [Ambats, 1974] and the coupling constant times slope parameter given by Eqn. (IV. D. 17) but corrected for the energy dependence of b using Eqn. (IV. D. 11). The hadron scattering cross sections in

Eqn. (IV. D. 15) are combined at the same c. m. (center-of-mass) energy, i. e. $s(\phi p)=s(Kp)=s(\pi p)$, and the equivalent photon energy of the quark model points is calculated so as to give a $\gamma p$ c. m. energy equal to the $\phi p$ c. m. energy. The cross section calculation takes into account the minimum momentum transfer required for the $\gamma \rightarrow \phi$ transition. The agreement of the lower energy quark model points with the data is probably better than would be expected at these low energies.

Elastic scattering cross sections in the forward direction can be obtained from (very accurate) total cross section measurements with the help of the optical theorem, Eqn. (IV. D. 8). However, the real part of the forward scattering amplitude is not well known and can not be assumed equal to zero at lower energies.

For $E_\gamma = 100$ GeV ($s = 188$ GeV$^2$) the slope parameter given by Eqn. (IV. D. 11) is

$$b = 6.65 \pm 0.30 \text{ GeV}^{-2} \qquad \text{(IV. D. 18)}$$

and from Eqn. (IV. D. 17) the $\gamma$-$\phi$ coupling constant is

$$\frac{\gamma_\phi^2}{4\pi} = 4.7 \pm 0.3 \qquad \text{(IV. D. 19)}$$

This compares with the colliding beam value of $2.83 \pm .2$ [Gounaris, 1968] and the low energy A-dependence

photoproduction values of $10.7 \pm 4.1$ and $5.5 \pm 2.4$ for $\eta = 0.0$ and $\eta = -0.25$ respectively ($\eta$ = ratio of real to imaginary forward scattering amplitude) [McClellan, 1971].

In conclusion, the $\rho$ and $\phi$ photoproduction data of this experiment extend the agreement with VMD and an additive quark model to a new range of energy. The $\rho$ cross section is approximately constant with energy while the $\phi$ cross section rises from 0.5 μb to 0.7 μb with increasing energy. The $\phi$ results indicate a value of $\gamma_\phi^2$ intermediate between those obtained from $e^+e^-$ data and A-dependence of photoproduction at lower energies.

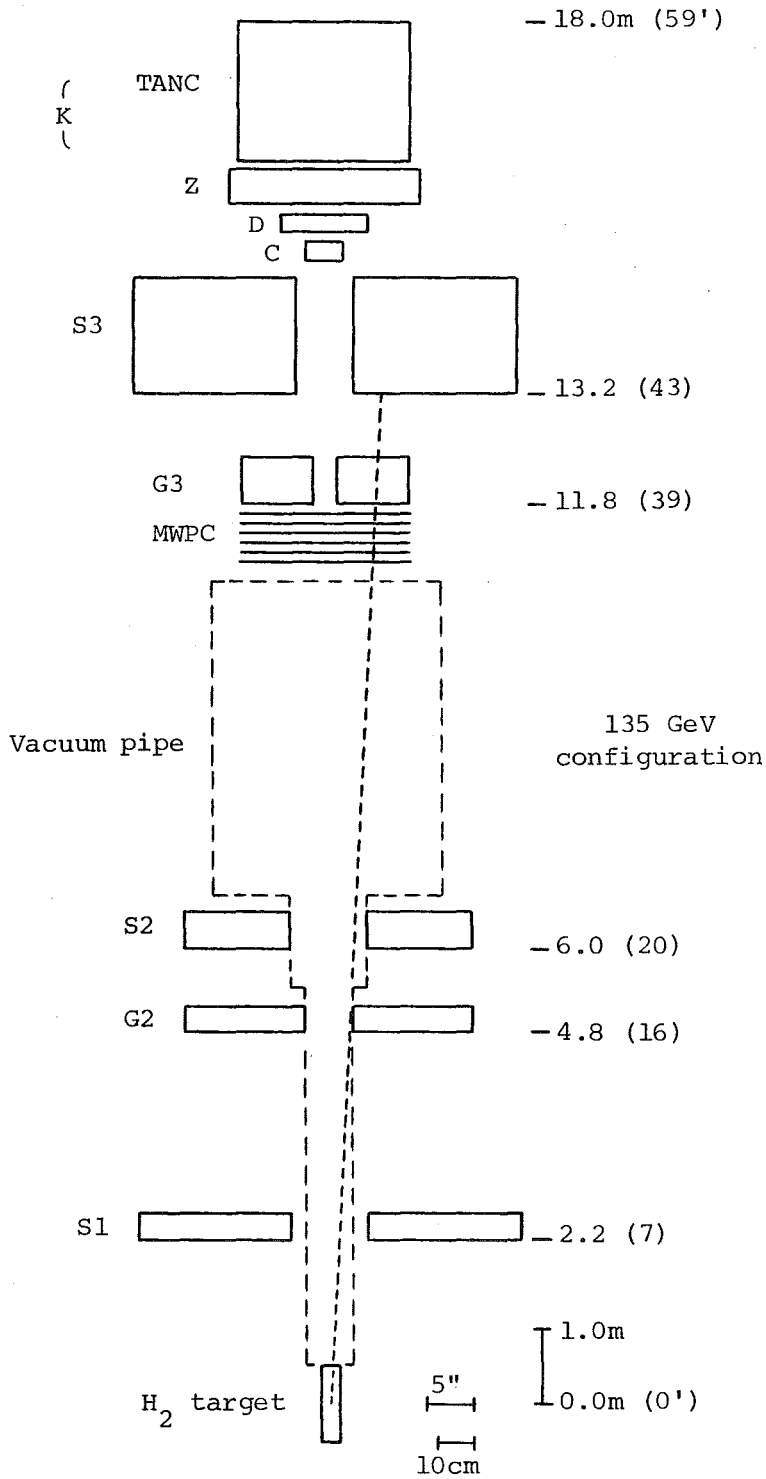


Figure (IV.A.1) Experimental apparatus

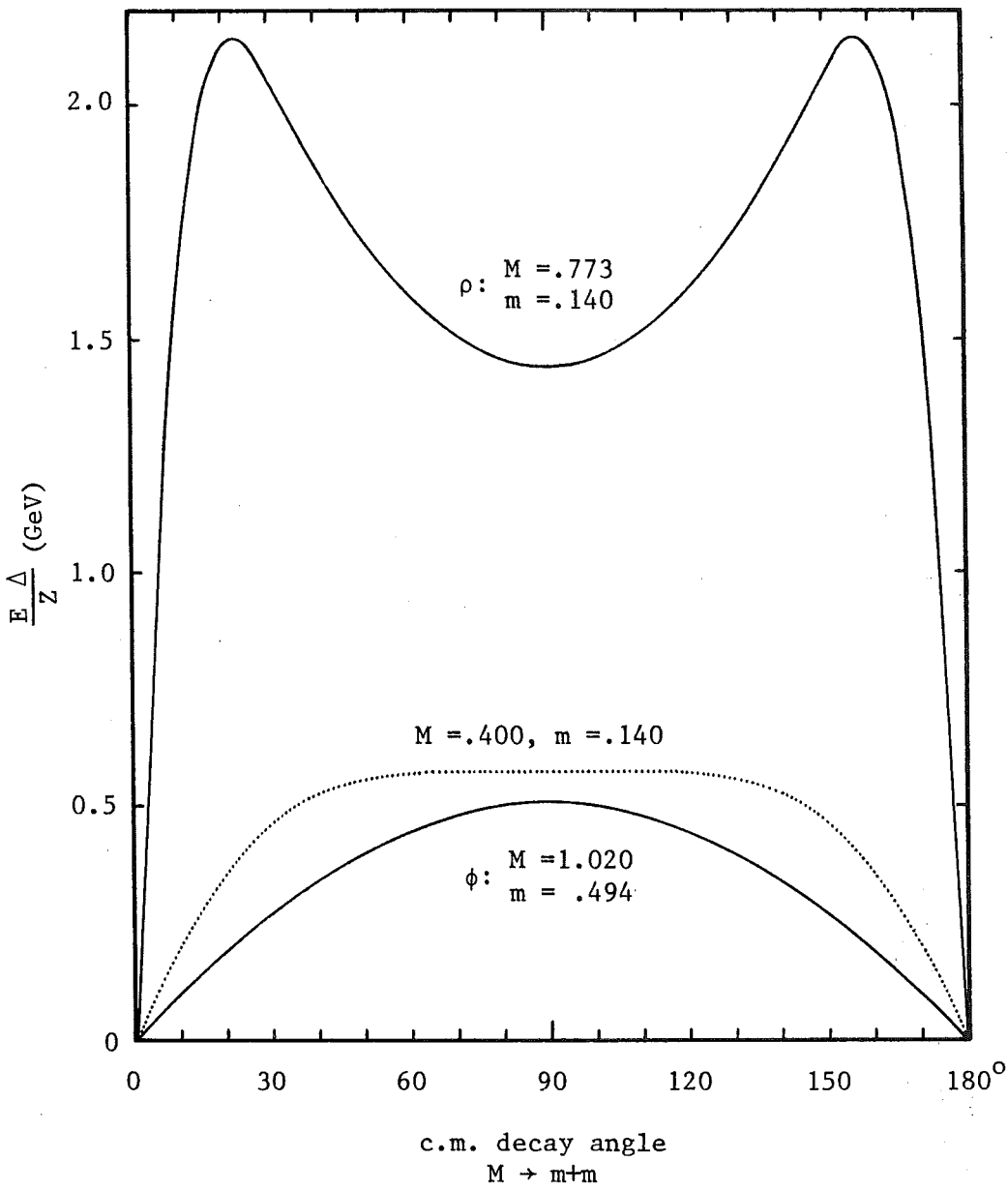


Figure (IV.A.2) Track separation (Δ) at the MWPC's versus decay angle for M → m+m. E is the lab energy of M and Z is the distance from the decay vertex to the MWPC's.

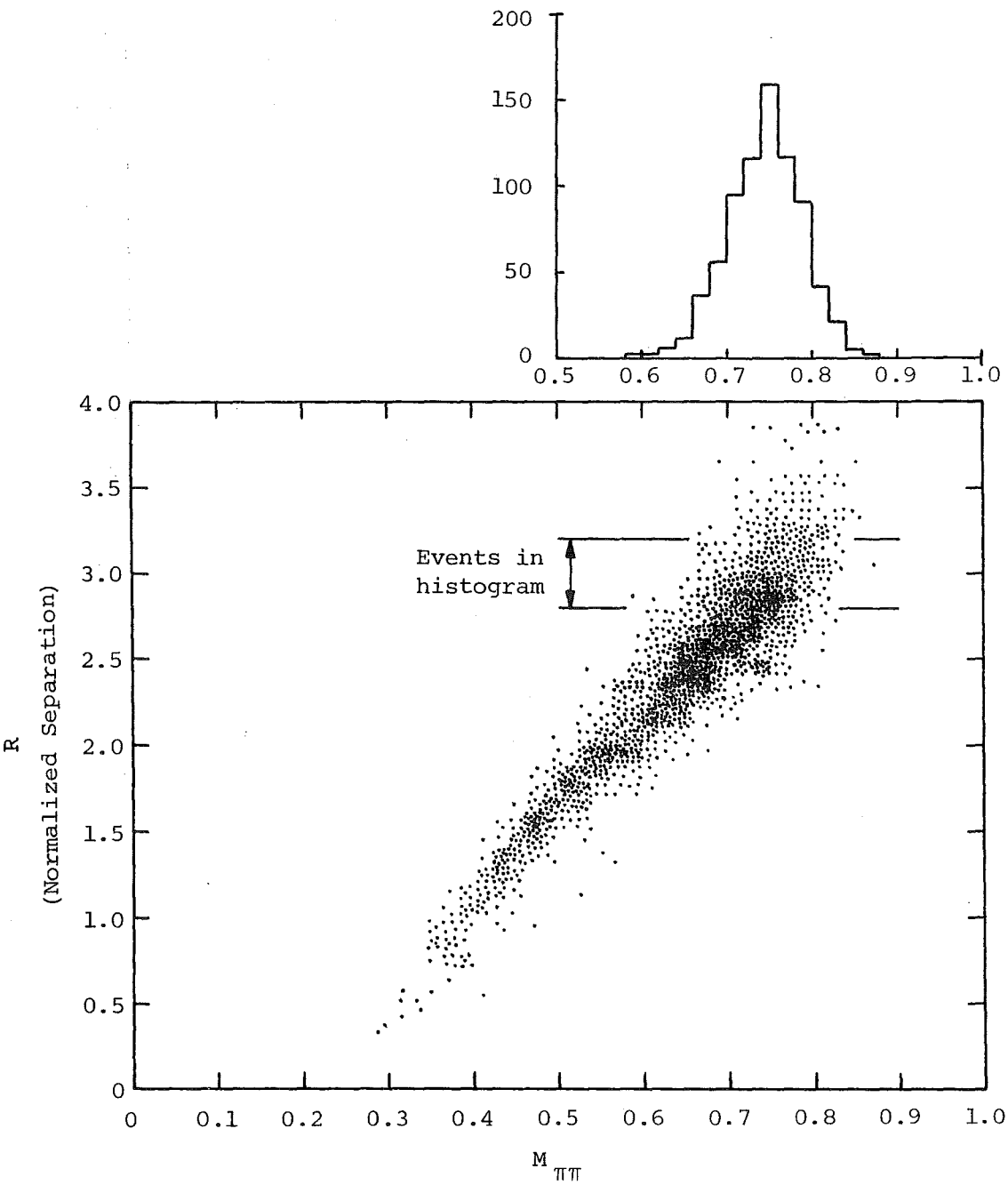


Figure (IV.A.3) Monte Carlo generated scatter plot of R versus $M_{\pi\pi}$ for $\rho \to \pi\pi$ .

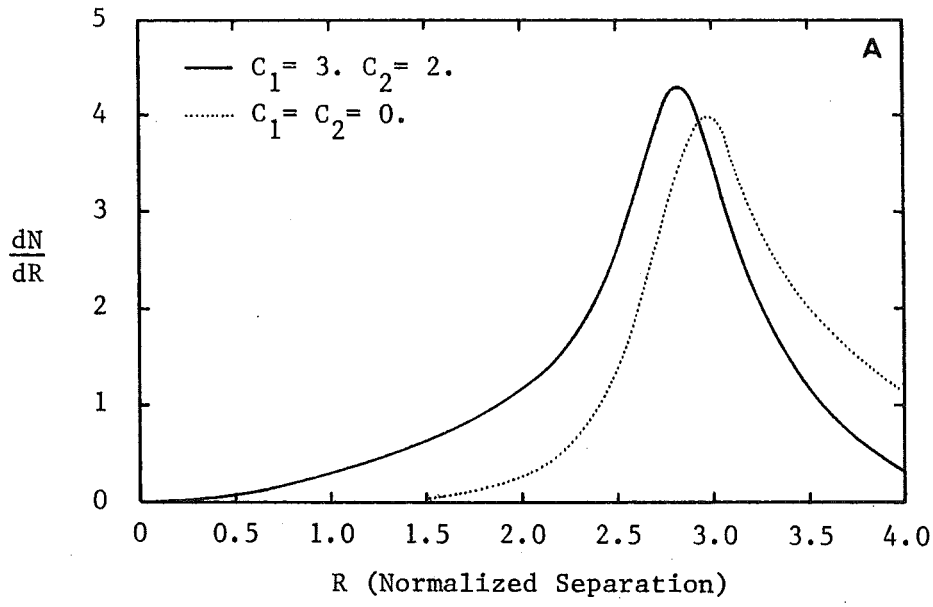


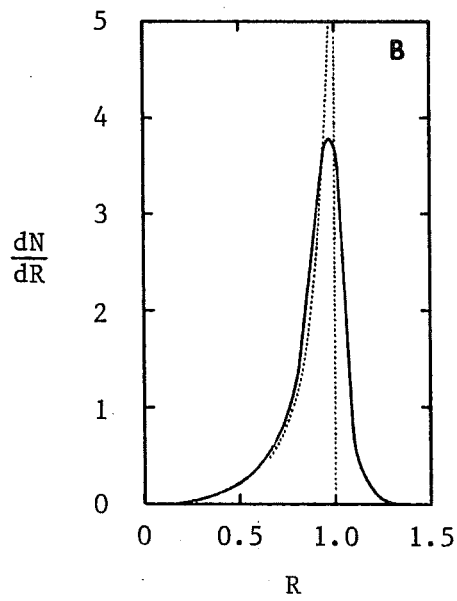


Figure (IV.A.4) A: Monte Carlo generated R distribution for $\rho \to \pi\pi$ with $C_1$=3.0 and $C_2$=2.0. The dotted curve corresponds to a Breit-Wigner resonance shape ($C_1$=$C_2$=0)

B: Monte Carlo generated R distribution for $\phi \to KK$. The broadening caused by the resolution of the apparatus is indicated by the solid curve.

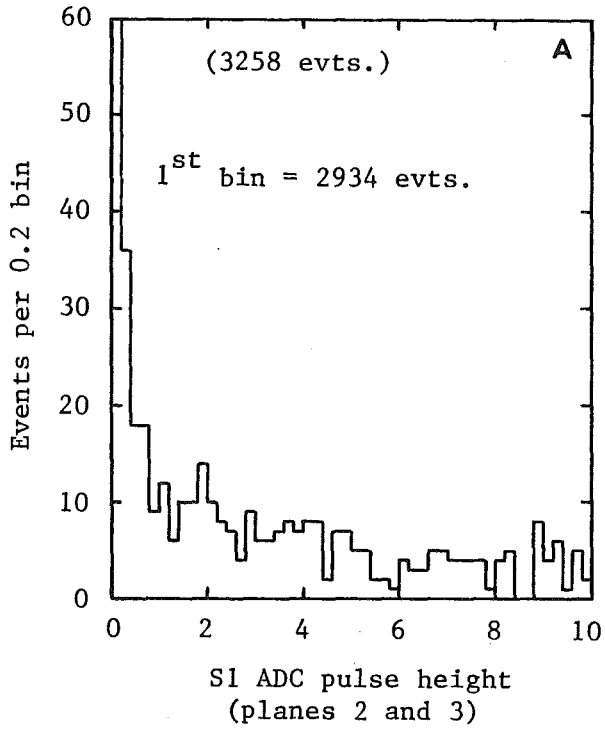


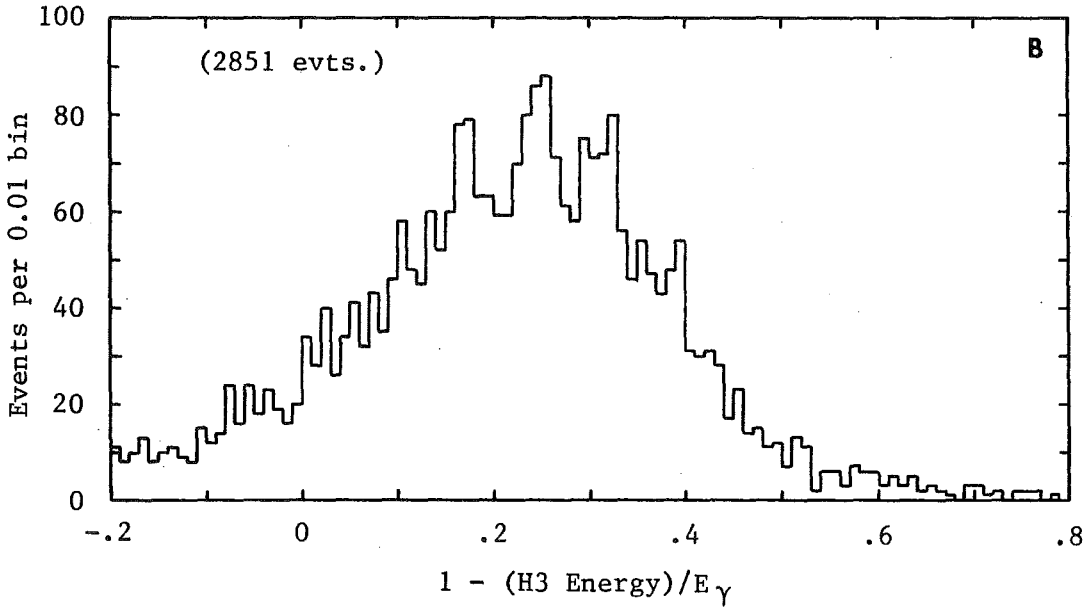


Figure (IV.C.1) A: Summed ADC pulse height spectrum for planes 2 and 3 of S1 for part of the $E_o$= 135 GeV data.

B: Missing energy spectrum for H3 for part of the $E_o$= 135 GeV data.

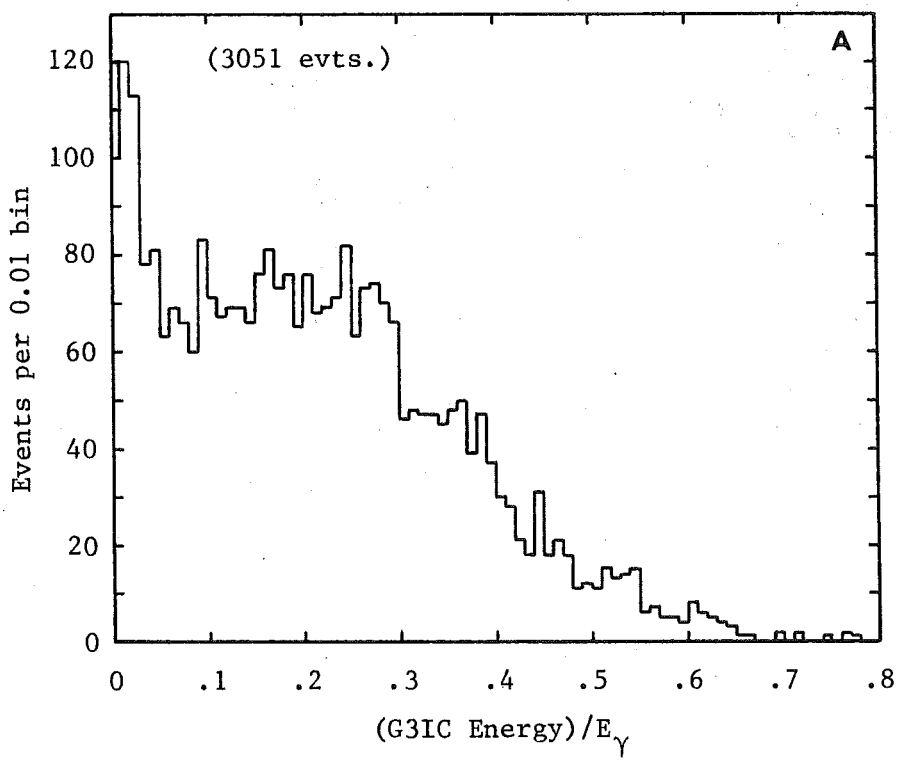


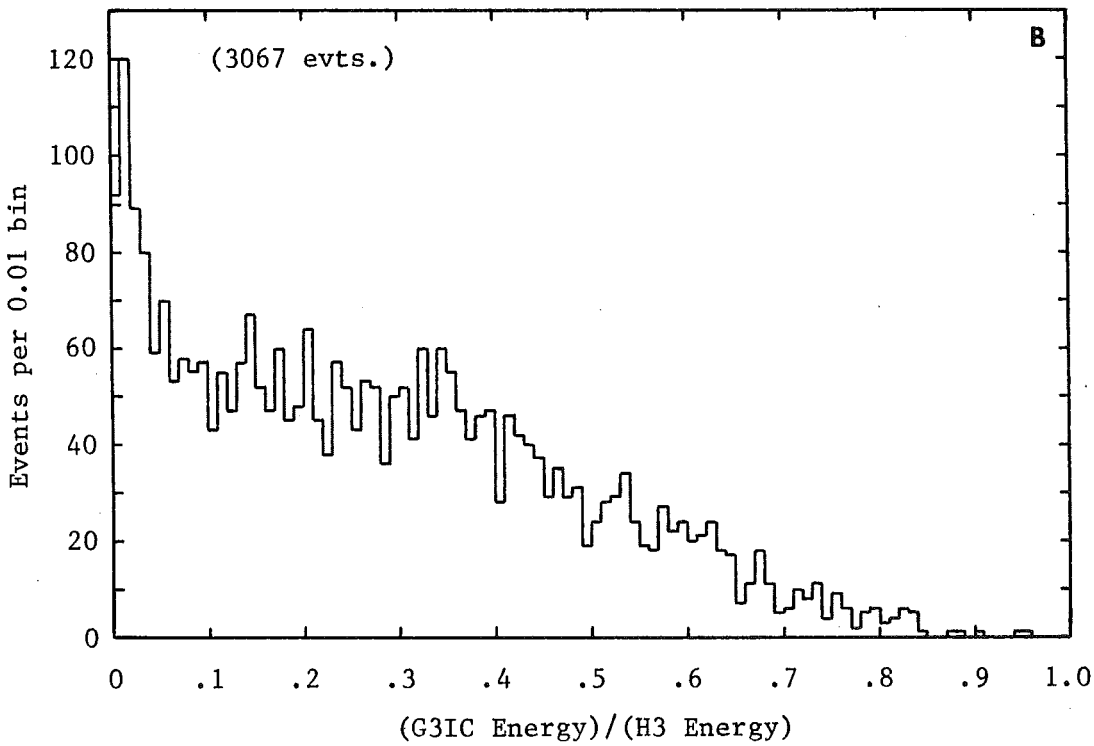


Figure (IV.C.2) Energy in the C-counter and G3 Pb glass array (G3IC) as a fraction of

A: the tagged photon energy,

B: the total energy in H3

for part of the $E_o$ = 135 GeV data

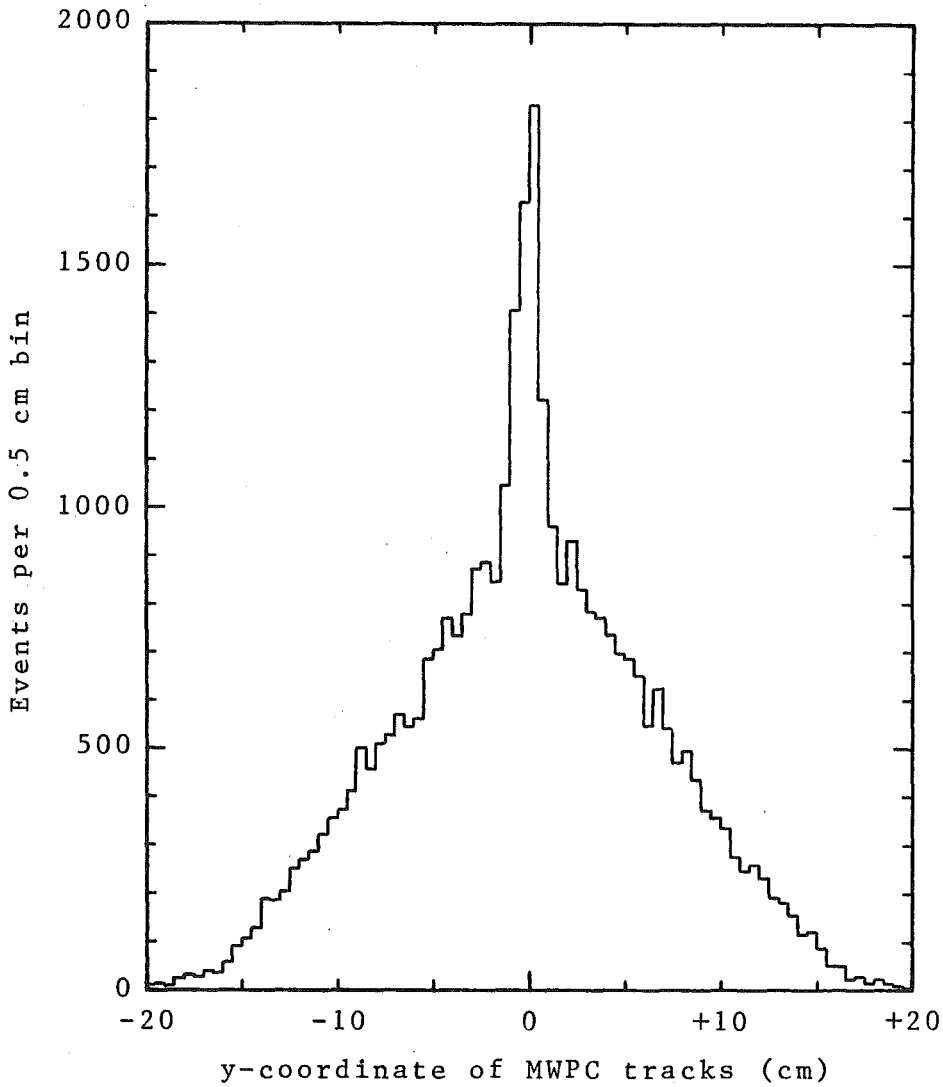


Figure (IV.C.3) Distribution of y-coordinate (vertical) for MWPC tracks ($E_o$= 135 GeV data)

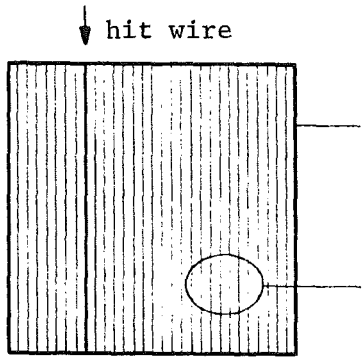


Schematic of a MWPC with one hit wire.

signal wires

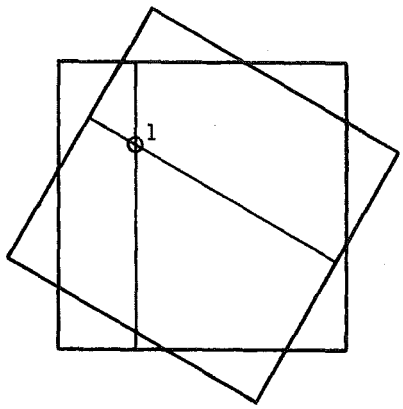


Two chambers, each with one hit wire: Consistent with one track passing through the chambers at the intersection point 1.

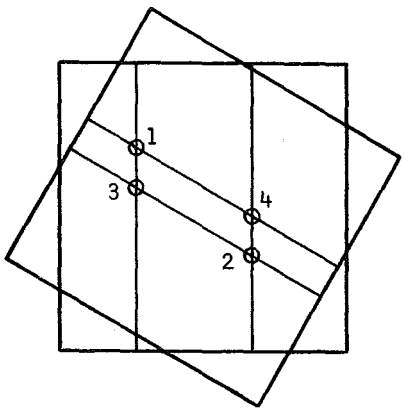


Two chambers, each with two hit wires: Consistent with two tracks passing through the chambers. Tracks are at intersection points 1 and 2, or 3 and 4 (ambiguous!)

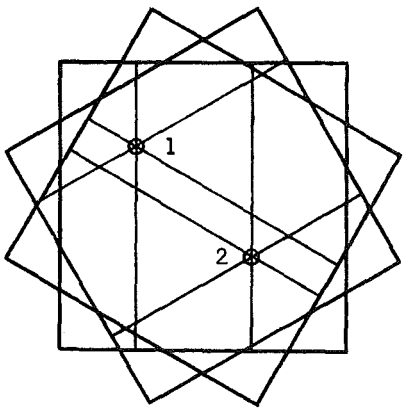


Three chambers, each with two hit wires: Consistent with two tracks passing through the chambers at the intersection points 1 and 2 (unambiguous!)

Figure (IV.C.4A) Schematic of track reconstruction.

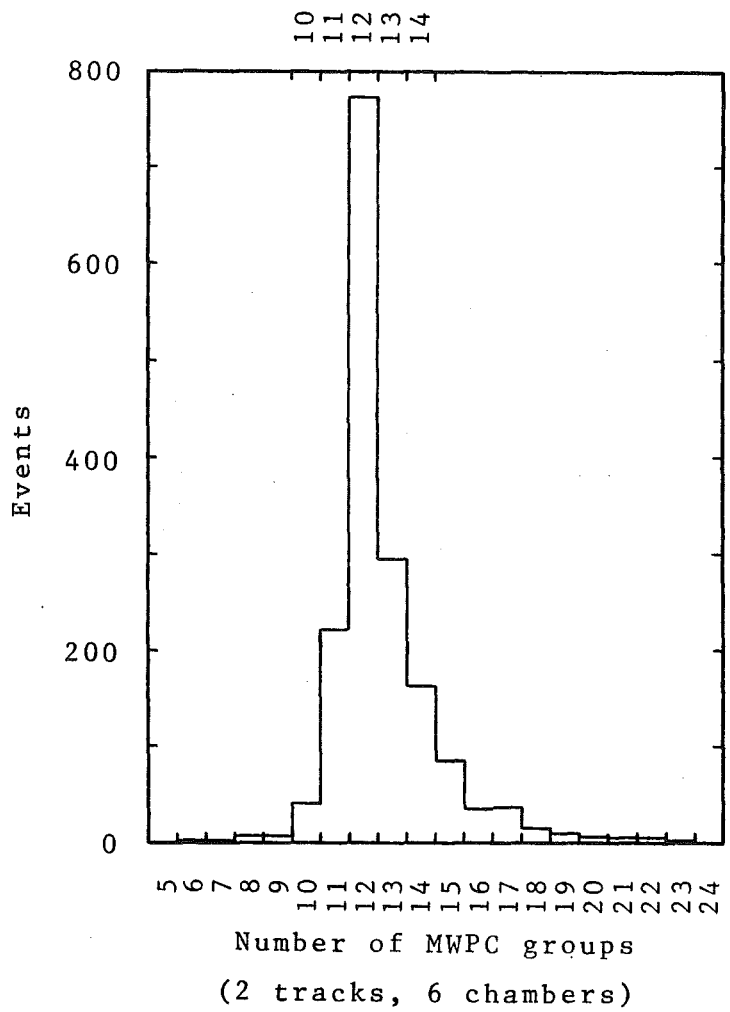


Figure (IV.C.4B) Number of MWPC groups for ρ-ϕ candidates.

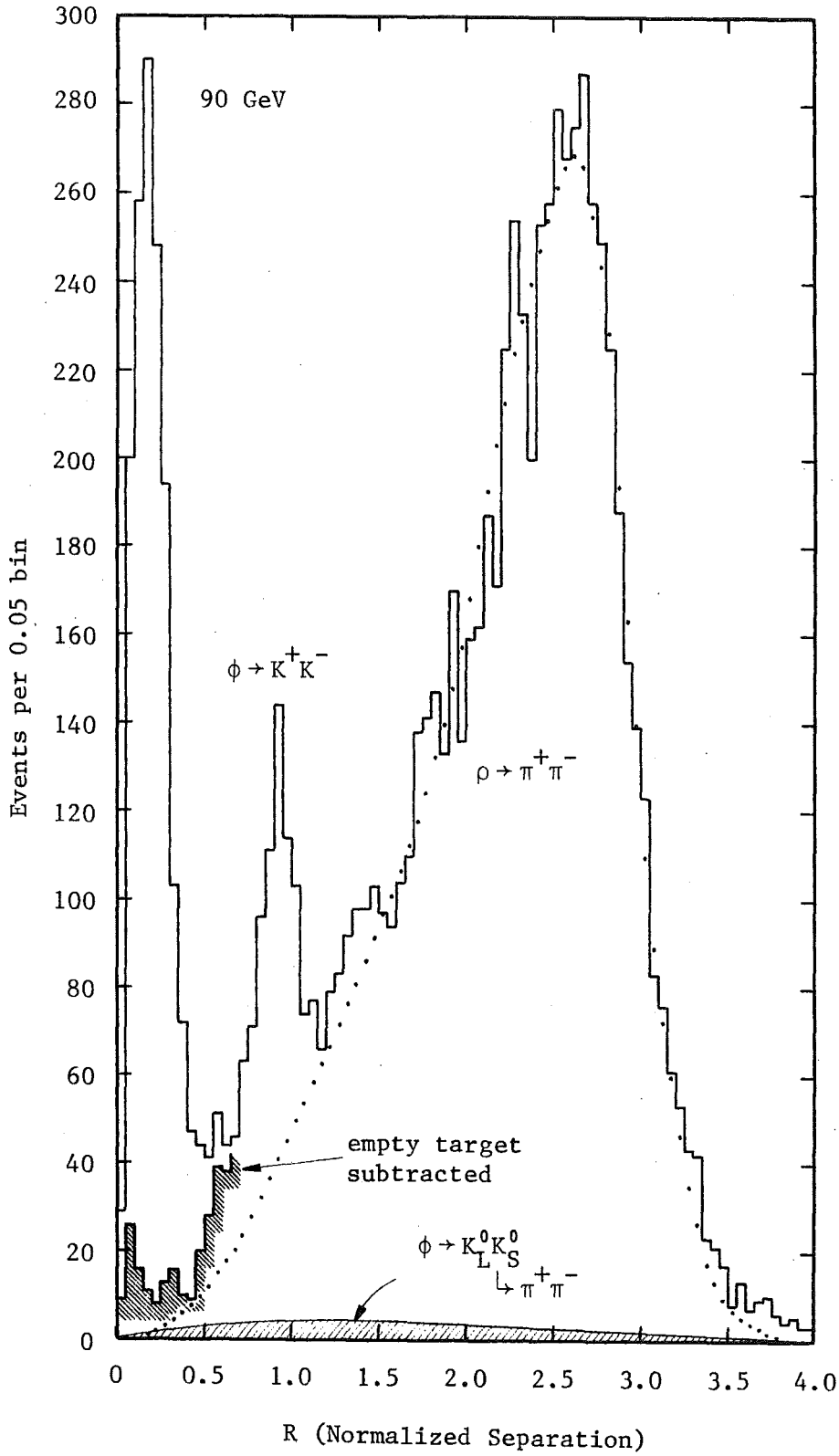


Figure (IV.C.5) R distribution for the $E_o$ = 90 GeV data. Dotted curve is a Monte Carlo fit to the ρ.

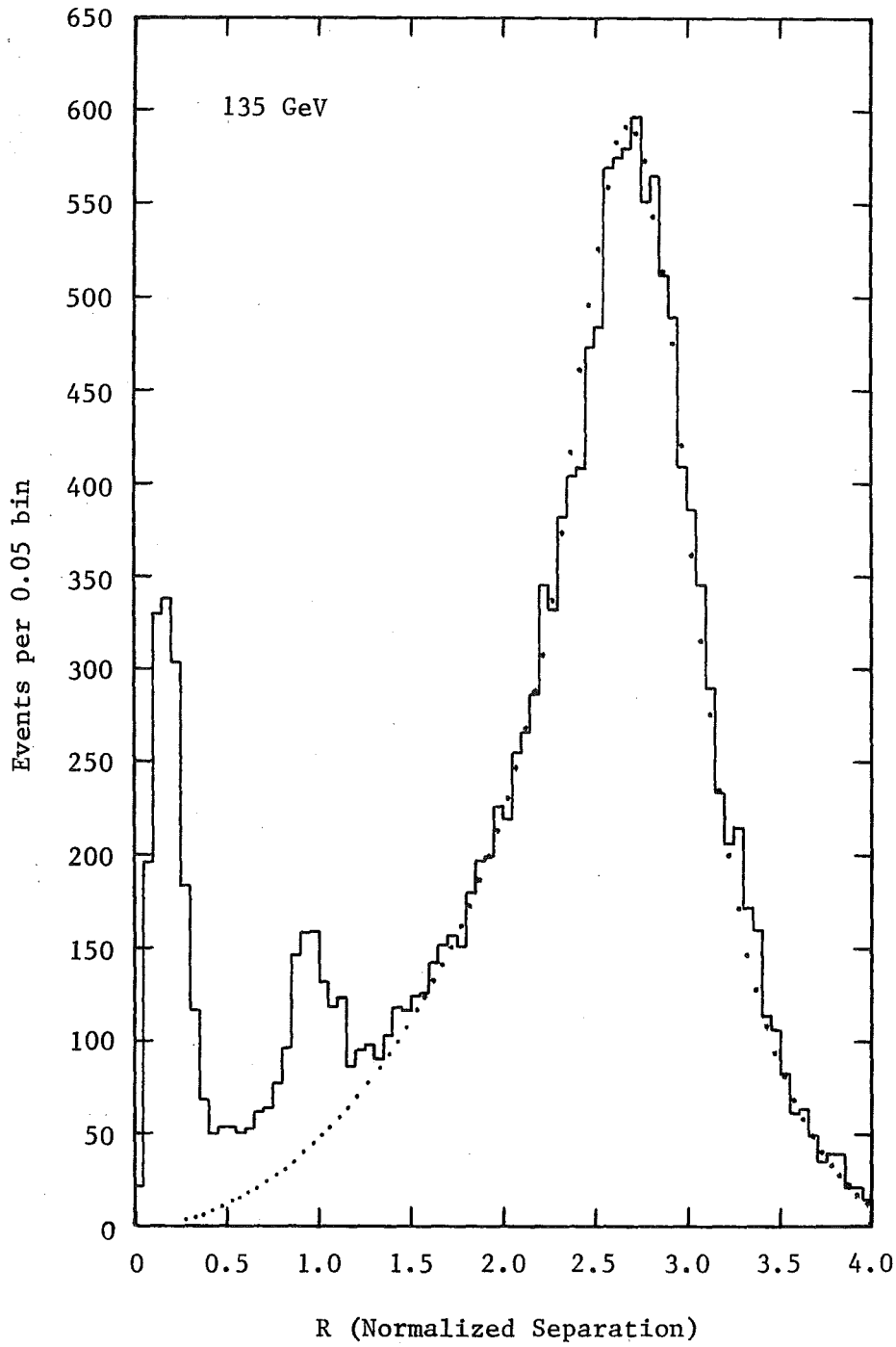


Figure (IV.C.6) R distribution for the $E_o$= 135 GeV data. Dotted curve is a Monte Carlo fit to the ρ.

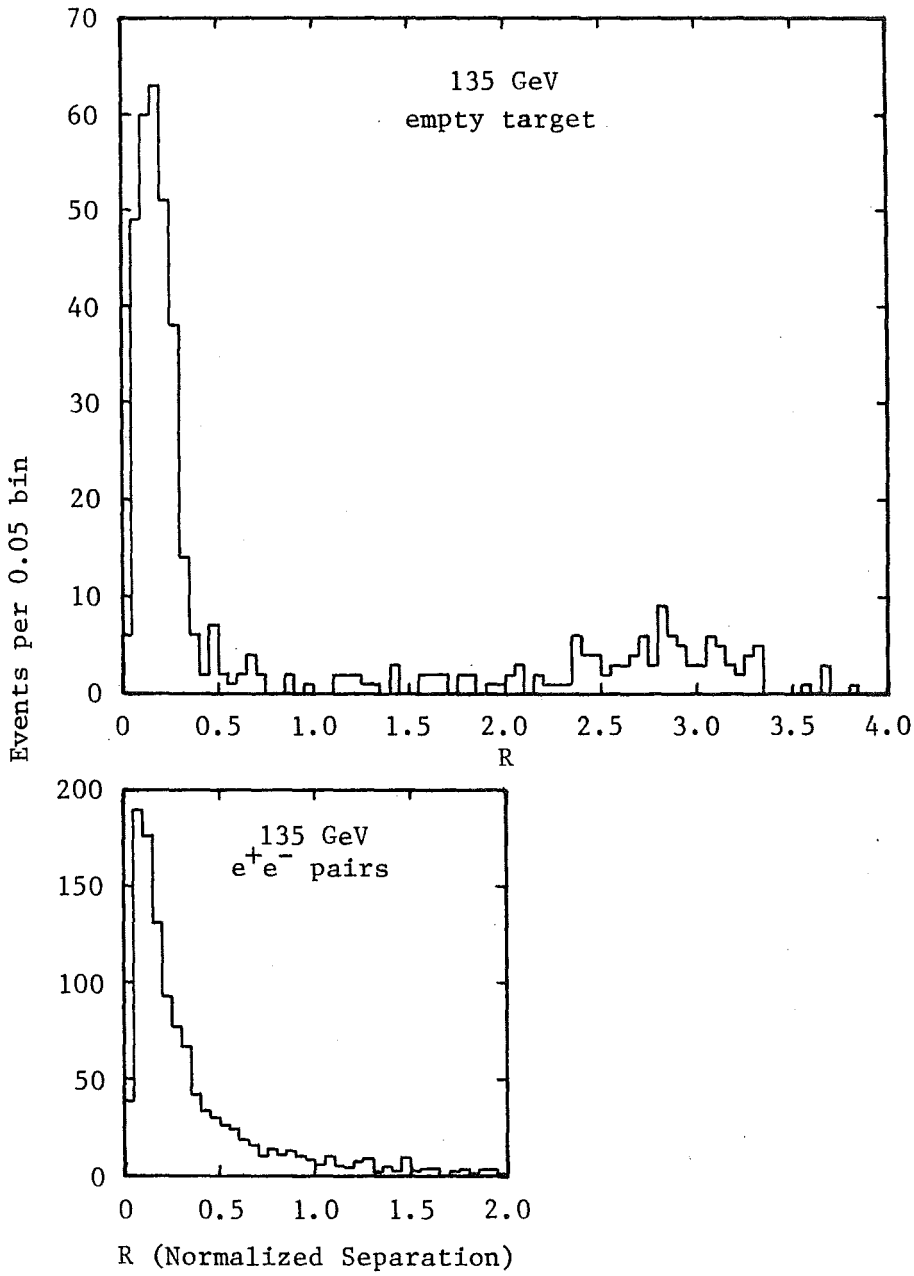


Figure (IV.C.7) (top) R distribution for the $E_o$= 135 GeV empty target data.

Figure (IV.C.8) (bottom) R distribution for non-interacting $e^+e^-$ pairs ($E_o$= 135 GeV).

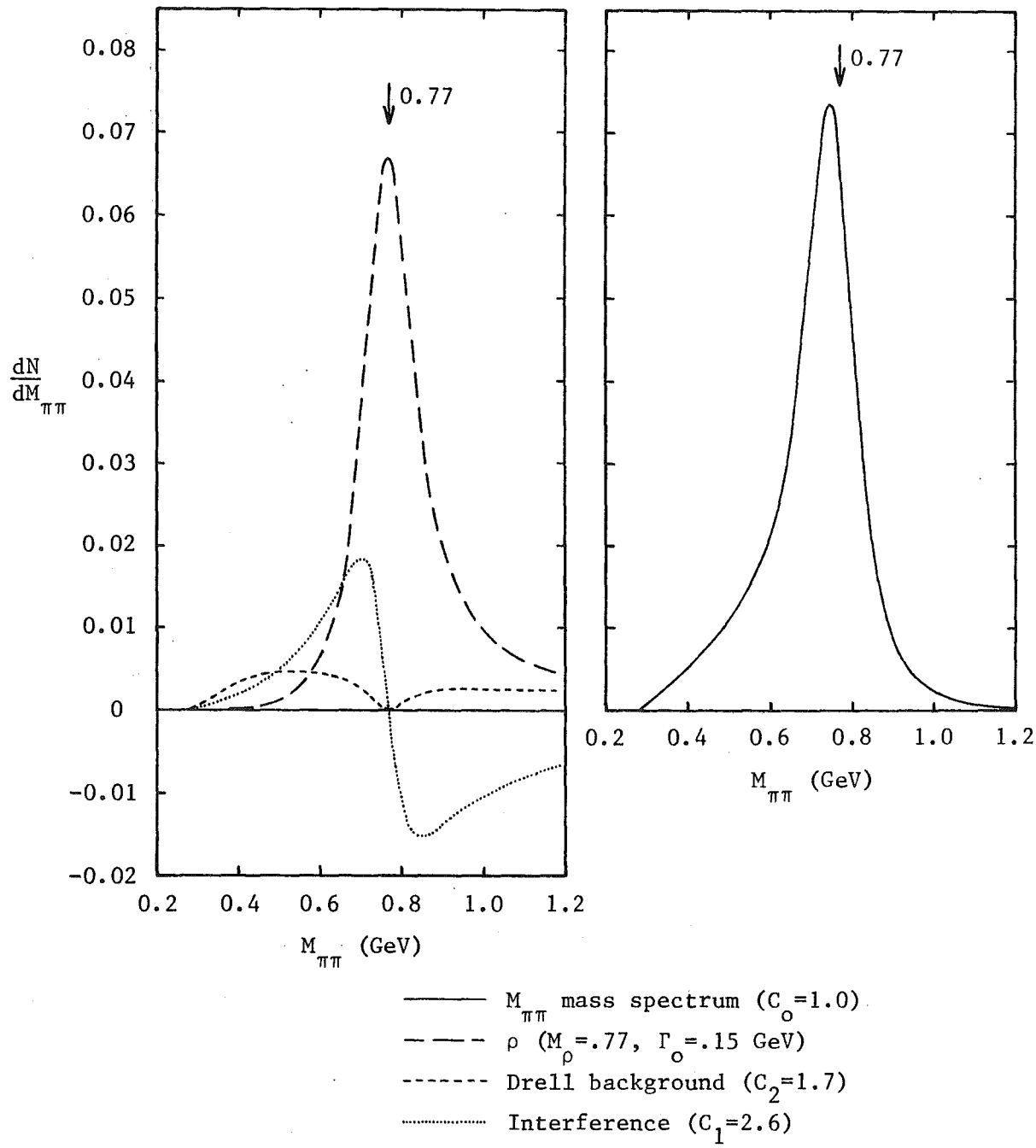


Figure (IV.C.9) Monte Carlo generated dipion mass spectrum resulting from the fit to the $E_o$= 135 GeV data (normalized to $C_o$= 1.0). The curve on the right is the sum of the three curves on the left.

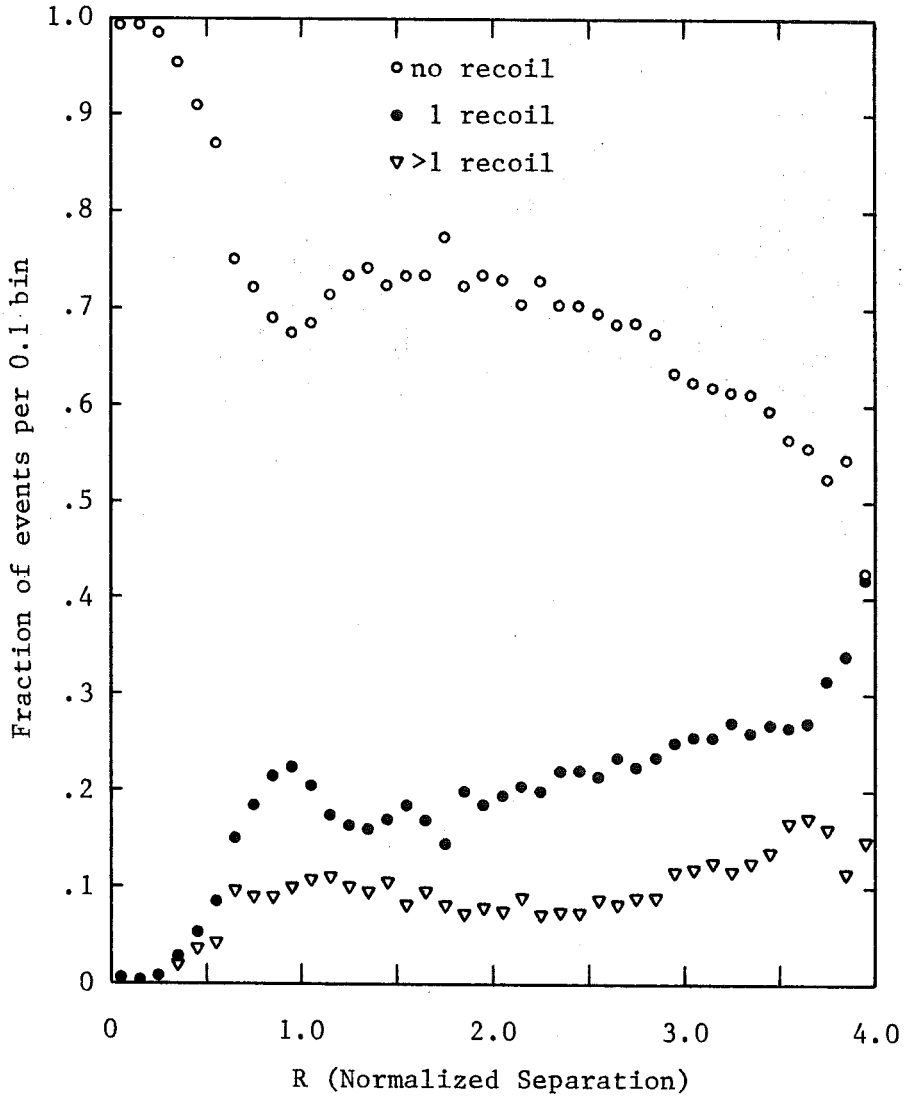


Figure (IV.C.10) Fraction of events with 0, 1 and >1 recoil counter signals in coincidence with the vector meson decay products (all the data).

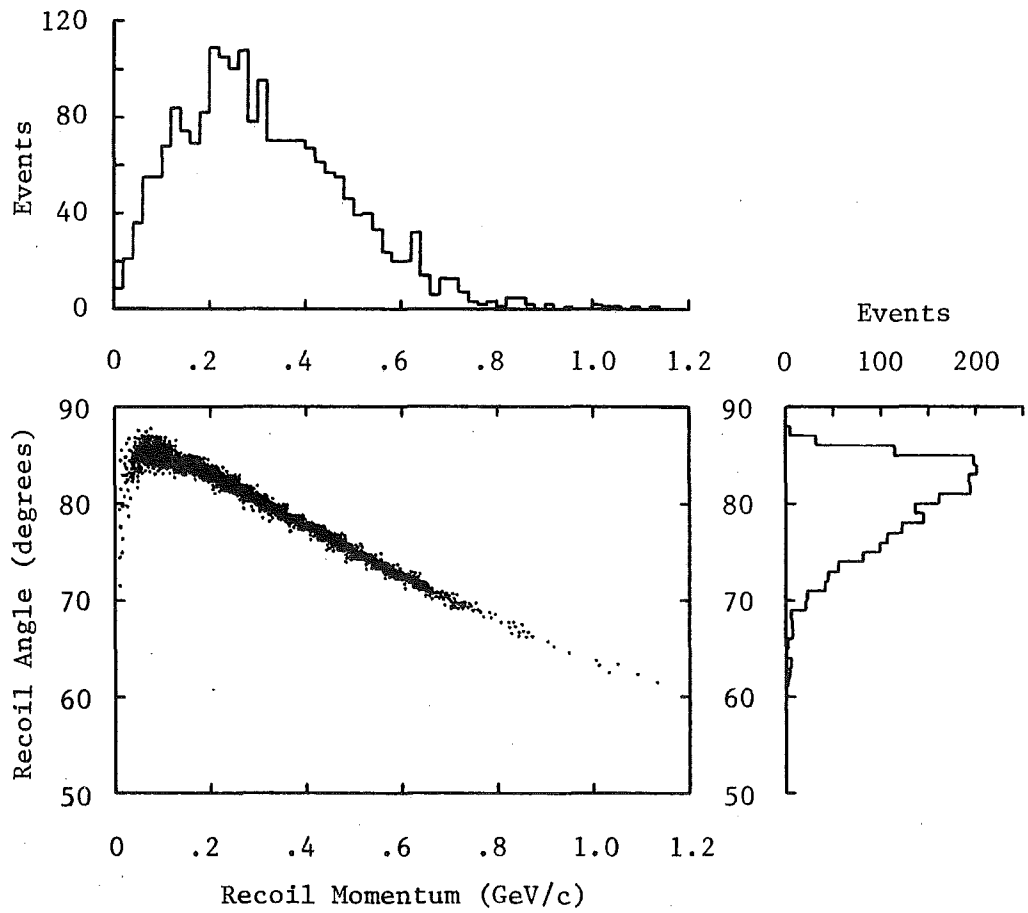


Figure (IV.C.11) Monte Carlo generated scatter plot of recoil proton momentum versus recoil angle for elastic ρ events.

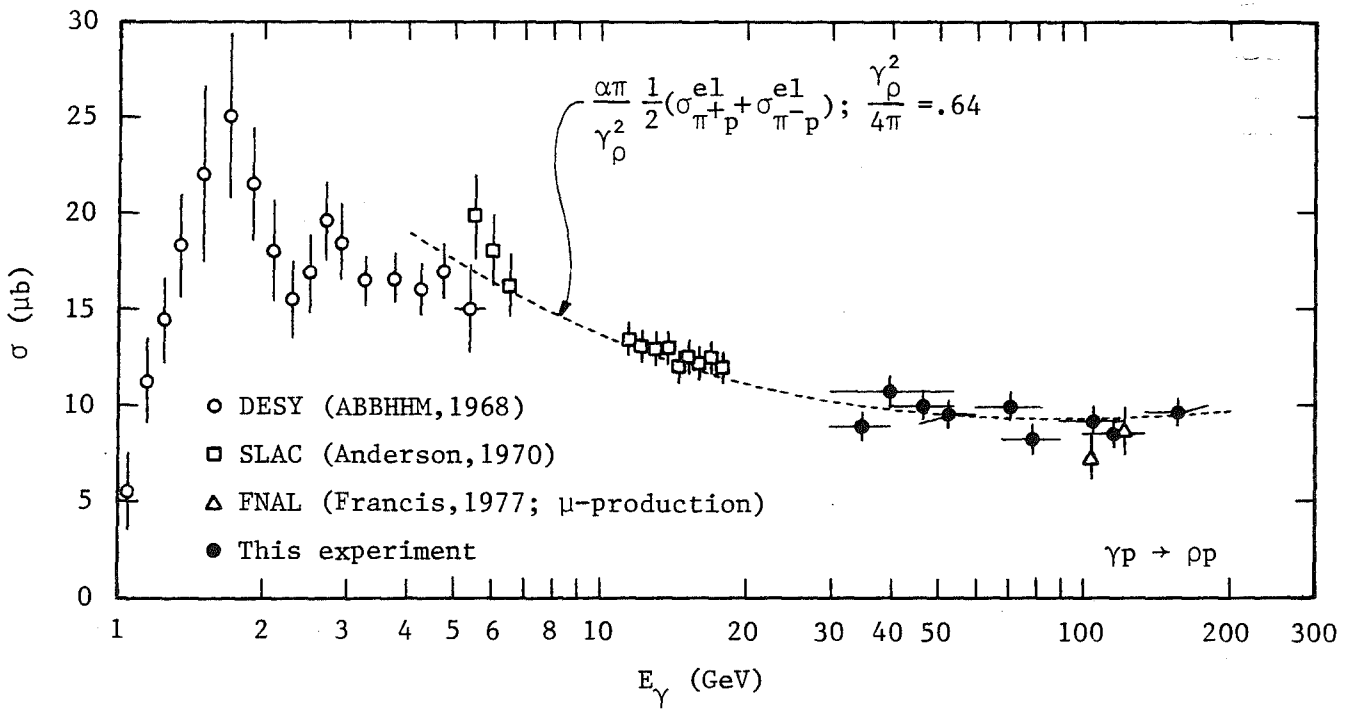


Figure (IV.D.1) Energy dependence of the ρ photoproduction cross section.

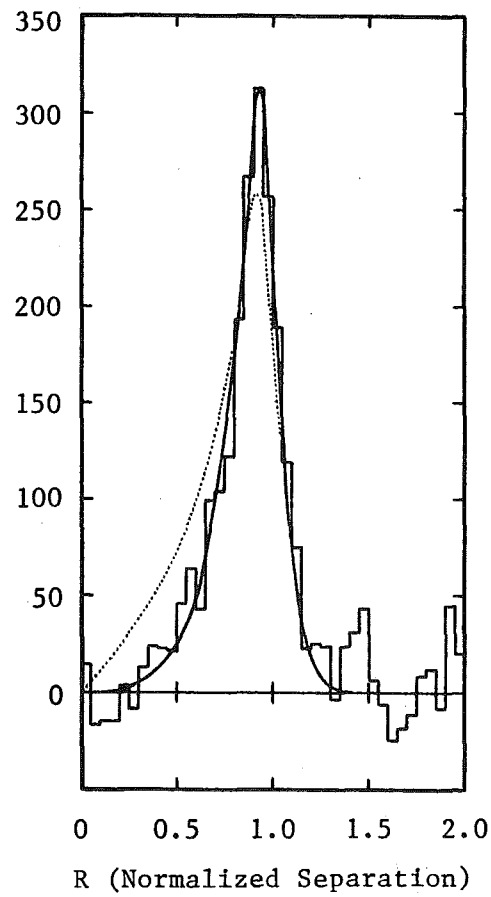


Figure (IV.D.2) $\phi$ signal above background (~2100 events, all the data). The solid curve is a Monte Carlo generated R distribution for the $\phi$ assuming s-channel helicity conservation; the dotted curve corresponds to an isotropic decay of the $\phi$ in its rest frame.

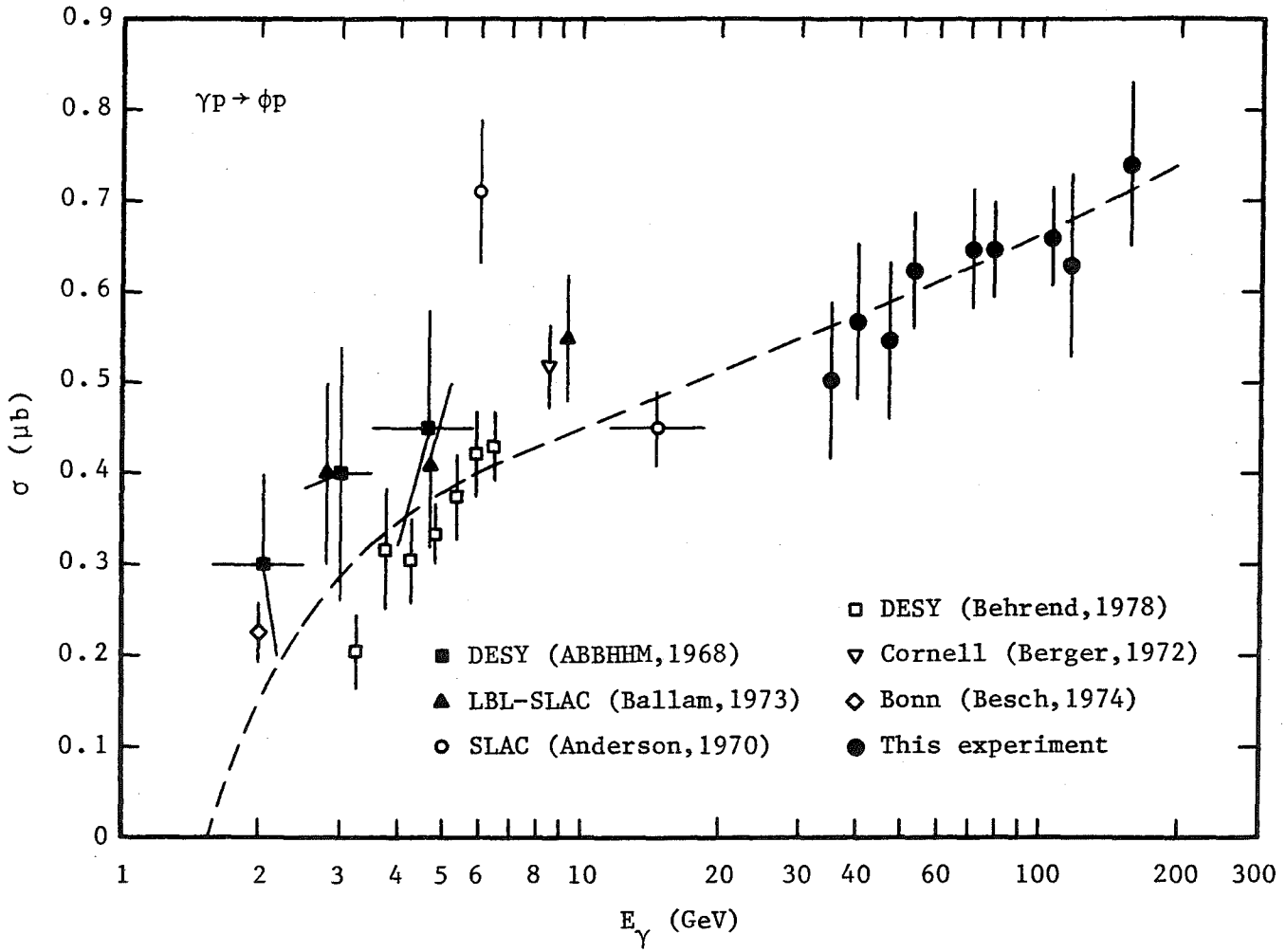


Figure (IV.D.3) Energy dependence of the $\phi$ photoproduction cross section.

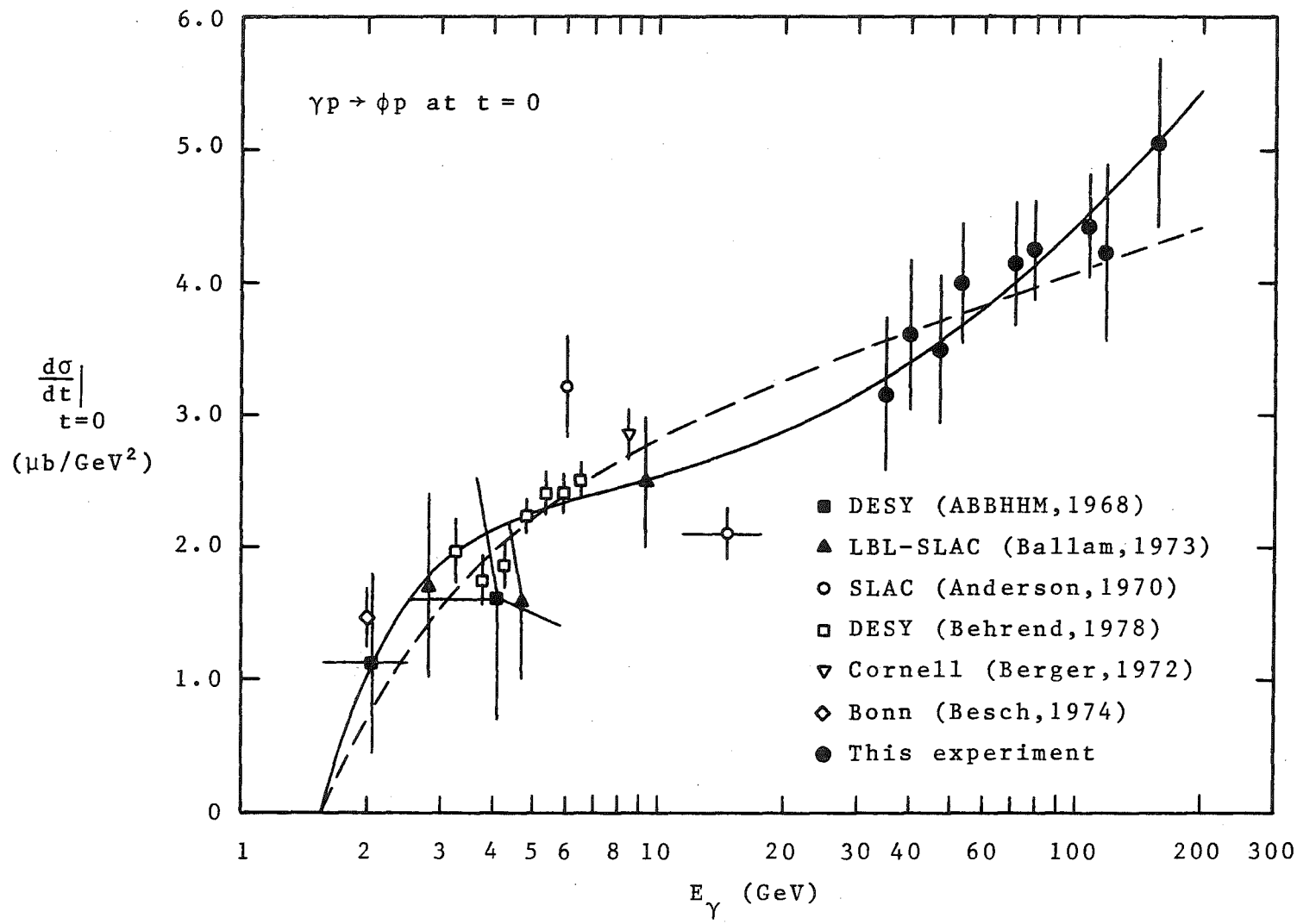


Figure (IV.D.4) Energy dependence of $d\sigma(\gamma p \to \phi p)/dt$ at $t = 0$. The data for this experiment is the measured integrated cross section multiplied by the quark model prediction for the momentum transfer slope parameter.

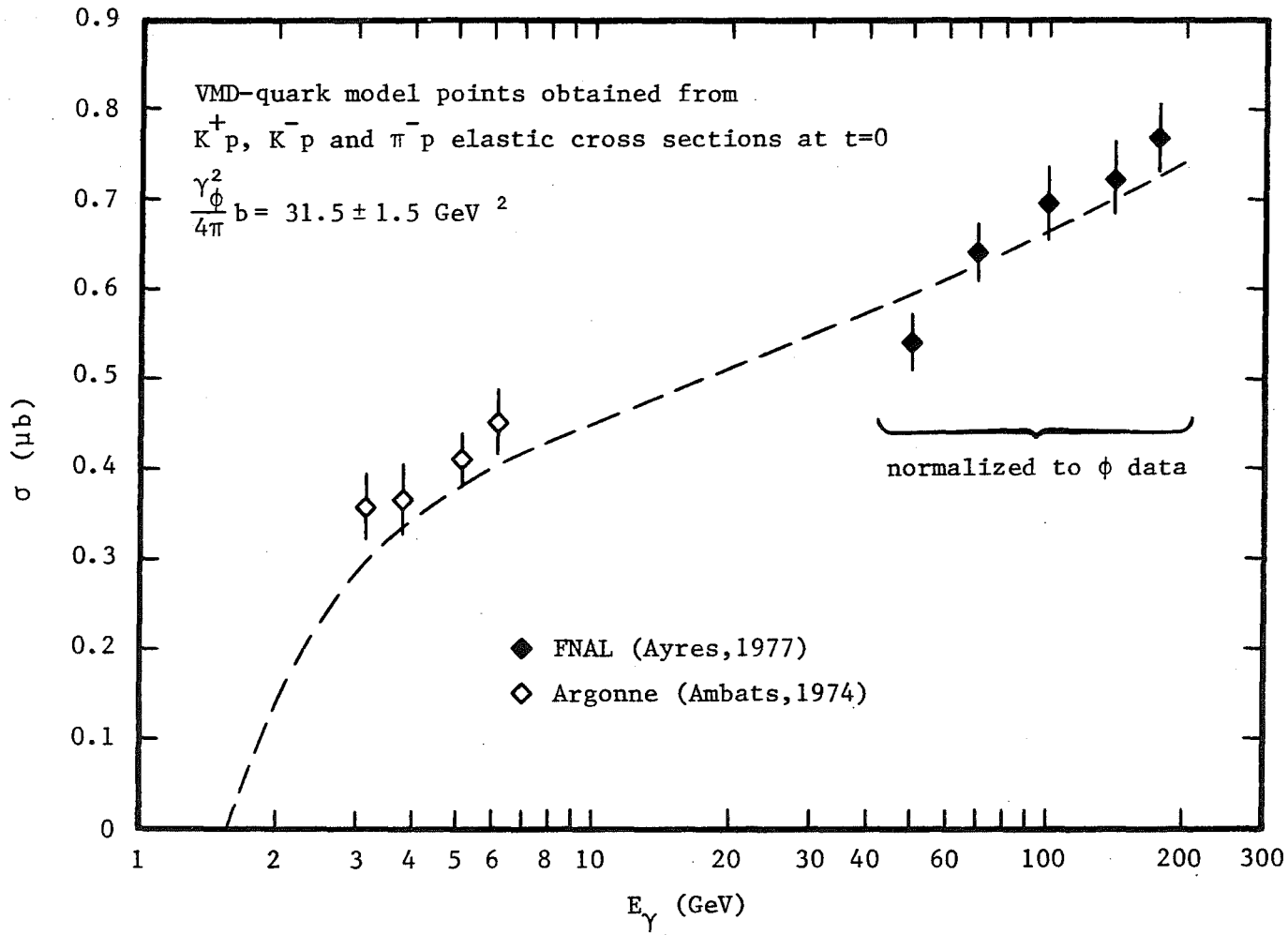


Figure (IV.D.5) VMD-quark model cross section normalized to the $\phi$ data of this experiment ($\gamma_\phi^2 b/4\pi$ is fitted parameter).

Table (IV.B.1)

Tagged Photon and TgH Trigger Totals

(for $\rho$-$\phi$ Data)

| $E_0$(GeV) | Z (m) | $\langle E_\gamma \rangle$ | Tg($\times 10^6$) | TgH($\times 10^3$) |
|---|---|---|---|---|
| 60 | 4.9 | 40 | 349 | 311 |
| 60* | 8.2 | 40 | 238 | 210 |
| 90 | 9.7 | 60 | 593 | 476 |
| 135 | 11.4 | 90 | 642 | 491 |
| 200 | 17.7 | 133 | 287 | 227 |

* Apparatus in the (approx.) 90 GeV configuration

$E_0$: Electron beam energy in GeV.

Z: Approximate distance from target to MWPC's in meters.

$\langle E_\gamma \rangle$: Average photon energy in GeV ($.50\ E_0 < E_\gamma < .92\ E_0$).

Tg: Number of tagged photons in millions.

TgH: Number of hadronic triggers in thousands.

Table (IV.C.1)

Analysis Cuts ($\rho$-$\phi$ Data)

| | |
|---|---|
| | (all events are trigger type = TgH) |
| 1 | Exactly 2 tracks in the MWPC's |
| 2 | S1, S2 and G2 "off" (i.e. no trigger) |
| 3 | Missing energy: 1-(H3 energy)/$E_\gamma$<0.65 |
| 4 | Pb glass energy: (G3IC energy)/$E_\gamma$<0.60 |
| 5 | S3 + K energy: (G3IC energy)/(H3 energy) <0.75 |

Note:

See Fig.(III.E.1) or (IV.A.1) for location of counters.

(G3IC energy) = energy sum in G3, I and C.

(H3 energy) = energy sum in G3IC, S3 and K.

Table (IV.C.2)

Fraction of events with 0, 1 and >1 recoil counter signals for $\rho$ and $\phi$ events

| | $\rho$ recoils | | | $\phi$ recoils | | |
|---|---|---|---|---|---|---|
| | 0 | 1 | >1 | 0 | 1 | >1 |
| A = Elastic events (Monte Carlo) | 0.76 | 0.23 | 0.01 | 0.59 | 0.39 | 0.02 |
| B = Inelastic evts. (calculated) | 0.02 | 0.23 | 0.75 | 0.02 | 0.23 | 0.75 |
| C = Data (elastic + inelastic) | 0.67 | 0.23 | 0.10 | 0.51 | 0.33 | 0.16 |
| D = Fit to data (*) | 0.67 | 0.23 | 0.10 | 0.49 | 0.36 | 0.15 |
| E = Inelastic fraction | 0.126 ± 0.02 | | | 0.182 ± 0.02 | | |

(*) $D = (1-E)\cdot A + E\cdot B$ is fit to C for the recoil = 0, 1 and >1 fractions with E the only adjustable parameter (the $\rho$ and $\phi$ are fit separately).

Table (IV.C.3)

Correction factors ($\rho$-$\phi$ data)

| | $\rho$ | | $\phi$ | | |
|---|---|---|---|---|---|
| Geometric acceptance: | (54%) | 1.85±0.09 | (96%) | 1.04±0.01 | -*- |
| Two-track reconstruction efficiency: | (92%) | 1.09±0.02 | (92%) | 1.09±0.02 | |
| Hadronic interactions of $\rho/\phi$ decay products in the target and the vacuum windows: | (13%) | 1.15±0.01 | (10%) | 1.11±0.01 | |
| Pion/kaon decay in flight: | (< 1%) | 1.01±<.01 | (6.5%) | 1.07±0.01 | -*- |
| Analysis cuts (events lost): | (4%) | 1.04±0.01 | (4%) | 1.04±0.01 | -*- |
| Inelastic events: | (12.6%) | 0.87±0.02 | (18.2%) | 0.82±0.02 | |
| Branching ratio $(\phi\to K^+K^-)/(\phi\to all)$: | --- | ------- | (46.6%) | 2.15 | |

-*- indicates average values for energy dependent factors.

(a double bremsstrahlung correction for the $E_o = 200$ GeV data is discussed in the text)

Table (IV.D.1)

Results for $\gamma p \to \rho p$ and $\gamma p \to \phi p$

| | | | | | | | | | |
|---|---|---|---|---|---|---|---|---|---|
| $E_\gamma$ (GeV) | 35±5 | $40^{+14}_{-10}$ | 47±7 | 53±7 | 71±11 | 79±11 | 106±16 | 117±17 | 157±23 |
| s ($GeV^2$) | 66.6 | 75.9 | 89.1 | 100.3 | 134.1 | 149.1 | 199.8 | 220.4 | 295.5 |
| $\sigma_{\gamma p \to \rho p}$ (μb) | 8.84 | 10.68 | 9.90 | 9.50 | 9.82 | 8.24 | 9.22 | 8.59 | 9.75 |
| $\Delta\sigma$ | ±.44 | ±.67 | ±.49 | ±.56 | ±.56 | ±.47 | ±.52 | ±.49 | ±.56 |
| $\sigma_{\gamma p \to \phi p}$ (μb) | 0.506 | 0.568 | 0.546 | 0.625 | 0.646 | 0.648 | 0.661 | 0.630 | 0.740 |
| $\Delta\sigma$ | ±.090 | ±.091 | ±.089 | ±.063 | ±.065 | ±.052 | ±.053 | ±.101 | ±.092 |

$\gamma$-$\phi$ coupling constant: (b = momentum transfer slope parameter for $\gamma p \to \phi p$)

$$\frac{\gamma_\phi^2}{4\pi}\, b = 31.48 \pm 1.54 \ (\mathrm{GeV}^{-2})$$

Fit to $\sigma(\gamma p \to \phi p)$: ($\sigma$ in μb, s in $GeV^2$)

$$\sigma_\phi = (p_\phi / k_\gamma)^2 \{a + (b/\sqrt{s}) + c \ln s\}\ , \quad a = -.103 \pm .329$$

$$b = .939 \pm .641$$

$$c = .135 \pm .057$$

$$\chi^2 = 26.2 \,/\, 22 \text{ df}$$

# CHAPTER V OMEGA ANALYSIS AND RESULTS

## A: Introduction

The elastic $\omega$ photoproduction cross section on protons has been measured from 46 to 180 GeV. The dominant $\pi^+\pi^-\pi^0$ decay mode of the $\omega$ is not suited for the detection apparatus of this experiment due to the nonexistence of an analysing magnet. The $\omega$ was instead detected by its all-neutral decay, $\omega \rightarrow \pi^0\gamma$ , with all three photons measured in lead glass shower counters. Schematics of the apparatus are shown in Figs. (III. E. 1) and (IV. A. 1). The Pb glass arrays G3 and G2 are shown in more detail in Fig. (V. A. 1). Also shown in the figure are the energies (ADC pulse heights) in the Pb glass blocks for a typical (relatively clean) $\omega \rightarrow \pi^0\gamma$ candidate. The total electromagnetic shower energy of the three photons from a diffractively produced $\omega$ must be equal to the tagged energy of the incident photon (within the energy resolution of the apparatus). The detectors other than G3 and G2 are used as veto counters to further ensure the selection of exclusive three photon events. Finally, two of the three photons must have an invariant di-photon mass consistent with neutral pion decay, $\pi^0 \rightarrow \gamma\gamma$. The resulting $\pi^0\gamma$ invariant mass distribution shows a clean peak at the $\omega$ mass with very little background.

The t-dependence of the $\omega$ photoproduction cross section

has been measured as well as the $\omega \rightarrow \pi^0\gamma$ polar angle distribution. The angular dependence is expected to be of the form $1+\cos^2\theta$ for s-channel helicity conservation, where $\theta$ is the decay angle of the $\pi^0$ with respect to the $\omega$ direction of flight in the $\omega$ rest frame.

## B: Data Accumulation

Data were taken with the electron beam energy $E_o$= 90, 135 and 200 GeV. Some of the 90 GeV data were taken with the H2 detector, which includes G2 (see Fig.[III.E.1]), moved downstream to a position appropriate for the $E_o$= 135 GeV configuration to check the effect of changes in geometrical acceptance. Due to insufficient space, the G2 Pb glass array was removed (leaving S2) from the detection apparatus for the $E_o$= 40 and 60 GeV total cross section measurement. The geometric acceptance of G3 alone is small for $\omega \rightarrow \pi^0\gamma$ events. As a result, the $E_o$= 40 and 60 GeV data are not included in the $\omega$ analysis.

An event is considered an elastic $\omega \rightarrow \pi^0\gamma$ candidate if it has a large fraction (≈100%) of the tagged photon energy in the Pb glass shower counter arrays G3 and G2. Events of this kind are recorded in the hadronic (TgH) trigger category (see Table [III.F.1]). The number of tagged photons and TgH triggers for the $\omega$ analysis are summarized

in Table (V.B.1).

## C: Data Analysis

### 1. General

All hadronic event candidates collected in the TgH trigger category (approx. 1.4 million for the ω analysis) are recorded on tape. From these events a subsample consistent with exclusive $\omega \rightarrow \pi^0\gamma$ production is obtained by requiring the events to pass a number of analysis cuts.

The electromagnetic energy in the Pb glass shower counter arrays G3 and G2 is required to be at least 90% of the tagged incident photon energy. The 10% error margin allows for the energy resolution of the apparatus and shower leakage for photons incident near the inside edges of the Pb glass counters surrounding the central hole in G3 and (more importantly) G2 (see Fig.[V.A.1]). The measured energies in each Pb glass block must be consistent with exactly three photons incident on G3 (including the I-counters) and G2. Events with a photon in the C-counter are rejected. Each of the three photons must have an energy no less than 1 GeV. The method used for shower fitting and reconstruction is discussed in the following section (V.C.2).

An event is rejected if there is more than one track in the MWPC's. If there is a track, its position given by the MWPC's must agree with a shower position in G3. Most events have zero chamber tracks. There is however a 10% to 20% probability (acceptance dependent) for one track due to a $\gamma \rightarrow e^+e^-$ conversion in the hydrogen target or the vacuum window just upstream of the MWPC's (see Fig. [IV. A. 1]). The probability for getting more than one track, either because the $e^+e^-$ pair diverges sufficiently (compared with the 2 mm wire spacing of the chambers) or due to double conversion, is less than 3%.

The summed ADC pulse height for planes 2 and 3 of S1 (the detector closest to the target) must be less than 1.0. This cut was also used in the analysis of the $\rho$-$\phi$ data and serves mainly to reject inelastic events (see Section [IV. C. 1]).

The measured energy in the hadrometers S2, S3 and K (Z+TANC) for events surviving all of the above cuts is typically at most a few percent of the tagged photon energy and consistent with shower leakage from G2 and G3. A small sample of events ($\simeq$5%) has anomalously large pulse heights in at least one of the hadrometers and is thus rejected.

For the final $\omega \rightarrow \pi^0\gamma$ event selection one of the two-photon invariant masses (three combinations per event) must be near $m_{\pi^0}$= 135 MeV for $\pi^0 \rightarrow \gamma\gamma$. The analysis cuts are summarized in Table (V. C. 1). Only about 0.03% of the TgH events survive all cuts.

## 2. Shower Reconstruction

The shower reconstruction is the heart of the $\omega$ analysis and is thus discussed at some length. The reader who is not interested in the details may want to read only the last three paragraphs of this section (starting on page 168) without much loss of continuity.

When a high energy photon or electron enters an absorber, an electromagnetic cascade shower develops as a result of the combined phenomena of bremsstrahlung and pair production. The number of electrons and photons in a shower increases exponentially with depth of material traversed until the ionization energy loss of the electrons (and positrons) begins to dominate over the radiation loss. The relativistic charged particles in the electromagnetic shower emit Cerenkov radiation. The Cerenkov light from the shower is proportional to the total path length of the charged particles in the shower which is in turn proportional to the energy of the incident particle [Rossi, 1952]. A measurement of the emitted Cerenkov light thus yields the energy of the incident photon or electron.

The total energy appearing in Cerenkov radiation per unit path length is [Rossi, 1952]

$$\frac{dE}{dx} \propto Z^2 \int \{1 - \frac{1}{\beta^2 n^2}\} \nu \, d\nu \qquad (\beta n > 1) \qquad \text{(V.C.1)}$$

$$\propto Z^2 \cdot \{1 - \frac{1}{\beta^2 n^2}\} \int \nu \, d\nu \text{ if } n \neq n(\nu)$$

where Z is the atomic number and n the refractive index of the absorber, $\beta = v/c$ is the relative velocity of the electron (positron), and $\nu$ is the frequency of the Cerenkov radiation. The energy dependent factor $1-(1/\beta n)^2$ is shown as a function of kinetic energy in Fig. (V.C.1A) for $n = 1.65$ (SF2 glass). The properties of Pb glass (see Table [II.E.1]) are well suited for use as electromagnetic shower detectors. The high average Z (short radiation length) ensures the rapid development of a cascade shower upon incidence of a high energy photon or electron. The clarity of the glass allows the Cerenkov light to be viewed by a single photomultiplier tube which can be attached (eg. glued) directly onto the polished surface of an appropriately dimensioned block of Pb glass.

The basic interactions of the electrons and photons in the shower are well established, but the analytical solutions of the cascade problem are prohibitively difficult to obtain. The most useful results are computed using Monte Carlo techniques which make fewer approximations and take into account exact (energy dependent) cross sections and angular distributions of the various electromagnetic processes [Longo, 1975].

According to the Monte Carlo results of Longo [ref.] the longitudinal development of a photon induced shower is well represented by

$$\pi(E_\gamma, E_c, t) = At^\alpha e^{-bt} \qquad \text{(V.C.2)}$$

where $\pi$ is the average number of charged particles (electrons and positrons) of kinetic energy greater than $E_c$ crossing a plane which is perpendicular to the direction of the incident photon and a distance t from the front surface of the Pb glass. For a 30 GeV shower

$E_\gamma$ = 30 GeV (incident photon energy)

$E_c$ = 0.5 MeV (cut-off energy)

A = 8.57

$\alpha$ = 3.33

b = 0.466

t in units of $X_o$ (radiation length)

The t dependence of $\pi(E_\gamma, E_c, t)$ is shown in Fig. (V.C.1B). The integral of Eqn. (V.C.2) for t > 0 gives the total path length of the charged particles, $T(E_\gamma)$, and has the energy dependence

$$T(E_\gamma) = \int_0^\infty \pi(E_\gamma, E_c, t)\,dt = \frac{A\alpha\Gamma(\alpha)}{b^{\alpha+1}} = K\,E_\gamma \qquad \text{(V.C.3)}$$

where

$$K = 71.85\ X_o/\text{GeV}$$
$$= 204\ \text{cm/GeV for SF2 Pb glass}$$

i.e. the total path length is linearly proportional to the energy of the incident particle as shown in Fig. (V.C.1C).

The position of the shower maximum is given by the differential of Eqn. (V.C.2),

$$\frac{d\pi}{dt} = \{\frac{\alpha}{t} - b\}\pi = 0 \qquad \text{(V.C.4)}$$

which yields

$$t_{max} = \alpha/b$$
$$= 7.15\ X_o \text{ for } E_\gamma = 30 \text{ GeV}$$
$$= 20.3 \text{ cm for SF2 Pb glass}$$

The energy dependence is approximately given by

$$t_{max} = 0.90 \ln E_\gamma + 4.1 \qquad \text{(V.C.5)}$$

with $t_{max}$ in units of $X_o$ and $E_\gamma$ in GeV and is shown in Fig. (V.C.1D). For comparison, the Pb glass blocks in the G3 array (see Section [III.E.5]) are over 20 $X_o$ long. Even showers of >100 GeV energy are thus easily contained in the Pb glass with insignificant leakage of energy through the back end. The energy of the incident photon or electron can be determined precisely from a measurement of the emitted Cerenkov light.

The lateral spread of a 30 GeV electromagnetic shower in Pb glass is shown in Fig. (V.C.1E) from the Monte Carlo

results of Longo [ref.]. The curve shows the fraction of the total path length, Eqn. (V.C.3), contained in a cylinder of infinite length and radius r centered on the shower axis. The dependence of the lateral spread on the depth t is shown in Fig. (V.C.1F). The curves represent the fraction of the path length contained in a cylindrical disc of radius r and thickness $t = 0.5\ X_o$ at a depth t. An important (and convenient) property of the showers is the apparent lack of energy dependence of the lateral development, i.e. the fraction of the total Cerenkov light emitted at a radius r is independent of the shower energy if the Pb glass counters are long enough to contain most of the shower. This property is utilized to obtain the coordinates of incident photons and electrons in a Pb glass shower counter detector.

Typically, the detector is constructed of a modular array of Pb glass blocks (see Fig. [V.A.1]), each viewed by a photomultiplier tube which measures the Cerenkov light emitted in the shower. The spatial resolution of the detector thus improves with decreasing transverse dimensions of the Pb glass blocks. The position of a shower can, however, be determined with an accuracy which is better than the block size. As a consequence of the modularized construction of the detector and the lateral spread of the shower the Cerenkov light is shared between neighboring blocks. A study of the relative amount of shower sharing between neighboring blocks leads to considerably improved

accuracy of shower position measurements. The fraction of the total Cerenkov light in a block as a function of shower position can be predicted from Monte Carlo generated shower distributions. The position of a real shower is then given by the spatial coordinates which give the best agreement between the experimentally observed energy fractions and those predicted by the Monte Carlo studies. There is thus a need for shower tables giving predicted energy fractions in a Pb glass block as a function of shower position.

The Cerenkov light from a shower is proportional to the total path length of the charged particles in the shower, $T(E_\gamma)$, given by Eqn. (V.C.3). The fraction of the total path length per unit area a distance r from the shower axis is denoted by f(r) and is related to $T(E_\gamma)$ by

$$\begin{aligned} T(E_\gamma) &= \int (dT/dr)\, dr \\ &= \iint f(r)\, r\, dr\, d\theta = \int f(r) 2\pi r\, dr \end{aligned} \qquad \text{(V.C.6)}$$

The Monte Carlo results of Longo [ref.] give values for $\Delta T$ for an infinitely long cylindrical ring of radius r and thickness $\Delta r$. A good fit to the radial dependence of $\Delta T$ is shown in Fig. (V.C.2) and is given by

$$\frac{dT}{dr} = \frac{\sqrt{a}\cdot r}{(r^2 + a)^{3/2}} \quad , \quad \int_0^\infty \frac{dT}{dr}\, dr = 1 \qquad \text{(V.C.7)}$$

with

$a = 0.02893$

$r$ in $X_o$ (radiation lengths)

From Eqn. (V.C.6), $f(r)$ is then given by

$$f(r) = \frac{dT}{dr}\frac{1}{2\pi r} = \frac{\sqrt{a}/2\pi}{(r^2+a)^{3/2}} \qquad \text{(V.C.8)}$$

and thus

$$f(x,y) = \frac{\sqrt{a}/2\pi}{(x^2+y^2+a)^{3/2}} \qquad \text{(V.C.9)}$$

i.e. $f(x,y)$ is the fraction of the total Cerenkov light per unit area emitted at the point $(x,y)$ where $x = y = 0.0$ are the coordinates of the shower axis. Equally valid, $f(x,y)$ is the fractional light at $x = y = 0.0$ with the shower axis at the point $(x,y)$. The light emitted from a square area of the shower counter is obtained by integrating Eqn. (V.C.9),

$$\begin{aligned} F(x,y) &= \iint f(x,y)\,dx\,dy \\ &= \frac{1}{4\pi}\sin^{-1}\left[\frac{2(xy)^2}{a(x^2+y^2)+a^2+(xy)^2} - 1\right] \end{aligned} \qquad \text{(V.C.10)}$$

and evaluating between the desired limits of $x$ and $y$. For a square area bounded by $x_1 \to x_2$ and $y_1 \to y_2$,

$$F(x,y) = \frac{1}{4\pi}\sum_{i=1}^{2}\sum_{j=1}^{2} c\left[\frac{\pi}{2} + \sin^{-1}\left[\frac{2(x_i y_j)^2}{a(x_i^2+y_j^2)+a^2+(x_i y_j)^2} - 1\right]\right] \qquad \text{(V.C.11)}$$

where

$$c = (-1)^{i+j} \frac{x_i y_j}{|x_i||y_j|}$$

with x and y in units of $X_o$. Eqn. (V.C.11) can be used to generate shower tables (energy fractions vs. shower position) for computer shower fitting programs. This is done easily for any size Pb glass block and as small a grid size (position increments) as is desired. Table (V.C.2) is a shower table for 6.35x6.35 $cm^2$ (2.5x2.5 $in^2$) blocks of glass type SF2 and a grid size of 0.635 cm (10 steps = width of block). The calculated energy fractions, F(x,y), as a function of shower position are also shown by the curves in Fig. (V.C.3). According to the shower table, at most 86.5% (=$F_{max}$) of the shower energy can be contained in a Pb glass block of the given size and type. The remaining 13.5% leak into the neighboring blocks. Experimental data suggest a somewhat lower value for the maximum energy fraction, i.e. $F_{max}$ = 82%. A corresponding correction in the calculated energy distribution is readily obtained by an appropriate change in the value of the parameter 'a' in Eqns. (V.C.7) to (V.C.11). Increasing the value of 'a' reduces $F_{max}$ which is compensated by increased energy in the shower tails and therefore more energy sharing by the neighboring blocks:

| a | $F_{max}$ | |
|---|---|---|
| 0.0289 | 0.865 | (fit to Monte Carlo) |

| | | |
|---|---|---|
| 0.0500 | 0.824 | (favored by data) |
| 0.0750 | 0.786 | |
| 0.1000 | 0.755 | |

The procedure for locating shower coordinates in a Pb glass array (such as G2 and G3 in this experiment) is a two-step process. First, the array is scanned with a computer pattern recognition program to locate groups of adjacent counters with measured energies (pulse heights) above some threshold (counter noise). Second, each group of counters thus isolated is analysed by a computer fitting routine which fits the measured energies in each block to those predicted according to the shower table. The shower coordinates are varied in small steps until the fit is optimized. The goodness of the fit, expressed by an overall chisquared, is used to decide whether the pattern being analysed is consistent with a single photon (or electron) incident on the counter with the most shower energy in the group. If the quality of the fit is good the fitted shower position and summed energy of the counters in the group become the parameters of a reconstructed shower and are recorded for final event analysis. A bad fit to the measured energies in the group of counters may indicate that the observed pattern is the result of two overlapping showers which were not resolved as such with the pattern recognition program. Problems of this kind are expected if

the shower separation is comparable to (or less than) the transverse dimensions of the Pb glass blocks. Overlapping showers most often result from the decay of a high energy neutral pion, $\pi^0 \rightarrow \gamma\gamma$. The minimum opening angle between the two photons is given by

$$\theta_{min} \simeq 2m_\pi c^2/E_\pi = (0.27\ \text{GeV})/E_\pi \qquad \text{(V.C.12)}$$

which corresponds to a shower separation of 5.4 cm for a 50 GeV neutral pion decaying 10 m upstream of the shower counter array. The fitting procedure for a two-shower pattern involves optimizing both the shower positions and energies to yield the best possible agreement between measured and predicted energy fractions in the individual counters.

It is possible to simplify the method used for shower fitting with little loss of accuracy. The shower counter array is imagined to be constructed of parallel slabs (horizontal or vertical) where each slab consists of a row of neighboring Pb glass blocks. The fraction of the total shower energy contained in a slab as a function of shower position is obtained from Eqn. (V.C.11) in the limit of very long slabs,

$$\begin{aligned} F(x) &= \lim_{y \rightarrow \pm\infty} F(x,y) \\ &= \frac{1}{2\pi}\left[\frac{x_2}{|x_2|}\sin^{-1}\left(\frac{x_2^2-a}{x_2^2+a}\right) - \frac{x_1}{|x_1|}\sin^{-1}\left(\frac{x_1^2-a}{x_1^2+a}\right)\right] \end{aligned} \qquad \text{(V.C.13)}$$

where

$$x_2 - x_1 = \text{width of slab (units of } X_o)$$

for slabs extending in the y direction. The fractional energy for three neighboring slabs is shown by the curves in Fig. (V.C.4). The energy in the outside slabs is strongly dependent on the shower position in the central slab. Eqn. (V.C.13) can be inverted to give the distance of a slab from the shower position as a function of the fractional energy in the slab,

$$d = \left(\frac{\Delta^2}{4} - a + \frac{\Delta\sqrt{a}}{\tan \pi F}\right)^{1/2} \qquad \text{(V.C.14)}$$

where

d = distance of center of slab from shower position

$\Delta = x_2 - x_1$ = width of slab

F = fractional energy in slab

(d, $\Delta$ in units of $X_o$)

The x and y coordinates of a shower can thus be calculated separately using slabs extending in the y and x direction, respectively. The shower energy in a slab is the summed energy in the Pb glass blocks which are part of the slab. In practice, Eqn. (V.C.14) is solved for each of the two outside slabs, i.e. the slabs on either side of the central

slab (the slab with the most energy). The two distances thus calculated can be averaged to give the shower coordinate perpendicular to the direction of the slabs. A large difference between the two calculated distances may indicate that the energy in the slabs is due to two overlapping showers. It then is necessary to resolve the two showers by fitting to the observed energies using Eqn. (V.C.13).

Unfortunately, the reconstruction of showers in the Pb glass arrays G2 and G3 of this experiment encounters several problems which result in reduced accuracy. As is apparent from the above discussion, a good position and energy resolution in the reconstruction of showers requires an accurate measurement of the shower sharing among the Pb glass blocks. The total shower energy is typically contained in a 3x3 array of Pb glass blocks of the size used in G2 and G3 (with the central block having the most energy). As a result, the position and energy of photons (and electrons) incident on the innermost ring of counters in G2 (see Fig.[V.A.1]) can not be determined very accurately. Some unknown (within limits) amount of the shower energy leaks into the central hole of G2 and is thus lost. In spite of this missing shower information, the position and energy of the incident particle can be found, within (known) errors, using the methods discussed above. The loss of accuracy is, however, reflected by a significant

broadening in the resulting $\pi^0 \rightarrow \gamma\gamma$ and $\omega \rightarrow \pi^0\gamma$ mass distributions.

A similar situation exists for photons incident on the I-counters, i.e. the counters surrounding the central hole of the G3 array. However, the hole in G3 is only the size of one Pb glass block (in G2 it is 2x2 blocks). As a consequence, a large fraction of the shower energy leaking into the hole is recovered by the counters surrounding the hole and the C-counter located further downstream (see Fig. [V.A.1]). The transfer of shower energy across the G3 hole can be studied with electron induced showers, using the MWPC's (multiwire proportional chambers) in front of G3 to determine the coordinates of the incident electron. Results obtained with a 90 GeV (low intensity) electron beam incident on an I-counter are shown in Fig. (V.C.5). The main features of the energy distributions shown in the figure can be used to aid in the reconstruction of I-counter showers.

Another problem, affecting all showers in both G2 and G3, is due to the method used to store measured energies in the memory of the PDP-15 on-line computer during the data taking. The amplified pulse heights from the photomultiplier tubes are digitized with 10-bit ADC's (analog to digital converters). The word length of a PDP-15 computer is 18 bits. In order to keep the number of computer words per event as small as possible (to save memory) the lowest order bit of all ADC words is dropped

thereby allowing two ADC words to be packed into one PDP-15 word. As a consequence, the number of ADC channels is effectively reduced from 1024 (10 bits) to 512 (9 bits) which adversely affects the accuracy of low energy (low pulse height) measurements. The result is seen in terms of decreased position resolution of the shower reconstruction as it depends heavily on knowing accurately the typically very low energy levels of the shower tails.

3. Data and Monte Carlo

The two-photon invariant mass spectrum for events surviving all analysis cuts and thus being consistent with $\omega \rightarrow \pi^0\gamma$ is shown in Fig. (V.C.6) for most of the data. The invariant mass of a two-photon state is given by

$$M^2_{\gamma\gamma} = 4\,E_1 E_2 \sin^2(\theta/2) \qquad \text{(V.C.15)}$$

where $E_1$ and $E_2$ are the energies of the photons and $\theta$ is the opening angle between the photon pair. Each event gives three two-photon combinations. About one-third of the combinations peak in the $\pi^0$ mass region, indicating that most events are compatible with a $\pi^0\gamma$ state. The $\pi^0$ candidate for each event is chosen to be that photon pair which has a mass nearest to 135 MeV (shown separately in Fig. [V.C.6]).

For the decay

$$V \rightarrow \gamma_1 P \ , \quad P \rightarrow \gamma_2 \gamma_3$$

(here $V=\omega$ and $P=\pi^0$) the theoretical two-photon invariant mass spectrum for $\gamma_1\gamma_2$ and $\gamma_1\gamma_3$ has the form

$$dN/dM_{\gamma\gamma} \propto M_{\gamma\gamma} \quad \text{for} \quad M^2_{\gamma\gamma} < (M^2_V - M^2_P)$$

as indicated by the straight line in Fig. (V.C.6). The deviation of the data from the theoretical prediction is due to background events (as evidenced by the tail in the $\pi^0$ mass distribution), the incomplete geometrical acceptance and the resolution (energy, position) of the apparatus.

The three-photon invariant mass spectrum for events which have a two-photon combination near the $\pi^0$ mass (135 MeV) is shown in Fig. (V.C.7) for most of the data. The invariant mass is calculated from

$$M^2_{\pi^0\gamma} = \sum_{i,j=1,3} 4E_iE_j\sin^2(\theta_{ij}/2) \qquad i \neq j \qquad \text{(V.C.16)}$$

where $E_i$ and $E_j$ are the energies of the photons and $\theta_{ij}$ the opening angle for the two-photon combinations. The mass distribution shows a clear peak at the $\omega$ mass (783 MeV) from $\pi^0\gamma$ events with little background.

Energy distributions for events in the $\omega$ mass region are shown in Fig. (V.C.8) for the $\pi^0$ ($E_\pi$) and the highest ($E_H$) and lowest ($E_L$) energy photon for each event. The quantities in histograms (A), (B) and (C) of Fig. (V.C.8) are expressed as a fraction of the tagged photon energy ($E_\gamma$) and

represent all the data. Histogram (D) shows $E_L$ in units of energy for the $E_o$= 135 GeV data ($E_L$ > 1. GeV).

Monte Carlo (M.C.) generated energy distributions for $E_\pi$, $E_H$ and $E_L$ are shown by the dashed curves in Fig. (V.C.8) normalized to the data. There is good agreement with the data, indicating that the geometric acceptance and shower reconstruction efficiency of the apparatus are understood.

Another consistency check is provided by the number of photons in G2 expressed as a fraction of all photons (G2+G3) for $\pi^0\gamma$ events in the $\omega$ mass region. The predicted fractions from M.C. generated events and the experimental values are listed below for the different apparatus configurations (i.e. electron beam energies, $E_o$):

| $E_o$ (GeV) | M.C. | data |
|---|---|---|
| 90 | 0.44 | 0.44 ± 0.03 |
| 90* | 0.52 | 0.54 ± 0.06 |
| 135 | 0.32 | 0.30 ± 0.03 |
| 200 | 0.32 | 0.33 ± 0.04 |

(see Table [V.B.1] for information on the different $E_o$ settings) The errors on the data are statistical. The agreement between the corresponding fractions is good at all energy settings.

The Monte Carlo event generation for $\gamma p \rightarrow \omega p$, $\omega \rightarrow \pi^0\gamma$

assumes s-channel helicity conservation (a $1+\cos^2\theta$ decay distribution) and a momentum transfer distribution given by $\exp(bt)$ with $b = 8.5\ \mathrm{GeV}^{-2}$. The incident photon spectrum and beam size are given the experimentally observed characteristics. Shower sharing between the individual Pb glass blocks of G3 and G2 is predicted according to the methods described in Section (V.C.2) and taking into account the geometric acceptance and energy resolution of the apparatus. The generated events are then reconstructed with the same computer analysis program which is used for the data.

4. Inelastic Events

The elastic $\omega$ photoproduction cross section is calculated from the yield of $\pi^0\gamma$ events in the $\omega$ mass region. The analysis cuts, listed in Table (V.C.1), ensure that the events are consistent with exclusive $\omega$ production. However, not all events are produced elastically, i.e.

$$\gamma p \rightarrow \omega X \ , \quad X \neq p \qquad \text{(V.C.17)}$$

where X denotes a missing mass different from the proton mass. Obvious low mass (low t) candidates for X are the $\pi$-nucleon resonances N (I=1/2) for diffractive (pomeron exchange) target dissociation [Wolf, 1971], and $\Delta$(I=3/2)

for t-channel pion exchange processes.

The fraction of inelastic $\omega$ events is estimated using the method described in Chapter IV for the $\rho$-$\phi$ analysis (for details see Section [IV.C.4]). Elastic and inelastic events can be stastistically distinguished by their different probabilities for firing n=0, 1 or >1 of the four recoil counters surrounding the hydrogen target (see Section [III.E.6]). Elastic events are expected to have n=0 or n=1 (usually n=0) with probabilities computable from range-energy relations. The results, obtained with the Monte Carlo event generation computer program described in the previous section, are listed in the first row of Table (V.C.3).

Inelastic events almost always have n=1 or n>1 (usually n>1) with probabilities determined from a simple Poisson model which agrees with hadronic studies of target dissociation (see Appendix C). The predicted fractions in each recoil category are listed in the second row of Table (V.C.3).

The measured fractions of $\omega$ events with 0, 1 or >1 recoil counter signals are listed in the third row of Table (V.C.3). The numbers represent averages for all of the data; the assigned uncertainties are statistical. The fraction of inelastic events in the data sample is obtained from a fit of the recoil predictions for elastic and inelastic $\omega$ production to the observed recoil distribution.

The best possible agreement with the data is given with an inelastic event contribution of 0.256+/-.035 as shown in the fourth row of Table (V.C.3).

A lower limit on the fraction of inelastic events can be obtained directly from the data. A criterion for elastic ω production is the coplanarity of the recoil proton and the ω. A knowledge of the ω direction of flight, calculated from the measured energies and positions of the decay photons, allows to predict the direction (specifically the azimuthal angle) of the recoiling proton. An event with a recoil signal in a counter other than the one predicted from the recoil proton direction may be classified as inelastic. The fraction of inelastic events thus determined is 0.21 for the n=1 recoil category and, including all n>1 events, gives an overall inelastic contribution of 0.25+/-.03, in agreement with the fraction obtained using the statistical method.

The amount of inelastic events in the ω data is larger than expected, especially when compared with the ρ data (13% inelastic) and φ data (18% inelastic). Inelastic event production due to diffractive target dissociation should be roughly the same for the ρ and the ω (comparable geometric acceptance and momentum transfer slope parameter). Unnatural parity t-channel exchange ω production has been measured at photon energies below 10 GeV [Ballam, 1973; Eisenberg, 1972] and is found to be consistent with one-pion

exchange (OPE) for both the production cross section and $\omega$ decay angular distribution (see Section [II.B.2] for more details). In particular, the OPE cross section decreases with incident photon energy approximately as $1/E_\gamma^2$. Reactions such as $\gamma p \rightarrow \omega\Delta^+$, due to OPE, should therefore be negligible in the energy range of this experiment.

The reaction $\gamma p \rightarrow \omega p \rightarrow \pi^+\pi^-\pi^0 p$ has been investigated, using Monte Carlo (M.C.) techniques, as a possible source of background to the $\omega \rightarrow \pi^0\gamma$ data. Of interest are those events which have one of the charged pions interact in the hydrogen target, possibly resulting in a recoil counter signal, with the non-interacting $\pi^0\pi^\pm$ pair simulating a $\pi^0\gamma$ event in the downstream detectors (events are allowed to have at most one MWPC track). The probability for one of the charged pions to interact in the target is approximately 10%. The relative event rate is enhanced due to the branching ratio [Particle properties, 1978]

$$(\omega \rightarrow \pi^+\pi^-\pi^0)/(\omega \rightarrow \pi^0\gamma) = 10.2$$

The analysis of M.C. generated $\omega \rightarrow \pi^+\pi^-\pi^0$ events shows that such processes are not expected to survive the analysis cuts for $\pi^0\gamma$ events.

A source for $\pi^0\pi^-$ events with a recoil counter signal might be from $\rho^-$ photoproduction, i.e. $\gamma p \rightarrow \rho^-\Delta^{++}$ ($\rho^- \rightarrow \pi^0\pi^-$). This reaction has been measured up to 7.5 GeV [Eisenberg, 1972] and has an energy dependence given by $\sigma(\mu b)=C\cdot E^b$, where C=3.5+/-1.2 and b=-0.6+/-0.2

(inconsistent with OPE!). An extrapolation to the energy range of this experiment indicates that $\rho^-\Delta^{++}$ production may not be completely negligible. However, most $\pi^0\pi^-$ events would be rejected due to insufficient energy in the lead glass arrays and/or too much hadronic energy in the counters S1, S2, S3 or K. Monte Carlo studies show that surviving $\pi^0\pi^-$ pairs peak at an invariant mass near 0.45 GeV (analysed as $\pi^0\gamma$) for which there is no obvious evidence in the $\pi^0\gamma$ data (Fig. [V.C.7]).

It is concluded that the $\pi^0\gamma$ data are not appreciably contaminated with $\pi^0\pi^\pm$ events. The excess inelastic contribution to the $\omega$ photoproduction data (compared to $\rho$ and $\phi$ production) is thus likely due to $\gamma p \to \omega X \to \pi^0\gamma X$ (X being a target excitation) and background which represents 10-15% of all events in the $\omega$ mass region.

## 5. Corrections

To calculate the $\omega$ photoproduction cross section, the observed number of $\pi^0\gamma$ events in the $\omega$ mass region needs to be corrected for:

- geometric acceptance of the apparatus and analysis cuts,
- inelastic events,
- background events (incl. $\rho \to \pi^0\gamma$), and
- branching ratio for $(\omega \to \pi^0\gamma)/(\omega \to \text{all})$

The values of the correction factors are listed in Table

(V.C.4). The acceptance correction takes into account events lost due to the geometry of the apparatus (energy dependent), the event reconstruction efficiency, and the analysis cuts used to select $\omega \rightarrow \pi^0\gamma$ candidates [see Table (V.C.1)].

The correction for the inelastic event contribution is discussed in the previous section. The number of background events is estimated for each data point and represents typically 10% to 20% of the events in the $\omega$ mass region (the higher percentage for the $E_o$= 90 GeV data). The contribution of $\pi^0\gamma$ events from $\rho \rightarrow \pi^0\gamma$ is 2-3% of the $\omega \rightarrow \pi^0\gamma$ data (branching ratio = 0.024%). The number of $\pi^0\gamma$ events attributed to $\omega$ decay is corrected for the unobserved decay modes of the $\omega$ (branching ratio = 8.8%).

The $\pi^0\gamma$ invariant mass distribution for the $E_o$= 135 GeV data are shown in Fig.(V.C.9A). Also shown are mass distributions for events which are rejected because of missing energy in the Pb glass shower counter arrays. There is no indication for lost $\omega \rightarrow \pi^0\gamma$ events due to the Pb glass energy cut.

Invariant mass distributions for events which fail $\omega \rightarrow \pi^0\gamma$ analysis cuts because of an extra photon (i.e. $\pi^0\gamma\gamma$ events) are shown in Fig.(V.C.10) for all of the data. Events with and without a track in the MWPC's are shown separately.

About 60% of the $E_o$= 200 GeV data were taken with a radiator of thickness 0.03 radiation lengths (normally

0.01 $X_o$) to compensate for the lower electron beam flux at 200 GeV (compared to $E_o$= 135 GeV and 90 GeV). The use of the thicker radiator results in a non-negligible probability for double bremsstrahlung (see Section [IV.C.5] for more details). Events with a photon of energy greater than 2 GeV incident on the C-counter are rejected. Energy in the C-counter is allowed only if it is consistent with shower leakage from a photon incident on the I-counters (the eight Pb glass counters surrounding the beam hole in G3). The correction factor for events lost due to a double bremsstrahlung photon in the C-counter is 1.06 for the $E_o$= 200 GeV data and is negligible for the $E_o$= 135 GeV and 90 GeV data.

## D: Results and Discussion

The ω photoproduction cross section is calculated using Eqn.(III.D.10) and the correction factors listed in Table (V.C.4). The results are given in Table (V.D.1) and shown in Fig.(V.D.1) together with some lower energy data. The $E_o$= 90 GeV data were divided into two photon energy bins, thus yielding two data points. The $E_o$= 135 GeV and 200 GeV data give one data point each. The quoted errors are statistical and include the uncertainty due to the correction for inelastic events. The systematic uncertainty

is estimated to be 8% for all data points and is primarily due to the geometric acceptance, including its dependence on the four-momentum transfer slope parameter. An additional systematic uncertainty is from the $\omega \to \pi^0\gamma$ branching ratio which is quoted as 8.8+/-0.5% [Particle properties, 1978].

In vector meson dominance (VMD) models, photoproduction of the $\omega$ is related to $\omega p$ elastic scattering. The $\omega p$ scattering can in turn be related to $\pi p$ elastic scattering by additive quark model relations. Specifically (see Chapter II for details),

$$\sigma(\gamma p \to \omega p) = \frac{p_\pi^2}{k_\gamma^2} \frac{\alpha\pi}{\gamma_\omega^2} \frac{1}{2}\left(\sigma^{el}(\pi^+ p) + \sigma^{el}(\pi^- p)\right) \exp(bt_{min}) \qquad (V.D.1)$$

where $\gamma_\omega$ represents the strength of the $\gamma$-$\omega$ coupling and $\alpha = e^2/\hbar c$. The threshold factor $(p_\pi/k_\gamma)^2$ is derived in Appendix B; the variables $p_\pi$ and $k_\gamma$ are the momenta of the $\pi$ and the photon, respectively, in the $\gamma p$ center of mass system. The $\exp(bt_{min})$ term accounts for the minimum four-momentum transfer ($t_{min}$) required in the $\gamma \to \omega$ transition (b = slope parameter). The threshold factor and the $\exp(bt_{min})$ term are negligible in the energy region of this experiment. Equation (V.D.1) is plotted in Fig.(V.D.1), using smoothed $\pi p$ elastic scattering data [Ayres, 1977; Foley, 1963; Ambats, 1974]. The curve is normalized to the $\omega$ cross section of this experiment. The value of the coupling constant resulting from the

normalization is

$$\frac{\gamma_\omega^2}{4\pi} = 5.5 \pm 0.4 \qquad \text{(V.D.2)}$$

and compares with 4.6+/-0.5 from colliding beam measurements [Gounaris, 1968] and 7.5+/-1.3 from photoproduction on complex nuclei [Leith, 1977]. It is interesting to see the deviation of the lower energy $\omega$ cross section from the VMD-quark model prediction in Fig. (V.D.1). The excess cross section is attributed to pion exchange in the t-channel and decreases with increasing photon energy approximately as $1/E_\gamma^2$ [Ballam, 1973; see also Chapter II].

The differential cross section for $\omega$ photoproduction is determined from a fit of the form

$$\frac{d\sigma}{dt} = A \cdot e^{bt} \qquad \text{(V.D.3)}$$

to the $\pi^0\gamma$ data in the $\omega$ mass region (t = four-momentum transfer). Events with greater than one recoil counter signal, or a recoil signal in a counter which is inconsistent with the calculated direction (azimuthal angle) of the recoil proton are not included in the fit. This eliminates most inelastic events (see Section [V.C.5]) which are expected to have a smaller slope parameter, b, than elastic events. The data are corrected for the t-dependence of the geometric acceptance. The fitted parameters A and b,

defined by Eqn. (V.D.3), are given in Table (V.D.1). The t-distributions are shown in Fig. (V.D.2) for the three E settings. Figure (V.D.3) shows the t-distribution of the combined data for elastic events. Also shown in the figure is the t-distribution for inelastic events (recoil signals inconsistent with elastic production). An inelastic cross section can not be determined due to the unknown geometric acceptance for inelastic events.

The slope of the $\gamma p \rightarrow \omega p$ (elastic) differential cross section, b, measured by this experiment is shown in Fig. (V.D.4) as a function of energy together with some lower energy data. VMD-quark model relations predict (see Appendix D)

$$b(\omega) = \frac{1}{2}\{ b(\pi^+ p) + b(\pi^- p) \} \qquad \text{(V.D.4)}$$

where $b(\pi p)$ is the slope parameter for $\pi p$ elastic scattering. Equation (V.D.4) is shown by the solid curve in Fig. (V.D.4), using smoothed $\pi p$ data [Ayres, 1977; Foley, 1963; Ambats, 1974].

The decay polar angle distribution for $\omega \rightarrow \pi^0 \gamma$ ($J^P$: $1^- \rightarrow 0^- + 1^-$) is shown in Fig. (V.D.5) for all the data. The number of events in each $\cos\theta$ bin is corrected for acceptance losses. The error bars on the data points are statistical. The angular dependence expected for s-channel helicity conservation is $1+\cos^2\theta$, shown by the curve in

Fig. (V.D.5). The data are consistent with s-channel helicity conservation, in agreement with lower energy measurements [Ballam, 1973; see also Chapter II].

In conclusion, the ω photoproduction data of this experiment extend the agreement with VMD and an additive quark model to a new range of energy. The cross section is approximately constant with energy. The t-dependence of the differential cross section is of the form $A \cdot \exp(bt)$. The γ-ω coupling constant obtained from this data, using VMD-quark model relations, is consistent with colliding beam data and A-dependence of photoproduction at lower energies. The decay angular distribution for $\omega \rightarrow \pi^0\gamma$ has the characteristics expected for s-channel helicity conservation.

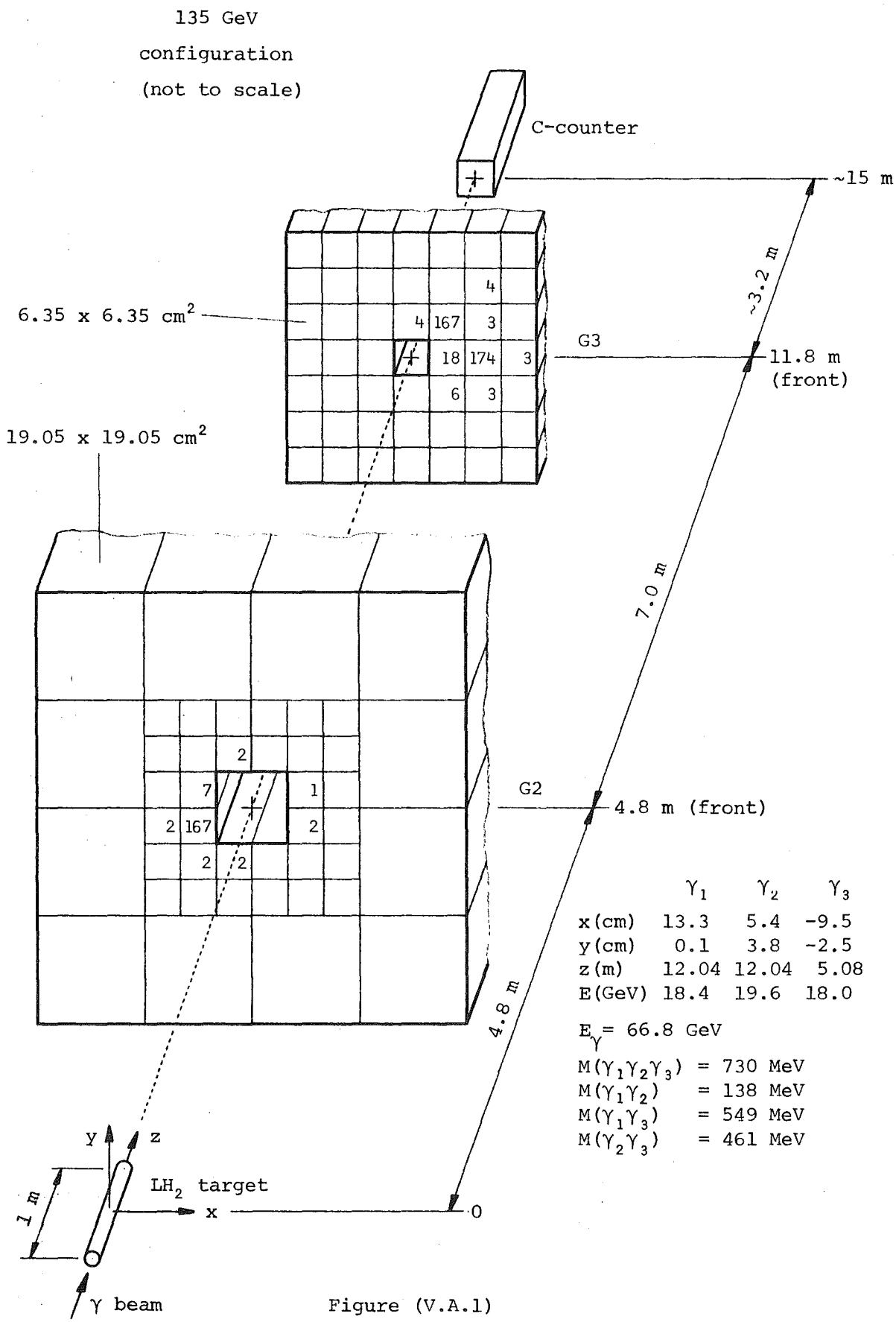


| | $\gamma_1$ | $\gamma_2$ | $\gamma_3$ |
|---|---|---|---|
| x(cm) | 13.3 | 5.4 | -9.5 |
| y(cm) | 0.1 | 3.8 | -2.5 |
| z(m) | 12.04 | 12.04 | 5.08 |
| E(GeV) | 18.4 | 19.6 | 18.0 |

$E_\gamma$ = 66.8 GeV

$M(\gamma_1\gamma_2\gamma_3)$ = 730 MeV
$M(\gamma_1\gamma_2)$ = 138 MeV
$M(\gamma_1\gamma_3)$ = 549 MeV
$M(\gamma_2\gamma_3)$ = 461 MeV

Figure (V.A.1)

Schematic of Pb glass arrays G3 and G2

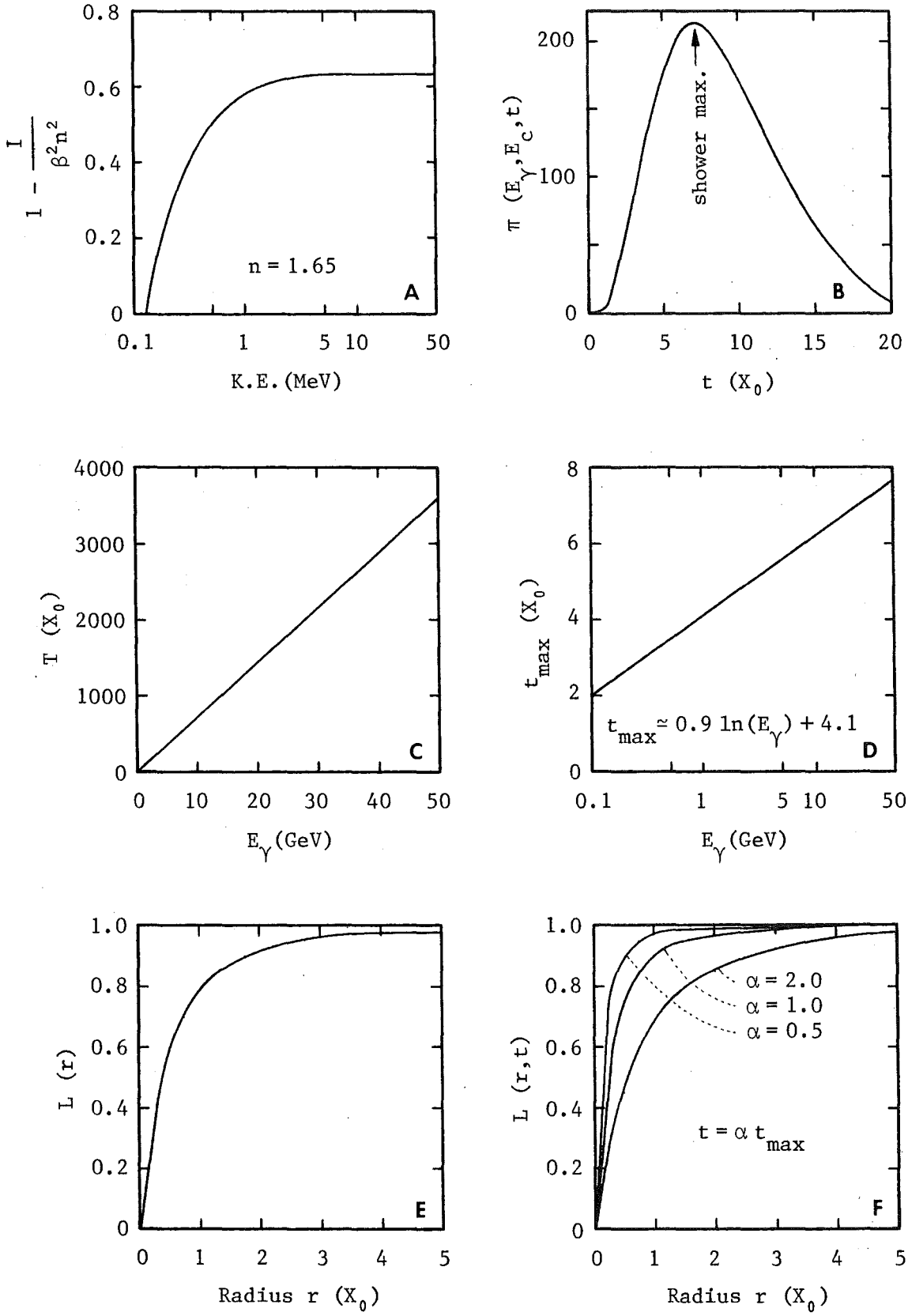


($X_0$= 2.84 cm for SF2 Pb glass)

Figure (V.C.1) contd. next page

Figure (V.C.1) contd.

A: Energy dependent factor $1-(1/\beta n)^2$ as a function of kinetic energy for $n = 1.65$ (refractive index for SF2 Pb glass).

B: Charged particle density, $\pi(E_\gamma, E_c, t)$, as a function of depth, t.

C: Total path length, $T(E_\gamma)$, of charged particles versus energy of incident photon.

D: Position of shower maximum versus energy of incident photon.

E: Lateral spread of a 30 GeV shower contained in an infinitely long Pb glass block.

F: Lateral spread of a 30 GeV shower as a function of depth, t.

Data shown in figures B - F are from Monte Carlo generated showers (Longo, 1975).

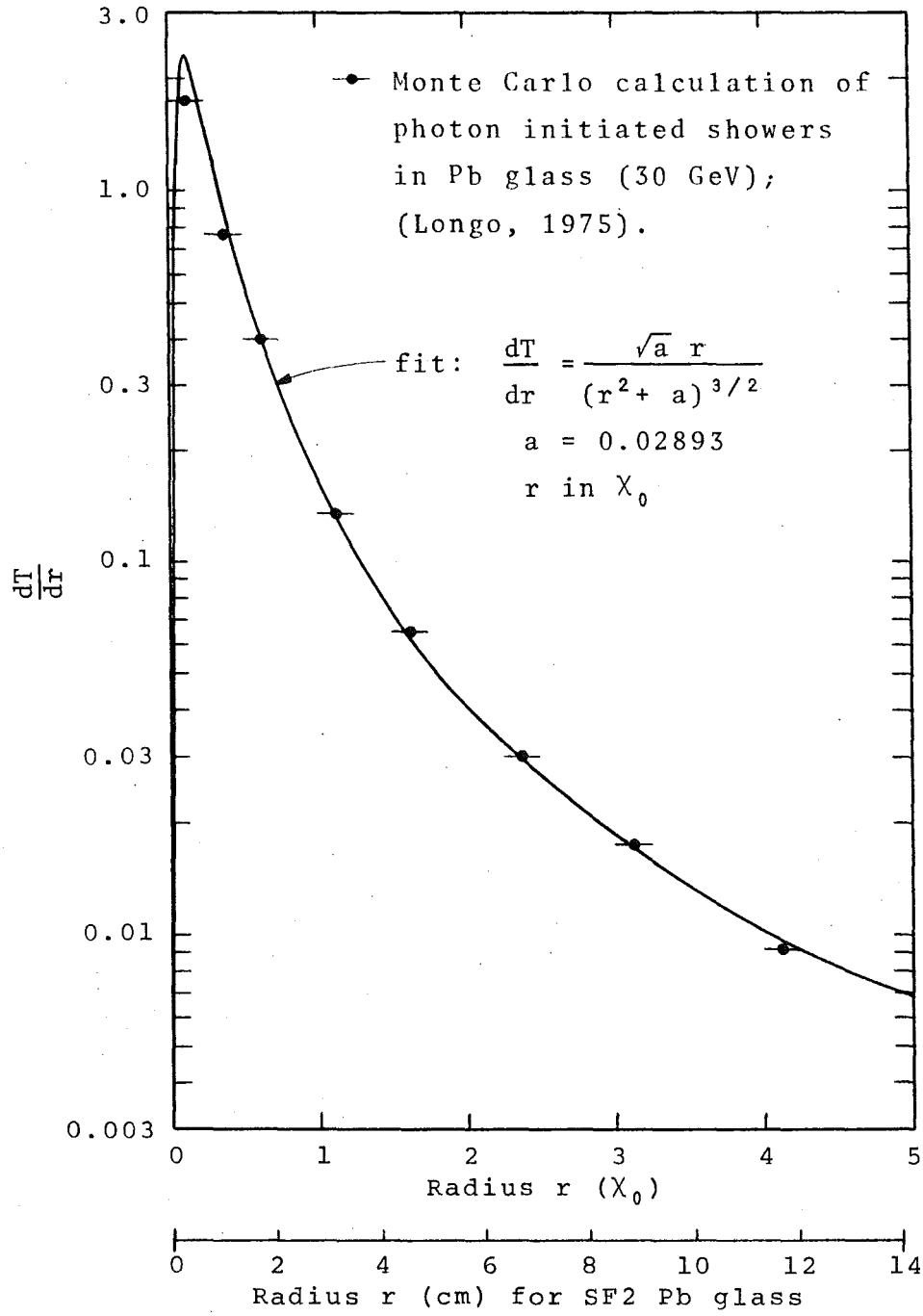


Figure (V.C.2) Radial dependence of dT/dr.

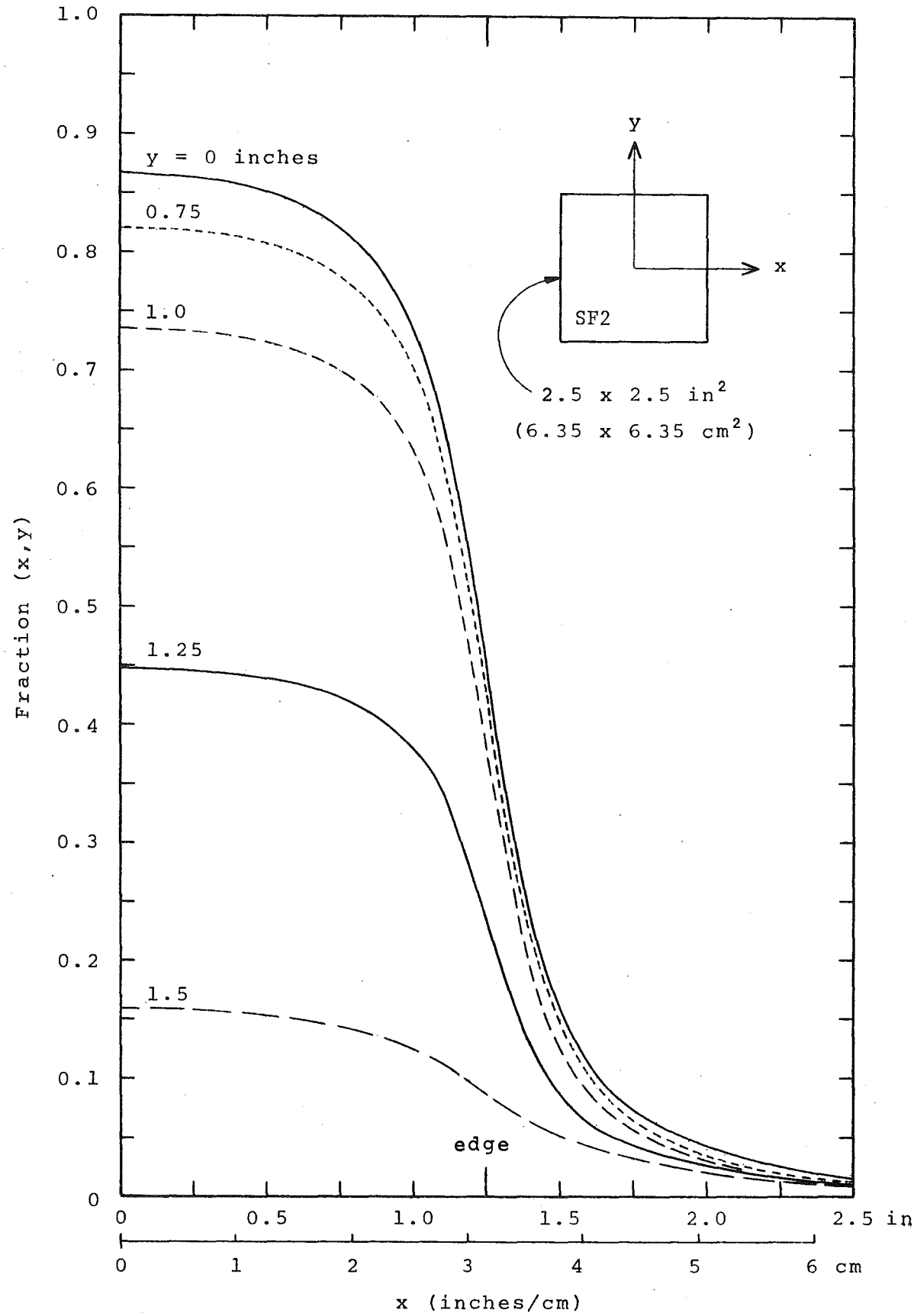


Figure (V.C.3) Fraction of the total shower energy contained in a Pb glass block as a function of shower position.

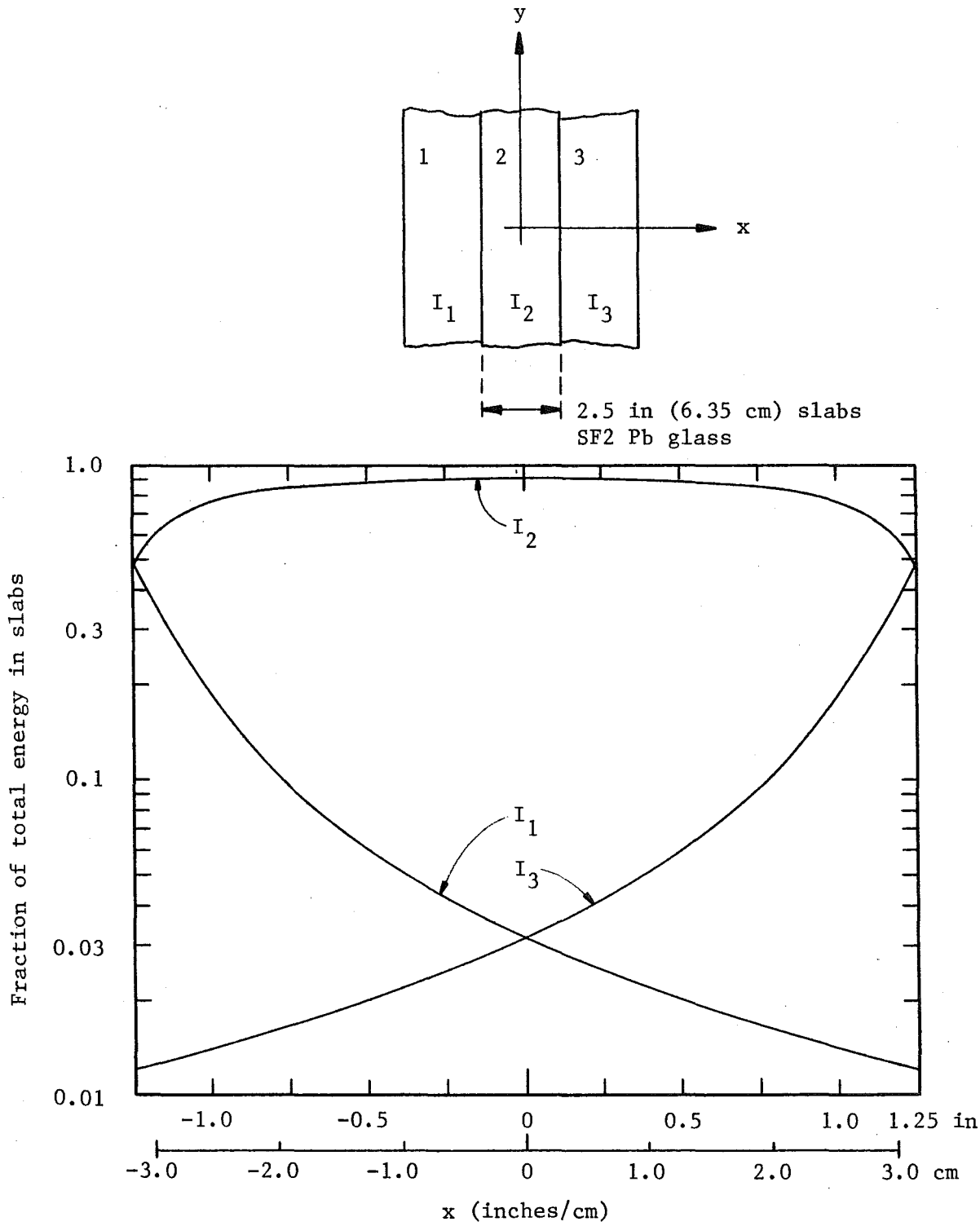


Figure (V.C.4) Fraction of the total shower energy contained in a slab of Pb glass as a function of shower position.

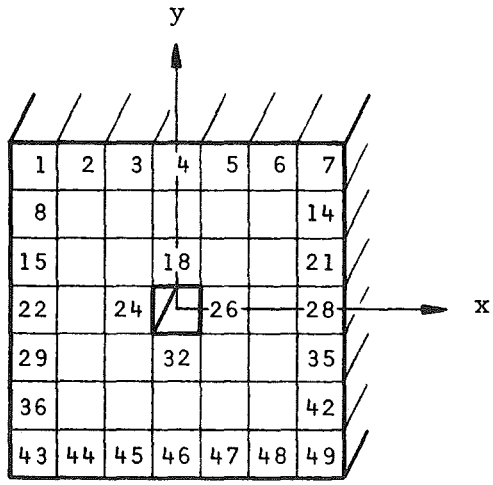


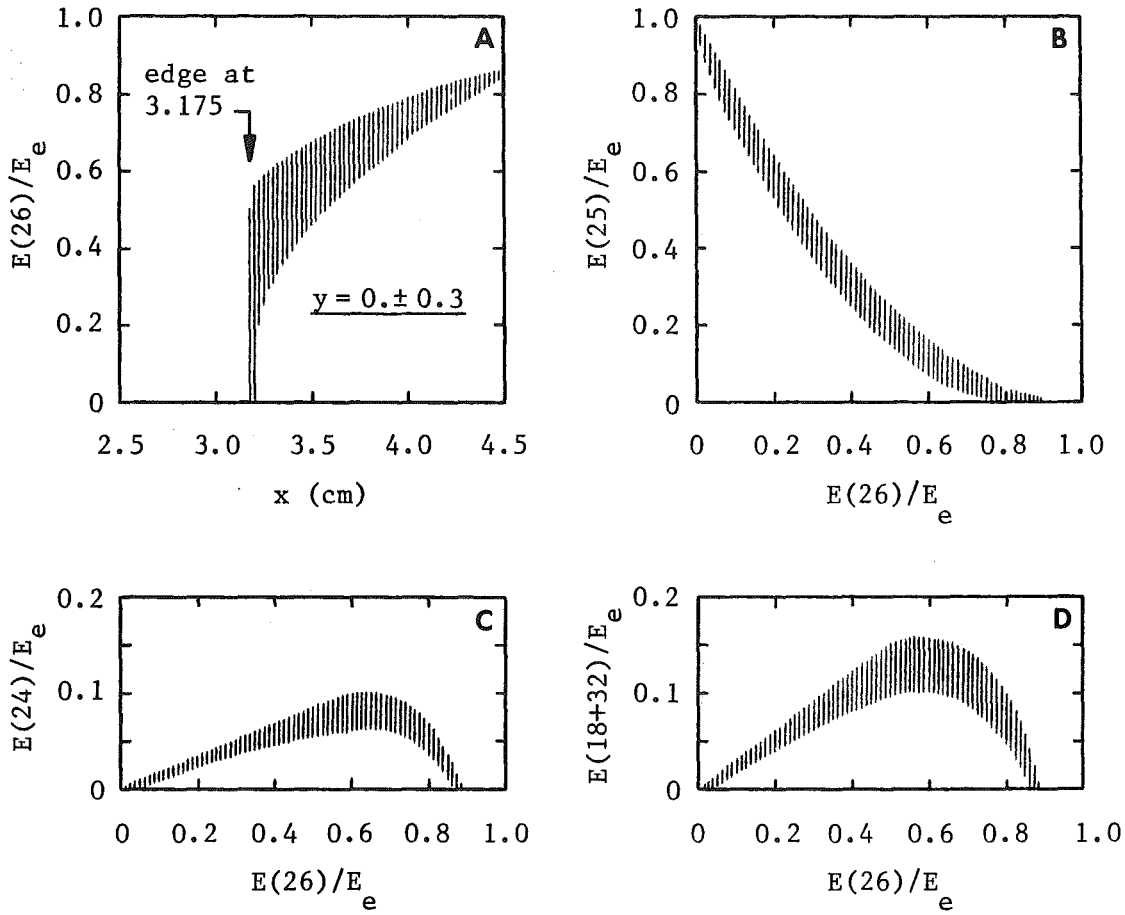


Figure (V.C.5) contd.

Figure (V.C.5) contd.

Shower data obtained with $E_e = 90$ GeV electrons incident on I-counter number 26. Energies shown in the figure are normalized by $E_e$.

A: Energy in counter 26 as a function of shower position (the coordinates of the incident electron determined with MWPC's).

B: Energy lost through the hole in G3, denoted E(25), versus energy in counter 26.

C, D: Shower energy transferred across the hole in G3 versus energy in counter 26.

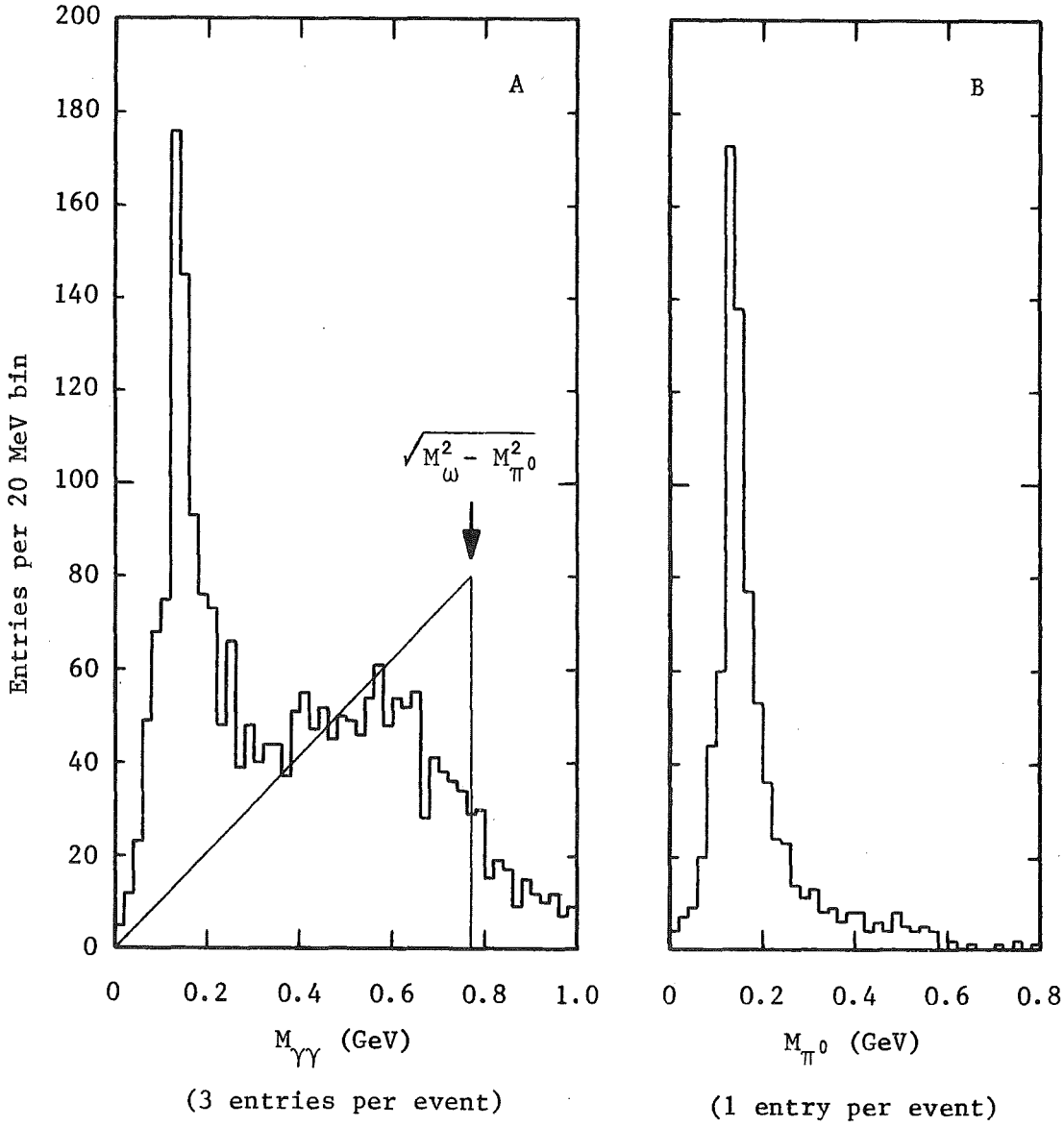


Figure (V.C.6) Two-photon invariant mass spectrum for $\omega \to \pi^0\gamma$ candidates (all the data). Each event gives three $M_{\gamma\gamma}$ combinations, shown in (A). In (B) only the combination nearest the $\pi^0$ mass (one per event) is shown.

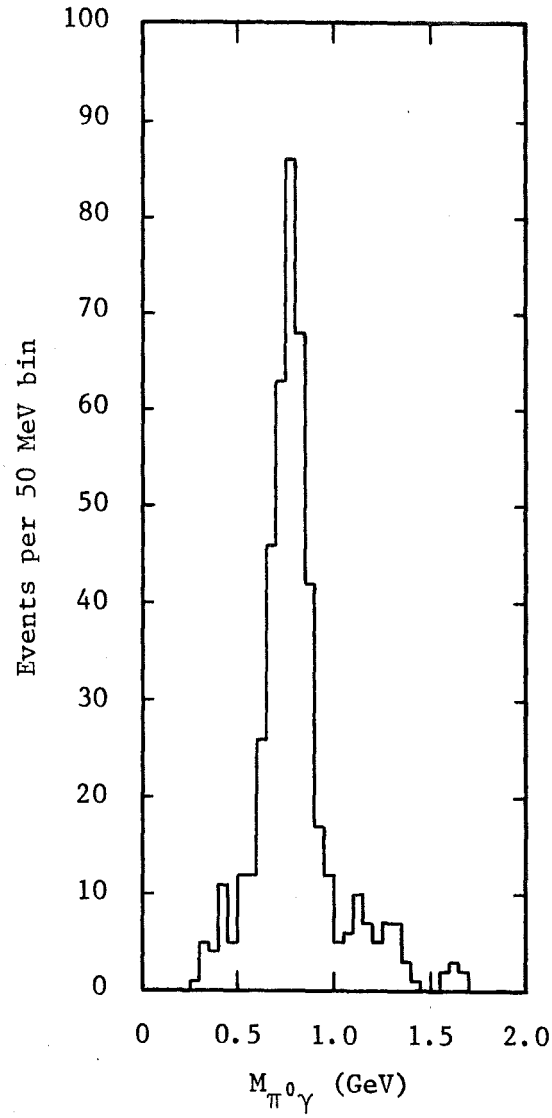


Figure (V.C.7) Three-photon invariant mass spectrum consistent with $\omega \to \pi^0\gamma$ (most of the data).

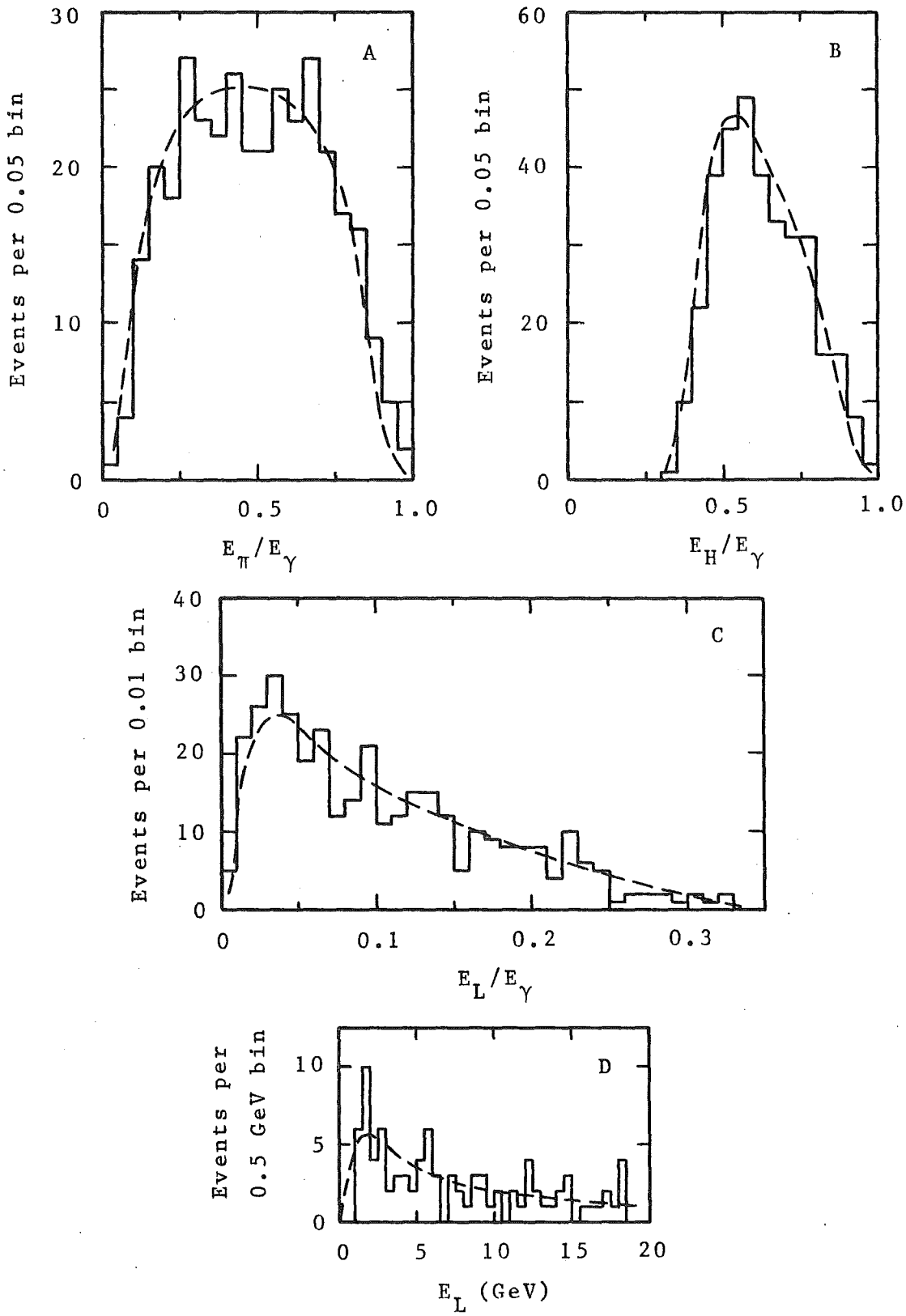


Figure (V.C.8) contd.

Figure (V.C.8) contd.

Energy distributions for $\omega \rightarrow \pi^0\gamma$ candidates in the $\omega$ mass region.

Figures A, B, C: all the data.

Figure D: $E_0 = 135$ GeV data.

$E_\gamma$ = tagged photon energy

$E_\pi$ = $\pi^0$ energy

$E_H$ = energy of highest energy photon

$E_L$ = energy of lowest energy photon (>1 GeV)

The dashed curves are Monte Carlo generated distributions normalized to the data.

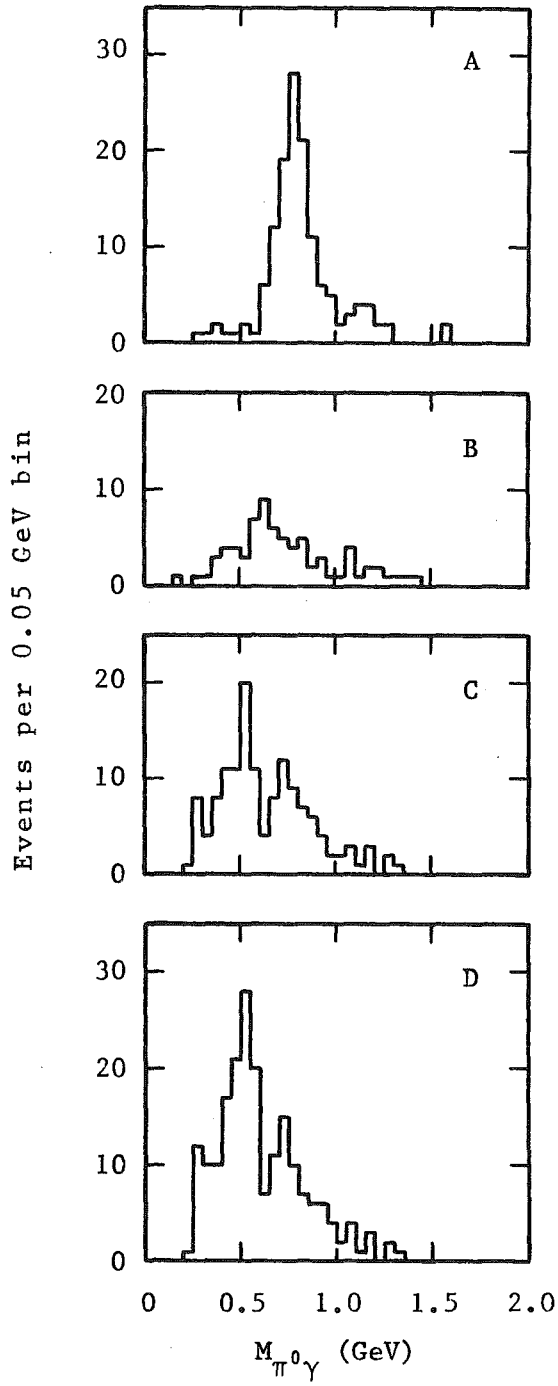


Figure (V.C.9) contd.

Figure (V.C.9) contd.

Mass distribution for $\pi^0\gamma$ events ($E_0 = 135$ GeV data). Events in (A) are good $\omega \to \pi^0\gamma$ candidates (survive all analysis cuts). Events in (B, C, D) are rejected because of missing energy in Pb glass arrays.

| | | | | |
|---|---|---|---|---|
| A: | $0.9 < E_G/E_\gamma$ | $E_{S3}/E_\gamma < 0.03$ | 136( 24) | events |
| B: | $0.8 < E_G/E_\gamma < 0.9$ | as above | 73( 31) | " |
| C: | $0.6 < E_G/E_\gamma < 0.8$ | as above | 141( 72) | " |
| D: | as above | no $E_{S3}$ cut | 198(104) | " |

$E_\gamma$ = tagged photon energy
$E_G$ = energy in Pb glass arrays
$E_{S3}$ = energy in S3

The number of events which have a MWPC track is given in brackets following the total (0 and 1 track) number of events.

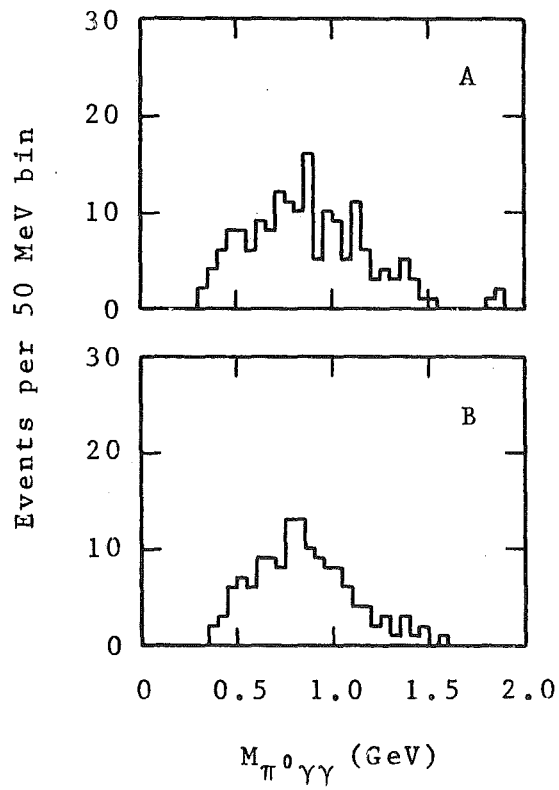


A: No MWPC tracks (169 evts.)

B: One MWPC track (138 evts.)

Figure (V.C.10) Mass distribution for events which fail $\omega \to \pi^0\gamma$ analysis cuts because of an extra photon (all the data).

Figure (V.D.1)

Energy dependence of the ω photoproduction cross section. The curve is a VMD-quark model prediction given by Eqn.(V.D.1) and normalized to the data of this experiment.

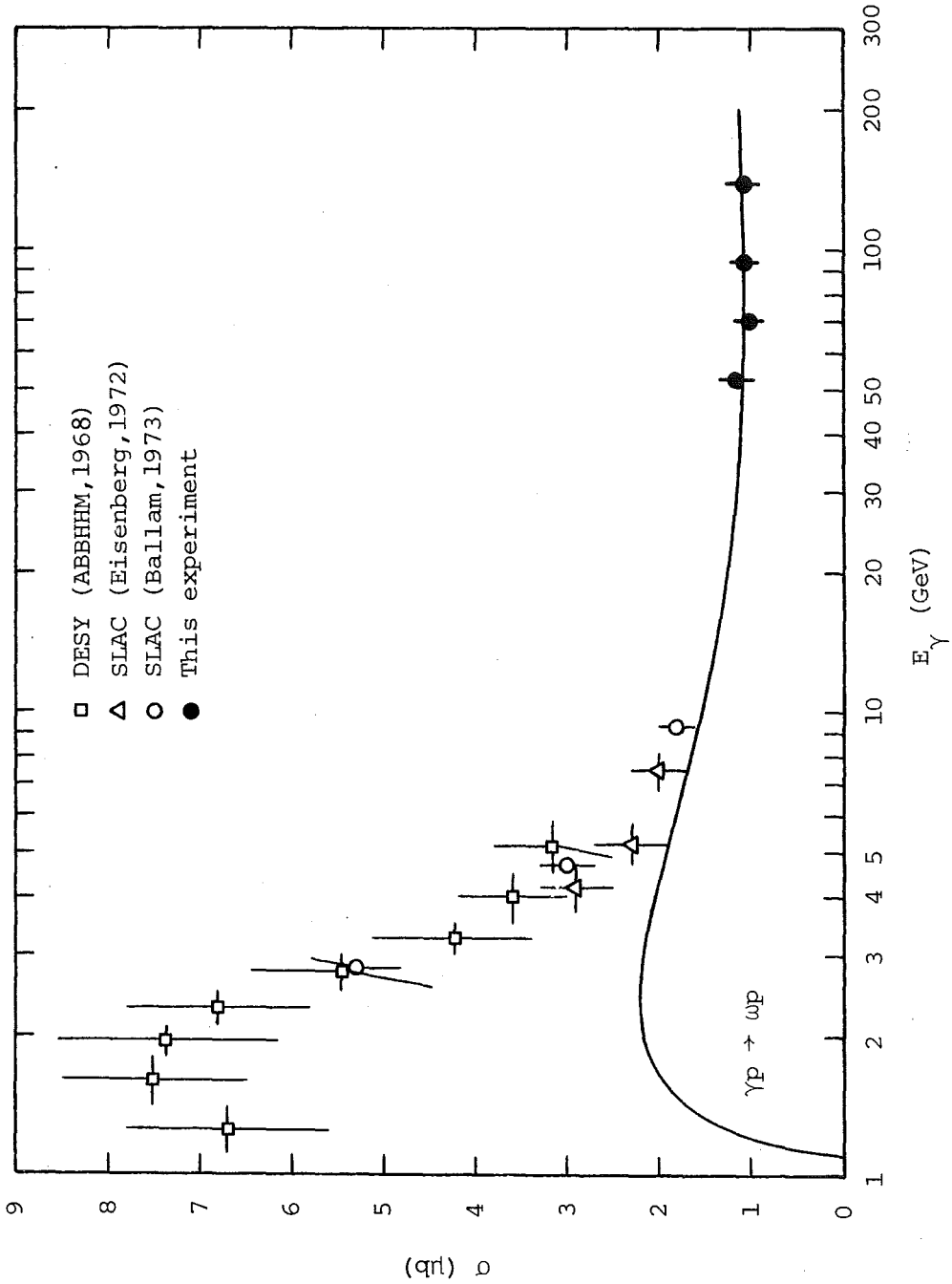

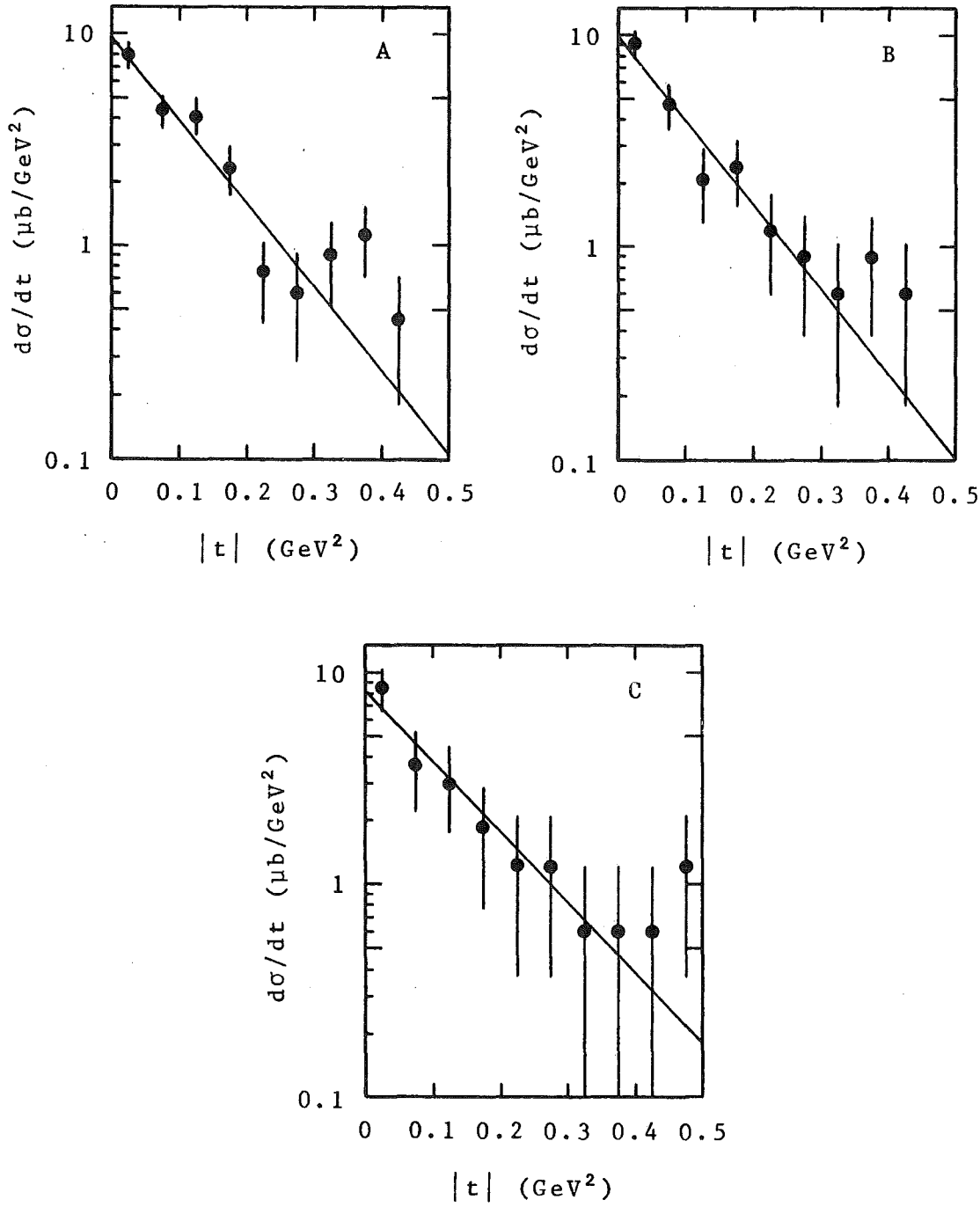


Figure (V.D.2) Differential cross section for ω photoproduction (elastic events).
A: $E_0$= 90 GeV data, B: $E_0$= 135 GeV data,
C: $E_0$= 200 GeV data.

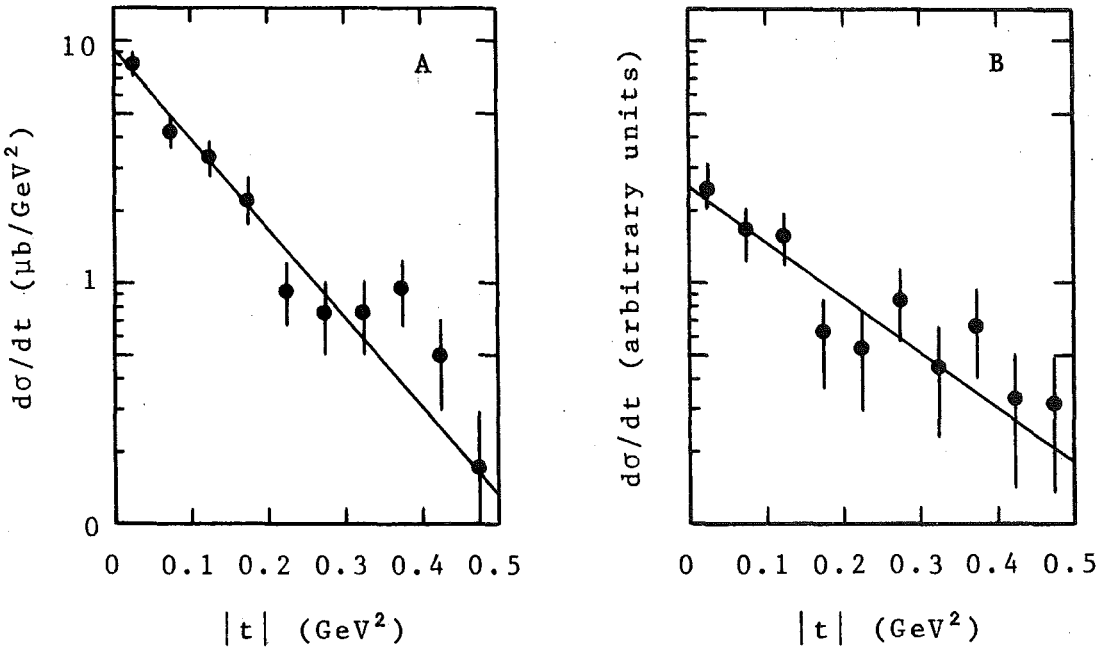


Figure (V.D.3) Differential cross section for ω photoproduction (all the data).
A: elastic events,
B: inelastic events.

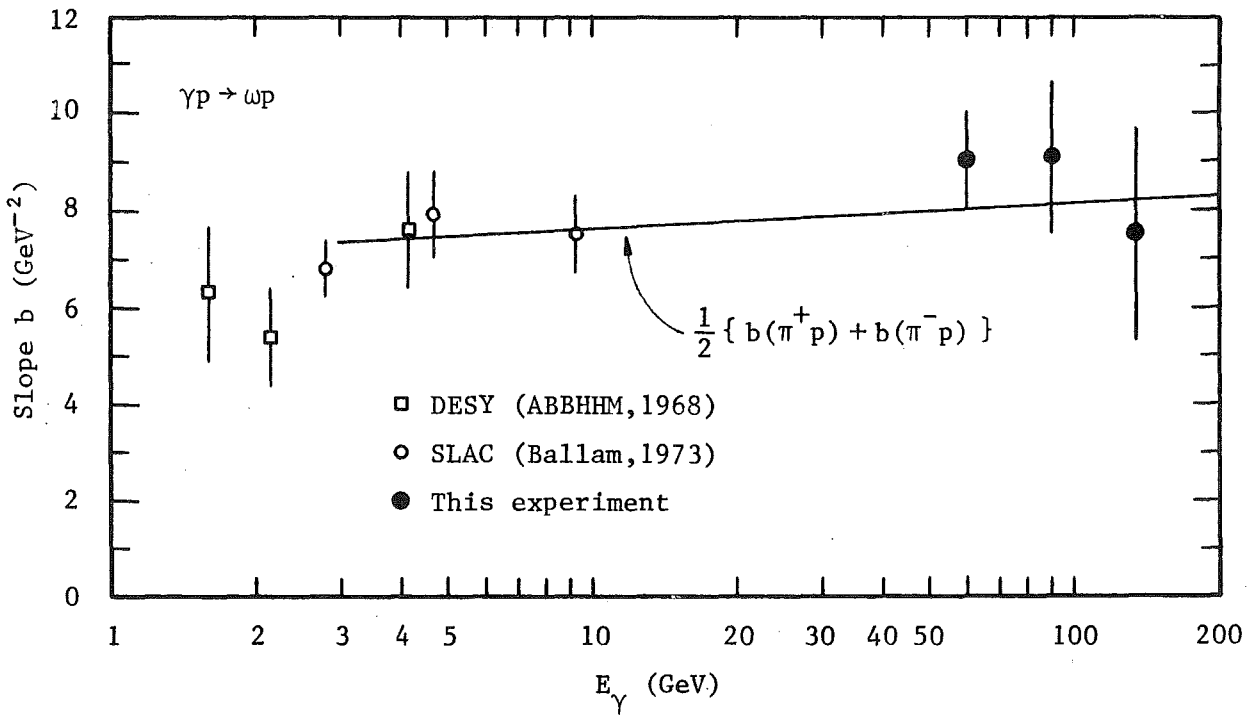


Figure (V.D.4) The slope of the $\gamma p \to \omega p$ differential cross section as a function of energy. The solid curve is the average slope for $\pi^+ p$ and $\pi^- p$ elastic scattering.

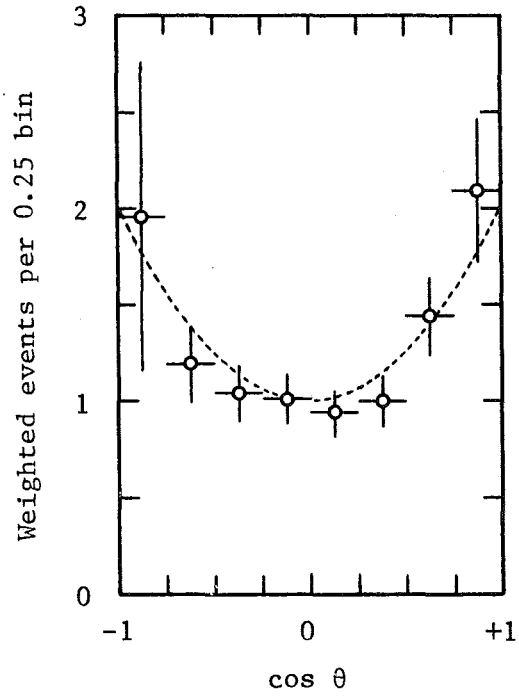


Figure (V.D.5) Decay polar angle distribution for $\omega \to \pi^0\gamma$ (all the data). The number of events in each bin is corrected for acceptance losses. The error bars on the data points are statistical. The angular dependence expected for s-channel helicity conservation is $1 + \cos^2\theta$ (shown by the dashed curve).

Table (V.B.1)

Tagged Photon and TgH Trigger Totals

(for $\omega$ data)

| $E_0$(GeV) | Z2(m) | Z3(m) | $\langle E_\gamma \rangle$ | Tg($\times 10^6$) | TgH($\times 10^3$) |
|---|---|---|---|---|---|
| 90 | 4.5 | 10.3 | 60 | 593 | 476 |
| 90* | 5.1 | 10.3 | 60 | 298 | 248 |
| 135 | 5.1 | 12.0 | 90 | 642 | 491 |
| 200 | 7.3 | 18.3 | 133 | 287 | 227 |

* Apparatus with H2 in the $E_0 = 135$ GeV position.

$E_0$: Electron beam energy in GeV.

Z2: Distance from target to G2 Pb glass array in meters.

Z3: Distance from target to G3 Pb glass array in meters.

$\langle E_\gamma \rangle$: Average photon energy in GeV ($.50 < E_\gamma / E_0 < .92$).

Tg: Number of tagged photons in millions.

TgH: Number of hadronic triggers in thousands.

Note: Z2 and Z3 measure 25 cm into the Pb glass (position of shower maximum)

Table (V.C.1)

Analysis Cuts ($\omega$ Data)

| | |
|---|---|
| | (all events are trigger type = TgH) |
| 1 | Pb glass energy: $(G3I + G2)/E_\gamma > 0.90$ |
| 2 | Exactly three photons in the Pb glass arrays |
| 3 | Low energy cut for photons: $E > 1.0$ GeV |
| 4 | At most one track in the MWPC's |
| 5 | S1 "off" |
| 6 | Energy in S2, S3 and K consistent with shower leakage from G3 and G2 |
| 7 | $\pi^0$ mass cut for $\omega \to \pi^0\gamma$ candidates |

Table (V.C.2) Shower Table

Block size: $(6.35\ \text{cm})^2$; $(2.5\ \text{in})^2$

Pb glass type: SF2

Coefficient a = 0.02893

Grid size: 0.635 cm ; 0.25 in

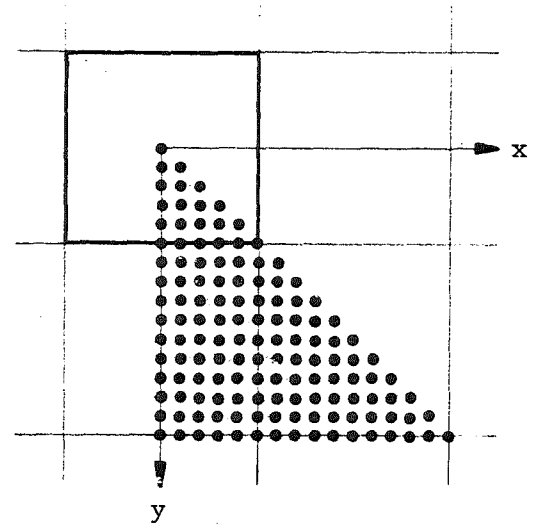


| | | | | | | | | | | | | | | | |
|---|---|---|---|---|---|---|---|---|---|---|---|---|---|---|---|
| .8652 | | | | | | | | | | | | | | | |
| .8618 | .8584 | | | | | | | | | | | | | | |
| .8496 | .8464 | .8350 | | | | | | | | | | | | | |
| .8195 | .8166 | .8062 | .7797 | | | | | | | | | | | | |
| .7346 | .7322 | .7234 | .7011 | .6334 | | | | | | | | | | | |
| .4466 | .4447 | .4381 | .4221 | .3784 | .2330 | block edge | | | | | | | | | |
| .1582 | .1569 | .1524 | .1429 | .1232 | .0874 | .0514 | | | | | | | | | |
| .0724 | .0715 | .0687 | .0634 | .0548 | .0431 | .0312 | .0221 | | | | | | | | |
| .0405 | .0400 | .0383 | .0353 | .0311 | .0259 | .0206 | .0160 | .0123 | | | | | | | |
| .0254 | .0250 | .0240 | .0223 | .0200 | .0173 | .0145 | .0118 | .0096 | .0078 | | | | | | |
| .0171 | .0168 | .0162 | .0152 | .0139 | .0123 | .0106 | .0090 | .0076 | .0064 | .0053 | | | | | |
| .0121 | .0119 | .0116 | .0109 | .0101 | .0091 | .0081 | .0070 | .0061 | .0052 | .0045 | .0038 | | | | |
| .0089 | .0088 | .0086 | .0081 | .0076 | .0070 | .0063 | .0056 | .0049 | .0043 | .0038 | .0033 | .0028 | | | |
| .0068 | .0067 | .0065 | .0062 | .0059 | .0055 | .0050 | .0045 | .0040 | .0036 | .0032 | .0028 | .0025 | .0022 | | |
| .0053 | .0052 | .0051 | .0049 | .0047 | .0044 | .0040 | .0037 | .0034 | .0030 | .0027 | .0024 | .0022 | .0019 | .0017 | |
| .0042 | .0042 | .0041 | .0039 | .0038 | .0035 | .0033 | .0031 | .0028 | .0026 | .0023 | .0021 | .0019 | .0017 | .0015 | .0014 |

Table (V.C.3)

Fraction of events with 0, 1 and >1 recoil counter signals for ω events

| | recoils | | |
|---|---|---|---|
| | 0 | 1 | >1 |
| A = Elastic events (Monte Carlo) | 0.71 | 0.28 | 0.01 |
| B = Inelastic evts. (calculated) | 0.02 | 0.23 | 0.75 |
| C = Data (elastic + inelastic) | 0.57 ±.04 | 0.22 ±.03 | 0.21 ±.03 |
| D = Fit to data | 0.54 | 0.26 | 0.20 |
| E = Inelastic fraction | 0.256 ± 0.035 | | |

Error on C (data) is statistical.

$D = (1-E)\cdot A + E\cdot B$ is fit to C for the recoil = 0, 1 and >1 fractions with E the only adjustable parameter.

Table (V.C.4)

Correction factors ($\omega$ data)

| | | |
|---|---|---|
| Geometric acceptance and analysis cuts (*): | (33%) | 3.0 ±.2 |
| Inelastic events: | (25.6%) | 0.744±.035 |
| $\rho \to \pi^0\gamma$: | (∿2.5%) | 0.98 |
| Branching ratio $(\omega \to \pi^0\gamma)/(\omega \to \text{all})$: | (8.8%) | 11.4 |

(*) includes: Pb glass energy cut,
low energy cut for photons,
events lost due to >1 MWPC tracks, and
$\pi^0$ mass cut.

Table (V.D.1)

Results for $\gamma p \to \omega p$

| | | | | |
|---|---|---|---|---|
| $E_\gamma$ (GeV) | 53±7 | 71±11 | 95±27 | 140±40 |
| s ($GeV^2$) | 100.3 | 134.1 | 179.2 | 263.6 |
| $\sigma_{\gamma p \to \omega p}$ (μb) | 1.15±0.17 | 1.02±0.15 | 1.08±0.12 | 1.08±0.18 |
| | $E_\gamma = 60 \pm {}^{22}_{14}$ | | | |
| $\left.\frac{d\sigma}{dt}\right\|_{t=0}$ ($\mu b/GeV^2$) | 9.70±1.30 | | 9.82±2.05 | 8.10±2.51 |
| b ($GeV^{-2}$) | 9.05±1.00 | | 9.11±1.66 | 7.52±2.14 |

Combined data:

$$\sigma(\mu b) = 1.08 \pm 0.08$$

$$d\sigma/dt(\mu b/GeV^2) = 9.06 \pm 0.95$$

$$b\ (GeV^{-2}) = 8.42 \pm 0.74$$

$$\frac{\gamma_\omega^2}{4\pi} = 5.49 \pm 0.39$$

(fit to differential cross section is of the form $d\sigma/dt = A \cdot e^{bt}$ )

# CHAPTER VI SUMMARY

The elastic rho ($\rho$), omega ($\omega$) and phi ($\phi$) photoproduction cross sections on protons have been measured in the photon energy range 30 to 180 GeV. The data were taken at the Tagged Photon Facility of Fermilab with a particle detection apparatus consisting of multilayer lead-iron-scintillator hadrometers, lead glass shower counter arrays, and multiwire proportional chambers. The observed decay modes were

$$\rho \to \pi^+\pi^- \qquad \omega \to \pi^0\gamma \qquad \phi \to K^+K^-$$

The energy dependences of the $\rho$, $\omega$ and $\phi$ photoproduction cross sections agree well with predictions made by using vector meson dominance (VMD) and an additive quark model. The $\rho$ and $\omega$ cross sections are approximately constant with photon energy while the $\phi$ cross section rises from 0.5 μb to 0.7 μb with increasing energy. Average values for the cross sections measured by this experiment are

$$(\gamma p \to \rho p) \simeq 9.27 \pm 0.17 \ \mu b$$

$$(\gamma p \to \omega p) \simeq 1.08 \pm 0.08 \ \mu b$$

$$(\gamma p \to \phi p) \simeq 0.635 \pm 0.024 \ \mu b$$

The cross sections are corrected for the contribution of inelastic events which amount to 13% for the $\rho$, 26% for the $\omega$, and 18% for the $\phi$. The relative ratio of the (average) $\rho$, $\omega$ and $\phi$ cross sections is given by

$$\sigma(\rho) : \sigma(\omega) : \sigma(\phi) = 9 : (1.05 \pm 0.08) : (0.617 \pm 0.026)$$

(remember that $\sigma(\phi)$ rises with energy). This can be compared with the ratio of the $\gamma \to \rho, \omega, \phi$ coupling strengths as calculated from the measured leptonic decay widths in $e^+e^-$ colliding beam experiments [Leith, 1978],

$$(1/\gamma_\rho^2) : (1/\gamma_\omega^2) : (1/\gamma_\phi^2) = 9 : (1.25 \pm 0.1) : (2.04 \pm 0.2)$$

and the SU(6) prediction,

$$9 : 1 : 2$$

The $\gamma$-V (V= $\rho$, $\omega$, $\phi$) coupling constants, obtained from a normalization of hadron elastic scattering cross sections to the photoproduction data of this experiment (using VMD and an additive quark model) are given by

$$(\gamma_\rho^2/4\pi) = 0.65 \pm 0.03, \quad (\gamma_\omega^2/4\pi) = 5.5 \pm 0.4$$

$$(\gamma_\phi^2/4\pi) = 4.7 \pm 0.3$$

The values are consistent with previous measurements at lower photon energies.

The differential cross section, $d\sigma/dt$ (t = four momentum transfer squared), has been measured for $\omega$ photoproduction. A fit to the combined data of the form

$$d\sigma/dt(\gamma p \to \omega p) = A \cdot \exp(bt)$$

gives

$$A = 9.06 \pm 0.95 \ \mu b/GeV^2$$

$$b = 8.42 \pm 0.74 \ GeV^{-2}$$

The observed decay angular distribution for $\omega \to \pi^0\gamma$ is consistent with a $1+\cos^2\theta$ polar angle dependence as expected for s-channel helicity conservation.

# NOTES

# APPENDIX A

## DERIVATION OF Δ (TRACK SEPARATION)

Center of mass system:

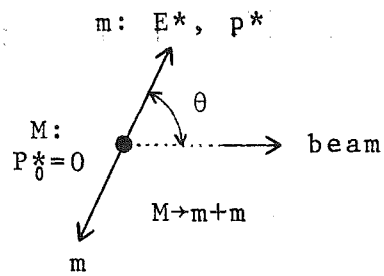


Laboratory system:

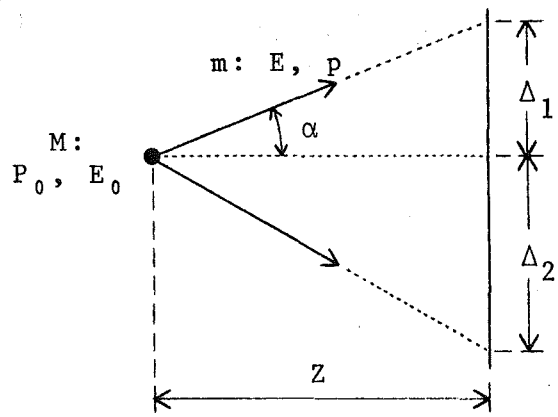


The lab system and center of mass (c.m.) system momenta are related by

$$p_{\perp} = |\bar{p}^*| \sin\theta$$
$$p_{||} = \gamma(p^*_{||} + \beta E^*) \qquad \text{A1}$$

where

$$p_{\perp} = |\bar{p}| \sin\alpha$$
$$p_{||} = |\bar{p}| \cos\alpha$$
$$p^*_{||} = |\bar{p}^*| \cos\theta$$
$$|\bar{p}^*| = \{(M/2)^2 - m^2\}^{1/2}$$
$$\gamma = E_0/M$$
$$\beta = P_0/E_0$$

The lab system and c.m. system decay angles are therefore related by

$$\tan\alpha = \frac{P_{\perp}}{P_{\parallel}} = \frac{\{(M/2)^2 - m^2\}^{1/2}\sin\theta}{(E_0/M)\{\{(M/2)^2 - m^2\}^{1/2}\cos\theta + (P_0/E_0)(M/2)\}}$$

or, after rearranging

$$\tan\alpha = \frac{M\sin\theta}{E_0\cos\theta + P_0/\{1 - (2m/M)^2\}^{1/2}} \qquad \text{A2}$$

From Eqn.(A2), as expected

$$\alpha = 0 \text{ for } 2m = M$$

$$\alpha < 90^0 \text{ for } m = 0 \text{ if } \cos\theta > -\beta$$

and in general

$$\alpha < 90^0 \text{ if } \cos\theta > -\frac{\beta}{\{1 - (2m/M)^2\}^{1/2}} \qquad \text{A3}$$

<u>For $\alpha < 90^0$:</u> The track separation is given by

$$\Delta = \Delta_1 + \Delta_2 = Z(\tan\alpha_1 + \tan\alpha_2) \qquad \text{A4}$$

$\sin\theta_1 = \sin\theta_2$ and $\cos\theta_1 = -\cos\theta_2$. Hence from Eqns.(A2) and (A4)

$$\Delta = \frac{2ZMP_0\{1 - (2m/M)^2\}^{1/2}\sin\theta}{P_0^2 - E_0^2\{1 - (2m/M)^2\}\cos^2\theta} \qquad \text{A5}$$

For $P_0 \approx E_0$

$$\Delta = \frac{2ZM\ \{1 - (2m/M)^2\}^{1/2}\sin\theta}{E_0\ \{\sin^2\theta + (2m/M)^2\cos^2\theta\}} \qquad \text{A6}$$

With M=1.0197 GeV and m=0.49371 GeV ($\phi \rightarrow K^+K^-$) Eqn.(A6) yields

$$\Delta_\phi = \frac{0.50908\ Z\ \sin\theta}{E_0\ \{\sin^2\theta + 0.93769\ \cos^2\theta\}} \qquad \text{A7}$$

and for symmetric decay ($\theta=90^0$)

$$\Delta_\phi = (\Delta_\phi)_{max} = \frac{0.50908\ Z}{E_0} \qquad \text{A8}$$

# APPENDIX B

## DERIVATION OF THE THRESHOLD FACTOR $p_\phi^2/k_\gamma^2$

The cross section for the reaction

$$a + b \rightarrow 1 + 2 \qquad \text{B1}$$

can be written as

$$\sigma_{\alpha\beta} = \frac{1}{J} \int\int d(\text{LIPS}) \sum_{\alpha}\sum_{\beta} |\langle\beta|T|\alpha\rangle|^2 \qquad \text{B2}$$

where

J = flux factor, i.e. the number of incoming particles per unit time and unit area.

d(LIPS) = Lorentz Invariant Phase Space factor.

$|\langle\beta|T|\alpha\rangle|^2$ = transition probability per unit space-time for the transition $\alpha\rightarrow\beta$, the initial and final state, respectively.

$\sum_\alpha$ and $\sum_\beta$ denote averaging over initial spin states and summing over final spin states.

To obtain an invariant expression for the flux factor we first consider a frame in which the two colliding particles are moving towards each other. In that special frame the flux factor is given by

$$J = \frac{v_a + v_b}{V_a V_b} = \frac{|\bar{p}_a| E_b + |\bar{p}_b| E_a}{V_a V_b E_a E_b} \qquad \text{B3}$$

where $v_i = |\bar{p}_i|/E_i$ is the magnitude of the velocity of

particle i with momentum $\overline{p}_i$ and energy $E_i$. The normalization volume is $V_i$. The numerator of Eqn.(B3) can be written as

$$|\overline{p}_a|E_b + |\overline{p}_b|E_a = \{(p_a \cdot p_b)^2 - m_a^2 m_b^2\}^{1/2} \qquad \text{B4}$$

where $p_i$ is the four-momentum of particle i. Therefore, if the normalization volume is chosen as $V_i = 1/E_i$, the invariant flux factor in an arbitrary frame is

$$\begin{aligned} J &= \{(p_a \cdot p_b)^2 - m_a^2 m_b^2\}^{1/2} \\ &= m_b |\overline{p}_a| \quad \text{in the lab frame } (\overline{p}_b = 0) \\ &= \sqrt{s}\ |\overline{p}_a^*| \quad \text{in the c.m. frame} \end{aligned} \qquad \text{B5}$$

The Lorentz invariant phase space factor is given by

$$d(\text{LIPS}) = \frac{1}{(2\pi)^6} \frac{d\overline{p}_1 d\overline{p}_2}{4E_1E_2} \delta^4(p_\alpha - p_\beta) \qquad \text{B6}$$

where the four-dimensional Dirac delta function ensures energy and momentum conservation between initial and final states, $\alpha$ and $\beta$. In the center of mass system, for which $\overline{p}_1^* = -\overline{p}_2^*$,

$$\begin{aligned} \iint d\overline{p}_1^* d\overline{p}_2^*\ \delta^4(p_\alpha - p_\beta) &= \iint d\overline{p}_1^* d\overline{p}_2^*\ \delta^3(\overline{p}_1^* + \overline{p}_2^*)\ \delta(E_\alpha^* - E_\beta^*) \\ &= \int d\overline{p}_1^*\ \delta(E_\alpha^* - E_\beta^*) \end{aligned} \qquad \text{B7}$$

The cross section, Eqn.(B2), can now be written as

$$\sigma_{\alpha\beta} = \frac{1}{\sqrt{s}\ |\overline{p}_a^*|\ (2\pi)^6} \int \frac{d\overline{p}_1^*}{4E_1^*E_2^*} \delta(E_\alpha - E_\beta) \overline{\sum_{\alpha}}\sum_{\beta} |\langle\beta|T|\alpha\rangle|^2 \qquad \text{B8}$$

We put

$$d\bar{p} = dp_x dp_y dp_z = |\bar{p}|^2 d|\bar{p}| \sin\theta \, d\theta \, d\phi$$
$$= |\bar{p}| \, E \, dE \sin\theta \, d\theta \, d\phi \qquad \text{B9}$$

The invariant momentum transfer squared between particles a and 1 is

$$t_{a1} = t = (p_a - p_1)^2 = m_a^2 + m_1^2 + 2(E_a E_1 - \bar{p}_a \cdot \bar{p}_1)$$

and

$$dt = -2|\bar{p}_a||\bar{p}_1| \, d\cos\theta = 2|\bar{p}_a||\bar{p}_1| \sin\theta \, d\theta \qquad \text{B10}$$

Hence

$$d\bar{p}_1^* = \frac{E_1^* dE_1^* d\phi_1^* dt}{2 \, |\bar{p}_a^*|} \qquad \text{B11}$$

and the cross section, Eqn.(B8), becomes

$$\sigma_{\alpha\beta} = \frac{1}{8\sqrt{s} \, |\bar{p}_a^*|^2 (2\pi)^5} \int \frac{dE_1^* dt}{E_2^*} \, \delta(E_\alpha^* - E_\beta^*) \sum_{\alpha\beta}\sum |\langle\beta|T|\alpha\rangle|^2 \qquad \text{B12}$$

To solve the integral over the $\delta$ function we make use of the property

$$\int dx \, \delta(f(x)) = \left|\frac{df}{dx}\right|^{-1}_{x=x_0}$$

where $x_0$ is a solution of the equation $f(x)=0$. Here $x=E_1^*$ and $f(x) = E_\alpha^* - E_\beta^* = E_a^* + E_b^* - E_1^* - E_2^*$. Hence,

$$\frac{df}{dx} = 1 + \frac{dE_2^*}{dE_1^*}$$

In the center of mass system,

$$\bar{p}_1^{*2} = \bar{p}_2^{*2}$$

or

$$(E_1^*)^2 - m_1^2 = (E_2^*)^2 - m_2^2$$

and hence

$$\frac{dE_2^*}{dE_1^*} = \frac{E_1^*}{E_2^*}$$

It follows that

$$\int dE_1^* \; \delta(E_\alpha^* - E_\beta^*) = \frac{E_2^*}{E_1^* + E_2^*} = \frac{E_2^*}{\sqrt{s}}$$

and substitution into Eqn.(B12) gives

$$\sigma_{\alpha\beta} = \frac{1}{8s|\bar{p}_a^*|^2(2\pi)^5} \int dt \; \bar{\sum_\alpha}\sum_\beta \; |\langle\beta|T|\alpha\rangle|^2 \qquad \text{B13}$$

It is evident that the differential cross section is

$$\frac{d\sigma_{\alpha\beta}}{dt} = \frac{1}{8s|p_a^*|^2(2\pi)^5} \bar{\sum_\alpha}\sum_\beta \; |\langle\beta|T|\alpha\rangle|^2 \qquad \text{B14}$$

We can now write

$$\frac{\frac{d\sigma}{dt}(\gamma p \to \phi p)}{\frac{d\sigma}{dt}(\phi p \to \phi p)} = \frac{|\langle\phi p|T|\gamma p\rangle|^2}{|\langle\phi p|T|\phi p\rangle|^2} \; \frac{|\bar{p}_\phi^*|^2}{|\bar{p}_\gamma^*|^2}$$

The ratio of the transition probabilities is expressed by the $\phi$-$\gamma$ coupling constant in vector meson dominance and hence

$$\frac{d\sigma}{dt}(\gamma p \to \phi p) = \frac{|\bar{p}_\phi^*|^2}{|\bar{k}_\gamma^*|^2} \; \frac{\alpha\pi}{\gamma_\phi^2} \; \frac{d\sigma}{dt}(\phi p \to \phi p) \qquad \text{B15}$$

where

$$|\overline{p}^*_\phi|^2 = \frac{\{s - m_p^2 - m_\phi^2\}^2 - 4\, m_p^2\, m_\phi^2}{4\, s}$$

$$|\overline{k}^*_\gamma|^2 = \frac{(s - m_p^2)^2}{4\, s} \qquad \text{B16}$$

$$s = m_p^2 + 2\, m_p\, E_\gamma$$

The threshold energy is given by

$$s = (m_p + m_\phi)^2$$

$$E_\gamma = (m_\phi^2 / 2\, m_p) + m_\phi \qquad \text{B17}$$

# APPENDIX C

## PARTICLE MULTIPLICITIES FOR DIFFRACTIVE DISSOCIATION OF A PROTON

The problem consists of arriving at a reasonable estimate for the number of hadrons resulting from the diffractive dissociation of the proton in the vector meson photoproduction reaction $\gamma p \rightarrow Vp$. The multiplicities are used to predict the fraction of events with 0, 1 and >1 recoil counter signals for the purpose of determining the contribution of inelastic events to the $\rho$, $\phi$ and $\omega$ photoproduction data.

It is assumed that the final system consists of pions and either a proton or a neutron with the overall quantum numbers of the proton. The I-spin state of the proton is

$$|p\rangle = |I, I_3\rangle = |\tfrac{1}{2}, \tfrac{1}{2}\rangle \qquad \text{C1}$$

Therefore, of interest are pion systems with I=0 and 1 only. The charge multiplicities (1,3,5,...) are assumed to be Poisson distributed with the mean of the distribution chosen so that the charge multiplicity=1 probability is about equal to the multiplicity=3 probability, consistent with pp and $\pi^- p$ diffractive dissociation data (Whitmore, 1974).

The 2-pion system is worked out as an example:

$$|\pi\pi\rangle = |I, I_3\rangle \text{ with } I = 2,\ 1,\ 0 \qquad \text{C2}$$

I=2 of no interest

$$I=1,\ I_3=1:\ |11\rangle = \frac{1}{\sqrt{2}}\{|\pi^+\pi^0\rangle - |\pi^0\pi^+\rangle\}$$

$$0:\ |10\rangle = \frac{1}{\sqrt{2}}\{|\pi^+\pi^-\rangle\ |\pi^-\pi^+\rangle\}$$

-1: of no interest

$$I=0,\ I_3=0\quad |00\rangle = \frac{1}{\sqrt{3}}\{|\pi^+\pi^-\rangle - |\pi^0\pi^0\rangle + |\pi^-\pi^+\rangle\}$$

There are thus two allowed states,

$$I=1 \text{ with } I_3=1,0 \quad \text{and} \quad I=0 \text{ with } I_3=0$$

The first state is

$$\begin{aligned}|p\rangle &= \frac{\sqrt{2}}{\sqrt{3}}|1,1;\tfrac{1}{2},\tfrac{-1}{2}\rangle - \frac{1}{\sqrt{3}}|1,0;\tfrac{1}{2},\tfrac{1}{2}\rangle \\ &= \frac{\sqrt{2}}{\sqrt{3}}\{\frac{1}{\sqrt{2}}(|\pi^+\pi^0\rangle - |\pi^0\pi^+\rangle)|n\rangle\} \\ &\qquad - \frac{1}{\sqrt{3}}\{\frac{1}{\sqrt{2}}(|\pi^+\pi^-\rangle - |\pi^-\pi^+\rangle\ |p\rangle\}\end{aligned} \qquad \text{C3}$$

and the second state is

$$\begin{aligned}|p\rangle &= |0,0;\tfrac{1}{2},\tfrac{1}{2}\rangle \\ &= \frac{1}{\sqrt{3}}(|\pi^+\pi^-\rangle - |\pi^0\pi^0\rangle + |\pi^-\pi^+\rangle)|p\rangle\end{aligned} \qquad \text{C4}$$

The probabilities for the different configurations are,

for the first state: $\frac{2}{3}(\pi^+\pi^0 n)$ and $\frac{1}{3}(\pi^+\pi^- p)$ C5

for the second state: $\frac{2}{3}(\pi^+\pi^- p)$ and $\frac{1}{3}(\pi^0\pi^0 p)$ C6

The average of the two states gives the probabilities

$$\frac{1}{2}(\pi^+\pi^-p),\ \frac{1}{3}(\pi^+\pi^0n),\ \frac{1}{6}(\pi^0\pi^0p) \qquad \text{C7}$$

The probabilities for the different configurations in each $N_\pi$-system, where $N_\pi$=0-4, are summarized in the table below.

<u>Notation:</u> $N_\pi$= pion multiplicity

$N_c$= charge multiplicity

ip= i charged pions and a proton, i=0,2,4

in= i charged pions and a neutron, i=1,3,5

| | $N_c=1$ | | $N_c=3$ | | $N_c=5$ | |
|---|---|---|---|---|---|---|
| $N_\pi$ | 0p | 1n | 2p | 3n | 4p | Poisson probability |
| 0 | 1 | | | | | $e^{-\mu}$ |
| 1 | $^1/_3$ | $^2/_3$ | | | | $\mu e^{-\mu}$ |
| 2 | $^1/_6$ | $^1/_3$ | $^1/_2$ | | | $(\mu^2/2)e^{-\mu}$ |
| 3 | $^1/_{20}$ | $^1/_5$ | $^9/_{20}$ | $^3/_{10}$ | | $(\mu^3/6)e^{-\mu}$ |
| 4 | $^1/_{45}$ | $^4/_{45}$ | $^{14}/_{45}$ | $^{16}/_{45}$ | $^2/_9$ | $(\mu^4/24)e^{-\mu}$ |

The charge multiplicity probabilities (Poisson distributed) are then given by

$$P(N_c=1) = e^{-\mu}\{\mu+\frac{1}{2}(\mu^2/2)+\frac{1}{4}(\mu^3/6)+\frac{1}{9}(\mu^4/24)+\ldots\}$$

$$P(N_c=3) = e^{-\mu}\{\frac{1}{2}(\mu^2/2)+\frac{3}{4}(\mu^3/6)+\frac{2}{3}(\mu^4/24)+\ldots\} \qquad \text{C8}$$

$$P(N_c=5) = e^{-\mu}\{\frac{2}{9}(\mu^4/24)+\ldots\}$$

The value for $\mu$ is chosen so that

$$P(N_c=1) \simeq P(N_c=3)$$

that is,

$$\mu \simeq 2.6 \qquad \text{C9}$$

and thus

$$P(N_c=1) \simeq 0.389$$

$$P(N_c=3) \simeq 0.383 \qquad \text{C10}$$

$$P(N_c=5) \simeq 0.031$$

Using the above table, the probabilities for the different final state configurations can be determined. For example,

$$P(\pi^+\pi^0\pi^0 n) = \frac{1}{0.389}\{\frac{1}{5}(\mu^3/6)e^{-\mu}\} = 0.112 \qquad \text{C11}$$

The probabilities for all final states with a given charge multiplicity are listed below.

<u>Charge multiplicity = 1</u> (overall probability $\simeq$ 0.389)

| state | probability |
|---|---|
| $\pi^+ n$ | 0.331 |
| $\pi^0 p$ | 0.166 |
| $\pi^+\pi^0 n$ | 0.215 |
| $\pi^0\pi^0 p$ | 0.108 |
| $\pi^+\pi^0\pi^0 n$ | 0.112 |
| $\pi^0\pi^0\pi^0 p$ | 0.028 |
| $\pi^+\pi^0\pi^0\pi^0 n$ | 0.032 |
| $\pi^0\pi^0\pi^0\pi^0 p$ | 0.008 |
| | 1.0 |

C12

<u>Charge multiplicity = 3</u> (overall probability = 0.383)

| state | probability |
|---|---|
| $\pi^+\pi^-p$ | 0.328 |
| $\pi^+\pi^+\pi^-n$ | 0.170 |
| $\pi^+\pi^-\pi^0p$ | 0.256 |
| $\pi^+\pi^+\pi^-\pi^0n$ | 0.131 |
| $\pi^+\pi^-\pi^0\pi^0p$ | 0.115 |
| | 1.0 |

C13

The fractions of events firing 0, 1 and >1 recoil counters are estimated as

$$\begin{aligned} \text{recoil} &= 0 : \quad 0.02 \\ &= 1 : \quad 0.23 \\ &> 1 : \quad 0.75 \end{aligned}$$

C14

(see Table (IV.C.2)).

# APPENDIX D

## VMD-QUARK MODEL PREDICTION FOR MOMENTUM TRANSFER SLOPE PARAMETER

According to VMD-quark model predictions

$$\sqrt{\frac{d\sigma}{dt}(\gamma p\to\rho p)} = \frac{p_\pi}{k_\gamma}\frac{\sqrt{\alpha\pi}}{\gamma_\rho}\left\{\frac{1}{2}\sqrt{\frac{d\sigma}{dt}(\pi^+ p)} + \frac{1}{2}\sqrt{\frac{d\sigma}{dt}(\pi^- p)}\right\} \qquad \text{D1}$$

where $\gamma_\rho$ is the photon-vector meson coupling constant, $p_\pi$ and $k_\gamma$ are the center of mass momenta of the pion and the photon, respectively (see Appendix B), and $d\sigma/dt(\pi p)$ denotes $\pi^+p$ and $\pi^-p$ elastic scattering. Assuming

$$\frac{d\sigma}{dt} = A\cdot e^{bt}, \quad \int\sqrt{\frac{d\sigma}{dt}}\,dt = \frac{2\sqrt{A}}{b} \qquad \text{D2}$$

Eqn.(D1) can be written as

$$\frac{\sqrt{A}_\rho}{b_\rho} = \frac{p_\pi}{k_\gamma}\frac{\sqrt{\alpha\pi}}{\gamma_\rho}\frac{1}{2}\left\{\frac{\sqrt{A}_+}{b_+} + \frac{\sqrt{A}_-}{b_-}\right\} \qquad \text{D3}$$

where the subscripts $\rho$, + and - indicate quantities (defined by Eqn.(D2)) for $\gamma p\to\rho p$, $\pi^+p\to\pi^+p$ and $\pi^-p\to\pi^-p$, respectively.

Also, Eqn.(D1) at $t = 0$ gives

$$\sqrt{A}_\rho = \frac{p_\pi}{k_\gamma}\frac{\sqrt{\alpha\pi}}{\gamma_\rho}\frac{1}{2}\left\{\sqrt{A}_+ + \sqrt{A}_-\right\} \qquad \text{D4}$$

From Eqns.(D3) and (D4)

$$b_\rho = \frac{\sqrt{A_+} + \sqrt{A_-}}{\dfrac{\sqrt{A_+}}{b_+} + \dfrac{\sqrt{A_-}}{b_-}} \qquad \text{D5}$$

and rearranging,

$$\boxed{b_\rho = \frac{b_+ b_- (\sqrt{A_+} + \sqrt{A_-})}{b_- \sqrt{A_+} + b_+ \sqrt{A_-}} \simeq \frac{1}{2}\,(b_+ + b_-)} \qquad \text{D6}$$

The approximate expression in Eqn.(D6) is obtained by letting $b_+ = b_o + \Delta$ and $b_- = b_o - \Delta$ which gives

$$b_\rho = \frac{b_o^2 - \Delta^2}{b_o - \Delta\,\dfrac{\sqrt{A_+} - \sqrt{A_-}}{\sqrt{A_+} + \sqrt{A_-}}} \simeq \frac{b_o^2 - \Delta^2}{b_o} \simeq b_o = \frac{b_+ + b_-}{2}$$

Eqn.(D6) is also valid for the $\omega$ meson. For the $\phi$ meson the slope parameter is

$$b_\phi = \frac{b^+ b^- b_- (\sqrt{A^+} + \sqrt{A^-} - \sqrt{A_-})}{b^- b_- \sqrt{A^+} + b^+ b_- \sqrt{A^-} - b^+ b^- \sqrt{A_-}} \qquad \text{D7}$$

where the superscripts + and - indicate quantities defined by Eqn.(D2) for $K^+p \to K^+p$ and $K^-p \to K^-p$, respectively, and the subscript - refers to $\pi^-p \to \pi^-p$.

# LIST OF REFERENCES

[ABBHHM, 1969] Aachen-Berlin-Bonn-Hamburg-Heidelberg-Munchen Collaboration (DESY), Phys. Rev. 175, 1669 (1968).

[Abramson, 1976] J. Abramson, D. E. Andrews, J. Harvey, F. Lobkowick, E. N. May, C. A. Nelson Jr., M. E. Nordberg Jr., M. Singer, E. H. Thorndike, Phys. Rev. Lett. 36, 1428 (1976),
and Y. Eisenberg, B. Haber, E. Kogan, U. Karshon, E. E. Ronat, A. Shapira, G. Yekutieli, Nucl. Phys. B104, 61 (1976),
and H. J. Behrend, C. K. Lee, F. Lobkowicz, M. E. Nordberg Jr., E. H. Thorndike, A. A. Wehmann, Phys. Rev. Lett. 26, 151 (1971).

[Alexander, 1975] G. Alexander, O. Benary, J. Gandsman, D. Lissauer, A. Levy, Y. Oren, L. M. Rosenstein, Phys. Lett. 57B, 487 (1975),
and Y. Eisenberg, B. Haber, E. Kogan, U. Karshon, E. E. Ronat, A. Shapira, G. Yekutieli, Nucl. Phys. B104, 61 (1976),
and P. Benz, O. Braun, H. Butenschon, D. Gall, U. Idschok, C. Kiesling, G. Knies, K. Muller, B. Nellen, R. Schiffer, P. Schlamp, H. J. Schnackers, P. Soding, J. Stiewe, F. Storim, Nucl. Phys. B79, 10 (1974).

[Alvensleben, 1970] H. Alvensleben, U. Becker, M. Chen, K. J. Cohen, R. T. Edwards, T. M. Knasel, R. Marshall, D. J. Quinn, M. Rohde, G. H. Sanders, H. Schubel, S. C. C. Ting, Phys. Ref. Lett. 25, 1377 (1970), and Nucl. Phys. B25, 342 (1971),
and P. J. Biggs, D. W. Braben, R. W. Clifft, E. Gabathuler, R. E. Rand, Phys. Ref. Lett. 27, 1157 (1971).

[Alvensleben, 1971] H. Alvensleben, U. Becker, W. Busza, M. Chen, K. J. Cohen, R. T. Edwards, P. M. Mantsch, R. Marshall, T. Nash, M. Rohde, H. F. W. Sadrozinski, G. H. Sanders, H. Schubel, S. C. C. Ting, Sau-Lan Wu, Phys. Rev. Lett. 27, 444 (1971).

[Ambats, 1974] I. Ambats, D. S. Ayres, R. Diebold, A. F. Greene, S. L. Kramer, A. Lesnik, D. R. Rust, C. E. W. Ward, A. B. Wicklund, D. D. Yovanovitch, Phys. Rev. D9, 1179 (1974).

[Anderson, 1970] R. Anderson, D. Gustavson, J. Johnson, W. G. Jones, D. Kreinick, F. Murphy, D. Ritson,

R. Weinstein, B. H. Wiik (SLAC),
Phys. Rev. D1, 27 (1970).

[Anderson, 1971] R. Anderson, D. Gustavson, J. Johnson,
I. Overman, D. M. Ritson, R. Talman, B. H. Wiik,
D. Worcester,
Phys. Ref. D4, 3245 (1971).

[Ayres, 1977] D. S. Ayres, R. L. Anderson, D. S. Barton,
A. E. Brenner, J. Butler, D. Cutts, C. DeMarzo, R. Diebold,
J. E. Elias, J. Fines, J. I. Friedman, B. Gittelman,
B. Gottschalk, L. Guerriero, D. Gustavson, H. W. Kendall,
R. E. Lanou Jr., P. Lavopa, L. J. Levinson, J. Litt,
E. C. Loh, G. J. Maclay, G. Maggi, J. T. Massimo,
R. Meunier, G. Mikenberg, B. Nelson, F. Posa, K. Rich,
D. M. Ritson, L. Rosenson, G. Selvaggi, M. Sogard,
P. Spinelli, F. Waldner, G. A. Weitsch, R. Verdier
(Fermilab Single Arm Spectrometer Group),
Phys. Rev. D15, 3105 (1977).

[Ballam, 1970] J. Ballam, H. H. Bingham, G. B. Chadwick,
W. B. Fretter, R. Gearhart, Z. G. T. Guiragossian,
M. Menke, R. H. Milburn, K. C. Moffeit, J. J. Murray,
W. J. Podolsky, M. S. Rabin, A. H. Rosenfeld, P. Seyboth,
A. Shapira, C. K. Sinclair, I. O. Skillicorn,
R. Windmolders, G. Wolf (SLAC-Berkeley-Tufts
Collaboration),
Phys. Ref. Lett. 24, 1364 (1970).

[Ballam, 1972] J. Ballam, H. H. Bingham, G. B. Chadwick,
W. B. Fretter, R. Gearhart, Z. G. T. Guiragossian,
R. H. Milburn, k. C. Moffeit, J. J. Murray, W. J. Podolsky,
M. S. Rabin, A. H. Rosenfeld, P. Seyboth, C. K. Sinclair,
I. O. Skillicorn, H. Spitzer, R. Windmolders, G. Wolf
(SLAC-Berkeley-Tufts Collaboration),
Phys. Ref. D5, 545 (1972).

[Ballam, 1973] J. Ballam, H. H. Bingham, G. B. Chadwick,
W. B. Fretter, Y. Eisenberg, E. Kogan, K. C. Moffeit,
W. J. Podolsky, M. S. Rabin, A. H. Rosenfeld, P. Seyboth,
I. O. Skillicorn, G. Smadja, H. Spitzer, G. Wolf (SLAC-
Berkeley Collaboration),
Phys. Ref. D7, 3150 (1973); see also [Ballam, 1970].

[Bauer, 1978] T. H. Bauer, R. D. Spital, D. R. Yennie,
F. M. Pipkin,
Rev. Mod. Phys. 50, 261 (1978).

[Behrend, 1978] H. J. Behrend, J. Bodenkamp, D. C. Fries,
P. Heine, W. P. Hesse, H. Hirschmann, A. Markou,
W. A. McNeely Jr., E. Seitz (DESY),
DESY publication 78/26 (May 1978, and Nucl. Phys. B144, 22
(1978).

Preliminary results in Phys. Lett. 56B, 408 (1975).
The integrated $\phi$ cross section shown in Fig. (IV.D.3) is calculated from $\sigma=1.05\cdot\int(d\sigma/dt)dt$ evaluated between $t_{min}$ and $t\rightarrow\infty$ with $d\sigma/dt=A\cdot\exp(bt)$, where A and b are obtained from fits to the data with $-t<0.4$ GeV$^2$. The constant 1.05 accounts for the flattening of the t distribution for $-t>0.4$ GeV$^2$ as observed by other experiments.

[Benz, 1974] P. Benz, O. Braun, H. Butenschon, D. Gall, U. Idschok, C. Kiesling, G. Knies, K. Muller, B. Nellen, R. Schiffer, P. Schlamp, H. J. Schnackers, P. Soding, J. Stiewe, F. Storim, Nucl. Phys. B79, 10 (1974),
and Y. Eisenberg, B. Haber, E. Kogan, U. Karshon, E. E. Ronat, A. Shapira, G. Yekutieli, Nucl. Phys. B104, 61 (1976),
and H. G. Hilpert, P. Benz, S. Brandt, O. Braun, H. Finger, U. Idschok, H. Kowalski, P. Lauscher, K. Muller, B. Nellen, E. Paul, P. Schlamp, P. Soding, H. Spitzer, J. Stiewe, F. Storim, J. Weigl, H. J. Willutzki, Nucl. Phys. B21, 93 (1970).

[Berger, 1972] C. Berger, n. Mistry, L. Roberts, R. Talman, P. Walstrom (Cornell), Phys. Lett. 39B, 659 (1972).

[Bertanza, 1962] L. Bertanza, V. Brisson, P. L. Connolly, M. Goldberg, L. Gray, E. L. Hart, J. Leitner, S. Lichtman, I. S. Mittra, G. C. Moneti, J. Westgard, Phys. Ref. Lett. 9, 180 (1962),
see also Phys. Ref. Lett. 10, 371 (1963).

[Besch, 1974] H. J. Besch, G. Hartmann, R. Kose, F. Krautschneider, W. Paul, U. Trinks (Bonn), Nucl. Phys. B70, 257 (1974).

[Biggs, 1970a] P. J. Biggs, R. W. Clifft, E. Gabathuler, P. Kitching, R. E. Rand, Phys. Ref. Lett. 24, 1201 (1970),
and H. J. Behrend, C. K. Lee, F. Lobkowicz, M. E. Nordberg Jr., E. H. Thorndike, A. A. Wehmann, Phys. Ref. Lett. 27, 61 (1971),
and H. Alvensleben, U. Becker, W. Busza, M. Chen, K. J. Cohen, R. T. Edwards, P. M. Mantsch, R. Marshall, T. Nash, M. Rohde, H. F. W. Sadrozinski, G. H. Sanders, H. Schubel, S. C. C. Ting, Sau-Lan Wu, Phys. Ref. Lett. 27, 888 (1971),
and K. C. Moffeit, J. Ballam, H. H. Bingham, G. B. Chadwick, W. B. Fretter, R. Gearhart, Z. G. T. Guiragossian, M. Menke, R. H. Milburn, J. J. Murray, W. J. Podolsky, M. S. Rabin, A. H. Rosenfeld, P. Seyboth, A. Shapira, C. K. Sinclair, I. O. Skillicorn, R. Windmolders, G. Wolf, Nucl. Phys. B29, 349 (1971).

[Biggs, 1970b] P. J. Biggs, D. W. Braben, R. W. Clifft, E. Gabathuler, P. Kitching, R. E. Rand, Phys. Ref. Lett. 24, 1197 (1970), and H. Alvensleben, U. Becker, W. K. Bertram, M. Chen, K. J. Cohen, R. T. Edwards, T. M. Knasel, R. Marshall, D. J. Quinn, M. Rohde, G. H. Sanders, H. Schubel, S. C. C. Ting, Phys. Ref. Lett. 25, 1373 (1970), and Nucl. Phys. B25, 333 (1971).

[Butler, 1973] W. R. Butler, D. G. Coyne, G. Goldhaber, J. MacNaughton, G. H. Trilling, Phys. Rev. D7, 3177 (1973).

[Caldwell, 1978] D. O. Caldwell, J. P. Cumalat, P. J. Davis, R. M. Egloff, A. M. Eisner, M. E. B. Franklin, A. Lu, G. J. Luste, J. F. Martin, R. J. Morrison, F. V. Murphy, T. Nash, J. D. Prentice, S. J. Yellin (FNAL), Phys. Rev. Lett. 40, 1222 (1978).

[Caldwell, 1979] D. O. Caldwell, J. P. Cumalat, P. J. Davis, M. G. Donnelly, R. M. Egloff, A. M. Eisner, A. Lu, G. J. Luste, J. F. Martin, R. J. Morrison, F. V. Murphy, T. Nash, J. D. Prentice, S. J. Yellin (FNAL), Phys. Rev. Lett. 42, 553 (1979).

[Carroll, 1976] A. S. Carroll, Phys. Lett. 61B, 303 (1976).

[Criegee, 1970] L. Criegee, P. W. Dougan, G. Franke, G. Loffler, K. P. Schuler, U. Timm, H. Werner, W. Zimmermann, Phys. Rev. Lett. 25, 1306 (1970), and G. Diambrini-Palazzi, G. McClellan, N. Mistry, P. Mostek, H. Ogren, J. Swartz, R. Talman, Phys. Rev. Lett. 25, 478 (1970).

[Cumalat, 1977] J. P. Cumalat, thesis, University of California, Santa Barbara, 1977 (unpublished).

[Damashek, 1970] M. Damashek, F. J. Gilman, Phys. Rev. D1, 1319 (1970).

[Das, 1967] T. Das, V. S. Mathur, S. Okubo, Phys. Rev. Lett. 19, 470 (1967).

[Drell, 1961] S. D. Drell, Rev. Mod. Phys. 33, 458 (1961).

[Eisenberg, 1972] Y. Eisenberg, J. Ballam, G. B. Chadwick, S. Dagan, B. Haber, A. Levy, M. M. Menke, E. E. Ronat, P. Seyboth, A. Shapira, Y. Stahl, G. Yekutieli (SLAC), Phys. Rev. D5, 15 (1972).

[Eisenberg, 1974] Y. Eisenberg,
Phys. Rev. D9, 2187 (1974).

[Eisenberg, 1976] Y. Eisenberg, B. Haber, E. Kogan,
U. Karshon, E. E. Ronat, A. Shapira, G. Yekutieli,
Nucl. Phys. B104, 61 (1976),
and P. Benz, O. Braun, H. Butenschon, D. Gall,
U. Idschok, C. Kiesling, G. Knies, K. Muller, B. Nellen,
R. Schiffer, P. Schlamp, H. J. Schnackers, P. Soding,
J. Stiewe, F. Storim,
Nucl. Phys. B79, 10 (1974),
and G. McClellan, N. Mistry, P. Mostek, H. Ogren,
A. Silverman, J. Swartz, R. Talman,
Phys. Rev. D4, 2683 (1971),
and H. G. Hilpert, S. Brandt, O. Braun, U. Idschok,
G. Knies, A. Kolb, P. Lauscher, D. Luke, M. Matziolis,
K. Muller, P. Raulefs, P. Schlamp, H. Spitzer, J. Stiewe,
F. Storim, J. Weigl,
Nucl. Phys. B23, 45 (1970).

[Erwin, 1961] A. Erwin, R. March, W. D. Walker, E. West,
Phys. Ref. Lett. 6, 628 (1961).

[Foley, 1963] K. J. Foley, S. J. Lindenbaum, W. A. Love,
S. Ozaki, J. J. Russell, L. C. L. Yuan (Brookhaven),
Phys. Rev. Lett. 11, 425 (1963).

[Francis, 1977] W. R. Francis, H. L. Anderson,
V. K. Bharadwaj, N. E. Booth, R. M. Fine, B. A. Gordon,
R. H. Heisterberg, R. G. Hicks, T. B. W. Kirk,
G. I. Kirkbride, W. A. Loomis, H. S. Matis, L. W. Mo,
L. C. Myrianthopoulos, F. M. Pipkin, S. H. Pordes,
T. W. Quirk, W. D. Shambroom, A. Skuja, L. J. Verhey,
W. S. C. Williams, Richard Wilson, S. C. Wright (FNAL),
Phys. Rev. Lett. 38, 633 (1977).

[Freund, 1967] P. G. O. Freund,
Nuovo Cimento 48A, 541 (1967),
and H. Joos,
Phys. Lett. 24B, 103 (1967),
and K. Kajantie, J. S. Trefil,
Phys. Lett. 24B, 106 (1967),
and V. Barger, D. Cline,
Phys. Rev. Lett. 24, 1313 (1970).

[Gell-Mann, 1962] M. Gell-Mann, D. Sharp, W. G. Wagner,
Phys. Rev. Lett. 8, 261 (1962).

[Glauber, 1966] V. Franco and R. J. Glauber,
Phys. Rev. 142, 1195 (1966).

[Gounaris, 1968] The coupling constants obtained from the
storage ring measurements are corrected for the finite

width of the vector meson line shapes:
G. J. Gounaris, J. J. Sakurai,
Phys. Rev. Lett. 21, 244 (1968),
and F. M. Renard,
Nucl. Phys. B15, 267 (1970).
See [Leith, 1977] for values of coupling constants.

[Halpern, 1972] H. R. Halpern, R. L. Anderson, B. Gottschalk, D. B. Gustavson, R. Prepost, D. M. Ritson, D. H. Tompkins, G. A. Weitsch, B. H. Wiik,
Phys. Rev. Lett. 29, 1425 (1972).

[Harari, 1969] H. Harari, Proceedings of IV International Symposium of Electron and Photon Physics, Liverpool (1969) (see also [Leith, 1977] and [Eisenberg, 1976]).

[Jackson, 1964] J. D. Jackson,
Nuovo Cimento 34, 1644 (1964).

[Leith, 1977] D. W. G. S. Leith, SLAC-PUB-1878 (January 1977) and in Electromagnetic Interactions of Hadrons, ed. A. Donnachie, G. Shaw, Plenum Publishing Corp. (1978).

[Lipkin, 1966] H. J. Lipkin,
Phys. Rev. Lett. 16, 1015 (1966),
and H. Joos,
Phys. Lett. 24B, 103 (1967),
and B. Margolis,
Nucl. Phys. B6, 687 (1968),
and Yehuda Eisenberg,
Phys. Rev. D9, 2187 (1974),
and H. J. Lipkin,
Nucl. Phys. B78, 381 (1974),
and H. J. Lipkin,
Phys. Rev. D11, 1827 (1975).

[Longo, 1975] Egidio Longo, Ignazio Sestili,
Nucl. Instr. and Methods 128, 283 (1975), and references therein.

[McClellan, 1971] G. McClellan, N. Mistry, P. Mostek, H. Ogren, A. Osborne, J. Swartz, R. Talman, G. Diambrini-Palazzi,
Phys. Rev. Lett. 26, 1593 (1971).

[McClellan, 1971a] G. McClellan, N. Mistry, P. Mostek, H. Ogren, A. Silverman, J. Swartz, R. Talman,
Phys. Rev. D4, 2683 (1971).

[Maglic, 1961] B. Maglic, L. W. Alvarez, A. H. Rosenfeld, M. L. Stevenson,
Phys. Ref. Lett. 7, 178 (1961).

[Morrison, 1975] R. J. Morrison et al., "A Light Pulser System for Shower Counter Arrays at Fermilab Energies", Internal Report, Department of Physics, University of California, Santa Barbara, California (1975).

[Morrison, 1977] R. J. Morrison, J. Cumalat, A. M. Eisner, C. Lauer,
Nucl. Instr. and Methods 143, 311 (1977).

[Nash, 1976] T. Nash, A. Belousov, D. O. Caldwell, J. P. Cumalat, P. J. Davis, R. M. Egloff, A. M. Eisner, B. Govorkov, G. J. Luste, R. J. Morrison, F. V. Murphy, J. D. Prentice, S. J. Yellin,
Phys. Rev. Lett. 36, 1233 (1976).

[Oakes, 1967] R. J. Oakes, J. J. Sakurai,
Phys. Rev. Lett. 19, 1266 (1967).

[Okubo, 1977] S. Okubo,
Phys. Rev. D16, 2336 (1977).

[Particle properties, 1976] Particle Data Group,
Rev. of Modern Phys. 48, No. 2, Part II (April, 1976).

[Particle properties, 1978] Particle Data Group,
Phys. Lett. 75B, No. 1 (April, 1978).

[Perkins, 1972] D. H. Perkins, Introduction to High Energy Physics, Addison-Wesly (1972).

[Renard, 1972] F. M. Renard in Springer Tracts in Modern Physics, ed. G. Hohler, volume 63 (1972), Springer-Verlag Berlin Heidelberg New York.

[Rossi, 1952] B. Rossi, High Energy Particles, Prentice-Hall, New York, 1952.

[Sakurai, 1960] J. J. Sakurai,
Ann. Phys. 11, 1 (1960),
and M. Gell-Mann, F. Zachariasen,
Phys. Rev. 124, 953 (1961),
and N. M. Kroll, T. D. Lee, B. Zumino,
Phys. Rev. 157, 1376 (1967),
and T. D. Lee, S. Weinberg, B. Zumino,
Phys. Rev. Lett. 18, 1029 (1967).

[Schildknecht, 1976] R. Devenish, D. Schildknecht,
Phys. Rev. D14, 93 (1976),
and H. Fraas, B. J. Read, D. Schildknecht,
Nucl. Phys. B88, 301 (1975),
and J. J. Sakurai, D. Schildknecht,
Phys. Lett. 40B, 121 (1972).

[Schilling, 1971] K. Schilling, P. Seyboth, G. Wolf,
Nucl. Phys. B15, 397 (1971).

[Soding, 1965] P. Soding,
Phys. Lett. 19, 702 (1965),
and A. S. Krass,
Phys. Rev. 159, 1496 (1967),
and J. Pumplin,
Phys. Rev. D2, 1859 (1970),
and T. Bauer, D. R. Yennie,
Phys. Rev. Lett. 25, 485 (1970).

[Spital, 1974] R. Spital, D. R. Yennie,
Phys. Rev. D9, 126 (1974).

[Tapper, 1965] R. J. Tapper, Rutherford High Energy Laboratory
Report No. NIRL/R/95 (March 1965).

[Tsai, 1974] Y. S. Tsai,
Rev. Mod. Phys. 46, 815 (1974).

[Whitmore, 1974] J. Whitmore,
Phys. Reports 10, 273 (1974).

[Williams, 1971] W. S. C. Williams, An Introduction to
Elementary Particles, Academic Press (1971).

[Wolf, 1971] Gunter Wolf,
Nucl. Phys. B26, 317 (1971).

[Yennie, 1971] D. R. Yennie in Hadronic Interactions of
Electrons and Photons, ed. J. Cumming, H. Osborn,
Academic Press (1971)
(see also Phys. Rev. 182, 1595 (1969)).